



applied sciences

Efficient Damping and Isolation Systems for Civil Structures

Edited by
Felix Weber

Printed Edition of the Special Issue Published in *Applied Sciences*

Efficient Damping and Isolation Systems for Civil Structures

Efficient Damping and Isolation Systems for Civil Structures

Editor

Felix Weber

MDPI • Basel • Beijing • Wuhan • Barcelona • Belgrade • Manchester • Tokyo • Cluj • Tianjin



Editor

Felix Weber
Maurer Switzerland GmbH
MAURER
Pfaffhausen
Switzerland

Editorial Office

MDPI
St. Alban-Anlage 66
4052 Basel, Switzerland

This is a reprint of articles from the Special Issue published online in the open access journal *Applied Sciences* (ISSN 2076-3417) (available at: www.mdpi.com/journal/applsci/special_issues/Efficient_Damping_and_Isolation_Systems_for_Civil_Structures).

For citation purposes, cite each article independently as indicated on the article page online and as indicated below:

LastName, A.A.; LastName, B.B.; LastName, C.C. Article Title. <i>Journal Name</i> Year , <i>Volume Number</i> , Page Range.
--

ISBN 978-3-0365-6561-3 (Hbk)

ISBN 978-3-0365-6560-6 (PDF)

Cover image courtesy of Felix Weber

© 2023 by the authors. Articles in this book are Open Access and distributed under the Creative Commons Attribution (CC BY) license, which allows users to download, copy and build upon published articles, as long as the author and publisher are properly credited, which ensures maximum dissemination and a wider impact of our publications.

The book as a whole is distributed by MDPI under the terms and conditions of the Creative Commons license CC BY-NC-ND.

Contents

Felix Weber

Special Issue on “Efficient Damping and Isolation Systems for Civil Structures”

Reprinted from: *Appl. Sci.* **2023**, *13*, 965, doi:10.3390/app13020965 1

Paolo Casini and Fabrizio Vestroni

Mitigation of Structural Vibrations of MDOF Oscillators by Modal Coupling Due to Hysteretic Dampers

Reprinted from: *Appl. Sci.* **2022**, *12*, 10079, doi:10.3390/app121910079 3

Máté Péntek, Andreas Riedl, Kai-Uwe Bletzinger and Felix Weber

Investigating the Vibration Mitigation Efficiency of Tuned Sloshing Dampers Using a Two-Fluid CFD Approach

Reprinted from: *Appl. Sci.* **2022**, *12*, 7033, doi:10.3390/app12147033 17

Felix Weber, Fredrik Borchsenius, Johann Distl and Christian Braun

Performance of Numerically Optimized Tuned Mass Damper with Inerter (TMDI)

Reprinted from: *Appl. Sci.* **2022**, *12*, 6204, doi:10.3390/app12126204 41

Michael Reiterer and Janez Schellander

A Novel Single Tube Semi-Active Tuned Liquid Gas Damper for Suppressing Horizontal Vibrations of Tower-like Structures

Reprinted from: *Appl. Sci.* **2022**, *12*, 3301, doi:10.3390/app12073301 57

Ryo Majima, Shigeki Sakai and Taiki Saito

Development of Vibration Control Structure on Suspended Ceiling Using Pulley Mechanism

Reprinted from: *Appl. Sci.* **2022**, *12*, 3069, doi:10.3390/app12063069 79

Mostafa Farajian, Mohammad Iman Khodakarami and Pejman Sharafi

Effect of MetaFoundation on the Seismic Responses of Liquid Storage Tanks

Reprinted from: *Appl. Sci.* **2022**, *12*, 2514, doi:10.3390/app12052514 101

Felix Weber, Simon Spensberger, Florian Obholzer, Johann Distl and Christian Braun

Semi-Active Cable Damping to Compensate for Damping Losses Due to Reduced Cable Motion Close to Cable Anchor

Reprinted from: *Appl. Sci.* **2022**, *12*, 1909, doi:10.3390/app12041909 123

Gyeong-Hoi Koo, Jin-Young Jung, Jong-Keun Hwang, Tae-Myung Shin and Min-Seok Lee

Vertical Seismic Isolation Device for Three-Dimensional Seismic Isolation of Nuclear Power Plant Equipment—Case Study

Reprinted from: *Appl. Sci.* **2021**, *12*, 320, doi:10.3390/app12010320 141

Zhenyuan Gu, Yahui Lei, Wangping Qian, Ziru Xiang, Fangzheng Hao and Yi Wang

An Experimental Study on the Mechanical Properties of a High Damping Rubber Bearing with Low Shape Factor

Reprinted from: *Appl. Sci.* **2021**, *11*, 10059, doi:10.3390/app112110059 163

Editorial

Special Issue on “Efficient Damping and Isolation Systems for Civil Structures”

Felix Weber 

Maurer Switzerland GmbH, Grossplatzstrasse 24, 8118 Pfaffhausen, Switzerland; f.weber@maurer.eu

Civil engineering structures may vibrate due to different sources of excitations such as earthquakes, wind, traffic, humans, etc. The resulting vibrations may not be acceptable from the perspective of vibration comfort or can even impair the structure’s safety. Depending on the excitation mechanism, anti-vibration measures range from increasing the structural damping using local dampers, decoupling the structure from the disturbance using vibration isolators and compensating for the excitation forces using vibration compensators. These three basic anti-vibration approaches were mainly developed over the last two centuries and are described in-depth in, e.g., Den Hartog’s famous book *Mechanical Vibrations*, first edited in 1934. Driven by the steadily increasing requirements of vibration reduction measures, engineers and researchers were, and still are, focused on further developing anti-vibration systems. New materials and computer technology have made it possible to consider not only passive systems but also anti-vibration systems with adaptive properties or properties controlled in real time. As a result, the variety and complexity of newly developed anti-vibration systems are very wide.

This Special Issue aimed to collect some of the recent advances in the field of efficient damping and isolation systems for civil engineering structures. A total of nine papers are published in this Special Issue. Casini and Vestroni [1] investigate the impact of hysteretic dampers on the total damping of civil structures that are modelled as multi-degree-of-freedom systems. Due to the nonlinear dynamics of hysteretic dampers, the phenomenon of modal coupling is demonstrated and explained. Péntek et al. [2] analyse the efficiency of Tuned Sloshing Dampers (TSD) at reducing the acceleration of wind-excited tall buildings and compared the results with those of the well-known Tuned Mass Damper (TMD). The paper by Weber et al. [3] on Tuned Mass Dampers with Inerters (TMDI) investigates the efficiency of these devices according to different TMDI topologies and with both analytically derived and numerically optimized TMDI parameters. Reiterer and Schellander [4] describe and analyse a new type of a Tuned Liquid Column Damper (TLCD), which only consists of one horizontal tube filled partially with water and partially with gas. This Featured Paper demonstrates that significant advances in the field of vibration compensation are possible. Majima et al. [5] present an innovative idea for how to use the vibrations of suspended ceilings to operate local dampers using the relative motion between the suspended ceilings and the main structure, thereby increasing the total damping of the building. Farajian et al. [6] describe an interesting approach to make liquid storage tanks safer against seismic excitation by including meta materials in the foundation. The paper by Weber et al. [7] on cable damping by transverse dampers shows that real-time controlled, semi-active transverse cable dampers can compensate for the efficiency losses of passive transverse cable dampers due to cable bending rigidity. Koo et al. [8] present an interesting case study on the challenging task of isolating vulnerable buildings, in this case, a nuclear power plant, from seismic excitation in all three principal directions. Gu et al. [9] describe an experimental study on High-Damping Rubber Bearings (HDRB) with low shape factors for various test conditions.

After approximately one year, the Special Issue on “Efficient Damping and Isolation Systems for Civil Structures” is now closed. Nevertheless, further research and develop-

Citation: Weber, F. Special Issue on “Efficient Damping and Isolation Systems for Civil Structures”. *Appl. Sci.* **2023**, *13*, 965. <https://doi.org/10.3390/app13020965>

Received: 21 December 2022

Accepted: 31 December 2022

Published: 11 January 2023



Copyright: © 2023 by the author. Licensee MDPI, Basel, Switzerland. This article is an open access article distributed under the terms and conditions of the Creative Commons Attribution (CC BY) license (<https://creativecommons.org/licenses/by/4.0/>).

ment are needed to make the built environment more resilient and safer against undesirable structural vibrations.

Funding: This research received no external funding.

Acknowledgments: Thanks go to all the authors, peer reviewers and staff of MDPI for their valuable contributions to this Special Issue.

Conflicts of Interest: The author declares no conflict of interest.

References

1. Casini, P.; Vestroni, F. Mitigation of Structural Vibrations of MDOF Oscillators by Modal Coupling Due to Hysteretic Dampers. *Appl. Sci.* **2022**, *12*, 10079. [CrossRef]
2. Péntek, M.; Riedl, A.; Bletzinger, K.-U.; Weber, F. Investigating the Vibration Mitigation Efficiency of Tuned Sloshing Dampers Using a Two-Fluid CFD Approach. *Appl. Sci.* **2022**, *12*, 7033. [CrossRef]
3. Weber, F.; Borchsenius, F.; Distl, J.; Braun, C. Performance of Numerically Optimized Tuned Mass Damper with Inerter (TMDI). *Appl. Sci.* **2022**, *12*, 6204. [CrossRef]
4. Reiterer, M.; Schellander, J. A Novel Single Tube Semi-Active Tuned Liquid Gas Damper for Suppressing Horizontal Vibrations of Tower-like Structures. *Appl. Sci.* **2022**, *12*, 3301. [CrossRef]
5. Majima, R.; Sakai, S.; Saito, T. Development of Vibration Control Structure on Suspended Ceiling Using Pulley Mechanism. *Appl. Sci.* **2022**, *12*, 3069. [CrossRef]
6. Farajian, M.; Khodakarami, M.I.; Sharafi, P. Effect of MetaFoundation on the Seismic Responses of Liquid Storage Tanks. *Appl. Sci.* **2022**, *12*, 2514. [CrossRef]
7. Weber, F.; Spensberger, S.; Obholzer, F.; Distl, J.; Braun, C. Semi-Active Cable Damping to Compensate for Damping Losses Due to Reduced Cable Motion Close to Cable Anchor. *Appl. Sci.* **2022**, *12*, 1909. [CrossRef]
8. Koo, G.-H.; Jung, J.-Y.; Hwang, J.-K.; Shin, T.-M.; Lee, M.-S. Vertical Seismic Isolation Device for Three-Dimensional Seismic Isolation of Nuclear Power Plant Equipment—Case Study. *Appl. Sci.* **2022**, *12*, 320. [CrossRef]
9. Gu, Z.; Lei, Y.; Qian, W.; Xiang, Z.; Hao, F.; Wang, Y. An Experimental Study on the Mechanical Properties of a High Damping Rubber Bearing with Low Shape Factor. *Appl. Sci.* **2021**, *11*, 10059. [CrossRef]

Disclaimer/Publisher's Note: The statements, opinions and data contained in all publications are solely those of the individual author(s) and contributor(s) and not of MDPI and/or the editor(s). MDPI and/or the editor(s) disclaim responsibility for any injury to people or property resulting from any ideas, methods, instructions or products referred to in the content.

Article

Mitigation of Structural Vibrations of MDOF Oscillators by Modal Coupling Due to Hysteretic Dampers

Paolo Casini * and Fabrizio Vestroni

Department of Structural and Geotechnical Engineering, Sapienza University of Rome, 00184 Rome, Italy

* Correspondence: p.casini@uniroma1.it

Abstract: In civil engineering, structural elements characterized by hysteresis are often encountered, such as materials with limited elastic fields, microsliding friction and elastomeric absorbers. Hysteretic nonlinearities produce a wide variety of dynamical phenomena, such as significant modal coupling, bifurcations and superabundant modes. This paper investigates nonlinear modal interactions in the dynamic response of a two-degree-of-freedom system (2DOF) with hysteretic elements. These phenomena are notably important in internal resonance conditions, where modal interactions produce strong modifications in the response with possible beneficial effects. In specific conditions, the transfer of energy between the two modes leads to a notable reduction in the maximum response amplitude; the exploitation of this feature to achieve vibration mitigation of the forced response is the main goal of the paper. Two configurations are investigated: the hysteretic element at the top (vibration damper) and the hysteretic element at the base (isolator). In both cases, several internal resonance conditions occur since, by increasing the excitation intensity, the frequencies of the hysteretic system change, as well as their ratio. Qualitative similar results are obtained, characterized by a transfer of energy between the two modes. For both configurations, the usefulness of exploiting these nonlinear phenomena in vibration mitigation has been shown.

Keywords: hysteresis; internal resonances; nonlinear modal interaction; vibration mitigation

Citation: Casini, P.; Vestroni, F. Mitigation of Structural Vibrations of MDOF Oscillators by Modal Coupling Due to Hysteretic Dampers. *Appl. Sci.* **2022**, *12*, 10079. <https://doi.org/10.3390/app121910079>

Academic Editor: Felix Weber

Received: 27 July 2022

Accepted: 29 September 2022

Published: 7 October 2022

Publisher's Note: MDPI stays neutral with regard to jurisdictional claims in published maps and institutional affiliations.



Copyright: © 2022 by the authors. Licensee MDPI, Basel, Switzerland. This article is an open access article distributed under the terms and conditions of the Creative Commons Attribution (CC BY) license (<https://creativecommons.org/licenses/by/4.0/>).

1. Introduction

In the last decades, great interest has been given to the dynamic phenomena typical of nonlinear systems in view of exploiting them to mitigate the effects of dynamic excitations [1–4]. One of the usual techniques used to reduce structural vibration is to introduce elements that guarantee a higher dissipation capacity [5]; here, the choice of introducing hysteretic elements allows the combination of two strategies, which increase the ability of the structure to dissipate energy and, at the same time, exploit the beneficial aspects of the nonlinear dynamic coupling caused by the hysteresis itself [6–9].

The variety of the nonlinear phenomena is very large [10]; in particular, the modification of the modal quantities, with the oscillation amplitude, assumes great importance and entails change in the natural frequencies and in the linear modes. They are no longer orthogonal, and in a periodic cycle, they change their shape, leading to modal trajectories that are no longer straight in the configuration plane [11,12]. The occurrence of internal resonance conditions is easily met, and in these conditions, the modal coupling is exalted [4,7].

Several nonlinear motions can take place, such as multifrequencies or quasiperiodic and chaotic oscillations [10,13,14]; however, the attention here is focused on more robust phenomena related to periodic motion and features related to cases of strong nonlinearities. Under these conditions, an unusual phenomenon occurs when a novel mode arises with respect to the linear ones, as already observed in [7,11,15,16].

Hysteretic behavior is widespread among materials and elements; it is easily encountered in civil, mechanical, aeronautical and electrical engineering, and it is characterized by an intrinsic capacity for energy dissipation [6–9,17,18]. Some examples are materials

with limited elastic fields, elastomeric absorbers, shape-memory alloys, contacts exhibiting microsliding friction and magnetostrictive materials. Compared to geometric nonlinearities, those introduced by hysteresis can produce more marked effects on the dynamic response [14,17–22] and give rise to phenomena typical of nonlinear dynamics, such as modal coupling, bifurcations and the emergence of superabundant modes [12,16,23,24].

A system is said to be endowed with hysteresis if the output depends, in a rate-independent way, on the history of the input [25]; however, this definition does not consider that rate-dependent hysteresis can be encountered in a number of applications involving smart materials, piezoelectric actuators or other specific devices [26]. According to this definition, the main characteristic of hysteresis is thus its dependence on the history of the input; while rate independence relatively eases the treatment of the problem, the dependence on the history makes it very difficult to obtain analytically tractable formulations. Thus, beyond the high number of different restoring forces encountered in the real world, this explains the high number of models proposed in the literature, even when limited to the mechanical field. Among the differential models, the Bouc–Wen model [27,28] was adopted because it is very versatile in describing various hysteretic behaviors and simple due to its ability to give analytical piecewise smooth representations of stress–strain relationships. The versatility of the model in describing restoring forces with different characteristics has been demonstrated in several papers [14,29–31]; however, here, the Bouc–Wen law was adopted in its basic formulation because the interest is mainly devoted to exploiting the use of generic hysteretic behaviors for vibration mitigation.

For this aim, a 2DOF system with one hysteretic element, representative of a multidegree-of-freedom system under harmonic excitation, was investigated. Two configurations were considered: in the first, the hysteretic element was between the two masses, and in the second, it was between the base and the first mass, developing and enlarging the results already obtained separately in [4,7] and updating the cases developed in [32] with specific attention to vibration mitigation. The favorable effects in the mitigation of the system response through the combined use of the nonlinear dynamic phenomena and the high dissipation capacity of hysteretic elements were illustrated, showing a very promising area for structural applications.

2. Response to Harmonic Excitation of a Hysteretic SDOF Oscillator

Several models have been proposed in the literature to represent hysteretic behavior. For its simplicity and versatility, the differential model by Bouc–Wen is used here; by properly tuning the model parameters, it is possible to capture the real mechanical characteristics of many mechanical devices with hysteresis [29–31].

A single-degree-of-freedom (SDOF) oscillator with Bouc–Wen hysteresis and under harmonic excitation was first investigated, Figure 1a. The mass m_1 was connected to the moving support by an element that provides a restoring force f due to an elastic and a hysteretic component:

$$f = k_1 x_1 + z \quad (1)$$

The elastic component was characterized by stiffness k_1 , whereas the hysteretic part z was provided by the Bouc–Wen law by solving the following nonlinear differential equation:

$$\frac{dz}{dt} = \left\{ k_d - \left[\gamma + \beta \operatorname{sgn} \left(z \frac{dx_1}{dt} \right) \right] |z|^n \right\} \frac{dx_1}{dt} \quad (2)$$

where k_d , γ , β , n are the constitutive parameters of the Bouc–Wen law.

The element stiffness depended on the oscillation amplitude, which varied from an initial value $k_A = k_1 + k_d$ to a final value k_B corresponding to the post-elastic stiffness, $k_B = k_1$, Figure 1b. The yield-restoring force f_y and the yield displacement $x_y = f_y/k_A$ are reported in Figure 1b. The ratio between the final and initial stiffness values is defined as the hardening coefficient and denoted by δ : $\delta = k_B/k_A$. The parameter n in Equation (2) defines the degree of smoothness of the transition from the elastic to post-elastic branches

and is assumed here to be unitary, as in most mechanical applications. The parameters β and γ tune the extent of the restoring force loop; more precisely, their sum ($\beta + \gamma$) affects the maximum value of the hysteretic force, while their ratio γ/β controls the shape of the cycles and, consequently, the dissipative capacity of the element, Figure 1c. In particular, for fixed ($\beta + \gamma$), the maximum loop area, and therefore, the maximum energy dissipation is obtained when $\gamma = \beta$ [7]; under this condition, the restoring force is defined as fully hysteretic. For $\frac{\gamma}{\beta} > 1$, there is a smaller cycle area and, therefore, decreasing dissipated energy; a reduced hysteresis is said to occur in this case.

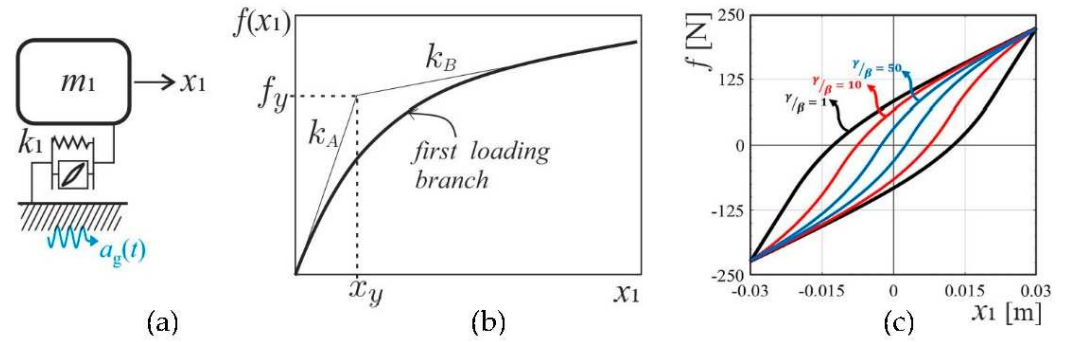


Figure 1. (a) SDOF Bouc–Wen oscillator; (b) first loading branch; (c) restoring force loops for $\gamma/\beta = 1, 10, 50$.

The equation of motion of a SDOF under a harmonic base excitation, which is characterized by amplitude a_g and frequency Ω , is:

$$m_1 \frac{d^2 x_1}{dt^2} + k_1 x_1 + z = -m_1 a_g \sin(\Omega t) \quad (3)$$

where z is provided by Equation (2). It is useful to introduce some quantities related to the parameters of the Bouc–Wen hysteretic element with clear mechanical meanings, such as the hardening coefficient δ , the yield strength f_y and the yield displacement x_y . These can be expressed as:

$$\delta = \frac{k_B}{k_A}, \quad f_y = \frac{k_A}{k_d} \left(\frac{k_d}{\beta + \gamma} \right)^{\frac{1}{n}}, \quad x_y = \frac{f_y}{k_A}, \quad (4)$$

Additionally, the initial and final frequency, ω_A and ω_B , which are associated with small and large oscillation amplitudes, the adimensional force intensity A and the driven frequency η are defined as:

$$\omega_A = \sqrt{\frac{k_A}{m}}, \quad \omega_B = \sqrt{\frac{k_B}{m}}, \quad A = \frac{m a_g}{f_y}, \quad \eta = \frac{\Omega}{\omega_A} \quad (5)$$

As demonstrated in [4], the stiffness and damping characteristics of the hysteretic absorber depend on the vibration amplitude \bar{x} . In particular, the equivalent stiffness k_e as a function of \bar{x} can be expressed in the following form:

$$k_e(\bar{x}) = k_1 + \frac{k_d}{\bar{x}(\beta + \gamma)} \left(1 - e^{-\bar{x}(\beta + \gamma)} \right) \quad (6)$$

According to Equation (6), it decreases with the excitation intensity varying from k_A to k_B . To characterize the damping properties, the equivalent damping coefficient ζ_e was introduced and defined as the value of damping of a viscoelastic oscillator that dissipates the same energy E_{BW} of the hysteretic device in an oscillation with the same frequency and amplitude \bar{x} :

$$\zeta_e(\bar{x}) = \frac{E_{BW}}{2\pi k_e \bar{x}^2} \quad (7)$$

The frequency response curves (FRCs) of the hysteretic SDOF (Table A1 in the Appendix A) with $\gamma/\beta = 1, 10$ are reported in Figure 2a,b for increasing values of the excitation intensity. In Figure 2a the case of full hysteresis (BW1) is illustrated. The nonlinearity of hysteresis is of the softening type, and the frequency–amplitude curve drawn by the resonance peaks is bent on the left. The nonlinear frequency of the oscillator is close to ω_A for low amplitudes and decreases, moving towards the post-elastic frequency ω_B for increasing response amplitudes. The curves are made by stable periodic solutions; the branch nearly vertical which connects the non-resonant and resonant branches is marginally stable [33].

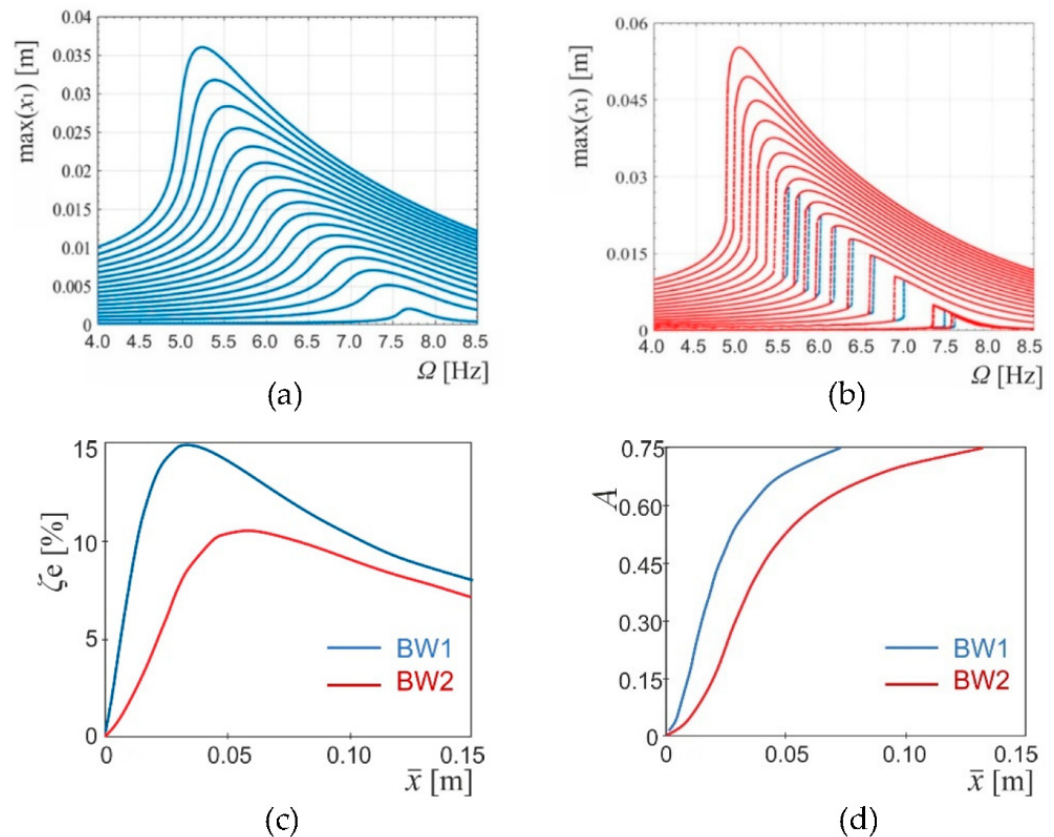


Figure 2. SDOF oscillator: frequency–response curves for varying excitation intensity: (a) $\gamma/\beta = 1$, $A = 0.01–0.63$; (b) $\gamma/\beta = 10$, $A = 0.01–0.57$ ($\omega_A = 7.83$ Hz, $\omega_B = 4.31$ Hz); (c) equivalent damping coefficient ζ_e vs. response amplitude; (d) excitation intensity vs. response amplitude.

Figure 2b shows a response with reduced hysteresis loops, $\gamma/\beta = 10$ (BW2). For the same excitation intensity, greater response amplitudes are obtained at resonance with respect to the previous case BW1, as evident in Figure 2d. This is expected behavior related to a lower level of equivalent damping, Figure 2c. A more specific difference is the coexistence of the resonant and non-resonant branches in a small range of frequency, leading to multivalued curves with the classical jump phenomenon. This range of coexisting solutions widens with γ/β , while disappearing with increasing force intensity, as evidenced by different constitutive laws [33]; this is because the dissipation capacity between full and reduced hysteresis is not more appreciable at high amplitudes.

The trend of the equivalent damping coefficient ζ_e versus the response amplitude (Equation (7)) is reported in Figure 2c for fully and reduced hysteretic systems; ζ_e increases with amplitude, reaches a maximum, and then decreases, which means that in the intermediate range of amplitudes, the dissipation capacity is greater. This is the reason why, although the equivalent stiffness decreases with amplitude, the relation between force and resonance response amplitude is steeper with respect to the ranges of small and large values, Figure 2d.

3. 2DOF Systems with Hysteretic Dampers

The phenomena of nonlinear modal interactions in a multidegree-of-freedom system can be suitably investigated by means of a 2DOF oscillator [7,24]. The analysis was developed for two different realizations: (a) top configuration (Figure 3a), where the second element was hysteretic, and the goal was to reduce the response of the main mass m_1 and (b) base configuration (Figure 3b), where the first element was hysteretic, and the goal was to reduce the action transmitted from the ground to the superstructure represented by mass m_2 and the elastic second element.

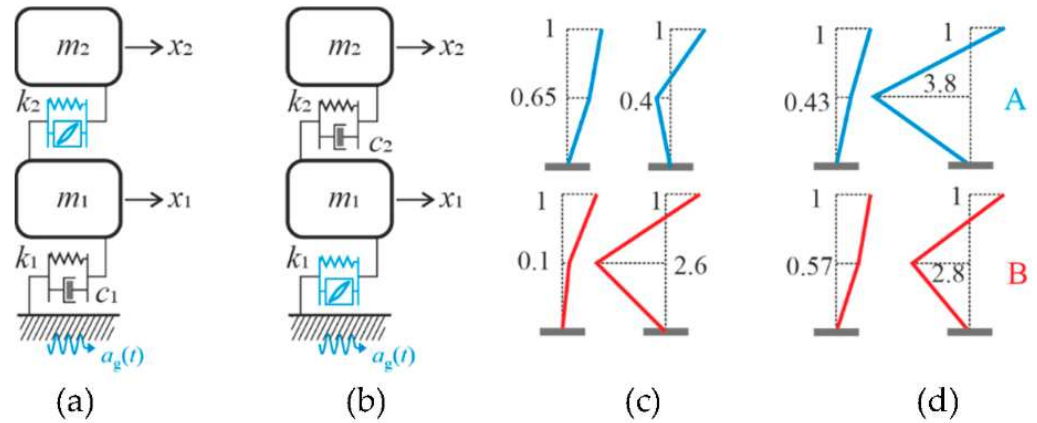


Figure 3. 2DOF system schemes: (a) top-hysteresis (TC); (b) base-hysteresis configurations (BC), examples of modes at small (A) and large (B) amplitudes; (c) TC2; (d) BC1.

The equations of motion which govern the forced vibrations of the two systems are two dynamic equilibrium equations of the two masses and the differential equation which describes the hysteretic restoring force, leading to a five first-order differential equations in the state space.

In the case of the TC scheme, Figure 3a, the equations of motion are:

$$m_1 \frac{d^2 x_1}{dt^2} + k_1 x_1 - k_2(x_2 - x_1) + c_1 \frac{dx_1}{dt} - z(x_2 - x_1) = -m_1 a_g \sin(\Omega t) \quad (8)$$

$$m_2 \frac{d^2 x_2}{dt^2} + k_2(x_2 - x_1) + z(x_2 - x_1) = -m_2 a_g \sin(\Omega t) \quad (9)$$

$$\frac{dz}{dt} = \left\{ k_d - \left[\gamma + \beta \operatorname{sgn} \left(z \frac{d(x_2 - x_1)}{dt} \right) \right] |z|^n \right\} \frac{d(x_2 - x_1)}{dt} \quad (10)$$

where the hysteretic component is a function of the relative displacement between the two masses ($x_2 - x_1$) and acts on both masses.

In the case of the BC scheme, Figure 3b, the equations of motion are:

$$m_1 \frac{d^2 x_1}{dt^2} + k_1 x_1 - k_2(x_2 - x_1) + z(x_1) = -m_1 a_g \sin(\Omega t) \quad (11)$$

$$m_2 \frac{d^2 x_2}{dt^2} + k_2(x_2 - x_1) = -m_2 a_g \sin(\Omega t) \quad (12)$$

$$\frac{dz}{dt} = \left\{ k_d - \left[\gamma + \beta \operatorname{sgn} \left(z \frac{dx_1}{dt} \right) \right] |z|^n \right\} \frac{dx_1}{dt} \quad (13)$$

where the hysteretic component acts on the mass m_1 only. The initial and post-elastic stiffnesses of the hysteretic element of the 2DOF oscillators are:

$$k_A = k_i + k_d, \quad k_B = k_i \quad (14)$$

where $i = 1, 2$ for the base and top configurations, respectively.

Modal Features

The hysteretic device introduced strong nonlinearity in the dynamic response of this type of oscillator. This means that the modal characteristics of the system in both the TC and BC configurations essentially depended on the response amplitude. As shown in [7], when the oscillation amplitudes were small, the hysteretic element exhibited an approximately linear behavior with stiffness k_A , Equation (14)₁. Conversely, when the amplitudes of oscillation were large, the hysteretic element exhibited an approximately linear behavior with stiffness k_B , Equation (14)₂. Two limit linear systems can therefore be identified: System A and System B, obtained by replacing the hysteretic element with a linear spring with stiffness k_A and k_B , respectively. As the response amplitude varies, the resonance frequency can be approximated by considering, in the place of the hysteretic element, a spring of which the stiffness k_e depends on the amplitude, according to Equation (6), $k_A \geq k_e \geq k_B$. Since the ratio between the two frequencies also depends on the response amplitude, depending on the mechanical parameters of the system, internal resonance conditions $n : m$ ($n\omega_1 \cong m\omega_2$, n and m integers) can easily arise. In such conditions, the response to the harmonic force is strongly modified by the nonlinear modal coupling.

In the following, due to the change in a period of the nonlinear modal shapes, the concept of *nonlinear modal shape* (NMS) is introduced; it represents the configuration of the system at one specific instant, as defined in [7]. This is also useful in characterizing the resonance response of the hysteretic oscillator at each excitation intensity. It is worth noticing that the NMSs can be compared with the linear modes by observing that for increasing amplitude they pass from the modal shapes of system A to those of system B.

Systems in the two configurations, TC and BC, will be examined below; the related mechanical and constitutive parameters are shown in Table A2 of the Appendix A. By way of example, Figure 3c,d report the modes of system A and system B in the case of an oscillator, respectively, with top and base configurations.

4. The Phenomenon of Modal Coupling

Nonlinearity creates the possibility for interaction among modes that are no longer orthogonal. In particular, in the presence of strong nonlinearities, peculiar dynamic phenomena occur through bifurcations of the steady-state motions. This subject is developed in the following, dealing separately with the cases of top and base configurations.

4.1. Top-Hysteresis Configuration (TC)

The top-hysteresis configuration models a primary structure, represented by the mass m_1 , connected to the base, and an attachment, represented by the mass m_2 , connected to the main structure with a hysteretic element. The hysteretic device, when properly designed, can mitigate the vibrations of the main structure using a mass m_2 which is much smaller than m_1 (light attachment). In the linear field, the importance of the Den Hartog viscoelastic tuned mass damper (TMD) [34,35] is well recognized. By adding a linear attachment with proper parameters, the peak exhibited by the FRC of the primary system response could be divided into two much lower peaks of equal value.

In recent years, much work has been devoted to nonlinear attachments after the pioneering work of [36]; however, few of these have dealt with hysteretic devices [3,4,6,37–42] or related to friction damping [43]. In the following, a hysteretic vibration absorber (HVA) was adopted, and therefore, the calibration of the parameters should be more accurate. In fact, as seen in the previous section, the 2DOF resonance frequencies depend on the oscillation amplitude; thus, at the design stage, it is necessary to take into account the oscillation amplitudes reached by the primary system to obtain the suitable frequency ratio ω_2/ω_1 that is close to optimal.

In order to simulate the behavior of the TMD, it is necessary to tune the characteristics of the added mass m_2 and of the constitutive law so that the frequency of the primary system is similar to that of the hysteretic attachment, approaching the 1:1 internal resonance condition. This requires greater attention, as shown by the analysis of the following cases.

Figure 4 depicts the response to the harmonically excited 2DOF system TC1; its mechanical characteristics are provided in Table A2 of the Appendix A. The system presents a ratio of the initial frequencies $\omega_{2A}/\omega_{1A} \cong 1.3$, which is greater than the optimal value of 1.25 of the TMD. As the amplitude increases, the frequency ratio approaches optimum, leading to a reduction in the response for a definite range of forcing amplitudes.

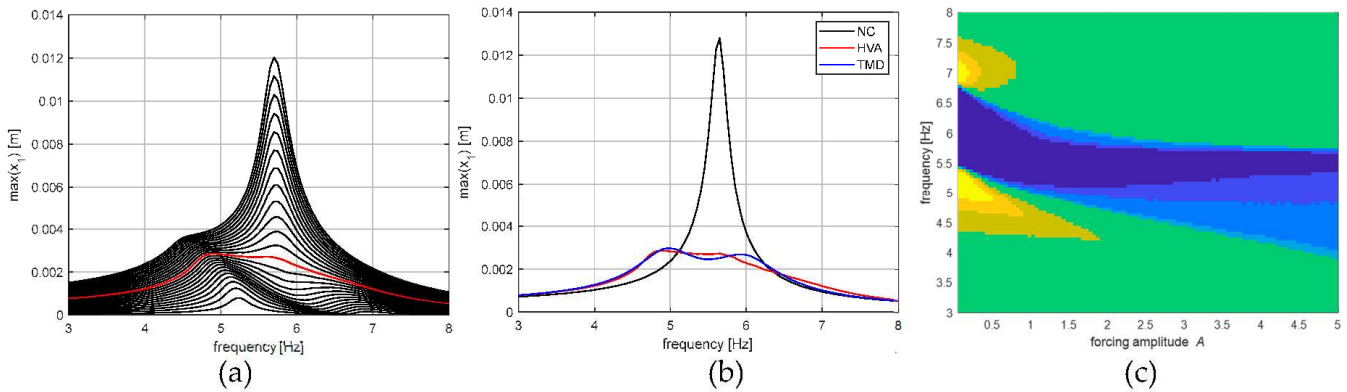


Figure 4. TC1 oscillator close to a (1:1) internal resonance $\omega_{2A}/\omega_{1A} \cong 1.3$): (a) FRCs of oscillation amplitudes of mass m_1 for increasing intensity ($a_g = [0.005–0.125]g$); (b) non controlled (black), HVA (red) and TMD (blue) responses at $a_g = 0.065g$; (c) color map comparing the maximum displacements of NC and HVA oscillators (cold colors reveal amplitude reductions and warm colors reveal amplitude increments).

The frequency response curves of the primary structure displacement are reported in Figure 4a with increasing excitation. For the optimal operation of the HVA, in analogy with the behavior of the TMD, the external excitation should generate two equal peaks in the FRC of m_1 ; this occurs for $a_g = 0.065g$, which corresponds with the red curve in Figure 4a,b. For lower intensities, the equivalent stiffness k_e of the device is lower than the optimal stiffness value of TDM, and as a result, the first peak exceeds the second. On the other hand, for larger amplitudes, the equivalent stiffness of the device exceeds the optimal stiffness of the TMD, and consequently, the second peak predominates. When the amplitude of the external excitation is close to $a_g = 0.065g$, the ratio $\frac{\omega_2}{\omega_1}$ of the system with a hysteretic attachment is close to the value of the optimal visco-elastic tuned mass damper. At this level of excitation, the HVA is as effective as the TMD; in fact, in Figure 4b, there is an 80% reduction in the oscillation amplitudes compared to those that would occur on the non-controlled primary structure (NC). As shown in Figure 4c, the effectiveness of the HVA is maintained even for higher values of the external intensity, provided that the driven frequency is close to the first resonance. In Figure 4c, by means of a color map, the maximum displacements of the NC and HVA oscillators are compared for different forcing intensities and frequencies: blue dots refer to reductions of 40 to 85% with respect to the non-controlled case; green dots are related to slight variations and warm colors indicate the cases where the HVA is not beneficial and leads to an increase in the response, even though this is in a small range of low excitation intensities (yellow regions).

In the previous case of internal resonance 1:1, a hysteretic nonlinear attachment used to reduce the vibrations of the primary structure, simply simulates the behavior of the classic TMD; therefore, the results described above are similar to what has already been observed within the framework of linear dynamics. Although the advantage of this device lies in its simplicity because hysteretic elements combine elastic and dissipative capacities without the need for a viscous damper [41], the effectiveness is, however, limited to definite excitation intensities. Furthermore, the nonlinearity resides in the constitutive law of the attachment. However, no typical phenomena of nonlinear dynamics are triggered; this novel contribution could be usefully investigated for the mitigation of vibrations, as illustrated below.

The occurrence of internal resonance conditions $n:1$, with $n > 1$ integer [43–46], is more interesting, and the relevant phenomena can be exploited to achieve a reduction in the forced response for certain values of excitation and frequency, as shown in the following. As the hysteretic restoring force is a highly nonlinear constitutive law, various internal resonance conditions are likely to occur. In the following, an oscillator that undergoes a 2:1 internal resonance was analyzed, Figure 5. Similar outcomes could be observed for $n > 2$ and also for other internal resonance conditions of the kind $n\omega_1 \cong m\omega_2$.

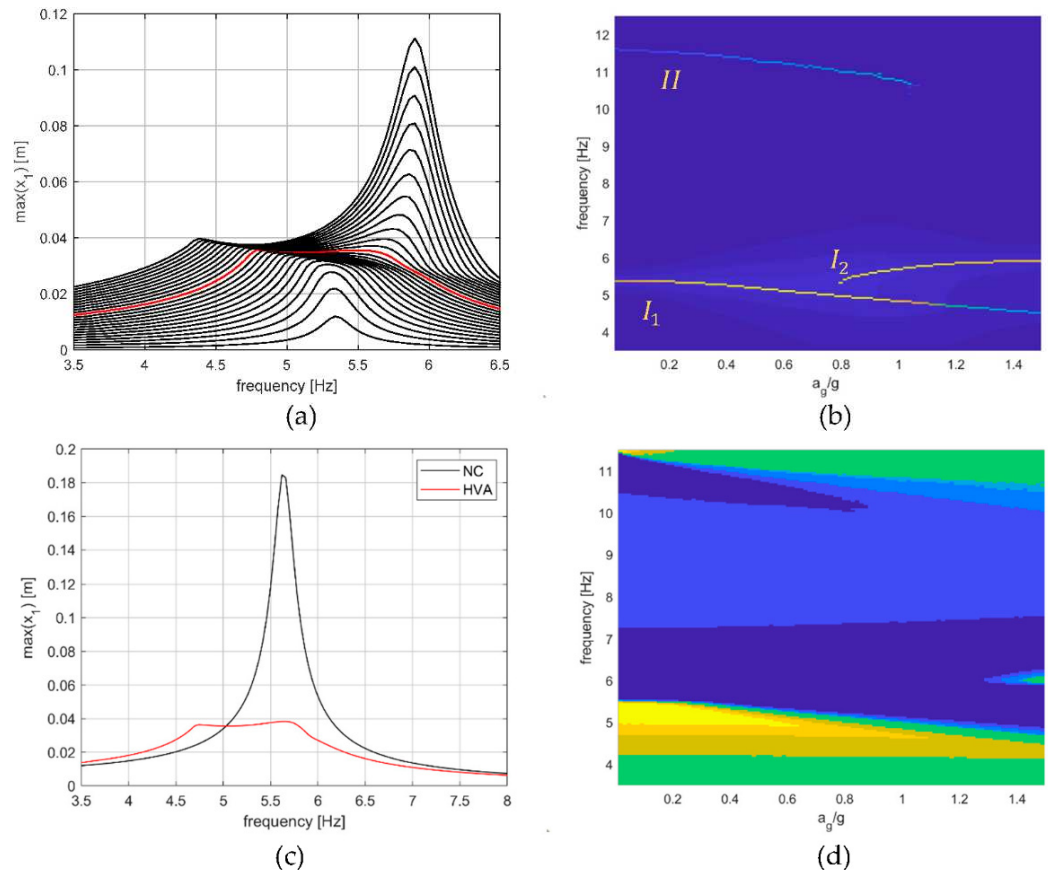


Figure 5. TC2 oscillator close to a (2:1) internal resonance ($\omega_{2A}/\omega_{1A} \cong 2.15$, $\omega_{2B}/\omega_{1B} \cong 1.46$): (a) FRCs of oscillation amplitudes of mass m_1 for increasing intensity ($a_g = [0.025\text{--}1.5]g$), optimal excitation $a_g = 0.83g$ (red curve); (b) color map of the maximum response normalized to the excitation amplitude for different excitation frequencies and intensities (warm colors reveal peaks related to modes); (c) non-controlled (NC) and HVA responses at $a_g = 0.83g$; (d) Color map comparing the maximum displacements of NC and HVA oscillators (cold colors reveal amplitude reductions, warm colors relate to amplitude increments, and green is related to slight variations).

On the same main structure of the TC1 system, an HVA was applied with mass m_2 , and the stiffness k_2 was calibrated in order to obtain a frequency ratio close to 2:1; the mechanical parameters of this oscillator (TC2) are reported in Table A2 of the Appendix A. In Figure 5a, the FRCs of the primary mass displacement is reported with increasing excitation intensity. For low intensities, the resonance frequencies were close to those of linear system A ($\omega_{1A} = 5.35$ Hz, $\omega_{2A} = 11.5$ Hz, with an initial value $r_A = \omega_{2A}/\omega_{1A} \cong 2.15$); for high intensities, the resonance frequencies were close to those of linear system B (with a final ratio $r_B = \omega_{2B}/\omega_{1B} \cong 1.5$). For intermediate intensities, the ratio approached the internal resonance condition 2:1, where the FRC around the first mode experienced a bifurcation and, instantaneously, the curve of the 2DOFs system showed two peaks (I_1 and I_2), in addition to the peak related to the second resonance (II), which was much

smaller due to the distribution of excitation, the projection of which was limited on the second mode.

In more detail, the I_1 peak, corresponding to the first resonance frequency, doubled, following a trend that recalls the response of the VMTD and the previous TC1 system. However, unlike those cases, a typical bifurcation scenario of the nonlinear dynamic response was activated here. In fact, in the TC2 system, the rise of the I_2 peak in the FRC is related to a novel superabundant mode generated by a bifurcation associated with an internal 2:1 resonance. An insight into this phenomenon is provided by the color map in Figure 5b, where, for different excitation amplitudes and frequencies, the resonance amplitudes of the m_1 steady-state responses are evidenced. For small excitation amplitudes, two branches develop, starting from the two linear frequencies A. At the critical value of $a_g = 0.79g$, the novel mode related to I_2 arises. For increasing excitation intensity, the value of peak I_2 equals that of peak I_1 at $a_g = 0.83g$ (red curve) and then prevails. Along the branch I_1 the nonlinear modal shape evolves passing from the linear mode A, for small excitation, to the linear mode B, for high excitation, Figure 3c. Similarly, the nonlinear modal shape of the superabundant mode evolves reaching the linear mode B, Figure 3c. At $a_g = 0.83g$, when the two peaks I_1 and I_2 are equivalent, the reduction in the vibration amplitude of the main structure reaches its maximum, about 80% with respect to the non-controlled case, Figure 5c. Then, the optimal excitation can be assumed as that which produces an extra peak I_2 , equal to the preexistent one I_1 in the FRC of m_1 . For different forcing intensities, the hysteretic absorber mitigated the system vibrations as well: as shown in Figure 5d, the effectiveness of the HVA was maintained in a wide range of intensities and frequencies (blue regions).

4.2. Base-Hysteresis Configuration (BC)

To explore the ability of a hysteretic isolator to reduce the transmission of excitation from the base to the superstructure by nonlinear modal coupling, the system with a hysteretic element at the base (Figure 3b) and with the BC1 characteristics (reported in Table A2 of the Appendix A), is considered in Figure 6. The small amplitude frequencies were $\omega_{1A} = 3.89$ Hz and $\omega_{2A} = 11.32$ Hz with a ratio $\omega_{2A}/\omega_{1A} = 2.90$, which are close to the internal resonance condition 3:1.

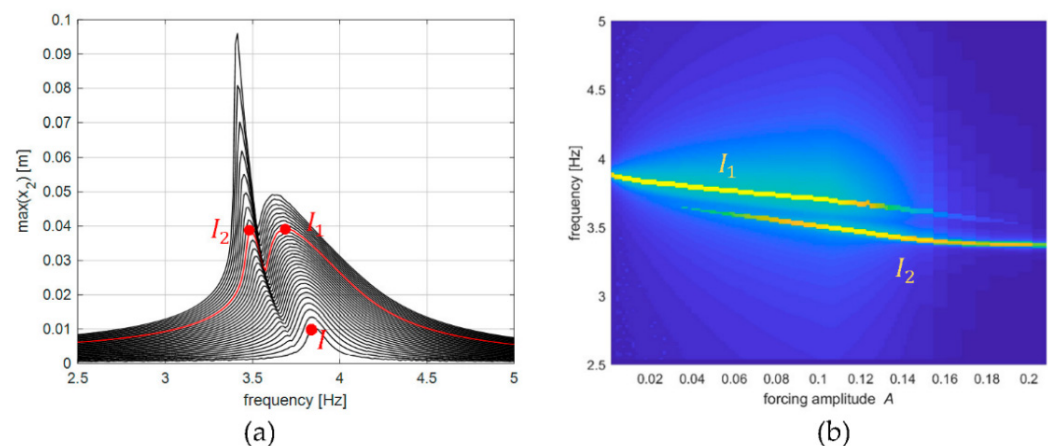


Figure 6. BC1 oscillator close to a (3:1) internal resonance ($\omega_{2A}/\omega_{1A} \cong 2.90$, $\omega_{2B}/\omega_{1B} \cong 3.0$): (a) FRCs around the first resonance for increasing excitation amplitude ($A = 0.007$ – 0.14), optimal intensity $A = 0.10$ (red); (b) color map of the maximum response normalized to the excitation amplitude for different excitation frequencies and intensities (warm colors reveal peaks related to modes).

Figure 6a focuses on the FRCs of the m_2 displacement amplitude centered on the first resonance. Initially, for small excitation intensities, the single peak I is present close to the first natural frequency; however, with increasing intensity, at the critical value $A = 0.024$,

a second peak I_2 appears which grows until it reaches I_1 , at $A = 0.1$ (red FRC curve), and then overcomes it. As shown by the color map in Figure 6b, the fundamental branch ω - A of the first resonance experiences a bifurcation and then shows a new branch in addition to the preexisting one, which is destined to disappear; the new branch I_2 is the only surviving one for large excitation intensities.

It is worth noticing that the nonlinear modal trajectories in the physical plane $x_1 - x_2$, related to the steady-state responses of I_1 and I_2 , always exhibit opposite curvatures. This is shown in Figure 7: the novel mode I_2 arises at $A = 0.024$, showing a \int -shaped modal trajectory, whereas the preexisting mode I_1 exhibits a λ -shaped one; as soon as I_2 prevails over I_1 ($A > 0.1$), its modal trajectory becomes λ -shaped, while the other turns \int -shaped and disappears. Finally, along both branches, the nonlinear modal shapes evolve, passing from the linear mode A , for small excitation, to the linear mode B , for high excitation, Figure 3d.

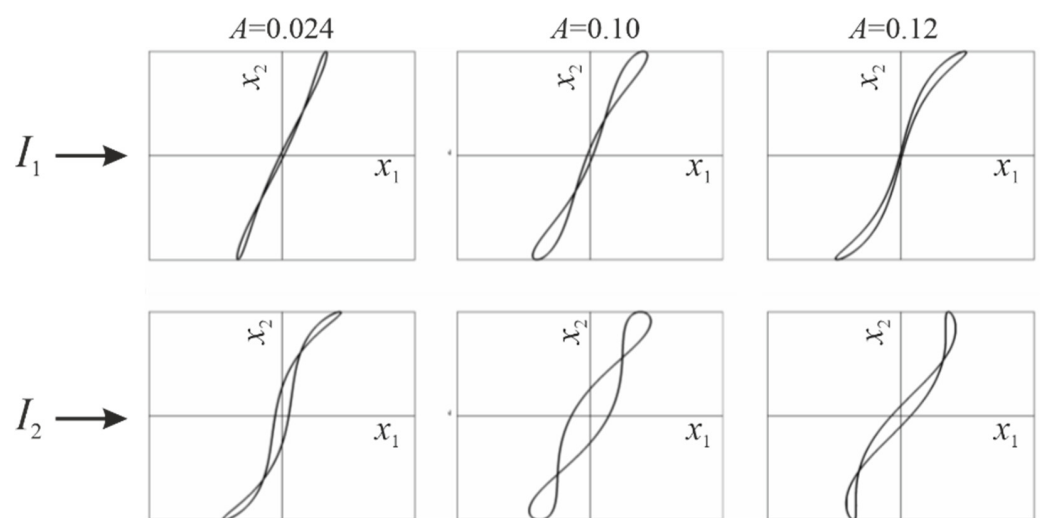


Figure 7. BC1 oscillator: evolution of the modal trajectories in the physical plane related to peaks I_1 and I_2 as excitation increases.

The comparison of the dynamic behavior of two different systems, BC1, close to an internal resonance condition 3:1, and BC1n, far from an internal resonance condition (Table A2 in the Appendix A) with a frequency ratio $\omega_{2A}/\omega_{1A} = 3.40$, makes it possible to clearly illustrate the favorable effects of nonlinear modal interactions [1,2,29]. For BC1n, in this case, there is only a single branch related to the first resonance, Figure 8a, which, as expected, occurs at lower frequencies for increasing forcing intensities due to hysteretic softening. On the contrary, the maximum displacement of the two masses is much smaller for the system BC1 in conditions of internal resonance, with a reduction of about 70% for m_2 with respect to the non-resonant case (BC1n), Figure 8b. As shown in Figure 8c, the closeness to internal resonance conditions leads to a relevant displacement reduction in a wide range of forcing frequency and amplitude in the blue regions.

Internal resonance conditions $n:1$ with n even can also occur. As an example, a BC2 system close to internal resonance 2:1 is considered in Figure 9.

At small intensities, the amplification of the second mode II is much smaller than the first I_1 due to the distribution of excitation. For increasing intensity, Figure 9a, the zone of the first resonance widens, and a novel peak I_2 emerges and reaches the peak I_1 near $A = 0.32$, leading to a flattening of the FRCs, with a notable reduction in the first resonance peaks in a large range of force intensities. The resonance amplitudes of the m_2 steady-state responses are evidenced in Figure 9b for different excitation amplitudes and frequencies: the branches related to the peaks I_1 , I_2 and II are well-evidenced, together with a short branch of superharmonic solutions arising for low excitation frequencies.

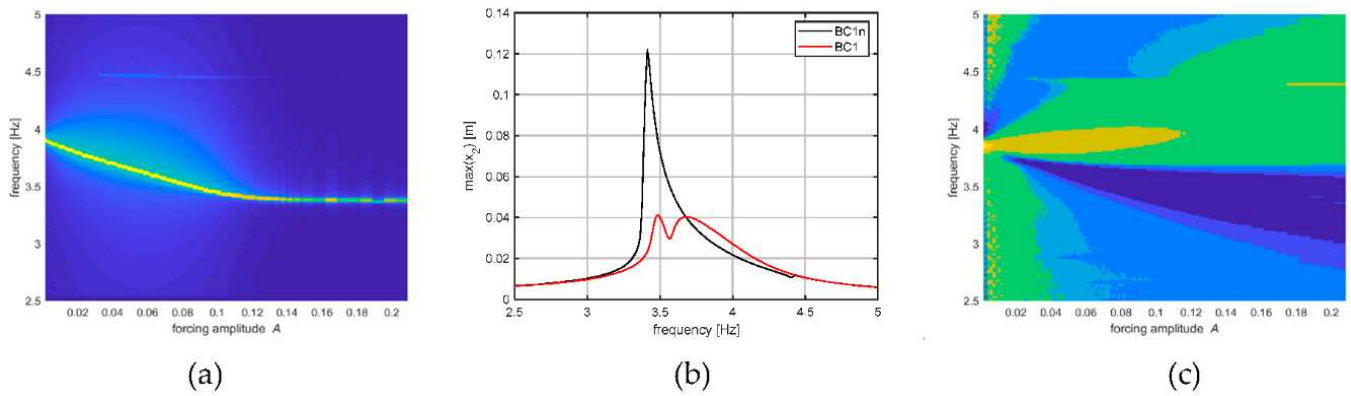


Figure 8. (a) color map of the maximum response of non-resonant system BC1n for different forcing frequencies and intensities; (b) non-resonant (BC1n) and resonant (BC1) FRCs responses at $A = 0.10$; (c) color map comparing the maximum displacements of BC1 and BC1n oscillators (cold colors reveal amplitude reductions, warm colors indicate amplitude increments, green indicates slight variations).

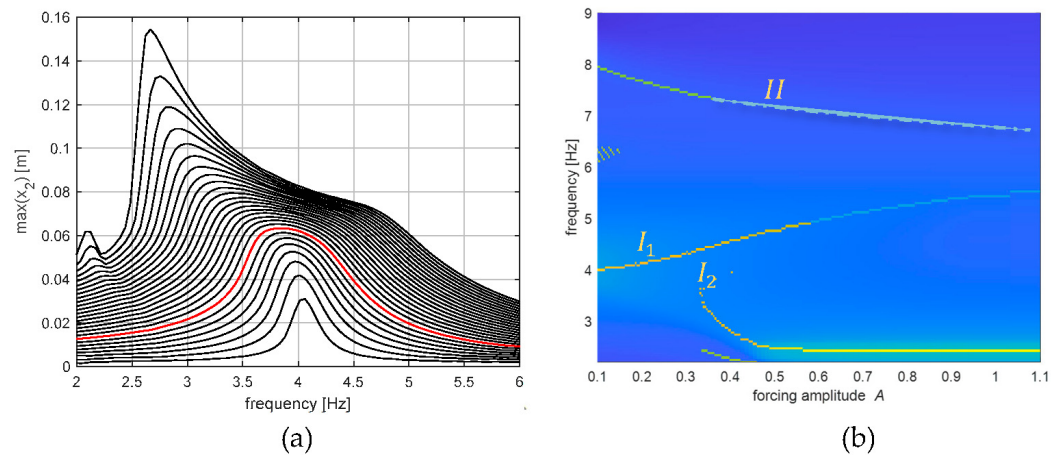


Figure 9. BC2 oscillator close to (2:1) internal resonance ($\omega_{2A}/\omega_{1A} \cong 2.09$): (a) FRCs for increasing force intensity ($A = 0.015\text{--}0.4$), red $A = 0.32$; (b) color map highlighting the main branches.

5. Conclusions

The aim of this paper is to investigate nonlinear modal interactions in multidegree-of-freedom systems with hysteresis in view of exploiting this phenomenon to achieve mitigation of the forced response. In particular, a simple 2DOF structure that consisted of two masses and two elements, one elastic and one hysteretic, was investigated by considering two different configurations: top configuration, with the hysteretic element at the top (TC) between the two masses; and base configuration (BC), with the hysteretic element at the base.

The nonlinearity of the hysteretic element is described by the Bouc–Wen model and can be classified as a strong nonlinearity due to the notable dependence of stiffness and damping on the oscillation amplitude. The main dynamic effects of hysteresis are first illustrated by the FRCs of a SDOF hysteretic system under harmonic excitation. The FRCs were always single-valued functions, which meant that the steady-state solutions were always stable for the full hysteresis model considered. Due to the reduction in stiffness with amplitude, the nonlinearity was of the softening type: the resonance frequency decreased from ω_A for small amplitudes, to ω_B for high amplitudes, where ω_A and ω_B were the frequencies of the linear oscillator with a stiffness that was, respectively, equal to the initial and post-elastic stiffness of the hysteretic element.

The nonlinear behavior the 2DOF system, as already observed for the SDOF, is again comprised between those of two linear systems: system A for small amplitudes, system B for large amplitudes. The modal properties of the system change with the oscillation amplitude. Accordingly, natural frequencies, and their ratio, changed and the conditions

of internal resonance, where the phenomena of nonlinear interaction are exalted, were easily met.

For the top configuration, first, the case where the hysteretic device had a frequency close to that of the main structure was considered, which recalled the case of the well-known tuned mass damper. The hysteretic element, which combined stiffness and dissipation characteristics, made it possible to avoid the viscous device, but the performance was similar to that of the viscoelastic damper, only in a certain range of force intensity, due to the dependence on the oscillation amplitude.

However, the introduction of a hysteretic element could take advantage of the phenomena of nonlinear interactions, which occurred when the system was close to internal resonance conditions $n:1$ with $n > 1$. The 2:1 condition was investigated for TC systems, and the 3:1 and 2:1 conditions were investigated for BC systems. A large variety of behaviors were observed; however, concerning the beneficial effects in vibration mitigation, similar outcomes were found for both configurations. At a certain force intensity, the FRCs around the resonance of the first mode exhibited a bifurcation with the arising of a novel mode. The existence of two resonant peaks around the first mode was the result of the involvement of the second mode, which strongly modified the modal trajectories and, mainly, the response amplitude.

In conclusion, the novel contribution of the paper is the enlightenment of the use of hysteretic devices, which offers the possibility of increasing the dissipation characteristics of the system and, at the same time, due to its intrinsic nonlinear behavior, facilitates the transfer of energy from the mode, directly excited to the other not directly excited, with appreciable mitigation of vibrations of the structure.

Author Contributions: Conceptualization, P.C. and F.V.; methodology, P.C. and F.V.; software, P.C.; supervision, F.V. All authors have read and agreed to the published version of the manuscript.

Funding: This work has been partially supported by the MIUR (Ministry of Education, University and Research) under the grant PRIN 2017-N. 2017L7X3CS.

Institutional Review Board Statement: Not applicable.

Informed Consent Statement: Not applicable.

Data Availability Statement: Not applicable.

Conflicts of Interest: The authors declare no conflict of interest. The funders had no role in the design of the study; the collection, analyses, or interpretation of data; the writing of the manuscript; or in the decision to publish the results.

Appendix A

In the following tables, the parameters of the SDOF and 2DOF hysteretic systems investigated in this paper are reported.

Table A1. Mechanical characteristics of SDOF systems.

SDOF Name	m_1 kg	k_1 kN/m	δ	γ [1/m]	γ/β	k_A kN/m	f_y kN	x_y m
BW1	600	440	0.3	55	1	1466.7	13.3	0.0091
BW2	600	440	0.3	100	10	1466.7	13.3	0.0091

Table A2. Mechanical characteristics of 2DOF systems.

2DOF Name	m_1 kg	m_2 kg	k_1 kN/m	k_d kN/m	γ [1/m]	γ/β	δ	ζ_1	k_2 kN/m	ζ_2	ω_{1A} Hz	ω_{2A} Hz
TC1 1:1	1220	61	1532.6	82	82	1	0.14	0.02	14.51	0	5.27	6.95
TC2 2:1	1220	101	1532.6	408	55	1	0.15	0.02	72	0	5.35	11.5

Table A2. Cont.

2DOF Name	m_1 kg	m_2 kg	k_1 kN/m	k_d kN/m	γ [1/m]	γ/β	δ	ζ_1	k_2 kN/m	ζ_2	ω_{1A} Hz	ω_{2A} Hz
BC1 3:1	256	420	440	300	55	1	0.6	0	440	0.01	3.89	11.32
BC1n	256	420	353	1606	55	1	0.6	0	889	0.01	3.93	13.3
BC2 2:1	1220	549	440	2493	55	1	0.15	0	440	0.01	4.1	8.57

References

- Jing, X.J.; Vakakis, A. Exploring nonlinear benefits in engineering. *Mech. Syst. Signal Process.* **2019**, *125*, 1–3. [CrossRef]
- Vakakis, A.F. Intentional utilization of strong nonlinearity in structural dynamics. *Proc. Eng.* **2017**, *199*, 70–77. [CrossRef]
- Ture Savadkoochi, A.; Lamarque, C.-H.; Contessa, M.V. Trapping vibratory energy of main linear structures by coupling light systems with geometrical and material non-linearities. *Int. J. Non-Linear Mech.* **2016**, *80*, 3–13. [CrossRef]
- Vestroni, F.; Casini, P. Mitigation of structural vibrations by hysteretic oscillators in internal resonance. *Nonlinear Dyn.* **2020**, *99*, 505–518. [CrossRef]
- Liang, Z.; Lee, G.C.; Dargush, G.F.; Song, J. *Structural Damping: Applications in Seismic Response Modification*; CRC Press: Boca Raton, FL, USA, 2011.
- Casalotti, A.; Lacarbonara, W. Tailoring of pinched hysteresis for nonlinear vibration absorption via asymptotic analysis. *Int. J. Non-Linear Mech.* **2017**, *94*, 59–71. [CrossRef]
- Casini, P.; Vestroni, F. Nonlinear resonances of hysteretic oscillators. *Acta Mech.* **2018**, *229*, 939–952. [CrossRef]
- Tsiatas, G.C.; Charalampakis, A.E. A new hysteretic nonlinear energy sink (HNES). *Commun. Nonlinear Sci. Numer. Simul.* **2018**, *60*, 1–11. [CrossRef]
- Basili, M.; Casini, P.; Morelli, L.; Vestroni, F. Vibration Mitigation of Rail Noise Barriers by Hysteretic Absorbers. *J. Appl. Comp. Mech.* **2021**, *7*, 1205–1217.
- Nayfeh, A.H.; Balachandran, B. *Applied Nonlinear Dynamics: Analytical, Computational, and Experimental Methods*; Wiley: New York, NY, USA, 1995.
- Vakakis, A.F. Non-linear normal modes and their applications in vibration theory: An overview. *Mech. Syst. Signal Process.* **1997**, *11*, 3–22. [CrossRef]
- Vestroni, F.; Luongo, A.; Paolone, A. A perturbation method for evaluating nonlinear normal modes of a piecewise linear 2-DOF system. *Nonlinear Dyn.* **2008**, *54*, 379–393. [CrossRef]
- Wiercigroch, M.; de Kraker, B. *Applied Nonlinear Dynamics and Chaos of Mechanical Systems with Discontinuities*; World Scientific Series in Nonlinear Science, Series A; World Scientific: Singapore, 2000; Volume 28.
- Awrejcewicz, J.; Dzyubak, L.; Lamarque, C.H. Modelling of hysteresis using Masing–Bouc–Wen’s framework and search of conditions for the chaotic responses. *Commun. Nonlinear Sci. Numer. Simul.* **2008**, *13*, 939–958. [CrossRef]
- Rand, R.H.; Pak, C.H.; Vakakis, A.F. Bifurcation of nonlinear normal modes in a class of two degree of freedom systems. *Acta Mech.* **1992**, *3*, 129–145.
- Casini, P.; Vestroni, F. Characterization of bifurcating Nonlinear Normal Modes in piecewise linear mechanical systems. *Int. J. Non-Linear Mech.* **2011**, *46*, 142–150. [CrossRef]
- Vestroni, F.; Noori, M. Hysteresis in mechanical systems: Modeling and dynamic response. *Int. J. Non-Linear Mech.* **2002**, *37*, 1261–1262. [CrossRef]
- Al-Bender, F.; Symens, W.; Swevers, J.; Van Brussel, H. Theoretical analysis of the dynamic behavior of hysteresis elements in mechanical systems. *Int. J. Non-Linear Mech.* **2004**, *39*, 1721–1735. [CrossRef]
- Masuda, A.; Noori, M. Optimization of hysteretic characteristics of damping devices based on pseudoelastic shape memory alloys. *Int. J. Non-Linear Mech.* **2002**, *37*, 1375–1386. [CrossRef]
- Lacarbonara, W.; Vestroni, F. Nonclassical responses of oscillators with hysteresis. *Nonlinear Dyn.* **2003**, *32*, 235–258. [CrossRef]
- Xiong, H.; Kong, X.; Li, H.; Yang, Z. Vibration analysis of nonlinear systems with the bilinear hysteretic oscillator by using incremental harmonic balance method. *Commun. Nonlinear Sci. Numer. Simul.* **2017**, *42*, 437. [CrossRef]
- Vaiana, N.; Sessa, S.; Marmo, F.; Rosati, L. Nonlinear dynamic analysis of hysteretic mechanical systems by combining a novel rate-independent model and an explicit time integration method. *Nonlinear Dyn.* **2019**, *98*, 2879–2901. [CrossRef]
- Pak, C.H. On the stability behaviour of bifurcated normal modes in coupled nonlinear systems. *J. Appl. Mech.* **1989**, *56*, 155–161. [CrossRef]
- Masiani, R.; Capecchi, D.; Vestroni, F. Resonant and coupled response of hysteretic two-degree-of-freedom systems using harmonic balance method. *Int. J. Non-Linear Mech.* **2002**, *37*, 1421–1434. [CrossRef]
- Visintin, A. *Differential Models of Hysteresis*; Springer: Berlin/Heidelberg, Germany, 1994.
- Antonelli, M.; Carboni, B.; Lacarbonara, W.; Bernardini, D.; Kalmar-Nagy, T. Quantifying Rate-Dependence of a Nonlinear Hysteretic Device. In *Nonlinear Dynamics of Structures, Systems and Devices, Proceedings of the 1st International Nonlinear Dynamics Conference, NODYCON, Rome, Italy, 17–19 February 2019*; Springer: Cham, Switzerland, 2020; pp. 347–355.

27. Bouc, R. Forced vibrations of mechanical systems with hysteresis. In Proceedings of the Fourth Conference on Nonlinear Oscillations, Prague, Czech Republic, 5–9 September 1967.
28. Wen, Y.K. Method of random vibration of hysteretic systems. *ASCE J. Eng. Mech.* **1976**, *102*, 249–263. [CrossRef]
29. Ni, Y.Q.; Ko, J.M.; Wong, C.W. Identification of non-linear hysteretic isolators from periodic vibration tests. *J. Sound Vib.* **1998**, *217*, 747–756. [CrossRef]
30. Ismail, M.; Ikhouane, F.; Rodellar, J. The Hysteresis Bouc-Wen Model, a Survey. *Arch. Comput. Methods Eng.* **2009**, *16*, 161–188. [CrossRef]
31. Zhang, Z.; Tian, X.; Ge, X. Dynamic Characteristics of the Bouc–Wen Nonlinear Isolation System. *Appl. Sci.* **2021**, *11*, 6106. [CrossRef]
32. Vestroni, F.; Casini, P. Nonlinear dynamics and phenomena in oscillators with hysteresis. In *Modern Trends in Structural and Solid Mechanics*; Challamel, N., Kaplunov, J., Takewaki, I., Eds.; ISTE: London, UK; Wiley: Hoboken, NJ, USA, 2021.
33. Capecchi, D.; Vestroni, F. Periodic response of a class of hysteretic oscillators. *Int. J. Non-Linear Mech.* **1990**, *25*, 309–317. [CrossRef]
34. Den Hartog, J.P. *Mechanical Vibrations*; McGraw-Hill: New York, NY, USA, 1934.
35. Dai, J.; Xu, Z.D.; Gai, P.P. Dynamic analysis of viscoelastic tuned mass damper system under harmonic excitation. *J. Vib. Control* **2019**, *25*, 1768–1779. [CrossRef]
36. Vakakis, A.F.; Manevitch, L.; Gendelman, O.; Bergman, L. Dynamics of linear discrete systems connected to local, essentially non-linear attachments. *J. Sound Vib.* **2003**, *264*, 559–577. [CrossRef]
37. Laxalde, D.; Thouverez, F.; Sinou, J.J. Dynamics of a linear oscillator connected to a small strongly non-linear hysteretic absorber. *Int. J. Non-Linear Mech.* **2006**, *41*, 969–978. [CrossRef]
38. Zeynalian, M.; Ronagh, H.R.; Dux, P. Analytical Description of Pinching, Degrading, and Sliding in a Bilinear Hysteretic System. *J. Eng. Mech.* **2012**, *138*, 1381–1387.
39. Carpineto, N.; Lacarbonara, W.; Vestroni, F. Hysteretic tuned mass dampers for structural vibration mitigation. *J. Sound Vib.* **2013**, *333*, 1302–1318. [CrossRef]
40. Carboni, B.; Lacarbonara, W. Nonlinear dynamic characterization of a new hysteretic device: Experiments and computations. *Nonlinear Dyn.* **2016**, *83*, 23–39. [CrossRef]
41. Bagheri, S.; Rahmani-Dabbagh, V. Seismic response control with inelastic tuned mass dampers. *Eng. Struct.* **2018**, *172*, 712–722. [CrossRef]
42. Salvatori, A.; Carboni, B.; Lacarbonara, W. Nonlinear dynamic response of an isolation system with superelastic hysteresis and negative stiffness. *Nonlinear Dyn.* **2022**, *107*, 1765–1790. [CrossRef]
43. Krack, M.; Bergman, L.A.; Vakakis, A.F. On the efficacy of friction damping in the presence of nonlinear modal interactions. *J. Sound Vib.* **2016**, *370*, 209–220. [CrossRef]
44. Jo, H.; Yabuno, H. Amplitude reduction of primary resonance of nonlinear oscillator by a dynamic vibration absorber using nonlinear coupling. *Nonlinear Dyn.* **2009**, *55*, 67–78. [CrossRef]
45. Ji, J.C. Design of a nonlinear vibration absorber using three-to-one internal resonances. *Mech. Syst. Signal Process.* **2014**, *42*, 236–246. [CrossRef]
46. Casini, P.; Vestroni, F. The role of the hysteretic restoring force on modal interactions in nonlinear dynamics. *Int. J. Non-Linear Mech.* **2022**, *143*, 104029. [CrossRef]

Article

Investigating the Vibration Mitigation Efficiency of Tuned Sloshing Dampers Using a Two-Fluid CFD Approach

Máté Péntek ^{1,*}, Andreas Riedl ¹, Kai-Uwe Bletzinger ¹ and Felix Weber ²

¹ Lehrstuhl für Statik, Technische Universität München, 80333 Munich, Germany; a.m.riedl@tum.de (A.R.); kub@tum.de (K.-U.B.)

² Maurer Switzerland GmbH, Grossplatzstraße 24, 8118 Pfaffhausen, Switzerland; f.weber@maurer.eu

* Correspondence: mate.pentek@tum.de

Abstract: The efficiency of a Tuned Sloshing Damper (TSD) when mitigating wind-induced structural vibrations is investigated. We assessed the performance in terms of peak structural displacements and accelerations, compared to that of the Tuned Mass Damper (TMD). One load scenario considers oncoming gusts due to natural turbulence, whereas the other assumes predominant vortex shedding at a low turbulence intensity. The known optimum tuning rules for TSDs and TMDs were adopted. We combined numerical models for fluids and structures to simulate the dynamic effects caused by wind loading. A two-fluid Computational Fluid Dynamics (CFD) approach was used for the realistic simulation of the TSD. The interaction between the flow, the structural behavior and the added devices was captured. All of these computational methods and respective models represent the necessary components of a modular and flexible simulation environment. The study demonstrates that this workflow is suited to model the inclusion of TSDs and TMDs, as well as to capture the effect of transient wind at full scale. We specifically used it to quantify the efficiency of added dampers. The process highlights challenges in properly tuning a TSD and its reduced efficiency compared to that of a TMD. Such an outcome is attributed to the water mass and potential added damping only being partially activated. The computational framework promises the ability to improve such designs by enabling numerical optimization for better efficiency.

Keywords: vibration mitigation; tuned sloshing damper; TSD; tuned mass damper; TMD; numerical simulation; coupled simulation; computational wind engineering; CWE

Citation: Péntek, M.; Riedl, A.; Bletzinger, K.-U.; Weber, F. Investigating the Vibration Mitigation Efficiency of Tuned Sloshing Dampers Using a Two-Fluid CFD Approach. *Appl. Sci.* **2022**, *12*, 7033. <https://doi.org/10.3390/app12147033>

Academic Editor: José A.F.O. Correia

Received: 30 May 2022

Accepted: 6 July 2022

Published: 12 July 2022

Publisher's Note: MDPI stays neutral with regard to jurisdictional claims in published maps and institutional affiliations.



Copyright: © 2022 by the authors. Licensee MDPI, Basel, Switzerland. This article is an open access article distributed under the terms and conditions of the Creative Commons Attribution (CC BY) license (<https://creativecommons.org/licenses/by/4.0/>).

1. Introduction

Our work presents a comparative study on the effectiveness of Tuned Sloshing Dampers (TSDs) and Tuned Mass Dampers (TMDs). The focus lies in assessing the efficiency in reducing vibrations, specifically displacements and accelerations, for a generic high-rise structure under wind load. In the case of a target construction, Building B is chosen, which is a standard tall building according to the study proposed by the Commonwealth Advisory Aeronautical Research Council (CAARC) [1,2], later readdressed by the International Association for Wind Engineering (IAWE) [3,4]. From herein, we refer to it simply as CAARC-B. There are two representative loading conditions for such constructions: one is the naturally turbulent approaching wind flow, and the other is characterized by low (even practically nonexistent) oncoming turbulence at the critical streamwise velocity. Whereas the former category typically leads to a broad-band excitation in an along-wind direction, the latter case generally results in resonance under a narrow-band force, implying dominant cross-wind motions. Our goal is to realistically model the functioning of a TSD for assessment purposes. Additionally, we show that the modular numerical workflow is a viable path in analyzing transient loading on structures, including added dampers as well as capturing the interaction between them. As we aim to exploit recent advances in numerical approaches, we focus on the usage and realistic modeling

of TSDs by means of Computational Fluid Dynamics (CFD). A so-called *two-fluid* (also known as *two-phase* –one being air, the other water) formulation enables capturing sloshing and wave breaking in a manner adequate for our goals. Similar approaches are of interest in various hydrodynamic application cases, such as general wave modeling [5], ocean engineering [6] or the multiphase flow of gases and liquids [7,8]. In our project, the comparison of sloshing-based mechanisms was made with TMDs because such devices represent a well-known benchmark in working principles and effectiveness. In addition, both devices are typically set up to optimal parameters for specific working conditions acting passively. TSDs represent a special category within Tuned Liquid Dampers (TLDs), which, together with TMDs, are also generically a part of Added Mass Dampers (AMDs). Essentially, such elements achieve mitigation by a combination of increased inertia and additional damping, which they contribute to the “host” system.

We took this well-documented structure under wind loading, optimally tuned a passive TSD and TMD and simulated the transient and coupled effects using a specific numerical environment. Assuming the same added mass is contributed by both devices (i.e., the added weight on the structure is equal), the characteristic kinematics is assessed and discussed. The goal is to outline the efficiency of TSDs when compared to TMDs under similar and representative load conditions. Numerical tools as part for Computational Wind Engineering (CWE) permit such investigations, not least because they enable a modular approach. Wind loading was captured using Large Eddy Simulations (LES) (a particular CFD model, specifically the VMS-ASGS formulation as detailed in [9]), whereas the behavior of the structure was assessed with Computational Structural Dynamics (CSD). These are coupled to permit Fluid–Structure Interaction (FSI), specifically of interest for the case of vortex-shedding-induced resonance. A feedback mechanism is not only restricted to the reciprocal influence of structural deformations on the wind loading conditions, but also must be extended to the connection between the building and an AMD. To summarize, each of these models were attributed a dedicated numerical setup and solver, best suited to its requirements, whereas a *partitioned* scheme (with theory and usage thoroughly discussed in [10–13]) connects them in the most appropriate manner to capture interaction between them. This is, at its basis, a divide et impera approach, harmonized by recent advances in computational multiphysics. The numerical models follow a discretization based on formulations using the Finite Element Method (FEM). Our contributions are, in part, contained in the Kratos Multiphysics open-source project [14,15], which is a joint research and development activity. Herein, scientists and engineers collaborate together, specifically striving for modularity and scalability. Depending on the required computational effort, we additionally leveraged our developments on a High Performance Computing (HPC) infrastructure. Our simulations benefit from the capabilities enabled by SuperMUC-NG.

2. Modeling of TSDs

The intention is to realistically model and use TSDs to efficiently mitigate wind-induced vibrations. These devices are basically liquid containers, where the sloshing motion under oscillations counteracts the base excitations of the structure that they are mounted in. TSDs contribute with added mass, damping and stiffness, similarly to TMDs. Such elements are added to highrise structures near the top. Design considerations rely on knowing the exact structural parameters that define their inherent deformations patterns. Specifically, we need to compute the particular eigenmodes and imply proper normalization. Figure 1 shows these main concepts. Here, the basic definition of a TSD is also included, specifically marking the initial water height h_0 and the definition of the wave in time t by the varying height $h(x, t)$ for the sloshing in direction x .

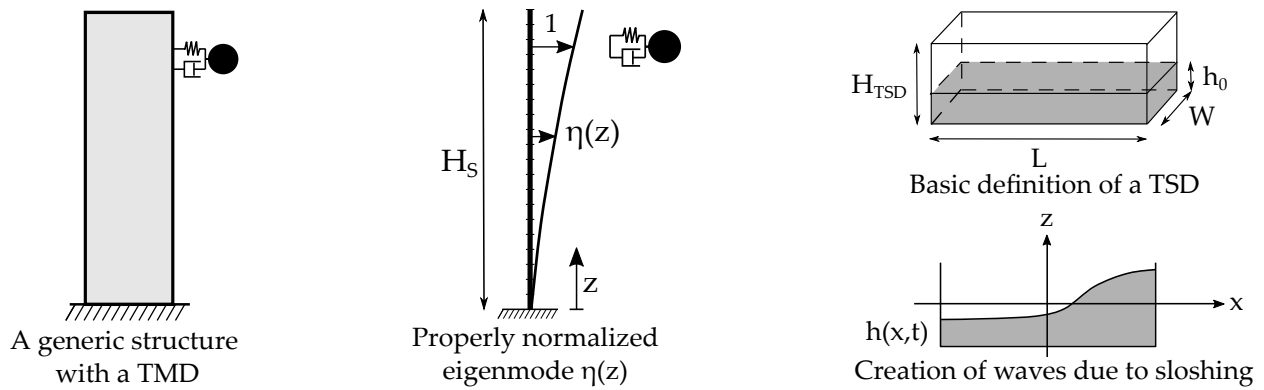


Figure 1. Scheme of a TMD attached to a structure (left) and the main parameters for defining a TSD (right).

All formulas needed for the design depend on the basic definition used in defining a TSD. The fundamental sloshing frequency of the water f_w inside a TSD can be expressed using the linear wave theory [16],

$$f_w = \frac{1}{2\pi} \sqrt{\frac{\pi g}{L} \tanh\left(\frac{\pi h_0}{L}\right)}. \tag{1}$$

In Equation (1), g is the gravitational acceleration and h_0 and L mark the basic geometric parameters of the initial water height and tank length. In the following, a denotes the amplitude of the horizontal displacement, whereas f_{ext} and ω_{ext} mark the (circular) frequency of the external excitation. Three main characteristics influencing the behavior of a TSD are summarized in Equation (2):

$$\begin{aligned} \text{depth ratio} & \quad \frac{h_0}{L}, \\ \text{frequency ratio} & \quad \beta = \frac{f_{ext}}{f_w} = \frac{\omega_{ext}}{\omega_w}, \\ \text{amplitude ratio} & \quad \frac{a}{L}. \end{aligned} \tag{2}$$

The water content can be calculated using the proper density ρ_w , according to Equation (3):

$$m_w = L W h_0 \rho_w. \tag{3}$$

For a rectangular device, only a part of the total liquid mass fully contributes to the sloshing motion. Other parts do not provide any momentum in the desired motion because of the existence of recirculation zones. Therefore, the water mass can be divided into the effective mass in motion m_{eff} and the rest m_0 . Equation (4) provides the relations based on the linear potential flow theory [17]:

$$\begin{aligned} m_{eff} &= \frac{8 \tanh\left(\frac{\pi h_0}{L}\right)}{\pi^3 h_0} m_w, \\ m_0 &= m_w - m_{eff}. \end{aligned} \tag{4}$$

2.1. Choice of an Adequate Numerical Model

An appropriate numerical model needs to be identified and set up properly. There are various numerical approaches that can, in principle, simulate the movement of sloshing liquids. Traditionally, models based on the shallow water equations were the choice as the computational requirements remained fairly low. These continue to provide a good initial approximate for certain scenarios of wave motions. Respective theories perform particularly well when the horizontal length scale is considerable larger than the vertical

scale, thus, the naming of *shallow*. Corresponding equations result from depth-integrating the Navier–Stokes relations, which are the generally accepted governing formulas for flow problems. Shallow water equations cannot represent quantities over height, as the resulting variables are the wave height and horizontal travelling velocity of the wave. Consequently, the outcomes solely describe the surface level of the sloshing and its speed. This poses strong limitations for nonlinear dynamic motions, where they are unable to tackle wave breaking or to provide a realistic insight into the inner dynamics, which is linked to the internal energy considerations of the sloshing tank. Another type of numerical model is represented by formulations using a particle analogy. These imply considering the sloshing liquid as the collection of movement of all particles in the container. Two main categories can be identified: one uses an explicit numerical mesh, which deforms according to the sloshing movement; the other type uses an implicit numerical mesh, meaning the existence of a background grid on which the particles are tracked. The former type suffers when large mesh distortions are present (the case of highly dynamic movement), whereas both models can have issues with the conservation of mass. Further investigations would be needed for more insight into the accuracy, robustness and scalability. Nonetheless, this type of approach still remains promising for the design of TSDs. The main result is represented by the positions and velocities of the particles. Internal forces and reactions on the tank can be derived mainly based on collision and cohesion. Specific implementations used for testing are part of the Kratos Multiphysics [14] project. From here, we explored the use of the *ShallowWaterApplication* (with various considerations outlined in [18]) for the depth-integrated theory, the *PfemFluidDynamicsApplication* (theory and applications reviewed in [19]) and the *ParticleMechanicsApplication* (with important principles focusing on material points described in [20]) as the approaches based on the particle analogy (implying a *Lagrangian* view of the governing physics), as well as the two-fluid formulation (with a *Eulerian* approach to the flow) of the Navier–Stokes equations contained in the *FluidDynamicsApplication*. A comparison is detailed in the work of [21]. The very last model of the flow equations can consider two phases in the flow: for our purposes, water and air. When used to model a TSD, the expected velocities are moderate, resulting in a Mach number $Ma < 0.3$, such that the assumption of incompressibility is appropriate [22]. The detailed derivation of the formulas below is presented in [23]. Corresponding numerical results describe the flow field being represented by the velocity and pressure in the domain. Under the assumption of the two phases being immiscible, this model enables the identification of the interface between water and air. The entire container domain Γ is divided into two complementary subdomains, seen in Equation (5),

$$\Gamma = \Gamma_{a(ir)} \cup \Gamma_{w(ater)}. \quad (5)$$

$$\begin{cases} \rho_i \left(\frac{\partial \mathbf{u}_i}{\partial t} + (\mathbf{u}_i \cdot \nabla) \mathbf{u}_i \right) - \mu_i \Delta \mathbf{u}_i + \nabla p_i = \mathbf{f}_i \\ \nabla \cdot \mathbf{u}_i = 0 \end{cases} \quad \text{in } \Gamma_i \text{ for } i = \text{air, water}. \quad (6)$$

Equation (6) presents a generic expression of the Navier–Stokes equations (ρ_i is the density, \mathbf{u}_i the velocity, μ_i is the dynamic viscosity, p_i marks pressure and \mathbf{f}_i is the body force), valid for both subdomains. The momentum equation is accompanied by the mass (i.e., continuity) conservation. This is the particular formulation and the accompanying governing equations of the CFD simulations that we used in this study. It provides a realistic model of the dynamic sloshing motion at a slightly higher computational effort. The transient analysis not only captures the interface of the wave at an appropriate level of accuracy and resolution but also provides critical insight into the motion of water below the surface level. This latter aspect is necessary for assessing the effect of added mass and damping from a TSD. Moreover, such a CFD formulation tends to scale well on HPC infrastructures, which is critical for detailed three-dimensional investigations. It is also promising when exploring various improvement possibilities, such as the detailed effect of screens or other beneficial alterations to the container shape.

2.2. Design Principles

Required design steps follow the line of thought representative for optimally tuning a TMD. Both are passive AMDs, aimed at reducing oscillations, specifically using the rules applicable for accelerations. Displacements will also be decreased. This process starts by identifying and decomposing the main directions of motion. In Figure 2, we show the schematic representation of the TMD and TSD, respectively. These are depicted in-plane on the cross-section of the structure. Mechanically, the TMD acts on each bending mode as a Single-Degree-of-Freedom (SDOF) system. Due to the fact that the mode shapes of the construction are uncoupled (i.e., bending modes neither affect each other, nor the torsional mode), the TMD can be tuned for each direction independently. This results in one-dimensional models. We are led to the total action by superposing the orthogonally functioning oscillators. TSDs follow an analogous principle. We considered two perpendicular sloshing directions, which are presented by a water in motion using a two-dimensional model (with sideways and vertical orientations) for each of the directions. This is actually a beneficial simplification, as it discards potential effects from the waves influencing each other.

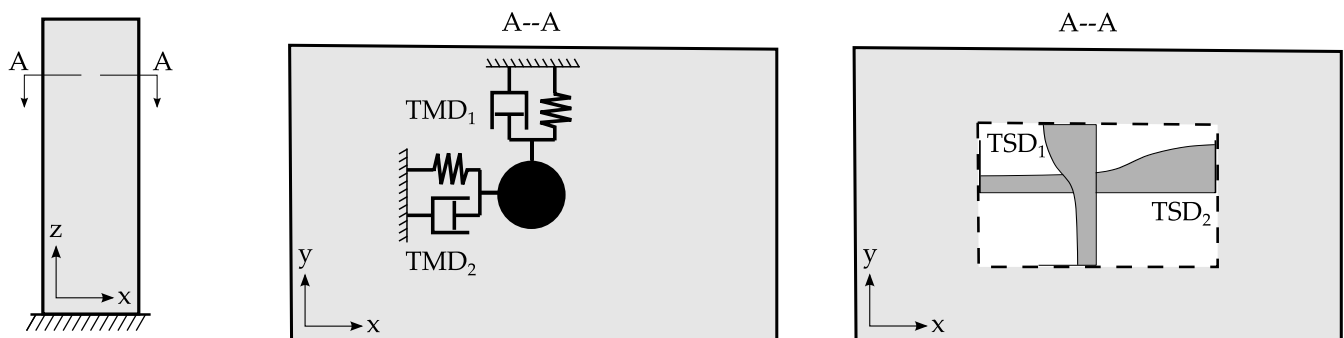


Figure 2. In-plane schematic representation of TMDs and TSDs.

The key design steps need to address the following major points:

1. Determine the mass ratio as an upper limit, depending on the maximum weight to be added to the structure;
2. Set a frequency (or tuning) ratio by determining at which frequency the added device should naturally vibrate;
3. Assess the damping ratio in the case of a TSD representing the estimate of the additional damping that could be achieved.

Optimizing AMDs in order to affect accelerations is analogous between the TMD and TSD. As the behaviour of TSDs is inherently nonlinear, this approach provide a starting basis for the design. We outline the necessary steps for a TMD in Setup 1. Such steps are applicable for setting up an equivalent linear SDOF mechanical model, with viscous damping. The process needs to take place for each of the dominant directions. Numerical values for the parameters are presented in Table 2. In the case of a TSD, this process is slightly modified, as highlighted in Setup 2. The workflow follows steps proposed by [24,25].

Setup 1 The steps for optimally tuning a TMD.

1	Choose the total mass ratio ¹	$\mu_{tot} \leq 1.5\%$	1
2	Calculate the added mass ²	$m = \mu_{tot} m_S$	2
3	Calculate the modal mass ratio	$\mu = \frac{m}{m_S^*} \eta^2$	3
4	Calculate the tuning (i.e., frequency) ratio	$\Omega_{opt} = \frac{1}{\sqrt{1+\mu}}$	4
5	Calculate the frequency of the damper based on the target structural frequency	$f_{opt} = \Omega_{opt} f_{S,target}$	5
6	Calculate the stiffness	$k = (2 \pi f_{opt})^2 m$	6
7	Calculate the optimal damping ratio	$\zeta_{opt} = \sqrt{\frac{3\mu}{4(1+\mu)(2+\mu)}}$	7
8	Calculate the damping coefficient	$c = 2 \zeta_{opt} m (2 \pi f_{opt})$	8

All parameters are for a TMD, unless specified otherwise and appropriately marked by a subscript. ¹ Here, we use as an upper limit the value typical for cantilever-type structures, as recommended by [26]. ² η is the value of the mode shape at the AMD.

Setup 2 The steps for optimally tuning a TSD

1	Choose the mass ratio similarly to how it is carried out for the TMD (we take the same exact value for our studies)	$\mu_{tot,TSD} \stackrel{!}{=} \mu_{tot,TMD}$	1
2	Calculate the effective damping ratio, as it should be optimally provided by the TSD	$\zeta_{eff,opt} = \frac{1}{4} \sqrt{\frac{\mu(1+\mu)}{1+3\mu/4}}$	2
3	Calculate the optimal damping ratio, which should be higher than the one previously determined	$\zeta_{opt} = \sqrt{\frac{\mu(1+3\mu/4)}{4(1+\mu)(1+\mu/2)}}$	3
4	Calculate the tuning (i.e., frequency) ratio, similar to the one for the TMD	$\Omega_{opt} = \frac{\sqrt{1+\mu/2}}{1+\mu}$	4
5	Calculate the frequency of the damper based on the target structural frequency	$f_{opt} = \Omega_{opt} f_{S,target}$	5
6	Calculate the optimal response ratio	$R_{opt} = \frac{1+\mu}{\sqrt{2\mu+3\mu^2/2}}$	6
7	Calculate the total damping ratio aimed to be achieved	$\zeta_{tot} = 0.8 \zeta_S + \zeta_{eff,opt}$	7
8	Calculate the RMS relative response motion of the equivalent linear mechanical model ¹	σ_r using $R = \frac{\sigma_r}{\sigma_S}$ and $\zeta_{tot} = \zeta_S \frac{\sigma_{S,initial}^2}{\sigma_{S,target}^2}$	8
9	Set the container dimensions L and h_0 such that the natural sloshing frequency fulfills the optimality criterion	$f_{opt} \stackrel{!}{=} f_w = \frac{1}{2\pi} \sqrt{\frac{\pi g}{L} \tanh\left(\frac{\pi h_0}{L}\right)}$	9
10	Set the relevant parameters for a screen (solidity ratio S , number of screens n and position x) such that the damping ratio ² fulfills the optimality criterion	$\zeta_{opt} \stackrel{!}{=} \zeta_{with\ screens} = C_1 \sqrt{\frac{32}{\pi^3}} \tanh^2\left(\frac{\pi h_0}{L}\right) \Delta \Xi \frac{\sigma_r}{L}$	10
11	Determine the number ³ N and width W of water containers such that the total target mass is reached	$m_w = N L W h_0 \rho_w \stackrel{!}{=} \mu_{tot} m_S$	11

All parameters are for a TSD, unless specified otherwise and appropriately marked by a subscript. ¹ The initial displacement can be achieved by a priori determining or assuming a typical value. ² The damping ratio for a TSD with screens under random excitation, as given by the mathematical model in [25]. ³ The total amount of water mass would typically be inefficient in one container and also difficult to allocate space for, so it needs to be distributed.

2.3. Efficiency Considerations

A typical setup for a TSD might assume the wave motions to be dominantly uni-directional. For more complex movement patterns, a coupling between various directions will be more realistic. Additionally, for such cases the shape of the container needs to be reconsidered, as sharp edges at the corners could be detrimental. This consideration not only holds in the horizontal plane, but also in the vertical one. Consequently, some use cases will lead to the adoption of sloped bottoms and avoid all kinds of sharp corners where possible. These measures intend to increase the amount of liquid in motion. Further improvements will lead to the usage of three-dimensional screens. Such elements, placed in the middle of the container, have the intention of increasing the friction (and thus dissipating kinetic energy through damping) of the sloshing water. The ideal placement will aim to locate the regions with the highest kinetic energy.

2.3.1. Vertical Slat Screens

Damping is typically proportional to the sloshing velocity. This means that the highest increase in dissipation can be achieved by placing additional slat screens, where the fluid motion is expected to be the largest. This would mean near the middle of the tank. Particular damping characteristics can be achieved by specific combinations of the number of slats and their placement. As practical recommendations are case-dependent, here, we outline the main ideas necessary for such tuning. Numerical solutions have the potential of assisting the design process and optimizing setups.

Kinetic energy is dissipated by the inherent viscous damping at the walls of the tanks, supplemented by wave breaking. This is typically suboptimal without additional elements to increase dissipation [25]. Poles, screens and various other objects can be inserted into the container for improved damping [27–29]. Vertical slat screens consist of stacked elements. The installation of such devices is simple. Varying spacing additionally permits the change in damping characteristics. These can be also used in semi-active damping devices [27,30] with changes possible during operation. Inclined and oscillating variations have also been tried [28]. The working principle is similar to the flow through porous media. Respective openings will induce an additional friction and pressure drop. Consequently, the primary influence of a screen is determined by the solidity ratio S . It is a characteristic of these devices, defined as the ratio of slat width d_{slat} to the slat spacing b_{slat} (i.e., of the solid material to the opening where the fluid can pass).

In recent works describing nonlinear models for TSDs [27,28,31], screens are taken into account by being numerically modeled by linear loss coefficients or with fixed pressure loss factors. For such cases, it is important to correctly evaluate the pressure loss. This influences the proper description of screens in transient flow conditions. For a steady flow, provisions are provided in [32]. Further consideration related to the detailed modeling of sharp-edged slat screen are described in [27–29]. Experimental values for relevant coefficients are provided by [33].

2.3.2. Sloped Bottoms and Rounded Corners

A shortcoming of rectangular containers is the increased non-effective mass. Sharp-edged corners of TSDs will result in zones where the water stays still. The inertia of the sloshing fluid has further undesired effects. In particular, beating [34] (or pulsating) is counter-productive, this happening due to continued sloshing once the motion of the base construction stops. This is an amplitude modulation of the structure. Such artifacts are improved when designing with inclined bottoms. This is in line with observations from ocean hydrodynamics and sloped beaches. The longitudinal motion can be dominant in a certain direction. It is well-matched by tanks particularly elongating in this specific orientation. Tall structures will undergo excitations in a combined mode, either due to the force acting in a skew angle or in the case of typical bending–torsion coupling. A rectangular shape in the horizontal plane might pose some more drawbacks, as uncontrolled or interfered waves can occur due to the corners. The positive aspect is that such side

effects can be overcome with careful geometric considerations. On the downside, each change will contribute with a nonlinear effect to the optimal tuning, thus complicating the design process.

3. Validation of the CFD Approach

Having outlined all typical considerations for setting up a TSD, the validation of the numerical model based on the two-fluid assumption follows. Consequently, a series of CFD simulations is planned, with the water tank undergoing controlled vibrations. They are induced in the form of imposed horizontal motions, with a series of prescribed amplitudes and frequencies. We use the extensive physical experimental results from [35] as a reference for comparison. Our aim is to replicate that setup, which was carried out on a shake table. The assessment was conducted at that reduced (i.e., model) scale, deriving the dimensionless characteristics supporting the final design of an optimally tuned TSD for our tall structure.

3.1. Experimental Setup

The numerical experiments focus on the sloshing of water in a rectangular container at a reduced scale. In [35], the dimensions length $L = 0.590$ m and width $W = 0.335$ m are used. The following combinations of water heights, excitation amplitudes and frequencies are planned: a constant excitation amplitude $a = 5$ mm with different water levels h_0 ; keeping a constant depth ratio $h_0/L = 0.102$ and varying amplitude ratios a/L . The investigations imply a harmonic horizontal forcing motion in time $x(t) = a \sin(\omega_{ext} t)$, with the prescribed circular forcing frequency being defined as $\omega_{ext} = \beta \omega_w$. The above characteristics need to be studied systematically because they lead to the design of TSDs aimed at mitigating structural vibrations. As the optimal working condition is at harmonic-dominant structural motions, this methodology represents the adequate preparatory phase. The critical outcome of the investigation is the total (dimensionless) sloshing force F_{sl} (and F'_{sl}) acting on the liquid container, as defined in Equations (7) and (8). The base shear mainly results from the difference in hydrostatic pressure on the two lateral walls (i.e., the water height: right h_R and left h_L). The denominator contains the maximum inertial force of the water treated as a solid mass m_w (being the total mass of liquid),

$$F_{sl} = \frac{1}{2} \rho g (h_R^2 - h_L^2), \tag{7}$$

$$F'_{sl} = \frac{F_{sl}}{m_w \omega_{ext}^2 a}. \tag{8}$$

We additionally recorded the physical work; here, the energy E transferred to or from the object. An appropriate relationship considering a forcing cycle is provided in Equation (9). The dimensionless dissipated energy per cycle $\Delta E'$ is also marked, being expressed in Equation (10). This is achieved by normalizing with the kinetic energy of the entire liquid considered as a solid mass,

$$\Delta E = \int_t^{t+T} F_{sl}(t) x(t) dt, \tag{9}$$

$$\Delta E' = \frac{\Delta E}{\frac{1}{2} m_w (\omega_{ext} a)^2}. \tag{10}$$

3.2. Imposed Motion Studies

The series of studies was designed using certain parameters from [35], such that the outcome supports the application case of a TSD, as described in [36,37]. We present the sloshing response in the form of the horizontal sloshing force, the shape of the hysteresis curve and the dissipated energy. These values are compared to the reference results in [35]. The comparison is supported by using the dimensionless expressions in Equations (8) and (10). The effect per

vibration cycle is of focus, where the enclosed area in the hysteresis loop represents the dissipated energy. We calculated the relative deviation of the assessed values from the results in [35].

Whereas the detailed results are contained in [21], here, we particularly focused on representing the characteristic outcome relevant for further design steps. The deviations observed in Figures 3 and 4 are low. Accompanying quantitative results are presented in Table 1. Not only are the areas of the hysteresis loops very close, but also the shape of the curves depict a comparable behaviour. For cases with a high water depth and small amplitude ratios, the simulations tend to slightly overestimate the sloshing response. We attribute this to additional internal numerical damping for such cases. Overall, the CFD-based approach reproduces the nonlinear sloshing forces very reliably. It can be seen that even higher harmonics are captured by the model, despite the hysteresis loops not identically overlapping with the reference ones.

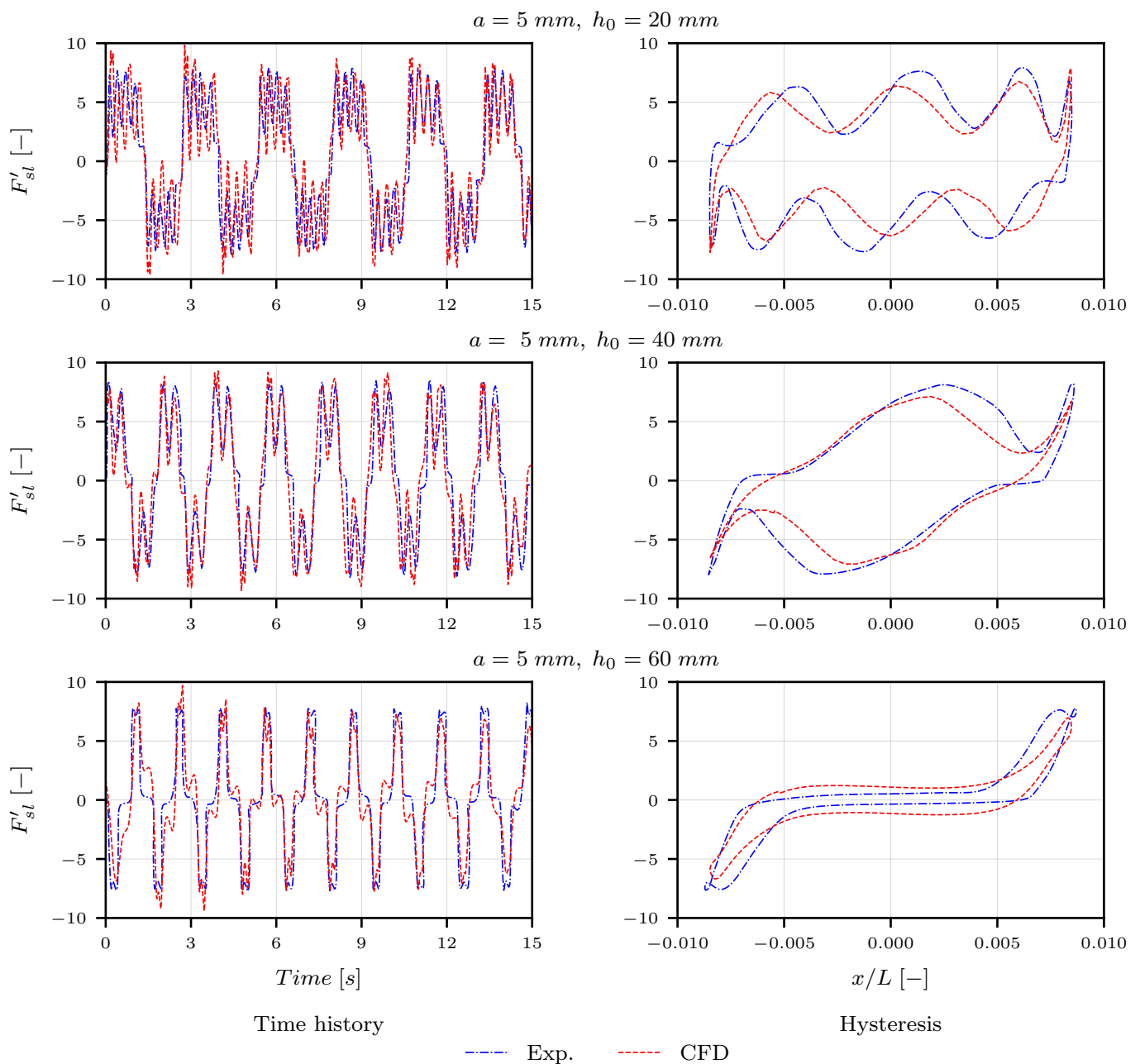


Figure 3. Validation results for varying the water height.

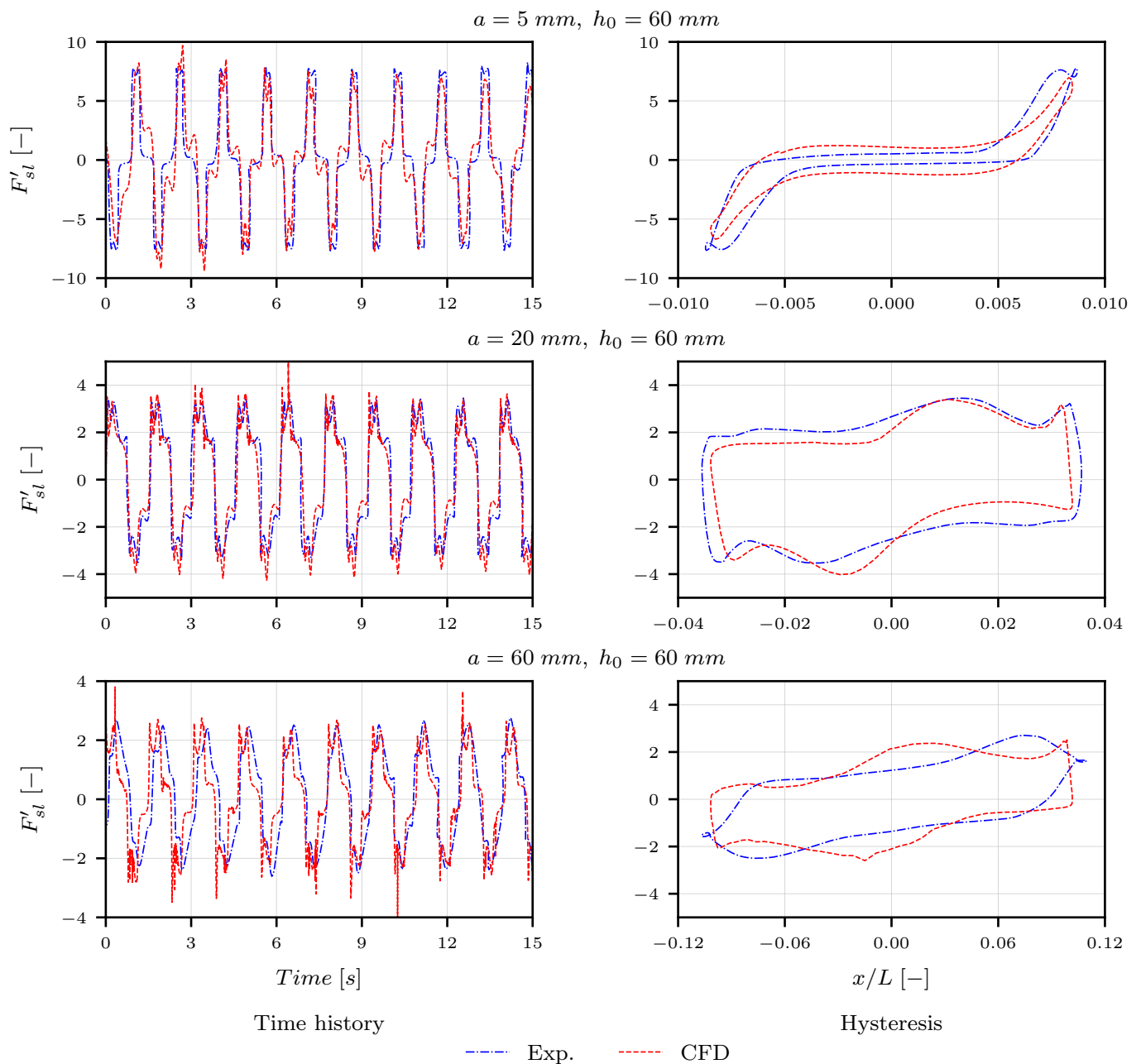


Figure 4. Validation results for varying the amplitude of excitation.

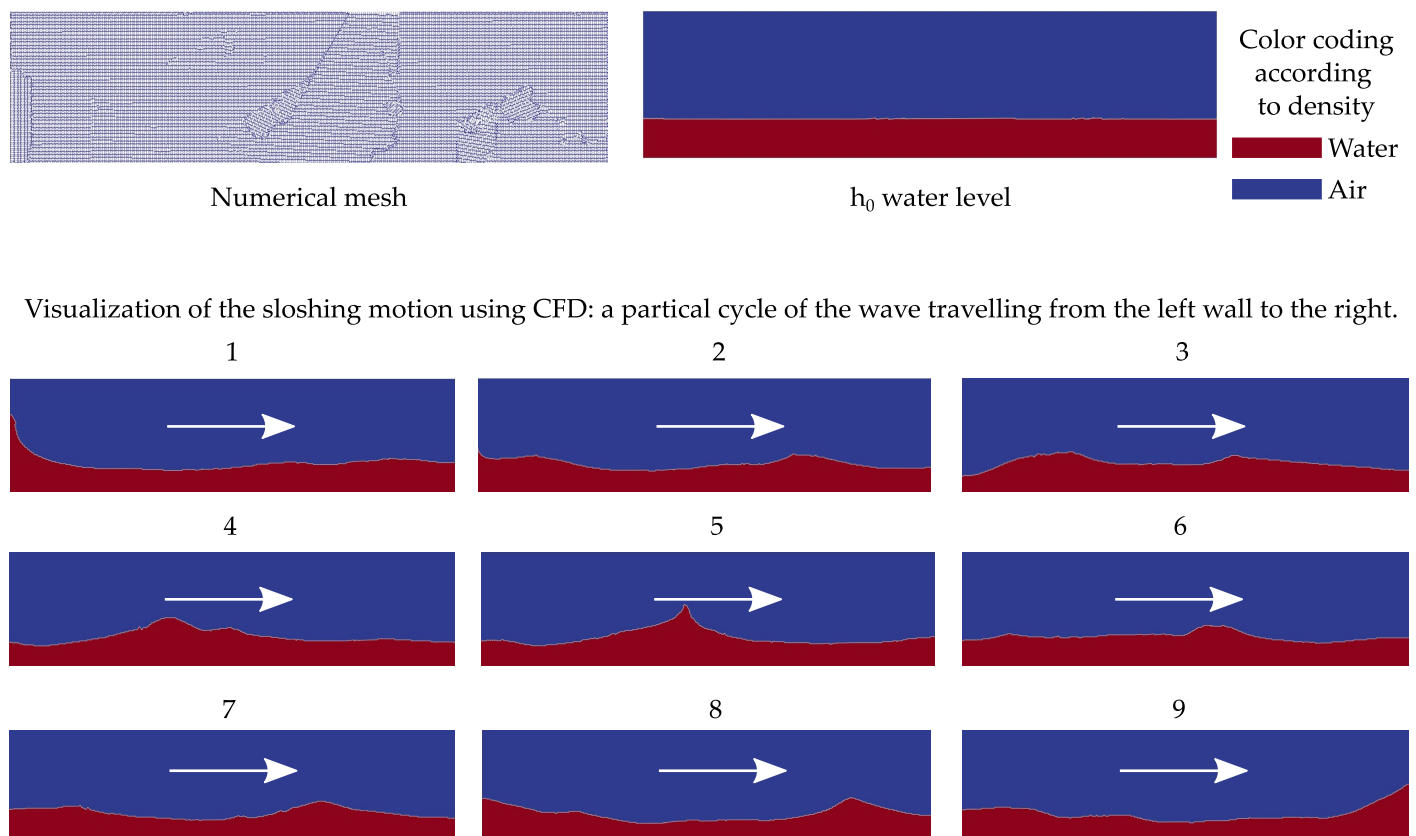
Table 1. Dimensionless energy per hysteresis cycle.

$\Delta E'$	$a = 5 \text{ mm}$		$a = 20 \text{ mm}$	$a = 60 \text{ mm}$	
	$h_0 = 20 \text{ mm}$	$h_0 = 40 \text{ mm}$	$h_0 = 60 \text{ mm}$		
Experiment	36.00	29.90	8.30	19.40	10.20
CFD	32.01	24.92	9.12	17.55	11.82
<i>Diff. to exp. [%]</i>	-11.1	-16.7	9.9	-9.5	15.9

Such studies can be designed in various ways, depending on the exact aim. For our use case, we limited them to a two-dimensional domain, without extensive focus on varying the excitation frequency. The results are mainly related to the effect of varying depth and amplitude ratios at a frequency characteristic for our building. It is expected of the TSD to

have to mitigate motions that are unidirectional, so this assumption is deemed appropriate. For other cases, three-dimensional simulations might be the only viable alternative, which is possible with CFD simulations.

Computational methods make it possible to visualize various results. In Figure 5, we include one of these, as a selection of variables and properties can be captured. Here, we see the clear distinction between air and water based upon density (similarly possible based upon viscosity). Additionally, the velocity and pressure fields are also available to aid in various discussions and design purposes.



Visualization of the sloshing motion using CFD: a partial cycle of the wave travelling from the left wall to the right.

Figure 5. Showcasing the representative setup and qualitative results for the imposed motion of $a = 5$ mm and $h_0 = 40$ mm: the water surface being best identified by the border between the densities of air and water.

4. Wind Loading and Vibration Mitigation

Wind loading represents a characteristic load case for tall buildings. It is critical to ensure structural safety and occupational comfort during the design process. Due to the inherent slenderness, high-rises are prone to vibrations. This leads to the necessity to find ways to mitigate such oscillations. Added devices constitute a common way to counteract these effects, with them being either planned already in early design phases or sometimes even considered as part of retrofitting measures. In particular, passive AMDs represent a common solution to wind-induced vibrations. We choose the prototypical case of a sharp-cornered construction, the CAARC-B building. The advantage of this example is that the load conditions are thoroughly studied. Multiple references substantiate the knowledge base, as it represents a benchmark for building aerodynamics. Not only is the oncoming naturally turbulent wind described in detail, but also vortex-shedding characteristics are well-known. This cuboid shape is prone to such a phenomenon, typically resulting in a *von Kármán* vortex street [38]. Clear vortical structures (more dominant in the case of *low-to-no* incoming turbulence) are linked to nearly harmonic cross-wind excitation forces.

4.1. Structural Model

The benchmark building has the aspect ratio of its dimensions height H : depth D : width W of 6:1.5:1, with $H = 180$ m. With a prescribed density of 160 kg/m^3 , the total mass results in 38.880 tonnes. It is a generic structure, with the mass, stiffness and damping characteristics distributed homogeneously. Further provisions give the target modes of vibrations and respective frequencies. The first three for such a cantilever structure are as follows: weak bending at $f_{bending,weak} = 0.20$ Hz, strong bending at $f_{bending,strong} = 0.23$ Hz and torsion at $f_{torsion} = 0.40$ Hz. These eigenmodes are uncoupled.

The initial study aimed to use this model for base-force measurements according to the High-Frequency Force Balance (HFFB) method. The peculiarity for that method is that the fixity is flexible, but the building is rigid along its height. As a result, the mode shapes are linear. We created a model setup for Finite Element Analysis (FEA). This numerical replica was built up with elements using a formulation corresponding to the FEM. It led to a structure detailed with multiple types of elements, such as shells, trusses and beams, tuned to match the prescribed geometric and mechanical properties. This directly led to more realistic shapes of vibration, similar to those known for cantilever-type structures.

4.2. Considered Load Cases

Wind loading is numerically captured using a LES approach, typical in CFD for transient flow fields [39,40]. The respective numerical domain follows the setup as presented in [41]. There are certain particularities to this setup, depending on whether the aim is to realistically model the natural turbulence in the Atmospheric Boundary Layer (ABL) or whether the scope is to trigger strong vortex shedding. The former case implies nonzero turbulence, whereas the latter can become critical for very low (to practically zero) turbulence intensity. In Figure 6, we show the main aerodynamic considerations and definitions.

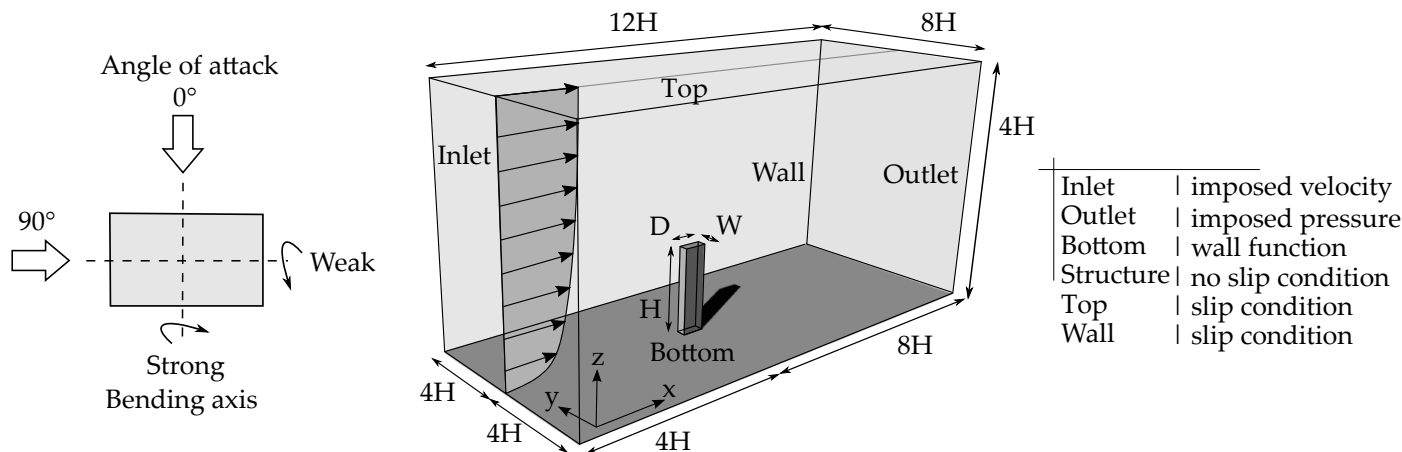


Figure 6. Definition of the wind loading: direction and simulation domain.

4.2.1. Turbulent Wind Loading

Here, we focus on the excitation typically arising in the Atmospheric Boundary Layer (ABL). Fluctuations in the wind field occur naturally for the CAARC-B, with available provisions describing the target state. This is characterized by the (streamwise, time-averaged) mean velocity profile along the height, accompanied by the turbulence intensity, as well as the (integral) turbulence length scale for this velocity component at the top of the structure. To achieve this state, we numerically modeled the inlet by synthetic turbulence, a specific type of generated condition (using the WindGen generator [42] based on the theory by [43]). We provide our assessment, additionally including the Power Spectral Density (PSD) for the streamwise velocity component. As the velocity is directly linked to the surface pressure, the along-wind excitation force will have a similar spectrum.

This scenario is thus characterized by a broad-band excitation, mostly in a streamwise (i.e., along-wind) direction.

The load mechanism is typically dominated by the oncoming flow, this being the gustiness approaching the ABL. It is acceptable to assume that the deformation state of the structure will not have a strong influence on the flow field itself. Consequently, we recorded the wind forces by CFD and applied it on the structural model, as typically carried out in Computational Structural Dynamics (CSD). Following the approach defined as One-Way Coupling (OWC), forces are transferred to the structure, but the resulting deformation state is not updated in CFD.

4.2.2. Oscillations in Smooth Flow

Fluctuations in the flow can either exist without the presence of the structure, such as the case in the previous scenario, or additional ones can arise due to a body being immersed into the flow. The CAARC-B is a bluff body that will facilitate vortex creation around it. Of particular interest is the case of a smooth flow, which triggers dominant shedding around the building. The critical situation is when the vortex shedding frequency f_{sh} matches one of the lower eigenmodes of the structure. We planned a setup to trigger this mechanism for the weak bending mode.

At a particular angle of attack, this occurs for a given streamwise velocity. This is described in detail by [41]. It leads to a practically constant along-wind force accompanied by a close-to-harmonic cross-wind component. If the narrow-banded excitation force [44] exactly matches the underlying structural frequency, we are led to the situation of mechanical resonance. However, in the case of (wind) flow, vortex-shedding can trigger a feedback mechanism, also called *lock-in* [38]. This means that not only is the exact overlap of the frequencies dangerous, but also the slight shifts might need considering, as the oscillating systems could synchronize. This leads to the necessity of the approach labeled as Two-Way Coupling (TWC). In the numerical context, this means that forces simulated by CFD trigger deformations in the CSD model, which, in turn, will require an update of the shape in the flow field.

4.2.3. Simulated Conditions

Wind flow conditions are characterized with typical metrics of the streamwise velocity component, presented in Figure 7. The turbulent flow approaches the building at a 0° angle of attack (streamwise perpendicular to the wide face). This is defined by a lower mean magnitude at a higher turbulence intensity TI . The energy spectrum of this velocity contains higher energy distributed over multiple frequencies. Smooth flow (i.e., minimal to no oncoming fluctuations) is seen in the case of the 90° angle of attack (streamwise parallel to the wide face). For this latter scenario, the along-wind velocity component has lower energy, as observed in the spectrum.

The energy content of the flow is inherent to the natural conditions of the approaching wind. The shape of the building determines the characteristics of the aerodynamic forces that arise under such conditions. These are presented in Figure 8. Along-wind, the vertical lines (dashed) represent the weak and strong bending frequencies, with 0.2 Hz and 0.23 Hz. We can see that there is no peak in the energy content at these values. Conversely, for the cross-wind component, the smooth flow peaks at approximately 0.2 Hz (dashed), with it matching the weak bending mode. In the case of approaching turbulence, we can also observe a cross-wind peak at 0.08 Hz (marked as dash-dotted). This peak is expected as, also in turbulent conditions, vortex shedding will exhibit itself. However, the mechanism overlaps with the fluctuations already present in the oncoming flow field.

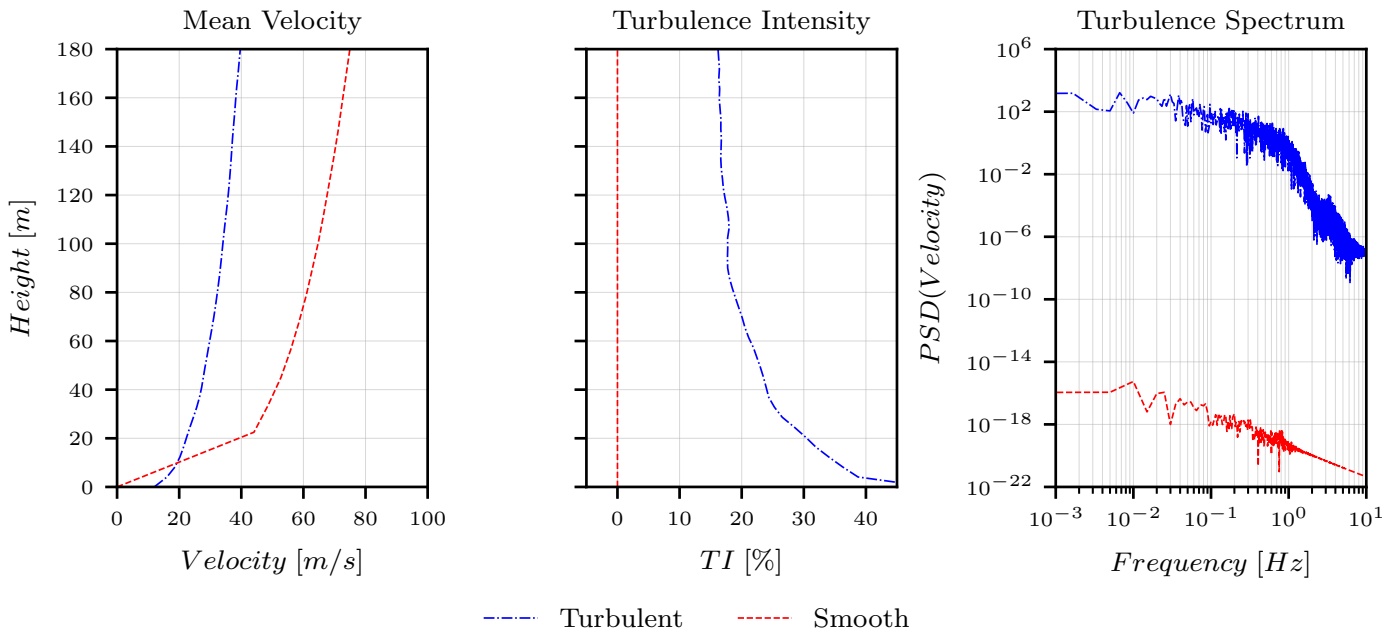


Figure 7. The typical metrics for characterizing the flow conditions: turbulent for the 0° angle of attack, smooth (i.e., low turbulent) for 90° angle of attack.

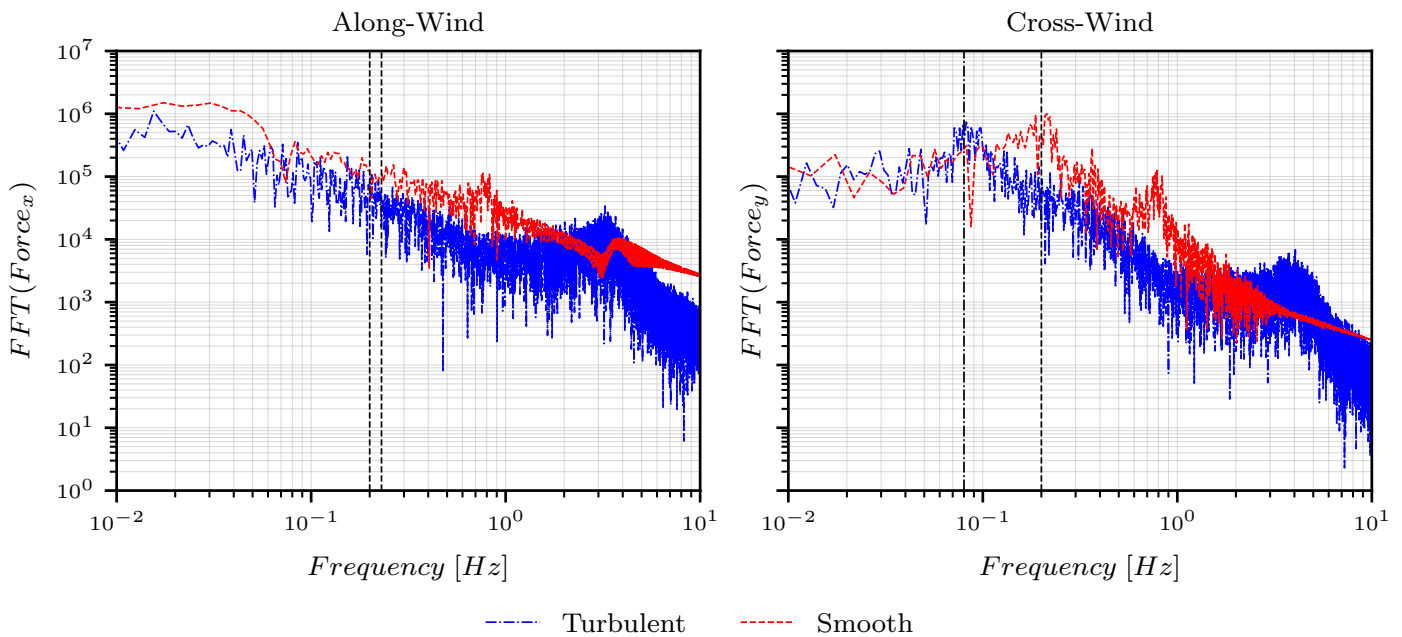


Figure 8. Spectral assessment of the energy content in the aerodynamic forces: turbulent flow for the 0° angle of attack, smooth in case of 90° angle of attack.

4.3. Coupled Simulations in CWE

Wind effects on structures often imply a feedback mechanism, thus rendering arising phenomena as challenging to be investigated. This means that the force deforms the structure, whereas such changes in shape will alter the flow field, leading to a modification of the excitation itself. This is a crucial characteristic in the case of flexible constructions. Numerical methods constitute one of the viable ways to investigate such effects. The main advantage is that corresponding simulations are not affected by scaling as the digital models are created at full (i.e., real) size. Following a *partitioned approach*, dedicated solvers are linked to the wind flow and structure, respectively. Nonetheless, this will lead to particular requirements of corresponding computing power, alongside issues related to the accuracy,

robustness and stability of the scheme. Additional details characterize the kind of coupling schemes used, OWC or TWC. This choice is problem-dependent, with potential effects being highlighted by the aerodynamic and elastic studies in [45]. Further generalizing the partitioning, numerical simulations permit the inclusion of additional components, such as AMDs, as shown in Figure 9. Whereas extending a structural model with a TMD would be straightforward by adding additional entries in the mass, damping and stiffness matrices (native to the FEM-formulation of structures), this is not a universal solution. For the particular case of a CFD model for a TSD, this submodule (or component) has to be treated in a dedicated manner. It also needs to be included in the broader computational scheme. The generalized concept follows the developments in [41,46]. This is a viable approach for investigating the efficiency of TSDs and TMDs alike, at full scale, while capturing all relevant details. It is also possible to use it for general controllers, with the applicability highlighted by [47].

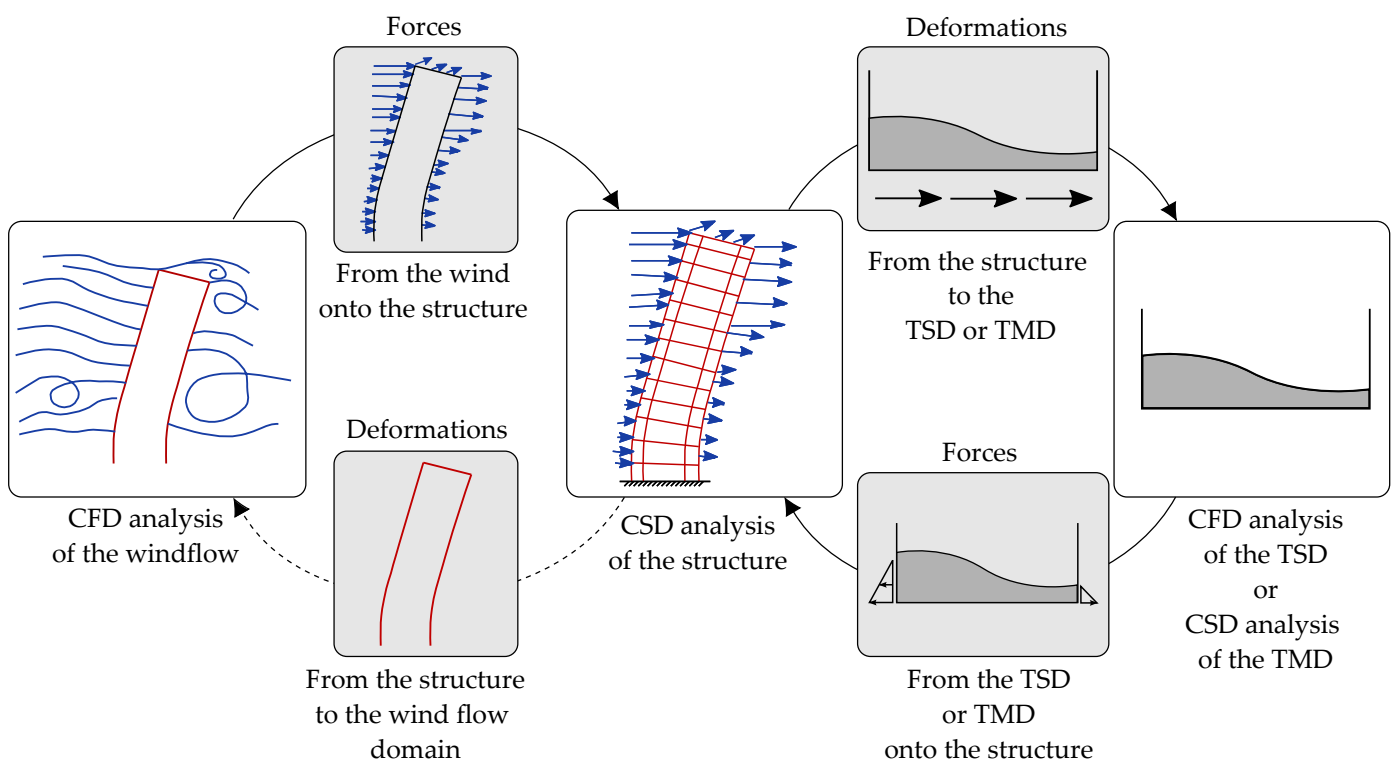


Figure 9. Representation of the coupled wind–structure–damper simulation.

For our purpose, we set up the TMD and the TSD based on the presented structural properties and following the principles enumerated in Section 2. In Table 2, all crucial parameters are detailed for the weak and strong bending mode, respectively.

Table 2. Setup of the interacting systems—structure and AMDs—using the definitions based on the structure-attached coordinate system.

System	Property	Symbol	Unit	Weak Bending	Strong Bending
Structure ^{1,2}	Height	H	[m]	180	
	Width	W	[m]	30	
	Depth	D	[m]	45	
	Total mass	m	$[\times 10^3 \text{ kg}]$	39,875	
	Equivalent density	ρ	$[\text{kg}/\text{m}^3]$	164	
	Mode shape number	i	[–]	1	2
	Eigenfrequency	f	[Hz]	0.20	0.23
	Value of the mode shape at the AMD	η	[–]	0.94	0.96
	Generalized modal mass of the mode shape	m^*	$[\times 10^3 \text{ kg}]$	10,144	12,698
Damping ratio	ζ	[%]	1.00	1.00	
TMD ^{1,3}	Mass	m	$[\times 10^3 \text{ kg}]$	180	
	Frequency	f	[Hz]	0.20	0.23
	Stiffness	k	$[\text{kg}/\text{s}^2]$	280,321	371,690
	Damping ratio	ζ	[%]	7.61	6.96
	Damping	c	$[\text{kg}/\text{s}]$	34,215	36,031
	Total mass ratio	μ_{tot}	[%]	0.45	
	Modal mass ratio	μ_{mod}	[%]	1.57	1.32
TSD ^{1,4}	Length	L	[m]	9.50	7.00
	Width	W	[m]	3.00	2.30
	Resting water height	h_0	[m]	1.57	1.12
	Location of screens	x	[–]	$(0.4, 0.6)L$	
	Solidity ratio of screens	S	[–]	0.32	0.30
	Mass per unit	m_N	$[\times 10^3 \text{ kg}]$	45	18
	Number of TSD units	N	[–]	4	10
	Total mass	m_w	$[\times 10^3 \text{ kg}]$	180	
	Total mass ratio	μ_{tot}	[%]	0.45	
	Modal mass ratio	μ_{mod}	[%]	1.57	1.32
	Effective mass per unit	$m_{eff,N}$	$[\times 10^3 \text{ kg}]$	33	13
	Effective mass	m_{eff}	$[\times 10^3 \text{ kg}]$	135	
	Total mass ratio	μ_{tot}	[%]	0.34	
Modal mass ratio	μ_{mod}	[%]	1.17	0.99	
Damping ratio with screens	ζ	[%]	5.59	4.88	
Labeling of the flow-attached axis	Turbulent flow at 0° angle of attack			Along-wind—X	Cross-wind—Y
	Smooth flow at 90° angle of attack			Cross-wind—Y	Along-wind—X

¹ Respective symbols will be attributed the initials of the systems—*Structure*, *TMD*, *TSD*—as subscripts to be able to differentiate. ² The total mass m_s will be used to compute μ_{tot} and the generalized modal mass m_s^* for μ_{mod} . ³ In case of a TMD the total and effective mass are the same. ⁴ Here we present results of the tuning process for a TSD with vertical slat screens. The mass ratios are provided for the total mass as well as the effective one.

5. Results

This section focuses on presenting the kinematics at the top of the building. We included the time series for the two orthogonal directions, for the displacement as well as the acceleration. These are the typical quantities of interest for the design. Baseline results characterize the motion of the structure under wind loading, without any AMD.

The broad-band excitation is caused by naturally turbulent wind. For this, engineers typically consider a 10-minute time frame, as that is deemed statistically stationary and representative for relevant actions on structures [48]. The initial time phase of 45 s (as seen in Figure 10) represents the initiation phase, with these values being discarded for the quantitative evaluation. Specific metrics are evaluated and shown in Table 3. The along-wind response is comparable, with the TMD and TSD performing similarly, at approximately

$\pm 5\%$ relative of each other. For the cross-wind direction, the TSD performs at around 25% worse than a TMD under these settings. Both AMDs improve the structural response by mitigating deflections up to 50%. We mention that such devices aim to perform well for excitation forces near the natural vibration of the underlying construction. However, this load case is broad-banded, so less efficiency is to be expected.

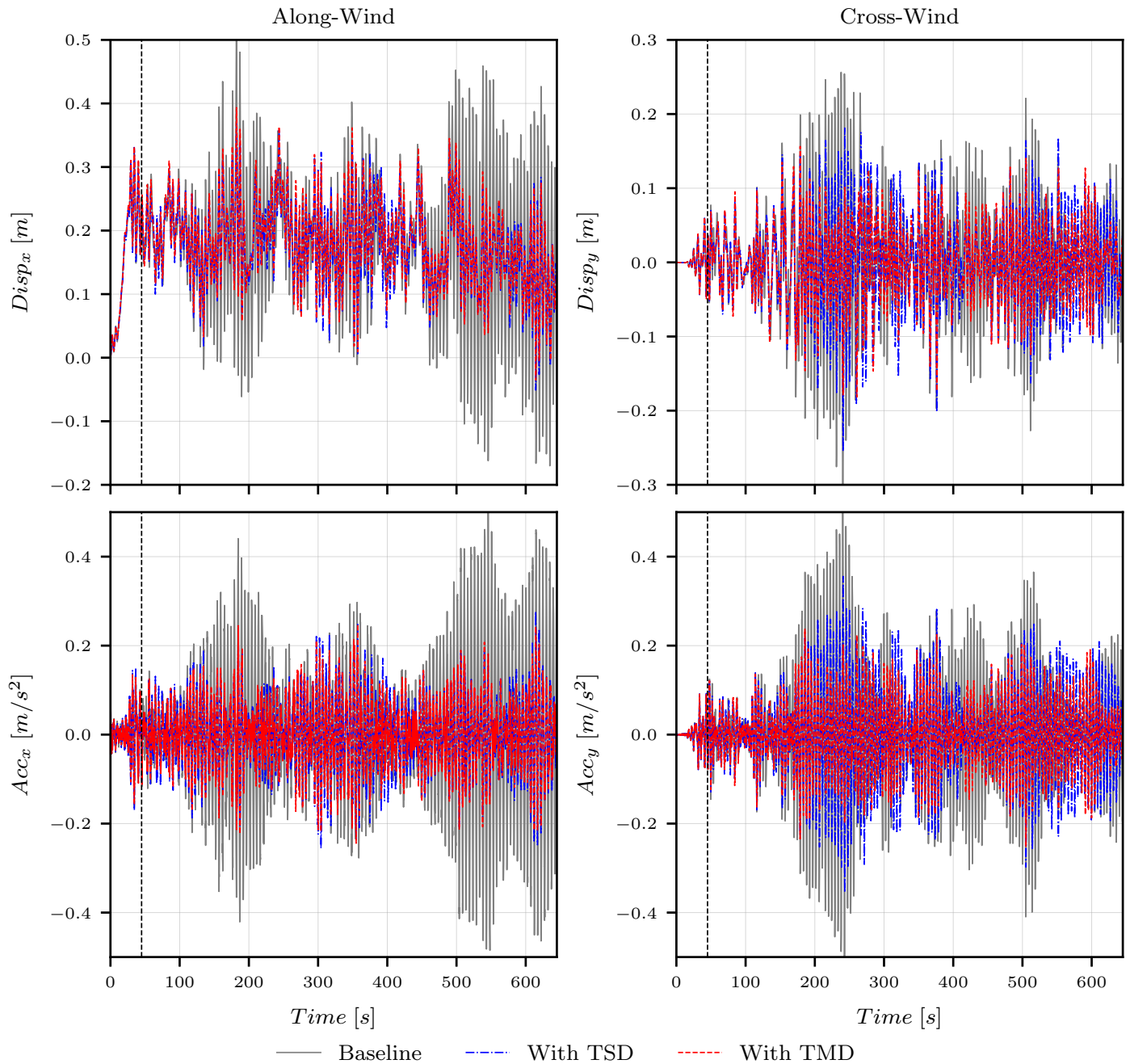


Figure 10. Time series of the kinematics of the top point under turbulent wind loading.

Table 3. Statistics of the kinematics of the top point under turbulent wind loading.

Case	Along-Wind						Cross-Wind					
	$Disp_x$ [m]			Acc_x [m/s ²]			$Disp_y$ [m]			Acc_y [m/s ²]		
	Mean	RMS	Max	Mean	RMS	Max	Mean	RMS	Max	Mean	RMS	Max
Baseline	0.18	0.21	0.53	0.00	0.17	0.52	0.00	0.09	0.26	0.00	0.16	0.47
With TMD	0.18	0.19	0.39	0.00	0.08	0.23	0.00	0.06	0.17	0.00	0.08	0.25
Diff. to baseline [%]	0.0	−9.5	−26.4	0.0	−52.9	−55.8	0.0	−33.3	−34.6	0.0	−50.0	−46.8
With TSD	0.18	0.19	0.38	0.00	0.08	0.25	0.00	0.07	0.20	0.00	0.11	0.33
Diff. to baseline [%]	0.0	−9.5	−28.3	0.0	−52.9	−51.9	0.0	−22.2	−23.1	0.0	−31.3	−29.5
Diff. to TMD [%]	0.0	0.0	−2.6	0.0	0.0	8.7	0.0	16.7	17.6	0.0	37.5	32.0

Time series are accompanied by a quantitative statistical evaluation. As an additional metric, we define a maximum value based upon derived quantities, instead of the sample maximum. In Equation (11), the estimate is shown using a peak factor $G = 3$ (with an estimate provided in this magnitude by [48]) alongside the mean and standard deviation σ of the time series,

$$Max = Mean(series) + G \sigma(series). \tag{11}$$

A dedicated discussion on the exact choice of the peak factor is out of the scope of the current study, as it serves here as an amplification factor. It is taken as the same throughout the statistical analysis, with its magnitude deemed representative. For special design cases, this term needs a more in-depth investigation. Table 3 provides a summary. Alongside the absolute values, the relative error is also displayed, being evaluated in pairs, between the *TMD–baseline*, *TSD–baseline* and *TSD–TMD*.

Our second scenario represents narrow-banded loading in the cross-wind direction. The dominant force arises in the smooth flow as a result of vortex shedding. Such an excitation case is more typical for the setting that is aimed to be mitigated by AMDs. Passive devices typically work well at particular frequencies. In Figure 11, we include the time series for displacements and accelerations. This is amended by the statistical evaluation in Table 4. The total time used for the evaluation is 200 s, with the initialization being 25 s. This choice resulted from capturing at least ≈ 25 periods of the vortex shedding (with $T = 5$ s for the shedding frequency $f_{sh} = 0.2$ Hz matching the weak bending). We can clearly see in the time series that, for the baseline case, around 150 s are necessary to reach the stationary state of damped harmonic oscillations. To put this in context, these very specific flow conditions for a tall structure would need to be stable for 2.5 min to arrive at this state, where it would imply ± 3 m oscillations at a 180 m height. Both AMDs would be able to reduce this to well under 1 m.

Table 4. Statistics of the kinematics of the top point in smooth flow.

Case	Along-Wind						Cross-Wind					
	$Disp_x$ [m]			Acc_x [m/s ²]			$Disp_y$ [m]			Acc_y [m/s ²]		
	Mean	RMS	Max	Mean	RMS	Max	Mean	RMS	Max	Mean	RMS	Max
Baseline	0.40	0.41	0.56	0.00	0.24	0.72	0.00	1.62	4.88	0.00	2.58	7.75
With TMD	0.39	0.39	0.45	0.00	0.10	0.30	0.00	0.13	0.39	0.00	0.21	0.62
Diff. to baseline [%]	−2.5	−4.9	−19.6	0.0	−58.3	−58.3	0.0	−92.0	−92.0	0.0	−91.9	−92.9
With TSD	0.39	0.39	0.50	0.00	0.18	0.53	0.00	0.26	0.78	0.00	0.41	1.22
Diff. to baseline [%]	−2.5	−4.9	−10.7	0.0	−25.0	−26.4	0.0	−84.0	−84.0	0.0	−84.1	−84.3
Diff. to TMD [%]	0.0	0.0	11.1	0.0	80.0	76.7	0.0	100.0	100.0	0.0	95.2	96.8

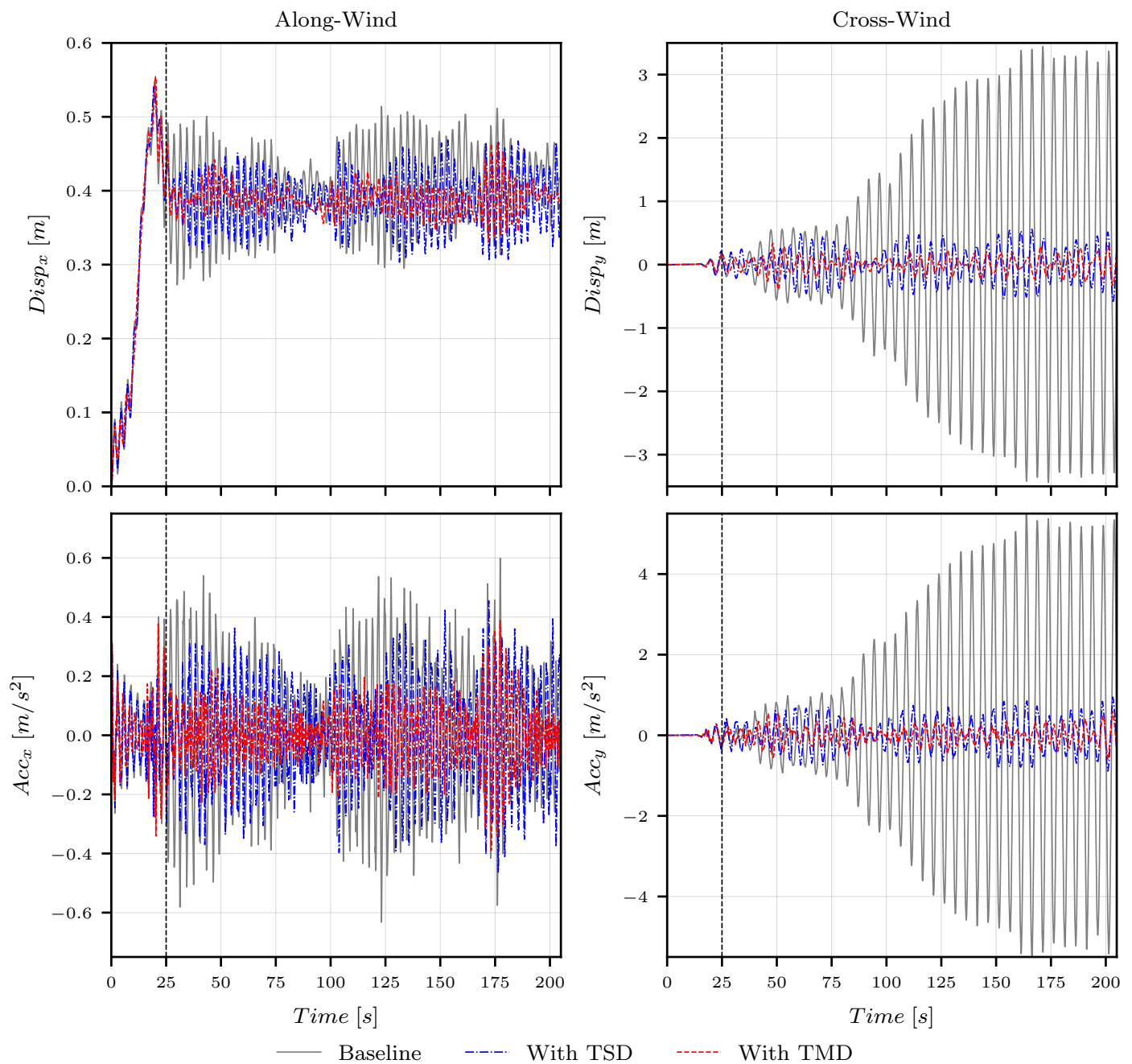


Figure 11. Time series of the kinematics of the top point in smooth flow.

A TMD was set up using an assumption of the linear mechanical model particularly tuned to the eigenfrequencies of the building. For TSDs, this is the analogous workflow, yet the tuning process is more complicated. It needs additional considerations of the initial representative response and the amount of mitigation that is aimed to be achieved. Thus, the design is a function of the response amplitude. Altering load conditions would theoretically lead to different optima. We based our considerations on a representative amplitude of acceleration of around (0.15–0.2) m/s² for the baseline structure. This value seems to be more appropriate for the broad-band load case, and sub-optimal for the narrow-banded one. A proper decision for each particular design will need to be taken, weighing in the relative importance of specific load cases.

For the particular scenario of smooth flow, both AMDs achieve a considerable improvement of close to 100% cross-wind. In the along-wind direction, the TSD performs

clearly worse than the TMD. It needs to be mentioned that, for this load case, the harmonic loading around the weak axis is more critical. Still, the relative performance in this direction shows a considerable difference of 100%, in favor of the TMD.

Accompanying these qualitative and quantitative outcomes on the direct effect of AMDs on structures in wind, we provide a snapshot of representative results. Using computational methods permits analyzing all systems involved at full scale, at various levels of detail. In Figure 12, we include typical data that help to visualize: wind loading using CFD, the structural response captured with CSD and the sloshing motion enabled by CFD. This depiction complements the abstraction of the workflow shown in Figure 9.

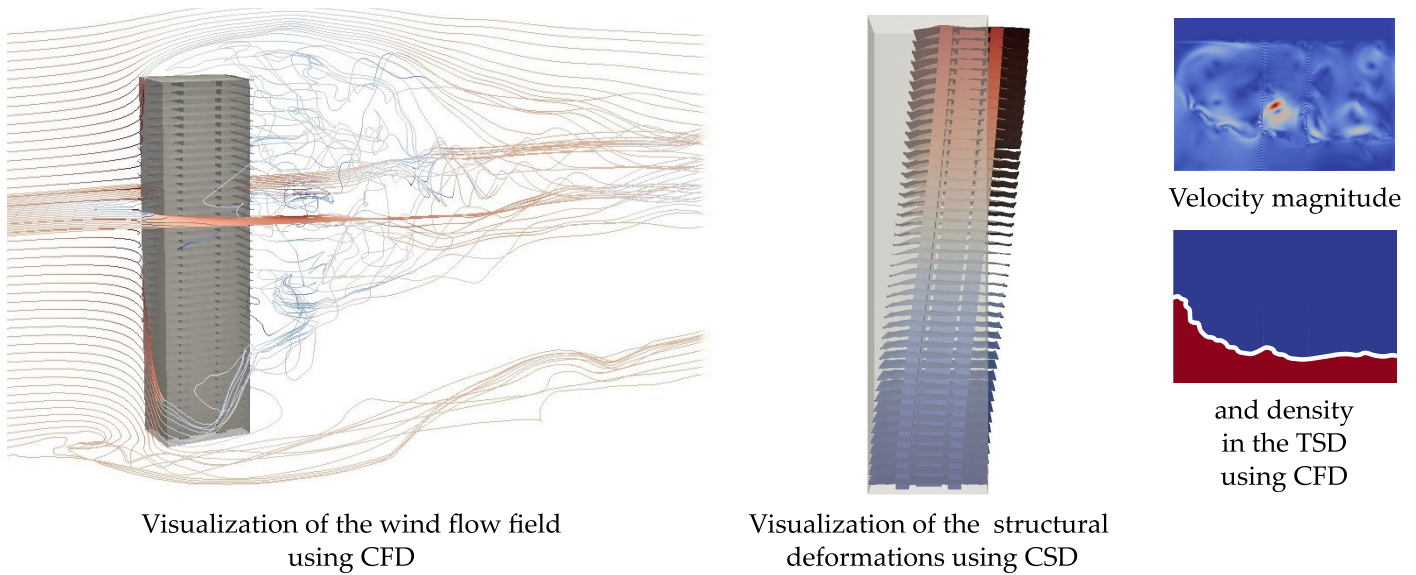


Figure 12. Representative visual results using a computational workflow.

The complexity of the models and computational effort for the analyses are substantiated by Tables 5 and 6. Here, we document certain characteristics related to the detailing of the numerical setup. This is best represented by the number nodes and respective variables, the key quantities for a FEM-based formulation. The total duration and amount of time steps will further influence the requirements in the case of transient simulations. The second table includes the approximate computational cost in the form of core hours. We provide it as the magnitude should be meaningful for the engineering practice, as well as to those aiming at similar studies.

Table 5. Complexity of the numerical models.

Type of Simulation	Number of		Nodal Variables Name & Type	Degrees of Freedom		Total Time [s]	Time Step	
	Elements	Nodes		per Node	Total		Size [s]	Number
Turbulent wind CFD	7.0×10^6	1.3×10^6	Pressure (scalar) and velocity (vector)	4	5.2×10^6	645	0.02	3.2×10^4
Smooth flow CFD	4.0×10^6	0.7×10^6	Pressure (scalar) and velocity (vector)	4	2.8×10^6	200	0.01	2.0×10^4
Structure CSD	2.1×10^6	6.0×10^4	Displacement and rotation (vector)	6	3.6×10^5	Will depend on what the structure or AMDs are coupled to		
TSD CFD	7.5×10^4	3.9×10^4	Pressure (scalar) and velocity (vector)	3	1.2×10^5			
TMD CSD	2	1	Displacement (vector)	2	2			

Table 6. Numerical effort required for assessment.

Type of Simulation		Core Hours ¹ [CPUh]
Turbulent wind CFD		12,000
Smooth flow CFD		7000
<i>Diff. to wind turbulent CFD</i>	[%]	−41.6
Smooth flow FSI		15,000
<i>Diff. to smooth flow CFD</i>	[%]	114.3
Smooth flow FSI + TMD		23,000
<i>Diff. to smooth flow FSI</i>	[%]	53.3
Smooth flow FSI + TSD		32,000
<i>Diff. to smooth flow FSI</i>	[%]	113.3

¹ Using MPI distributed memory parallelism on Intel Skylake—Xeon Platinum 8174 processors with a base frequency of 3.10 GHz and 33 MB cache.

In Table 6, computed core hour values are shown, which we documented for simulations carried out on the same hardware. It can be observed that CFD simulations with turbulent wind will require more capacities because there needs to be a refinement of the mesh from the inlet to the structure to maintain approaching turbulence. Additionally, the total simulation time is typically longer. Despite a larger time step (in this particular case), the resulting effort can be two to three times higher than for the CFD simulation in the case of smooth flow. FSI approaches tend to increase the cost by a factor of at least 2 due to TWC. Including AMDs into the workflow further magnifies requirements by at least a factor of (1.5–2).

6. Conclusions and Outlook

Our work focused on modeling and numerically simulating the effect of added damping systems on structures excited by wind. In particular, we contributed a fully computational workflow that uses CFD not only to capture wind flow but also to include TSDs. This happens in a coupled manner to enable interaction at full scale. Consequently, such an approach currently represents the highest fidelity method for these kinds of assessments. Further innovation lies in developing proper algorithms, with an implementation supporting modularity and scaling on dedicated computing units. Our results support the argument for applicability in the case of similar user scenarios.

We investigated the vibration mitigation efficiency of TSDs using a two-fluid CFD approach. The results show that these can be considerably less efficient than TMDs for the load cases covered. The specific metrics are related to the displacement and acceleration at the top of the building, under wind load. In particular, the RMS and estimated maximum values of the time series are of interest. The optimal tuning was oriented towards accelerations. This baseline comparison shows that a simple passive TMD will tend to perform better than the equivalent setup of a TSD. We need to recall the challenging design process for this latter category. As this is mostly based on a linear mechanical model, more effort is needed to improve the process itself. The nonlinear behavior of the TSD should be investigated at full scale, ideally with coupling to the structure being modeled and simulated. Additionally, there is much room for improvement when considering the possibilities of sloping bottoms, rounding corners and including screens. One specific configuration of vertical slat screens that we do consider, and its effect, are included in our results. Further numerical optimization would potentially lead to improvements in the performance of TSDs. Additionally, we explored recent numerical advances in finding an appropriate model for the mechanical effects of the considered AMDs. The sloshing motion is realistically simulated by the two-fluid CFD approach. The validation studies of a rectangular container under prescribed motion are well in-line with the experimental reference. This ensures that the effect of sloshing is correctly captured, as substantiated by the time histories and hysteresis curves. The combination of CFD and numerical optimization is a viable way to investigate the effects of TSDs, as well as to find improved designs.

The chosen load cases relate to two representative scenarios, both describing various facets of wind loading on tall structures. Atmospheric turbulence is modeled by a generated synthetic wind, whereas the other scenario aims to trigger strong vortex shedding. Yet again, CFD-based methods are able to properly model such flow phenomena, which contribute to the realistic loading of constructions. The loading itself is set up based on referenced work. Furthermore, the structure is modeled by a detailed numerical replica, including all structural details and resulting in a particular mass, stiffness and damping distribution in space. It is defined at its full size.

Our numerical workflow and framework permits capturing the interaction between the excitation source and the considered structure, as well as the AMDs. This leads to an integrated process where all effects can be simulated at the proper scale and necessary resolution. The current contribution showcased its usability by including AMDs that were tuned for the two orthogonal directions separately, modeled one-dimensional (for the TMD) and two-dimensional (for the TSD). The total damping effect was yielded from superposing reactions. Future work will focus on validating this assumption using three-dimensional models. This shall also enable their usability in structures with coupled bending and torsion.

Author Contributions: Conceptualization, M.P., K.-U.B. and F.W.; methodology, M.P. and A.R.; software, M.P. and A.R.; validation, A.R. and M.P.; formal analysis, M.P., A.R. and F.W.; investigation, A.R. and M.P.; resources, M.P., K.-U.B. and F.W.; data curation, M.P. and A.R.; writing—original draft preparation, A.R. and M.P.; writing—review and editing, M.P., F.W. and A.R.; visualization, A.R. and M.P.; project administration, M.P., K.-U.B. and F.W. All authors have read and agreed to the published version of the manuscript.

Funding: This research received no external funding.

Institutional Review Board Statement: Not applicable.

Informed Consent Statement: Not applicable.

Data Availability Statement: The data presented in this study are available on request from the corresponding author.

Acknowledgments: The authors gratefully acknowledge the Gauss Centre for Supercomputing e.V. (www.gauss-centre.eu) (accessed on 29 May 2022) for funding this project by providing computing time on the GCS Supercomputer SuperMUC-NG at Leibniz Supercomputing Centre (www.lrz.de) (accessed on 29 May 2022). The authors additionally remark the support of Maurer SE, Maurer Engineering GmbH and Maurer Switzerland GmbH.

Conflicts of Interest: The authors declare no conflict of interest.

References


1. Wardlaw, R.L.; Moss, G.F. A Standard Tall Building Model for the Comparison of Simulated Natural Wind in Wind Tunnels. *CAARC CC 662m Tech* **1970**, *25*.
2. Melbourne, W.H. Comparison of measurements on the CAARC standard tall building model in simulated model wind flows. *J. Wind Eng. Ind. Aerodyn.* **1980**, *6*, 73–88. [CrossRef]
3. Benchmark Buildings for an International HFFB Comparison. The Study as Proposed by the International Association for Wind Engineering (IAWE). Available online: <https://www.iawe.org/committees/HFFB-spec.pdf> (accessed on 29 May 2022).
4. Holmes, J.; Tse, K.T. International high-frequency force balance benchmark study. *Wind Struct.* **2014**, *18*, 457–471. [CrossRef]
5. Wang, W.; Kamath, A.; Martin, T.; Pákozdi, C.; Bihs, H. A Comparison of Different Wave Modelling Techniques in an Open-Source Hydrodynamic Framework. *J. Mar. Sci. Eng.* **2020**, *8*, 526. [CrossRef]
6. Li, Z.; Deng, G.; Queutey, P.; Bouscasse, B.; Ducroz, G.; Gentaz, L.; Le Touzé, D.; Ferrant, P. Comparison of wave modeling methods in CFD solvers for ocean engineering applications. *Ocean Eng.* **2019**, *188*, 106237. [CrossRef]
7. Godderidge, B.; Turnock, S.; Tan, M.; Earl, C. An investigation of multiphase CFD modelling of a lateral sloshing tank. *Comput. Fluids* **2009**, *38*, 183–193. [CrossRef]
8. Hwang, S.Y.; Lee, J.H. The Numerical Investigation of Structural Strength Assessment of LNG CCS by Sloshing Impacts Based on Multiphase Fluid Model. *Appl. Sci.* **2021**, *11*, 7414. [CrossRef]
9. Cotela, J.; Oñate, E.; Rossi, R. *Applications of Turbulence Modeling in Civil Engineering*; Monograph CIMNE: Barcelona, Spain, 2016. Available online: https://www.scipedia.com/public/Cotela_2016 (accessed on 29 May 2022).

10. Heil, M.; Hazel, A.L.; Boyle, J. Solvers for large-displacement fluid–structure interaction problems: Segregated versus monolithic approaches. *Comput. Mech.* **2008**, *43*, 91–101. [CrossRef]
11. Degroote, J.; Haelterman, R.; Annerel, S.; Bruggeman, P.; Vierendeels, J. Performance of partitioned procedures in fluid–structure interaction. *Comput. Struct.* **2010**, *88*, 446–457. [CrossRef]
12. Mok, D.P.; Wall, W.A. Partitioned analysis schemes for the transient interaction of incompressible flows and nonlinear flexible structures. In *Trends in Computational Structural Mechanics*; CIMNE: Barcelona, Spain, 2001; pp. 688–698.
13. Dettmer, W.G.; Perić, D. A new staggered scheme for fluid–structure interaction. *Int. J. Numer. Methods Eng.* **2012**, *93*, 1–22. [CrossRef]
14. The Kratos Multiphysics Open-Source Project. Available online: <https://github.com/KratosMultiphysics/Kratos> (accessed on 29 May 2022).
15. Dadvand, P.; Rossi, R.; Gil, M.; Martorell, X.; Cotela, J.; Juanpere, E.; Idelsohn, S.; Oñate, E. Migration of a generic multi-physics framework to HPC environments. *Comput. Fluids* **2013**, *80*, 301–309. [CrossRef]
16. Lamb, H. *Hydrodynamics*; University Press: Cambridge, MA, USA, 1924.
17. Graham, E.; Rodriguez, A. The Characteristics of Fuel Motion Which Affect Airplane Dynamics. *J. Appl. Mech.* **1952**, *19*, 381–388. [CrossRef]
18. Masó, M.; de Pouplana, I.; Oñate, E. A FIC-FEM procedure for the shallow water equations over partially wet domains. *Comput. Methods Appl. Mech. Eng.* **2022**, *389*, 114362. [CrossRef]
19. Cremonesi, M.; Franci, A.; Idelsohn, S.; Oñate, E. A State of the Art Review of the Particle Finite Element Method (PFEM). *Arch. Comput. Methods Eng.* **2020**, *27*, 1709–1735. [CrossRef]
20. Iaconeta, I.; Oñate, E.; Larese, A. *Discrete-Continuum Hybrid Modelling of Flowing and Static Regimes*; Monograph CIMNE: Barcelona, Spain, 2019. Available online: https://www.scipedia.com/public/Iaconeta_et_al_2020a (accessed on 29 May 2022).
21. Riedl, A.M. Numerical Modeling and Simulation of Coupled TLD-Structure Response under Time History Loading. Master’s Thesis, Technical University of Munich, Munich, Germany, 2021.
22. Ferziger, J.; Peric, M.; Street, R. *Numerische Strömungsmechanik*; Springer Vieweg: Berlin, Germany, 2020.
23. von Wenczowski, S. Two-Fluid Finite Element Formulation for Flood Simulation in Mountain Terrain. Master’s Thesis, Technical University of Munich, Munich, Germany, 2019.
24. Love, J.; Tait, M.; Toopchi-Nezhad, H. A hybrid structural control system using a tuned liquid damper to reduce the wind induced motion of a base isolated structure. *Eng. Struct.* **2011**, *33*, 738–746. [CrossRef]
25. Tait, M. Modelling and preliminary design of a structure-TLD system. *Eng. Struct.* **2008**, *30*, 2644–2655. [CrossRef]
26. Petersen, C.; Werkle, H. *Dynamik der Baukonstruktionen*; Springer Vieweg: Wiesbaden, Germany, 2017. [CrossRef]
27. Hamelin, J. The Effect of Screen Geometry on the Performance of a Tuned Liquid Damper. Master’s Thesis, McMaster University, Hamilton, ON, Canada, 2007.
28. Cassolato, R. The Performance of a Tuned Liquid Damper Equipped with Inclined and Oscillating Damping Screens. Master’s Thesis, McMaster University, Hamilton, ON, Canada, 2007.
29. Tait, M. The Performance of 1-D and 2-D Tuned Liquid Dampers. Ph.D. Thesis, University of Western Ontario, London, ON, Canada, 2004.
30. Tait, M.; Isyumov, N.; El Damatty, A. Effectiveness of a 2D TLD and its numerical modeling. *J. Struct. Eng.* **2007**, *133*, 251–263. [CrossRef]
31. Tait, M.; El Damatty, A.; Isyumov, N. An investigation of tuned liquid dampers equipped with damping screens under 2D excitation. *Earthq. Eng. Struct. Dyn.* **2005**, *34*, 719–735. [CrossRef]
32. Baines, W.; Peterson, E. An investigation of flow through screens. *Trans. Am. Soc. Mech. Eng.* **1951**, *73*.
33. Weisbach, J. *Die Experimental-Hydraulik*; JG Engelhardt: Freiberg, Germany, 1855.
34. Gardarsson, S.; Yeh, H.; Reed, D. Behavior of sloped-bottom tuned liquid dampers. *J. Eng. Mech.* **2001**, *127*, 266–271. [CrossRef]
35. Krabbenhøft, J. Shallow Water Tuned Liquid Dampers. Ph.D. Thesis, Department of Civil Engineering, Technical University of Denmark, Lyngby, Denmark, 2011. Available online: https://backend.orbit.dtu.dk/ws/portalfiles/portal/6470255/PhD_Thesis_Krabbenhøft2010.pdf (accessed on 29 May 2022).
36. Sun, L.; Fujino, Y.; Pacheco, B.; Isobe, M. Nonlinear Waves and Dynamic Pressures in Rectangular Tuned Liquid Damper (TLD) Simulation and Experimental Verification. *Doboku Gakkai Ronbunshu* **1989**, *1989*, 81–92. [CrossRef]
37. Sun, L.; Fujino, Y. A semi-analytical model for tuned liquid damper (TLD) with wave breaking. *J. Fluids Struct.* **1994**, *8*, 471–488. [CrossRef]
38. Hucho, W.H. *Aerodynamik der Stumpfen Körper*, 2nd ed.; Vieweg+Teubner: Wiesbaden, Germany, 2011.
39. Bitsuamlak, G.; Simiu, E. CFD’s potential applications: A wind engineering perspective. In Proceedings of the The Fifth International Symposium on Computational Wind Engineering (CWE2010), Chapel Hill, NC, USA, 23–27 May 2010.
40. Blocken, B. 50 years of Computational Wind Engineering: Past, present and future. *J. Wind Eng. Ind. Aerodyn.* **2014**, *129*, 69–102. [CrossRef]
41. Péntek, M.; Winterstein, A.; Vogl, M.; Kupás, P.; Bletzinger, K.U.; Wüchner, R. A multiply-partitioned methodology for fully-coupled computational wind-structure interaction simulation considering the inclusion of arbitrary added mass dampers. *J. Wind Eng. Ind. Aerodyn.* **2018**, *177*, 117–135. [CrossRef]

42. Andre, M. WindGen: A Synthetic Wind Simulation Library. Available online: <https://github.com/msandre/WindGen> (accessed on 29 May 2022).
43. Mann, J. Wind field simulation. *Probabilistic Eng. Mech.* **1998**, *13*, 269–282. [CrossRef]
44. Holmes, J. *Wind Loading of Structures*, 3rd ed.; CRC Press: Boca Raton, FL, USA, 2015.
45. Andre, M.; Péntek, M.; Bletzinger, K.U.; Wüchner, R. Aeroelastic simulation of the wind-excited torsional vibration of a parabolic trough solar collector. *J. Wind Eng. Ind. Aerodyn.* **2017**, *165*, 67–78. [CrossRef]
46. Uekermann, B.; Gatzhammer, B.; Mehl, M. Coupling algorithms for partitioned multi-physics simulations. In *Informatik 2014*; Plödereder, E., Grunske, L., Schneider, E., Ull, D., Eds.; Gesellschaft für Informatik e.V.: Bonn, Germany, 2014; pp. 113–124.
47. Winterstein, A. Modeling and Simulation of Wind-Structure Interaction of Slender Civil Engineering Structures Including Vibration Mitigation Systems. Ph.D. Thesis, Technical University of Munich, Munich, Germany, 2020. Available online: <https://mediatum.ub.tum.de/1542819> (accessed on 29 May 2022).
48. Tamura, Y.; Kareem, A. *Advanced Structural Wind Engineering*; Springer: Tokyo, Japan, 2013. [CrossRef]

Article

Performance of Numerically Optimized Tuned Mass Damper with Inerter (TMDI)

Felix Weber ^{1,*} , Fredrik Borchsenius ², Johann Distl ³ and Christian Braun ⁴¹ Maurer Switzerland GmbH, Grossplatzstrasse 24, 8118 Pfaffhausen, Switzerland² OTH Regensburg, Galgenbergstrasse 30, 93049 Regensburg, Germany; fredrik.borchsenius@oth-regensburg.de³ Maurer Engineering GmbH, Frankfurter Ring 193, 80807 Munich, Germany; j.distl@maurer.eu⁴ Maurer SE, Frankfurter Ring 193, 80807 Munich, Germany; c.braun@maurer.eu

* Correspondence: f.weber@maurer.eu

Abstract: In recent years, the Tuned Mass Damper with inerter (TMDI) has received significant attention. The inerter is defined to exert a force that is in proportion to the relative acceleration of the two inerter terminals. Here, two TMDI topologies are investigated. The conventional topology is given by the inerter being in parallel to the spring and viscous damper of the TMDI. The other topology is the serial arrangement of spring, inerter and viscous damper being in parallel to the stiffness of the mass spring oscillator of the TMDI. While the first topology intends to increase the inertial force of the TMDI, the second topology aims at producing an additional degree of freedom. The considered TMDI concepts are simulated for harmonic and random excitations, with parameters set according to those described in the literature and with numerically optimized parameters which minimize the primary structure displacement response. The classical TMD is used as a benchmark. The findings are twofold. The conventional TMDI with typical inertance ratio of 1% and the very small value of 0.02% performs significantly worse than the classical TMD with the same mass ratio. In contrast, the TMDI with an additional degree of freedom can improve the mitigation of the primary structure if the inertance ratio is set very small and if the TMDI parameters are numerically optimized.

Keywords: damping; inerter; optimization; TMD; TMDI; vibration

Citation: Weber, F.; Borchsenius, F.; Distl, J.; Braun, C. Performance of Numerically Optimized Tuned Mass Damper with Inerter (TMDI). *Appl. Sci.* **2022**, *12*, 6204. <https://doi.org/10.3390/app12126204>

Academic Editor: César M.

A. Vasques

Received: 11 April 2022

Accepted: 16 June 2022

Published: 18 June 2022

Publisher's Note: MDPI stays neutral with regard to jurisdictional claims in published maps and institutional affiliations.



Copyright: © 2022 by the authors. Licensee MDPI, Basel, Switzerland. This article is an open access article distributed under the terms and conditions of the Creative Commons Attribution (CC BY) license (<https://creativecommons.org/licenses/by/4.0/>).

1. Introduction

The Tuned Mass Damper (TMD), first described by Den Hartog [1], is a widely used passive device used to control resonant vibrations when the disturbing frequency is unknown. It is a damped one-degree-of-freedom oscillator that is connected to the primary structure, whereby the resulting system is a highly damped two-degrees-of-freedom system. The two optimization parameters of the TMD are its natural frequency and damping ratio. For the selected mass ratio between the TMD oscillating mass and the target modal mass of the vibrating structure, these parameters can be optimized for minimum modal displacement, velocity and acceleration for harmonic and broad band excitations [2]. TMDs are widely used in footbridges [3,4] and high-rise buildings [5,6] to guarantee the required acceleration limits [7–9], in street bridges to provide the required level of damping [10,11], in railway bridges to avoid the loss of contact between wheels and track [12], and in flag masts and wind power stations to reduce bending vibrations [13,14].

To enhance the mitigation efficiency and broadband characteristics of TMDs, several concepts have been developed. Active and semi-active TMDs are based on the real-time control of TMD natural frequency and damping according to the actual frequency of vibration [15–19]. The resulting enhanced vibration suppression can be used to guarantee lower vibration limits or to ensure vibration limits with reduced TMD mass [6]. Another approach to make TMDs more efficient is simply to increase their oscillating mass. However, limited TMD installation space and costs make this approach unfavorable. Given this, the

TMD with inerter, abbreviated as TMDI, has received much attention during the past decade. The ideal inerter is defined to exert a force in proportion to the relative acceleration of its two grounds or terminals, respectively. That the development of real inerters with minimum or even zero friction is a challenging task is seen from the works [20,21]. Originally, the inerter was used in vehicle suspension systems to improve ride comfort [22]. The use of inerters in the field of vibration isolation in a more general way is described in [23]. When the inerter is used in combination with the classical TMD, there are many possible TMDI topologies. Some topologies aim at replacing the TMD mass, some intend to increase TMD inertial force and some target producing an additional degree of freedom whereby the primary structure with TMDI behaves as a three-degrees-of-freedom system. A profound overview of possible TMDI topologies together with closed-form solutions of the related parameters can be found in [24–27]. TMDI efficiency has been investigated for various TMDI configurations for earthquake excitation [28–30], wind excitation [31–34], and harmonic and random excitations of the primary structure [35–37]. The studies in [35,36] were made for various TMDI parallel and serial arrangements of inerters, and stiffness and damping elements and optimum TMDI parameters in table format are provided. The authors of [37] show that even very complex inerter configurations are thinkable. Besides the investigations of various TMDI topologies, studies have also been performed to investigate the influence of the inerter ground on the primary structure [38,39]. This literature survey gives a brief overview of the topics related to inerters that are being investigated.

The present work aims at analyzing the mitigation efficiency of the TMDI not with analytical parameters but with numerically optimized parameters to ensure optimality. The optimization criterion is minimum primary structure displacement response. The TMDI is assumed to be located at the anti-node position of the first bending mode of the primary structure (Figure 1a), and the inerter is grounded to the antinode position as well because this is the most realistic scenario for real applications. Two typical TMDI configurations are considered. The conventional topology is given by the parallel arrangement of inerter, spring and viscous damper, aiming at increasing the inertial force of the TMDI mass, as in Figure 1b. The benchmark for this TMDI configuration is the classical TMD with the same mass ratio (Figure 1c). The other considered TMDI topology is the serial arrangement of spring, inerter and viscous damper together with the main spring of the TMDI mass, as proposed in [25] (Figure 1d). This topology aims to produce an additional degree of freedom of the inerter. The performance of the resulting three-degrees-of-freedom system is compared to the performance of the primary structure with two half TMDs, both with half mass ratio and different natural frequencies and damping ratios, leading to a three-degrees-of-freedom system as well (Figure 1e). The comparative study is performed for both harmonic and random excitations. The performances of the simulated TMDs and TMDIs are assessed by the primary structure displacement response and the damper relative motion response.

The structure of the paper is as follows. Section 2 describes the modelling of the considered TMDI concepts and the associated TMD benchmarks. To make the modelling closer to reality, an inerter model based on a fly wheel mechanism is considered as well. Section 3 describes the simulation procedure concerning the optimizations of the considered TMDI and TMD systems and their performance assessments. Section 4 shows the numerical results of the considered TMDI configurations and the benchmark TMD with the same mass ratio. The comparison is made in a systematic way. First, the conventional TMDI with the commonly used inertance ratio of 1% and with parameters according to those described in the literature is compared to the TMD with Den Hartog parameters that minimize the primary structure displacement response, assuming zero structural inherent damping [1]. Then, the conventional TMDI and TMD with numerically optimized parameters are compared and the very small inertance ratio of 0.02% is considered as well. For the serial TMDI, the parameters are numerically optimized for inertance ratios of 1% and 0.02% due to the lack of analytical optimum parameter solutions. For the TMDI with an inertance ratio of 1%, the frequency response function is characterized by two peaks. Therefore, the classical

TMD is used here as a benchmark. For the TMDI with an inertance ratio of 0.02%, the frequency response function shows three peaks due to the additional degree of freedom induced by the serial inverter with the low inertance ratio of 0.02%. Consequently, the benchmark is given here by two half TMDs with different natural frequencies and damping ratios. Discussions of these comparative studies are included in Section 4. The article ends with a short summary and conclusions in Section 5.

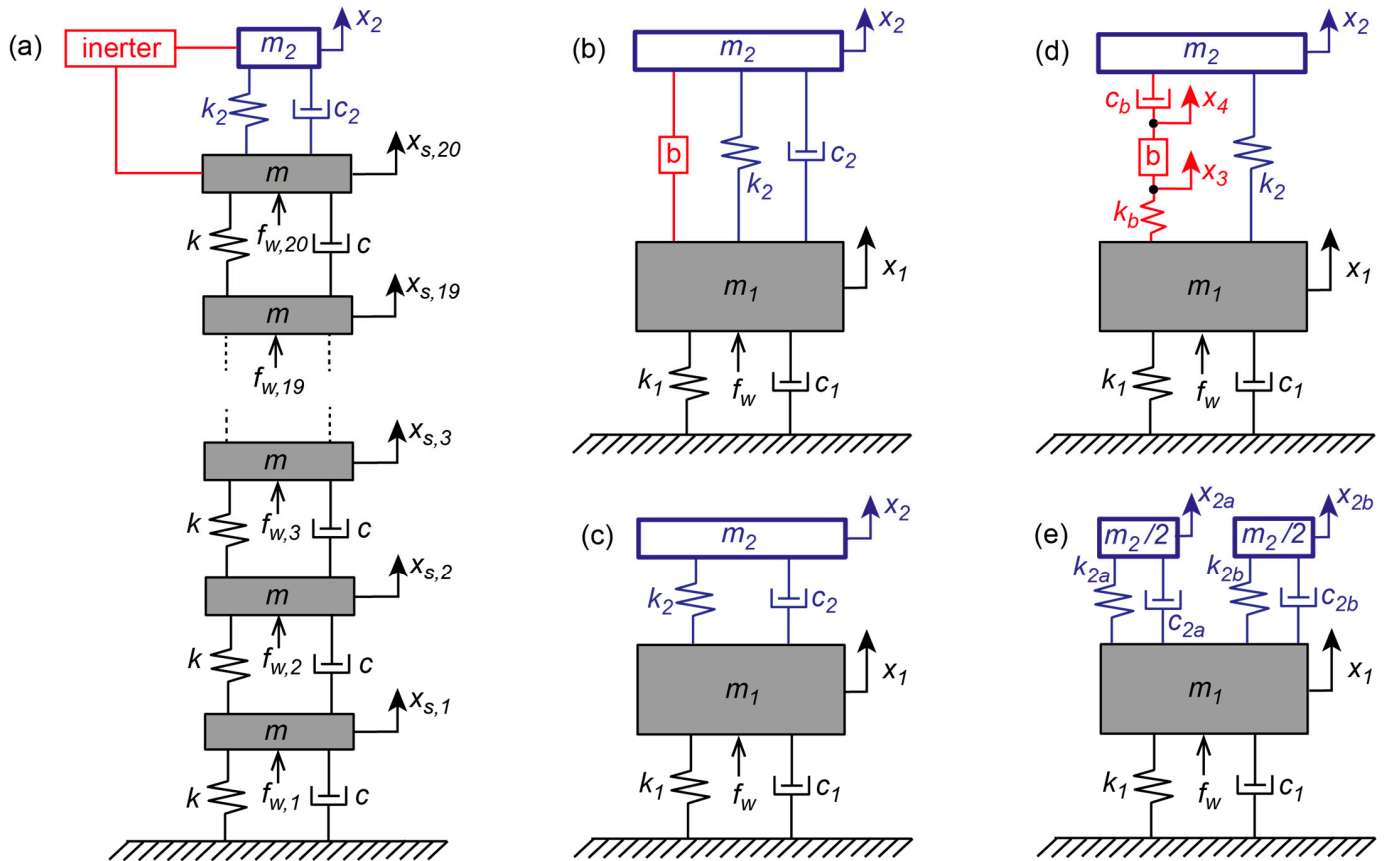


Figure 1. (a) Multi-degree-of-freedom system with TMDI at the anti-node position of the first bending mode. (b) Conventional TMDI with target structural mode (modeshape factor 1). (c) Classical TMD with target structural mode (modeshape factor 1). (d) TMDI with serial arrangement of stiffness, inverter and viscous damper with target structural mode (modeshape factor 1). (e) Two half TMDs with target structural mode (modeshape factor 1).

2. Modelling

2.1. Primary Structure

The primary structure is modelled by the modal component that needs to be mitigated by the damper. Therefore, the model is given by the following single-degree-of-freedom system [40]

$$m_1 \ddot{x}_1 + c_1 \dot{x}_1 + k_1 x_1 = f_{ex} \tag{1}$$

$$c_1 = 2 \zeta_1 m_1 (2 \pi f_1) \tag{2}$$

$$k_1 = m_1 (2 \pi f_1)^2 \tag{3}$$

where m_1 denotes the modal mass; c_1 is the viscous damping coefficient, which is given by the damping ratio ζ_1 ; k_1 is the stiffness coefficient, which results from the eigenfrequency f_1 ; \ddot{x}_1 , \dot{x}_1 , x_1 describe the modal acceleration, velocity and displacement; and f_{ex} is the excitation force. The chosen primary structure modal parameters represent typical values of a tall building that may be susceptible to wind excitation and therefore may require a

mass damper (Table 1). Notice that the choice of the structural modal parameters does not influence the outcome of the comparative study under consideration. However, the selection of the modal parameters influences the optimum mass damper parameters that are given for all considered mass damper topologies.

Table 1. Assumed primary structure modal parameters.

Modal Mass m_1 (t)	Eigenfrequency f_1 (Hz)	Damping Ratio ζ_1 (%)	Stiffness Coefficient k_1 (MN/m)	Viscous Damping Coefficient c_1 (kNs/m)
50,000	0.14	1%	38.689	879.65

2.2. Primary Structure with TMD

The model of the primary structure with TMD is given by the following two-degrees-of-freedom system (Figure 1c):

$$\begin{bmatrix} m_1 & 0 \\ 0 & m_2 \end{bmatrix} \begin{bmatrix} \ddot{x}_1 \\ \ddot{x}_2 \end{bmatrix} + \begin{bmatrix} c_1 + c_2 & -c_2 \\ -c_2 & c_2 \end{bmatrix} \begin{bmatrix} \dot{x}_1 \\ \dot{x}_2 \end{bmatrix} + \begin{bmatrix} k_1 + k_2 & -k_2 \\ -k_2 & k_2 \end{bmatrix} \begin{bmatrix} x_1 \\ x_2 \end{bmatrix} = \begin{bmatrix} f_{ex} \\ 0 \end{bmatrix} \quad (4)$$

where m_2 denotes the TMD mass, c_2 is the TMD viscous damping coefficient, k_2 is the TMD stiffness coefficient, $\dot{x}_1 - \dot{x}_2$ describes the TMD relative velocity, $x_1 - x_2$ is the TMD relative motion, and the modeshape factor of the first bending mode at TMD position is not included, as it is 1 (see Figure 1a). The parameters of the considered TMDs that are designed according to Den Hartog’s rules and numerically optimized for minimum structural displacement are given in Table 2. The optimization criterion for minimum structural displacement was chosen to ensure a fair comparison with the performance of the TMDI with analytical parameters according to [33], which are intended to yield at least a structural displacement response close to its minimum.

Table 2. Parameters of the considered TMDs.

Damper Type	Mass Ratio $\mu = m_2/m_1$	Tuning	Natural Frequency f_2 (Hz)	Damping Ratio ζ_2 (Hz)	Stiffness Coefficient k_2 (kN/m)	Viscous Damping Coefficient c_2 (kNs/m)
TMD	1%	Den Hartog	0.1386	6.03%	379.27	53.069
TMD	1%	Overdamped	0.1386	$2.3434 \times 6.03\%$	379.27	2.3434×53.069
TMD	0.5%	Numerically optimized	NA	NA	191.12	19.134
TMD	1%	Numerically optimized	NA	NA	378.11	54.648
Two half TMDs	1% (total)	Numerically optimized	$k_{2a} = 178.36$ kN/m	$c_{2a} = 17.123$ kNs/m	$k_{2b} = 201.62$ kN/m	$c_{2b} = 19.463$ kNs/m

2.3. Primary Structure with TMDI with Inerter in Parallel to the Spring and Viscous Damper

The topology of the conventional TMDI is given by the parallel arrangement of the inerter, spring and viscous damper, as depicted in Figure 1b. The idea behind this topology is that the inerter, although producing a force in proportion to the relative acceleration of its two terminals, increases the TMD inertial force without adding real mass. The model of the primary structure with conventional TMDI is given by the following two-degrees-of-freedom system:

$$\begin{bmatrix} m_1 + b & -b \\ -b & m_2 + b \end{bmatrix} \begin{bmatrix} \ddot{x}_1 \\ \ddot{x}_2 \end{bmatrix} + \begin{bmatrix} c_1 + c_2 & -c_2 \\ -c_2 & c_2 \end{bmatrix} \begin{bmatrix} \dot{x}_1 \\ \dot{x}_2 \end{bmatrix} + \begin{bmatrix} k_1 + k_2 & -k_2 \\ -k_2 & k_2 \end{bmatrix} \begin{bmatrix} x_1 \\ x_2 \end{bmatrix} = \begin{bmatrix} f_{ex} \\ 0 \end{bmatrix} \quad (5)$$

where b denotes the so-called inertance with unit (kg) that is determined by the selected inertance ratio β as follows:

$$b = \beta m_1 \tag{6}$$

Notice that the inertance b not only increases the mass m_2 of the TMDI but b occurs at all locations in the modal mass matrix of Equation (5) because the inerter force f_b is in proportion to the relative acceleration of the inerter grounds, which is here the difference between primary structure modal acceleration \ddot{x}_1 and acceleration \ddot{x}_2 of the TMDI mass m_2 .

$$f_b = b (\ddot{x}_1 - \ddot{x}_2) \tag{7}$$

For the TMDI with conventional topology and the often-adopted inertance ratio $\beta = 1\%$, the parameters f_2 , ζ_2 , k_2 and c_2 are, on the one hand, designed according to the closed-form solutions (8)–(11), according to [33], and, on the other hand, the parameters k_2 and c_2 are numerically optimized for minimum structural displacement (Table 3).

$$f_2 = f_1 \frac{\sqrt{1 + 0.5(\beta + \mu)}}{1 + \beta + \mu} \tag{8}$$

$$k_2 = (b + m_2) (2\pi f_2)^2 \tag{9}$$

$$\zeta_2 = \sqrt{\frac{(\beta + \mu)(1 + 0.75(\beta + \mu))}{4(1 + \beta + \mu)(1 + 0.5(\beta + \mu))}} \tag{10}$$

$$c_2 = 2 \zeta_2 (b + m_2) (2\pi f_2) \tag{11}$$

Table 3. Parameters of TMDIs with an inerter in parallel to stiffness and viscous damper.

Damper Type	Mass Ratio $\mu = m_2/m_1$	Inertance Ratio $\beta = b/m_1$	Tuning	Natural Frequency f_2 (Hz)	Damping Ratio ζ_2 (Hz)	Stiffness Coefficient k_2 (kN/m)	Viscous Damping Coefficient c_2 (kNs/m)
Parallel TMDI	1%	1%	[33]	0.1379	7.02%	751.17	121.66
Parallel TMDI	1%	1%	Numerically optimized	NA	NA	760.64	76.151
Parallel TMDI	1%	0.02%	Numerically optimized	NA	NA	385.77	54.919

According to [33], the closed-form solutions (8)–(11) do not minimize the structural displacement response but yield a reasonable suboptimal solution as these solutions are derived for a classical TMD with a total mass ratio $\mu + \beta$. This means that one can expect a good but not optimal performance of the conventional TMDI with parameters (8)–(11). For the inertance ratio $\beta = 0.02\%$, only the numerically optimized TMDI is used for the comparative study because the very small inertance ratio of 0.02% has not been considered in the literature so far.

2.4. Primary Structure with TMDI with Inerter in Series with Stiffness and Viscous Damper

Another topology is described in [25], where the spring k_2 is in parallel with the serial arrangement of the spring with stiffness k_b , the inerter with inertance b and the viscous damper with viscous coefficient c_b , as depicted in Figure 1d. The idea behind this topology is to produce an additional degree of freedom by setting the inerter between the spring and viscous damper. The relevant equations of motion are given as follows:

$$\begin{bmatrix} m_1 & 0 & 0 & 0 \\ 0 & m_2 & 0 & 0 \\ 0 & 0 & -b & b \\ 0 & 0 & 0 & 0 \end{bmatrix} \begin{bmatrix} \ddot{x}_1 \\ \ddot{x}_2 \\ \ddot{x}_3 \\ \ddot{x}_4 \end{bmatrix} + \begin{bmatrix} c_1 & 0 & 0 & 0 \\ 0 & 0 & 0 & 0 \\ 0 & 0 & 0 & 0 \\ 0 & -c_b & 0 & c_b \end{bmatrix} \begin{bmatrix} \dot{x}_1 \\ \dot{x}_2 \\ \dot{x}_3 \\ \dot{x}_4 \end{bmatrix} + \begin{bmatrix} (k_1 + k_2 + k_b) & -k_2 & -k_b & 0 \\ -k_2 - k_b & k_2 & k_b & 0 \\ k_b & 0 & -k_b & 0 \\ -k_b & 0 & k_b & 0 \end{bmatrix} \begin{bmatrix} x_1 \\ x_2 \\ x_3 \\ x_4 \end{bmatrix} = \begin{bmatrix} f_{ex} \\ 0 \\ 0 \\ 0 \end{bmatrix} \quad (12)$$

As for the first conventional TMDI layout, this TMDI topology was computed for the usually adopted inertance ratio $\beta = 1\%$ and for the very small value of 0.02% as well. For both inertance ratios, the parameters of the TMDI were numerically optimized for minimum structural displacement to ensure the optimality of this mass damper type (Table 4).

Table 4. Parameters of TMDIs with a serial arrangement of stiffness, inerter and viscous damper.

Damper Type	Mass Ratio $\mu = m_2/m_1$	Inertance Ratio $\beta = b/m_1$	Tuning	Stiffness Coefficient k_2 (kN/m)	Stiffness Coefficient k_b (kN/m)	Viscous Damping Coefficient c_b (kNs/m)
Serial TMDI	1%	1%	Numerically optimized	347.47	80.103	76.288
Serial TMDI	1%	0.02%	Numerically optimized	378.17	7.6402	50.441
Serial TMDI (fly wheel)	1%	0.02%	Numerically optimized	377.40	8.1045	50.275

2.5. Primary Structure with TMDI with Fly Wheel Inerter in Series with Stiffness and Viscous Damper

For the TMDI with a serial arrangement of spring, inerter and viscous damper, an inerter model based on the fly wheel principle is computed. The fly wheel that rotates accelerated when the relative motion $(x_3 - x_4)$ between the housing and the steel rod of the fly wheel was accelerated (Figure 2). The mass of the housing including the gear rod is denoted as m_3 and the mass of the fly wheel including the steel rod and the axle is m_4 (Table 5).

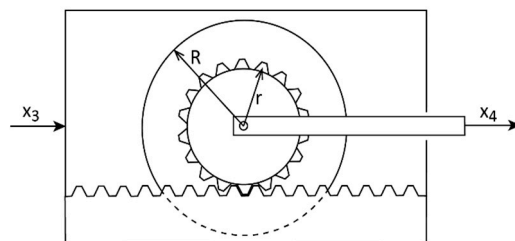


Figure 2. Fly wheel (without friction) as an ideal realization of an inerter.

Table 5. Parameters of the fly wheel inerter device.

Mass of Housing and Gear Rod (kg)	Radius of Fly Wheel (m)	Thickness of Fly Wheel (m)	Gear Radius of Fly Wheel (m)	Mass of Fly Wheel (kg)	Mass of Fly Wheel, Steel Rod, Axle (kg)
$m_3 = 500$	0.7	0.28	0.288	3388	$m_4 = 3500$

The moment of inertia I of the fly wheel with mass m_{wheel} and radius R is equal to the moment of inertia resulting from the envisaged inertance b and the gear radius r .

$$I = \frac{m_{wheel} R^2}{2} = b r^2 \quad (13)$$

r can be derived to obtain the envisaged inertance, which yields $r = 0.288$ m for $m_{wheel} = 3388$ kg and $R_{wheel} = 0.7$ m (Table 5). For this TMDI type, the equations of motion, which avoid the zeros in the fourth line of the mass matrix in (12), are as follows:

$$\begin{bmatrix} m_1 & 0 & 0 & 0 \\ 0 & m_2 & 0 & 0 \\ 0 & 0 & b + m_3 & -b \\ 0 & 0 & -b & b + m_4 \end{bmatrix} \begin{bmatrix} \ddot{x}_1 \\ \ddot{x}_2 \\ \ddot{x}_3 \\ \ddot{x}_4 \end{bmatrix} + \begin{bmatrix} c_1 & 0 & 0 & 0 \\ 0 & c_b & 0 & -c_b \\ 0 & 0 & 0 & 0 \\ 0 & -c_b & 0 & c_b \end{bmatrix} \begin{bmatrix} \dot{x}_1 \\ \dot{x}_2 \\ \dot{x}_3 \\ \dot{x}_4 \end{bmatrix} + \begin{bmatrix} (k_1 + k_2 + k_b) & -k_2 & -k_b & 0 \\ -k_2 & k_2 & 0 & 0 \\ -k_b & 0 & k_b & 0 \\ 0 & 0 & 0 & 0 \end{bmatrix} \begin{bmatrix} x_1 \\ x_2 \\ x_3 \\ x_4 \end{bmatrix} = \begin{bmatrix} f_{ex} \\ 0 \\ 0 \\ 0 \end{bmatrix} \quad (14)$$

The TMDI model (14) is computed for the inertance ratio $\beta = 0.02\%$, which turns out to be much more favourable than $\beta = 1\%$, with numerically optimized parameters k_2, k_b and c_b (Table 4).

2.6. Primary Structure with Two Half TMDs

The TMDI topology with the serial arrangement produces an additional degree of freedom, i.e., the primary structure with this TMDI behaves as a three-degrees-of-freedom system. Therefore, the appropriate benchmark is the primary structure with two different TMDs, resulting in a three-degrees-of-freedom system as well. The mass ratio of each TMD is selected to be 0.5%, whereby the mass ratio of both TMDs together is equal to 1%. The equations of motion of the primary structure with two different TMDs but with the same mass are as follows (Figure 1e):

$$\begin{bmatrix} m_1 & 0 & 0 \\ 0 & m_2/2 & 0 \\ 0 & 0 & m_2/2 \end{bmatrix} \begin{bmatrix} \ddot{x}_1 \\ \ddot{x}_2 \\ \ddot{x}_3 \end{bmatrix} + \begin{bmatrix} c_1 + c_{2a} + c_{2b} & -c_{2a} & -c_{2b} \\ -c_{2a} & c_{2a} & 0 \\ -c_{2b} & 0 & c_{2b} \end{bmatrix} \begin{bmatrix} \dot{x}_1 \\ \dot{x}_2 \\ \dot{x}_3 \end{bmatrix} + \begin{bmatrix} k_1 + k_{2a} + k_{2b} & -k_{2a} & -k_{2b} \\ -k_{2a} & k_{2a} & 0 \\ -k_{2b} & 0 & k_{2b} \end{bmatrix} \begin{bmatrix} x_1 \\ x_2 \\ x_3 \end{bmatrix} = \begin{bmatrix} f_{ex} \\ 0 \\ 0 \end{bmatrix} \quad (15)$$

The parameters k_{2a}, c_{2a}, k_{2b} and c_{2b} are numerically optimized for minimum primary structure displacement (Table 2). Notice that the numerically optimized stiffness and viscous damping coefficients are not equal because one half of the TMD is tuned to mitigate the left peak of the primary structure with classical TMD and the other half of the TMD is tuned to the right peak.

3. Simulation Procedure

3.1. TMDI Optimization

The Matlab (1994–2022 The MathWorks, Inc.) functions “fminsearch” and “optimset” were used for the optimization of the parameters of the considered TMDI concepts. The optimization criterion is the minimization of the steady-state displacement response of the primary structure under harmonic excitation (16). The fact that optimum parameters were obtained will be demonstrated by the equal peaks of the two-peak curve of the structure with parallel TMDI and of the three-peak curve of the structure with TMDI with an additional degree of freedom.

$$\text{optimization criterion} = \min(X_1) \quad (16)$$

3.2. TMD Optimization

The classical TMD is computed for the same mass ratio as the TMDI to ensure the same masses. The stiffness and viscous damping coefficients of the classical TMD are designed according to two methods. First, the well-known Den Hartog’s rules are adopted, which minimize the structural displacement response if the primary structure damping ratio is negligible [1]. Second, TMD parameters are numerically optimized using the same optimization functions as for the TMDI in order to obtain equal normalized displacement peaks, even for $\zeta_1 = 1\%$, and also for the benchmark of the two half TMDs with different natural frequencies and damping ratios.

3.3. Assessments of TMDI and TMD

For harmonic excitation, TMDI and TMD are assessed by their steady state primary structure displacement response, which is normalized by the static displacement $X_{1,static} = k_1/F_{ex}$, where F_{ex} denotes the excitation force amplitude (17). The relative motion amplitudes of the TMDI and TMD, respectively, are normalized by the maximum value of the TMD with 1% mass ratio and by adopting Den Hartog parameters (18).

$$X_1 / X_{1,static} = X_1 k_1 / F_{ex} \quad (17)$$

$$(X_1 - X_2) / \{ \max(X_1 - X_2) \}_{TMD} \quad (18)$$

For random excitation, the primary structure displacement response and the damper relative motion response were assessed by their transfer functions TF_{x1} and TF_{xd} , respectively, between these displacements and the excitation force ((19) and (20)). The transfer function of the damper relative

motion is normalized by the maximum of the transfer function of the damper relative motion of the benchmark TMD with 1% mass ratio.

$$TF_{x1} = \frac{PSD(x_1)}{PSD(f_{ex})} \quad (19)$$

$$TF_{xd} = \frac{PSD(x_1 - x_2)}{PSD(f_{ex})} / \left\{ \max \left(\frac{PSD(x_1 - x_2)}{PSD(f_{ex})} \right) \right\}_{TMD} \quad (20)$$

3.4. Excitation

Harmonic and random excitations were adopted. For harmonic excitation, steady state responses of the primary structure displacement and damper relative motion were computed for an excitation frequency range between $0.85 \times f_1$ and $1.15 \times f_1$. For random excitation, a zero-mean white noise signal at sampling frequency 200 Hz was generated that was high pass-filtered (second-order filter) at 0.005 Hz to remove any offset and low pass-filtered (second-order filter) at 99 Hz to remove unnecessary higher frequencies, considering $f_1 = 0.14$ Hz (Figure 3).

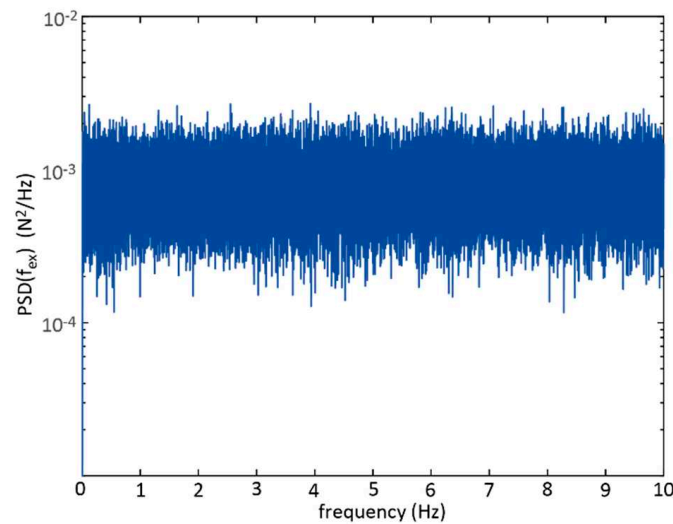


Figure 3. Power Spectral Density estimate via Welch's method of white noise excitation force (close-up of frequency range 0 Hz to 10 Hz).

4. Results

4.1. TMDI with Inerter in Parallel to Stiffness and Viscous Damper, $\beta = 1\%$, Tuning According to Parameters Described in the Literature

First, the normalized structural displacement and damper relative motion of the TMDI with an inerter in parallel to the stiffness and viscous damper, $\beta = 1\%$ and parameters set according to [33] were compared to the classical TMD with the same mass ratio for harmonic and random excitations; see Figures 4 and 5. The results demonstrate that the TMDI with tuning according to [33] led to a far greater structural displacement than the classical TMD. The shape of the primary structure response due to the TMDI corresponded well with the results presented in [32]. The response of the TMDI was similar to the response due to an overdamped TMD, which was confirmed by the simulation result due to a TMD with the same mass ratio and a viscous damping coefficient that was 2.3434 times greater than the value according to Den Hartog (Table 2). The observation that the design according to [33] leads to an overdamped TMDI was also seen from the viscous damping coefficient of 121.66 kNs/m (Table 3), which is very close to the value of the overdamped TMD 2.3434×53.069 kNs/m = 124.36 kNs/m (Table 2). The reason for the extremely suboptimal tuning of the TMDI according to [33] is that the TMDI parameters are derived for a TMD with a mass ratio $\mu + \beta$ that is not correct, since the inerter force is in proportion to the relative acceleration between the primary structure and the damper mass.

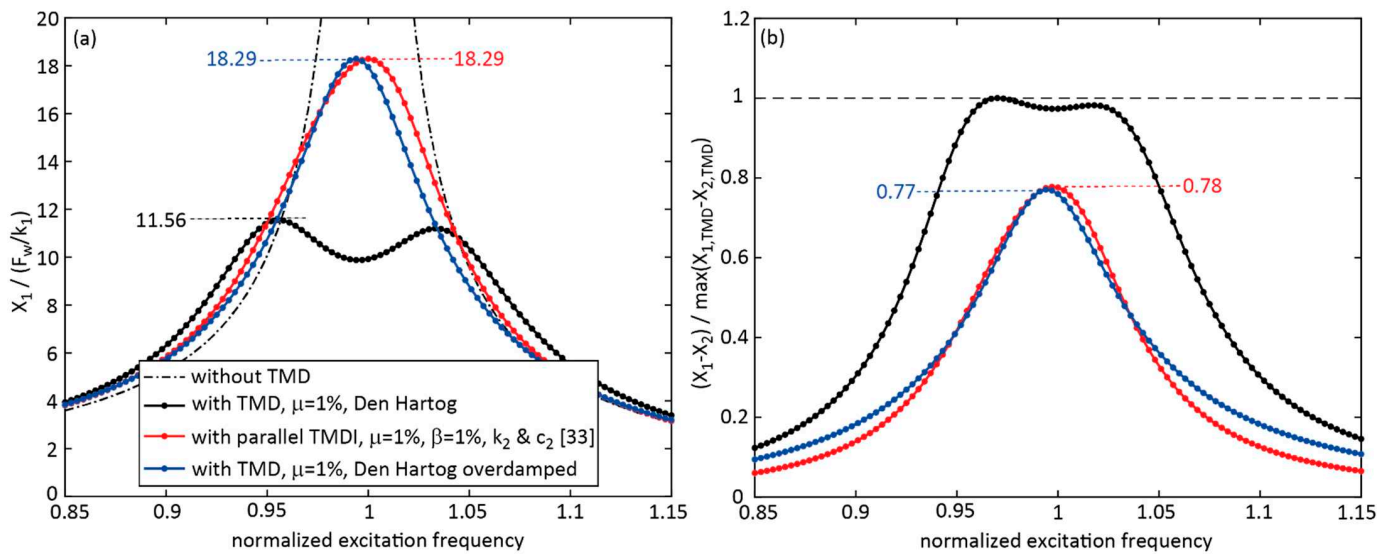


Figure 4. Performances of TMDI with inerter in parallel to stiffness and viscous damper ($\mu = 1\%$, $\beta = 1\%$, parameters as in [33]), TMD ($\mu = 1\%$, Den Hartog parameters) and overdamped TMD ($\mu = 1\%$) for harmonic excitation: (a) primary structure normalized displacement response and (b) normalized damper relative motion response.

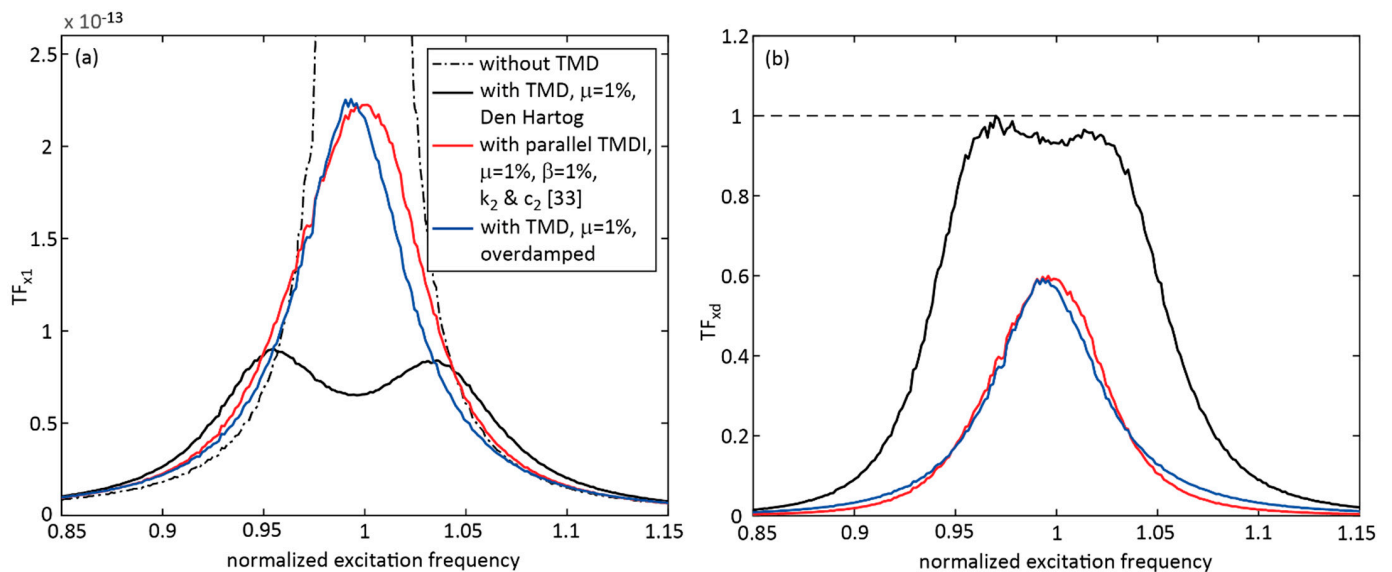


Figure 5. Performances of TMDI with inerter in parallel to stiffness and viscous damper ($\mu = 1\%$, $\beta = 1\%$, parameters as in [33]), TMD ($\mu = 1\%$, Den Hartog parameters) and overdamped TMD ($\mu = 1\%$) for random excitation: (a) primary structure normalized displacement response and (b) normalized damper relative motion response.

4.2. TMDI with Inerter in Parallel to Stiffness and Viscous Damper, $\beta = 1\%$, Numerically Optimized Parameters

The second case investigated the performance of the TMDI with an inerter in parallel to the stiffness and viscous damper, $\beta = 1\%$ and numerically optimized parameters. The results are depicted in Figures 6 and 7 for harmonic and random excitations and compared to the classical TMD with same mass ratio and Den Hartog parameters and the TMD with $\mu = 0.5\%$ and numerically optimized parameters. It can be seen that the classical TMD still performed significantly better than the TMDI with $\beta = 1\%$ and numerically optimized parameters. Notice that the left peak of the classical TMD is slightly higher than the right peak because $\zeta_1 = 1\%$ was used for the computations, but the Den Hartog formulae assume $\zeta_1 = 0\%$. Furthermore, it was observed that mitigation of the primary structure due to the TMDI was approximately equal to that due to a TMD with half mass. Needless

to say, the relative motion of the TMD with half mass was significantly greater than that of the TMD with $\mu = 1\%$ and that of the TMDI with $\mu = 1\%$ and $\beta = 1\%$.

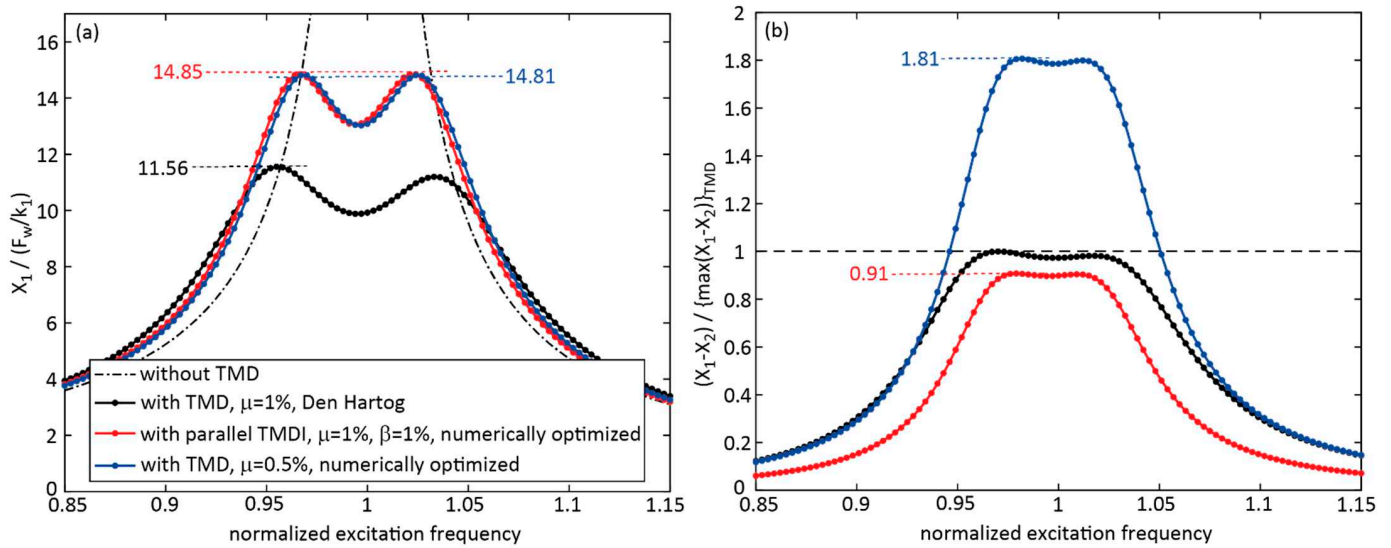


Figure 6. Performances of TMDI with inerter in parallel to stiffness and viscous damper ($\mu = 1\%$, $\beta = 1\%$, numerically optimized parameters), TMD ($\mu = 1\%$, Den Hartog parameters) and TMD ($\mu = 0.5\%$, numerically optimized parameters) for harmonic excitation: (a) primary structure normalized displacement response and (b) normalized damper relative motion response.

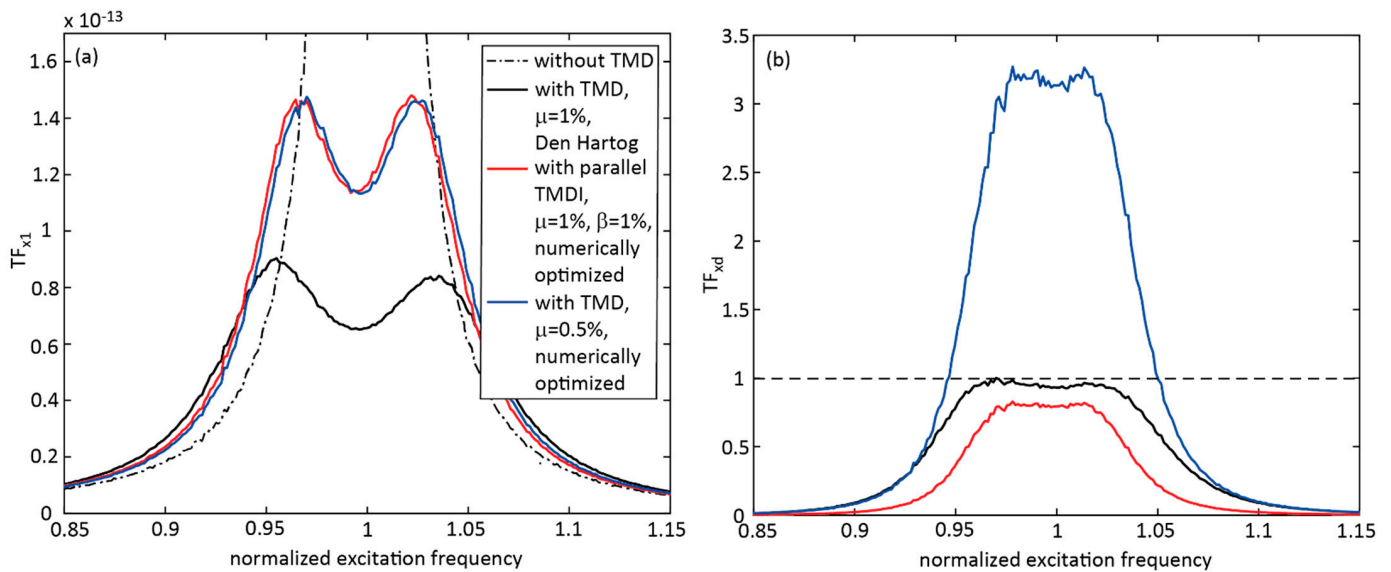


Figure 7. Performances of TMDI with inerter in parallel to stiffness and viscous damper ($\mu = 1\%$, $\beta = 1\%$, numerically optimized parameters), TMD ($\mu = 1\%$, Den Hartog parameters) and TMD ($\mu = 0.5\%$, numerically optimized parameters) for random excitation: (a) primary structure normalized displacement response and (b) normalized damper relative motion response.

4.3. TMDI with Inerter in Parallel to Stiffness and Viscous Damper, $\beta = 0.02\%$, Numerically Optimized Parameters

The third case investigated how the far smaller inertance ratio of $\beta = 0.02\%$ influenced the performance of the TMDI. For this case, only numerically optimized TMDI parameters were considered, as the first case demonstrated that the TMDI parameters set according to [33] led to a far suboptimal tuning. The results of the TMDI with $\beta = 0.02\%$ and numerically optimized parameters are plotted in Figures 8 and 9 for harmonic and random excitations and compared to the results of the TMD ($\mu = 1\%$) with Den Hartog parameters and the TMD ($\mu = 1\%$) with numerically optimized parameters.

Figure 8 shows that the TMDI with the very small inertia ratio of $\beta = 0.02\%$ and numerically optimized parameters led to a far better performance than the numerically optimized TMDI with $\beta = 1\%$. However, the primary structure displacement was slightly worse ($X_1 / (F_w / k_1) = 11.46$) than for the numerically optimized TMD with the same mass ratio ($X_1 / (F_w / k_1) = 11.37$). A difference in their maximum relative motions could not be observed.

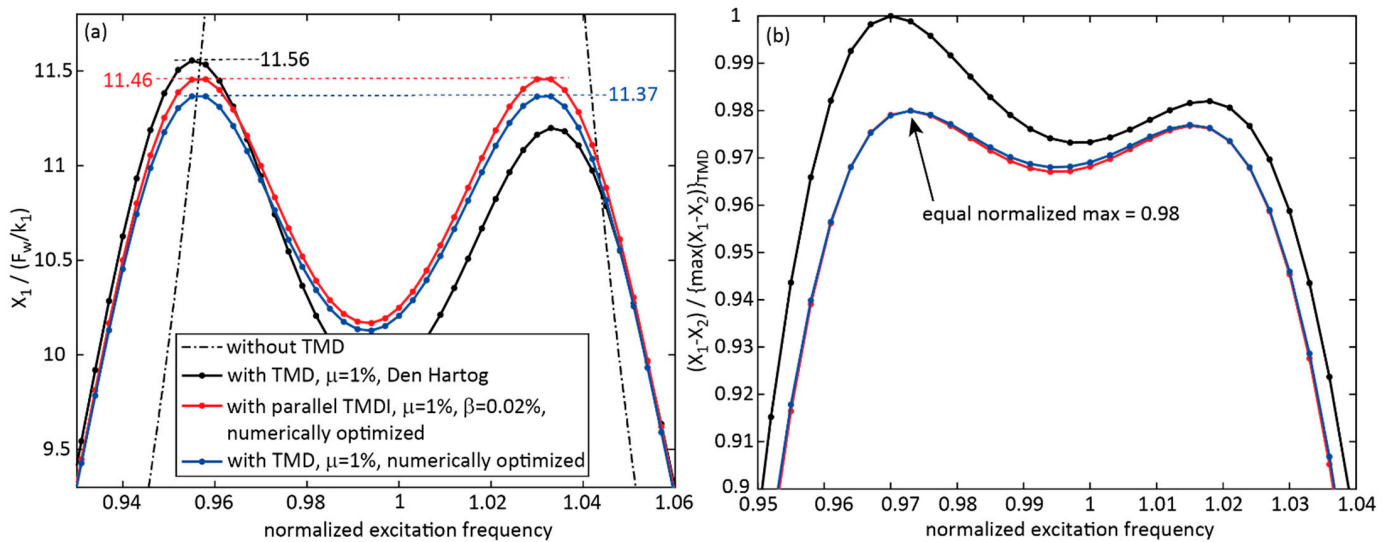


Figure 8. Performances of TMDI with inerter in parallel to stiffness and viscous damper ($\mu = 1\%$, $\beta = 0.02\%$, numerically optimized parameters), TMD ($\mu = 1\%$, Den Hartog parameters) and TMD ($\mu = 1\%$, numerically optimized parameters) for harmonic excitation: (a) primary structure normalized displacement response and (b) normalized damper relative motion response.

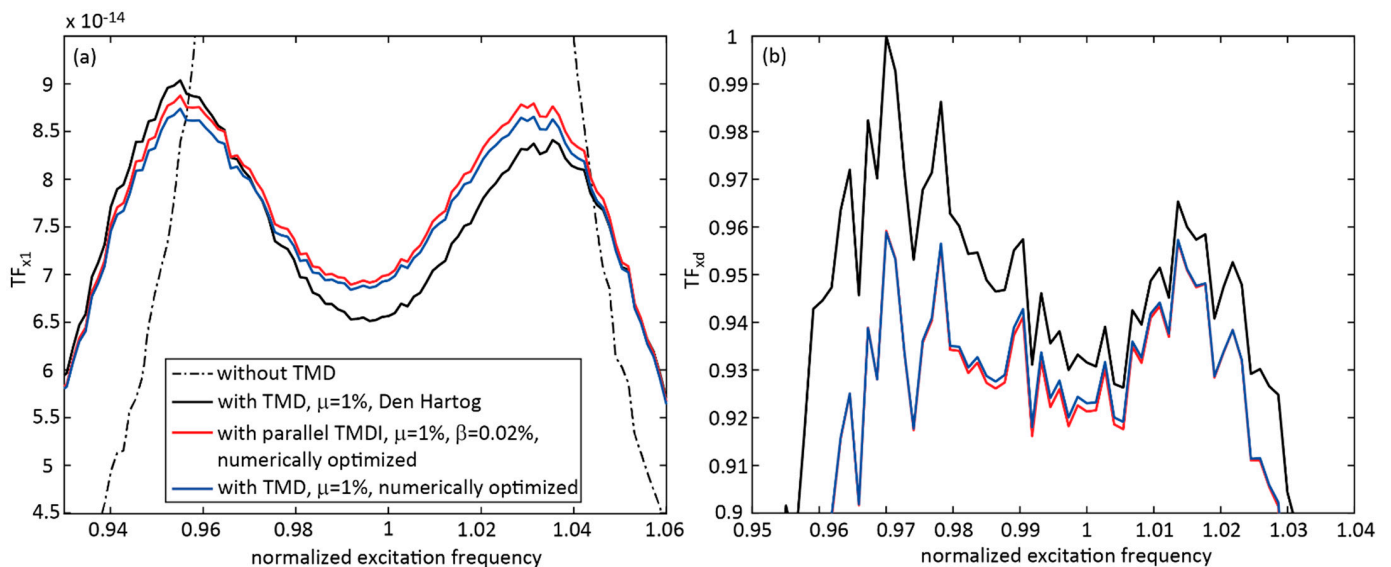


Figure 9. Performances of TMDI with inerter in parallel to stiffness and viscous damper ($\mu = 1\%$, $\beta = 0.02\%$, numerically optimized parameters), TMD ($\mu = 1\%$, Den Hartog parameters) and TMD ($\mu = 1\%$, numerically optimized parameters) for random excitation: (a) primary structure normalized displacement response and (b) normalized damper relative motion response.

4.4. TMDI with Serial Arrangement of Stiffness, Inerter and Viscous Damper, $\beta = 1\%$ and 0.02% , Numerically Optimized Parameters

The fourth case considered the TMDI with a serial arrangement of stiffness, inerter and viscous damper. First, the TMDI with $\mu = 1\%$, $\beta = 1\%$ and numerically optimized parameters was considered. The results for harmonic excitation depicted in Figure 10 demonstrate that this TMDI slightly reduced

the primary structure displacement by $(11.37-11.09)/11.37 = 2.5\%$, while the TMDI relative motion was almost the same. However, it was also observed that this TMDI topology with $\beta = 1\%$ did not show the envisaged three-degrees-of-freedom response characteristics; see Equation (12). This means that the serial arrangement of stiffness, inerter and viscous damper does not make sense for great inertance ratios. Therefore, the performance of the TMDI with serial topology but with the far smaller inertance ratio of $\beta = 0.02\%$ was analyzed next.

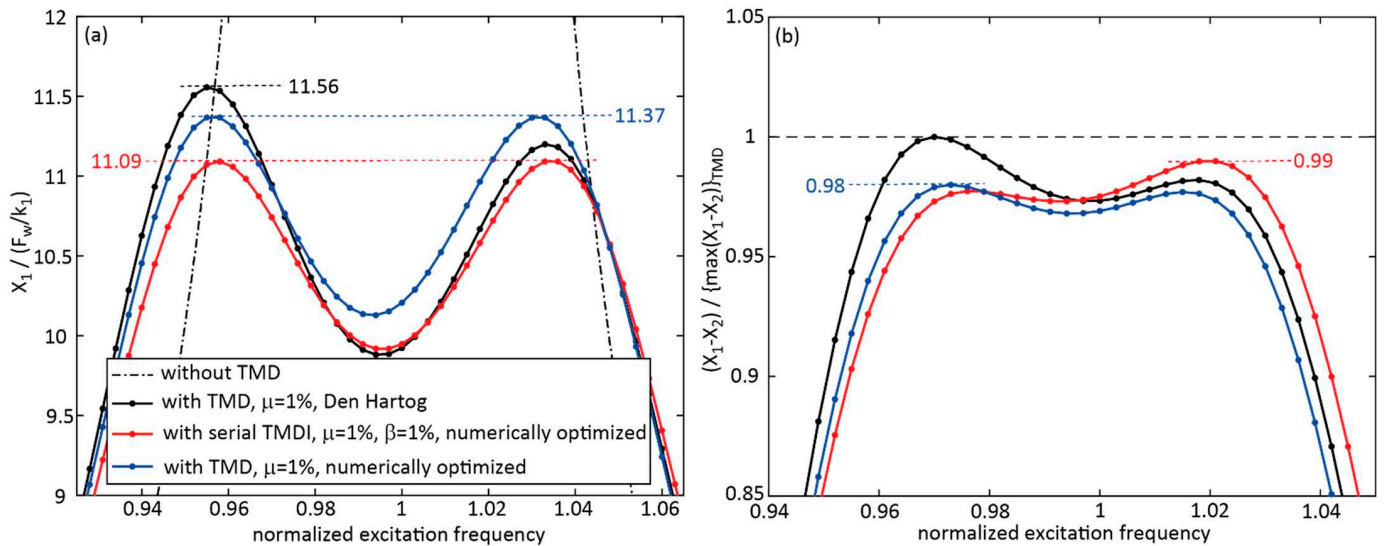


Figure 10. Performances of TMDI with serial arrangement of stiffness, inerter and damper ($\mu = 1\%$, $\beta = 1\%$, numerically optimized parameters), TMD ($\mu = 1\%$, Den Hartog parameters) and TMD ($\mu = 1\%$, numerically optimized parameters) for harmonic excitation: (a) primary structure normalized displacement response and (b) normalized damper relative motion response.

Figures 11 and 12 depict the normalized primary structure displacements and damper relative motions due to the numerically optimized TMDI with $\mu = 1\%$ and $\beta = 0.02\%$, the classical TMD ($\mu = 1\%$), Den Hartog tuning and the numerically optimized two half TMDs, each with $\mu = 0.5\%$, for harmonic and random excitations. For the case of harmonic excitation, the theoretical model of the TMDI and the physical model of the fly wheel were computed; for random excitation, the physical model only was computed, which was numerically more robust because it avoids the zeros in the fourth row of the mass matrix of the theoretical TMDI model (12). It was observed that the additional degree of freedom due to the serial arrangement of stiffness, inerter and viscous damper evoked the desirable three-degrees-of-freedom system response if the inertance ratio was small. Remember that this response characteristic was not observed for the same TMDI topology with $\beta = 1\%$; see Figure 10. The simulation results shown in Figures 11 and 12 demonstrate that the use of the inerter enhanced the mitigation of the primary structure response if the inerter topology and tuning were selected to evoke an additional degree of freedom and the associated TMDI parameters were numerically optimized. For harmonic excitation, the improvements were $(11.56-9.50)/11.56 = 17.8\%$ and $(10.31-9.50)/10.31 = 7.9\%$, respectively, compared to the classical TMD and two half TMDs, respectively. Similar results can be found in [35,36]. Another advantage of this TMDI solution is the reduced damper relative motion compared to the two half TMD solution, where the masses were not fully activated at one specific excitation frequency because of the different natural frequency tunings of the two half TMDs. Of course, these benefits of this TMDI solution must be related to the additional efforts that are needed for the technical realization of the serial arrangement of stiffness, frictionless inerter and viscous damper.

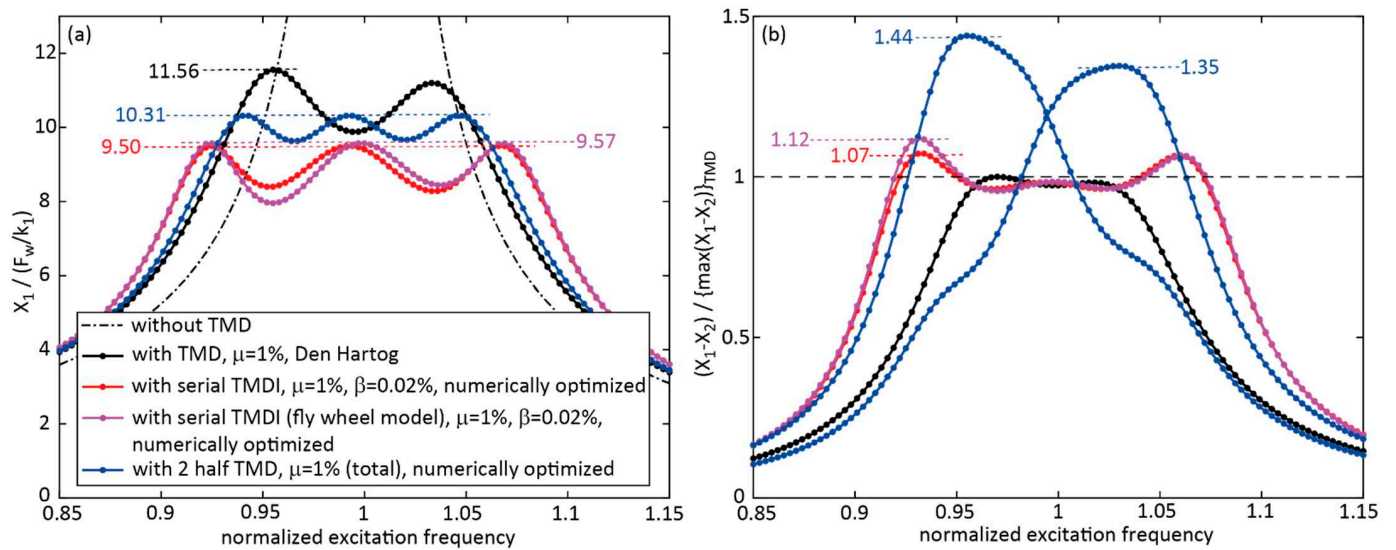


Figure 11. Performances of TMDI with serial arrangement of stiffness, inerter and damper ($\mu = 1\%$, $\beta = 0.02\%$, numerically optimized parameters), TMD ($\mu = 1\%$, Den Hartog parameters) and two half TMDs ($\mu = 1\%$, numerically optimized parameters) for harmonic excitation: (a) primary structure normalized displacement response and (b) normalized damper relative motion response.

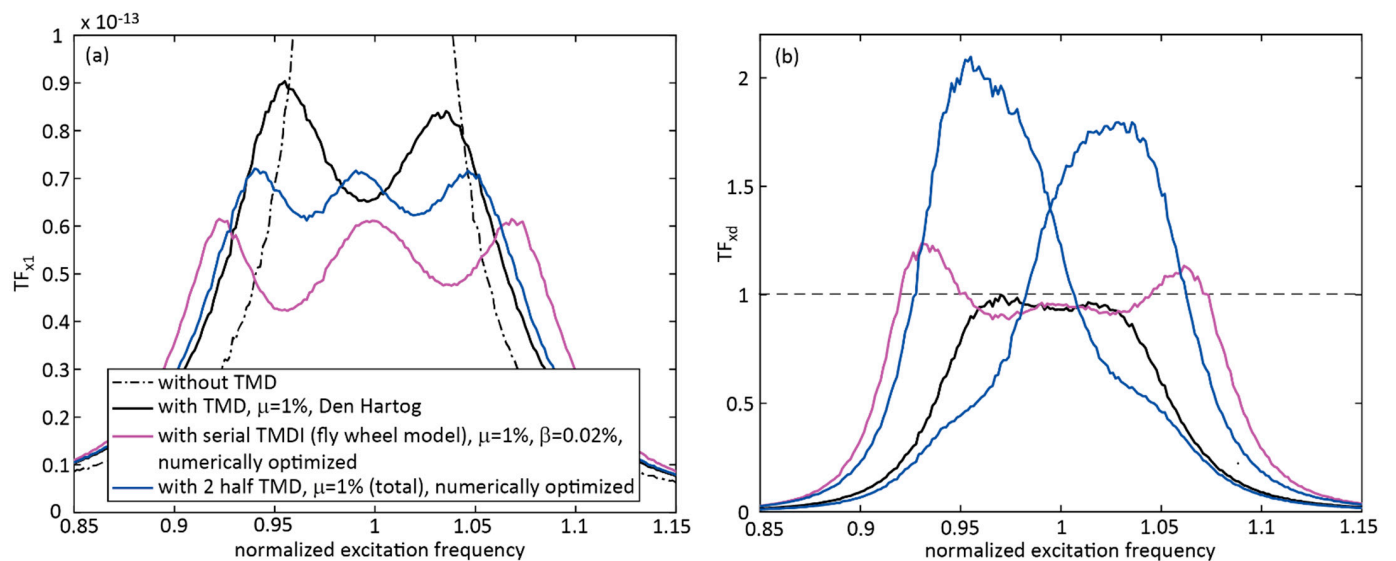


Figure 12. Performances of TMDI with serial arrangement of stiffness, inerter and damper ($\mu = 1\%$, $\beta = 0.02\%$, numerically optimized parameters), TMD ($\mu = 1\%$, Den Hartog parameters) and two half TMDs ($\mu = 1\%$, numerically optimized parameters) for random excitation: (a) primary structure normalized displacement response and (b) normalized damper relative motion response.

5. Conclusions

This study investigated the mitigation efficiencies of a TMDI and TMD with the same mass ratios for harmonic and random excitations. Two TMDI topologies were considered, i.e., the inerter in parallel to the spring and viscous damper of the damper mass and the serial arrangement of spring, inerter and viscous damper in parallel to the main spring of the damper mass. The TMDI was computed for the mass ratio of 1%, the commonly used inertance ratio of 1% and the far smaller inertance ratio of 0.02%, with analytical parameters set according to values described in the literature and numerically optimized parametric values. The results for harmonic and random excitation demonstrated:

- That the TMDI with parallel stiffness, damping and inerter and with the typical inertance ratio of 1% led to greater normalized primary structure displacement than the TMD; for harmonic

excitation the maximum displacement response was 27.47% greater than the response due to the classical TMD with Den Hartog parameters;

- That the parallel TMDI with the very small inertance ratio of 0.02% led to approximately the same primary structure displacement response as the classical TMD with numerically optimized parameters;
- That if the inertance ratio of the serial TMDI is too big, then the favorable three-degrees-of-freedom dynamics are not observed and;
- That the TMDI with the serial arrangement of spring, inerter and viscous damper besides the main spring of the damper resulted in an additional degree of freedom. This system, with numerically optimized parameters and the small inertance ratio of 0.02%, performed better than the TMD; for harmonic excitation, the structural displacement response was additionally reduced by 17.82%. This benefit must be related to the technical efforts that are needed to realize the serial arrangement of a spring, an inerter and a viscous damper without producing undesirable significant friction in the inerter and the connections between these three elements.

Author Contributions: Conceptualization, F.W., F.B., J.D. and C.B.; methodology, F.W., F.B. and J.D.; software, F.W. and F.B.; formal analysis, F.W. and F.B.; writing—original draft preparation, F.W., F.B., J.D. and C.B.; writing—review and editing, F.W. and F.B.; project administration, F.W., F.B., J.D. and C.B. All authors have read and agreed to the published version of the manuscript.

Funding: This research received funding from the Stiftung Maurer Söhne.

Institutional Review Board Statement: Not applicable.

Informed Consent Statement: Not applicable.

Data Availability Statement: The data presented in this study are available on request from the corresponding author.

Acknowledgments: The authors acknowledge the support of Maurer SE, Stiftung Maurer Söhne and OTH Regensburg.

Conflicts of Interest: The authors declare no conflict of interest.

References

1. Den Hartog, J.P. *Mechanical Vibrations*; McGraw-Hill Book Company, The Maple Press Company: York, PA, USA, 1934.
2. Asami, T.; Nishihara, O.; Baz, A.M. Analytical solutions to H_∞ and H_2 optimization of dynamic vibration absorber attached to damped linear systems. *J. Vib. Acoust.* **2020**, *124*, 284–295. [CrossRef]
3. Weber, F.; Obholzer, F.; Huber, P. Model-based TMD Design for the Footbridge “Inwilerstrasse” in Switzerland and its Experimental Verification. In Proceedings of the Footbridge International Conference, Madrid, Spain, 7–9 September 2020.
4. Rezende, F.; Brunet, O., Jr.; Diniz Varela, W.; Pereira, A.; Carvalho, E. Evaluation of TMD Performance in Footbridges Using Human Walking Probabilistic Models. *Vibration* **2021**, *4*, 21. [CrossRef]
5. Poon, D.; Shieh, S.-S.; Joseph, L.; Chang, C.-C. Structural Design of Taipei 101, the World’s Tallest Building. In Proceedings of the CTBUH 2004 Seoul Conference, Seoul, Korea, 10–13 October 2004; pp. 271–278.
6. Weber, F.; Huber, P.; Spensberger, S.; Distl, J.; Braun, C. Reduced-mass Adaptive TMD for Tall Buildings Damping. *Int. J. High-Rise Build.* **2019**, *8*, 117–123.
7. HIVOSS. *Design of Footbridges, Guidelines*; RFS2-CT-2007-00033. Footbridge_Guidelines_EN03-08; FIB: Lausanne, Switzerland, 2008.
8. HIVOSS. *Design of Footbridges, Background Information*; RFS2-CT-2007-00033. Footbridge_Background_EN02.doc-12.11; FIB: Lausanne, Switzerland, 2008.
9. ISO 10137; Bases for Design of Structures—Serviceability of Buildings and Walkways against Vibrations. ISO: Geneva, Switzerland, 2007.
10. Weber, F. Dynamic characteristics of controlled MR-STMDs of Volgograd Bridge. *Smart Mater. Struct.* **2013**, *22*, 095008. [CrossRef]
11. Meng, F.; Wan, J.; Xia, Y.; Ma, Y.; Yu, J. A Multi-Degree of Freedom Tuned Mass Damper Design for Vibration Mitigation of a Suspension Bridge. *Appl. Sci.* **2020**, *10*, 457. [CrossRef]
12. Zhai, W.; Han, Z.; Chen, Z.; Ling, L.; Zhu, S. Train–track–bridge dynamic interaction: A state-of-the-art review. *Veh. Syst. Dyn.* **2019**, *57*, 984–1027. [CrossRef]
13. Chapain, S.; Aly, A.M. Vibration attenuation in wind turbines: A proposed robust pendulum pounding TMD. *Eng. Struct.* **2021**, *223*, 111891. [CrossRef]
14. Chen, Y.; Jin, X.; Luo, M.; Cheng, P.; Wang, S. Vibration reduction methods of large-scale wind turbines based on system-TMD coupled algorithm. *Ocean. Eng.* **2021**, *226*, 108832. [CrossRef]

15. Kim, S.-M.; Wang, S.; Brennan, M.J. Robust broadband vibration control of a flexible structure using an electrical dynamic absorber. *Smart Mater. Struct.* **2011**, *20*, 75002. [CrossRef]
16. Chen, Z.Y.; Jiang, R.; Wang, R.Y.; Chen, T. Active TMD systematic design of fuzzy control and the application in high-rise buildings. *Earthq. Struct.* **2021**, *21*, 577–585.
17. Weber, F. Semi-active vibration absorber based on real-time controlled MR damper. *Mech. Syst. Signal Processing* **2014**, *46*, 272–288. [CrossRef]
18. Weber, F.; Distl, H.; Fischer, S.; Braun, C. MR Damper Controlled Vibration Absorber for Enhanced Mitigation of Harmonic Vibrations. *Actuators* **2016**, *5*, 27. [CrossRef]
19. Wang, Y.; Wang, L.; Shi, W. Two-dimensional air spring based semi-active TMD for vertical and lateral walking and wind-induced vibration control. *Struct. Eng. Mech.* **2021**, *80*, 377–390. [CrossRef]
20. Papageorgiou, C.; Houghton, N.E.; Smith, M.C. Experimental Testing and Analysis of Inerter Devices. *J. Dyn. Syst. Meas. Control.* **2009**, *131*, 011001. [CrossRef]
21. John, E.D.A.; Wagg, D.J. Design and testing of a frictionless mechanical inerter device using living-hinges. *J. Frankl. Inst.* **2019**, *356*, 7650–7668. [CrossRef]
22. Smith, M.C.; Wang, F.-C. Performance Benefits in Passive Vehicle Suspensions Employing Inerters. *Veh. Syst. Dyn.* **2004**, *42*, 235–257. [CrossRef]
23. Baduidana, M.; Kenfack-Jiotsa, A. Optimal design of inerter-based isolators minimizing the compliance and mobility transfer function versus harmonic and random ground acceleration excitation. *J. Vib. Control.* **2020**, *27*, 1297–1310. [CrossRef]
24. Krenk, S.; Høgsberg, J. Tuned resonant mass or inerter based absorbers: Unified calibration with quasi-dynamic flexibility and inertia correction. *Proc. R. Soc. A* **2016**, *472*, 20150718. [CrossRef]
25. Chen, M.; Hu, Y. *Inerter and Its Application in Vibration Control Systems*; Springer Nature Singapore Pte Ltd. and Science Press: Beijing, China, 2019; Volume 472, p. 20150718. ISBN 978-981-10-7088-4.
26. Krenk, S. Resonant inerter based vibration absorbers on flexible structures. *J. Frankl. Inst.* **2019**, *356*, 7704–7730. [CrossRef]
27. Wagg, D.J. A review of the mechanical inerter: Historical context, physical realisations and nonlinear applications. *Nonlinear Dyn.* **2021**, *104*, 13–34. [CrossRef]
28. Lazar, I.F.; Neild, S.A.; Wagg, D.J. Using an inerter-based device for structural vibration suppression. *Earthq. Eng. Struct. Dyn.* **2014**, *43*, 1129–1147. [CrossRef]
29. Lara-Valencia, L.A.; Farbiarz-Farbiarz, Y.; Valencia-González, Y. Design of a Tuned Mass Damper Inerter (TMDI) Based on an Exhaustive Search Optimization for Structural Control of Buildings under Seismic Excitations. *Shock. Vib.* **2020**, *2020*, 8875268. [CrossRef]
30. Jalali, H.H.; Maziar Farzam, F. Inerter-Connected Double Tuned Mass Damper for Passive Control of Buildings under Seismic Excitation. *Period. Polytech. Civ. Eng.* **2022**, *66*, 421–432.
31. Marian, L.; Giaralis, A. Optimal design of a novel tuned mass-damper-inerter (TMDI) passive vibration control configuration for stochastically support-excited structural systems. *Probabilistic Eng. Mech.* **2014**, *38*, 156–164. [CrossRef]
32. Giaralis, A.; Petrini, F. Optimum design of the tuned mass-damper-inerter for serviceability limit state performance in wind-excited tall buildings. *Procedia Eng.* **2017**, *199*, 1773–1778. [CrossRef]
33. Giaralis, A.; Petrini, F. Wind-induced vibration mitigation in tall buildings using the tuned mass-damper-inerter (TMDI). *J. Struct. Eng.* **2017**, *143*, 4017127. [CrossRef]
34. Zhang, Z.; Fitzgerald, B. Tuned mass-damper-inerter (TMDI) for suppressing edgewise vibrations of wind turbine blades. *Eng. Struct.* **2020**, *221*, 110928. [CrossRef]
35. Barredo, E.; Larios, M.; Mayén, J.; Flores-Hernández, A.A.; Colín, J.; Arias-Montiel, M. Optimal design for high-performance passive dynamic vibration absorbers under random excitation. *Eng. Struct.* **2019**, *195*, 469–489. [CrossRef]
36. Barredo, E.; Larios, M.; Colín, J.; Mayén, J.; Flores-Hernández, A.A.; Arias-Montiel, M. A novel high-performance passive non-traditional inerter-based dynamic vibration absorber. *J. Sound Vib.* **2020**, *485*, 115583. [CrossRef]
37. Alotta, G.; Failla, G. Improved inerter-based vibration absorbers. *Int. J. Mech. Sci.* **2021**, *192*, 106087. [CrossRef]
38. Dai, J.; Xu, Z.D.; Gai, P.P. Tuned mass-damper-inerter control of wind-induced vibration of flexible structures based on inerter location. *Eng. Struct.* **2019**, *199*, 109585. [CrossRef]
39. Weber, F.; Huber, P.; Borchsenius, F.; Braun, C. Performance of TMDI for Tall Building Damping. *Actuators* **2020**, *9*, 139. [CrossRef]
40. Meirovitch, L. *Fundamentals of Vibrations*; McGraw-Hill: New York, NY, USA, 2001.

Article

A Novel Single Tube Semi-Active Tuned Liquid Gas Damper for Suppressing Horizontal Vibrations of Tower-like Structures

Michael Reiterer ^{1,*}  and Janez Schellander ²¹ Institute of Structural Dynamics, Vienna University of Technology, 1040 Vienna, Austria² Department of Structural Dynamics, REVOTEC Engineering, 1070 Vienna, Austria; janez.schellander@revotec.at

* Correspondence: michael.reiterer@revotec.at; Tel.: +43-660-2999-363

Abstract: The purpose of this paper is to present a novel single tube semi-active tuned liquid gas damper (SA-TLGD) for suppressing horizontal vibrations of tower-like structures and to study its damping effectiveness. The main difference to the well-known state-of-the-art tuned liquid column damper (TLCD) is the special geometric shape of the developed SA-TLGD. Contrary to the TLCD, the presented SA-TLGD only consists of a single horizontal tube that is partially filled with water. A large deformable elastic membrane with neglectable stiffness is used as the interface between the liquid and the air. Both ends of the horizontal tube are sealed and the resulting gas spring is used as the restoring force and frequency tuning parameter, respectively. The developed SA-TLGD is a semi-active vibration damping device, where its natural frequency and magnitude of energy dissipation can be re-adjusted during operation. Due to the lack of any vertical tube parts, this new type of vibration absorber requires significantly less installation space compared to the classical TLCDs. The equations of motion of the SA-TLGD and the coupled main system are derived by the application of conservation of momentum. The procedure of optimal tuning of the SA-TLGD is presented, and computational numerical studies are performed to demonstrate the damper effectiveness. It is shown that the application of the developed SA-TLGD provides a large reduction in the maximum horizontal forced vibration amplitudes of tower like-structures and that its semi-active functionality enables the possibility of re-adjustment any time during the operation life of the structure.

Keywords: tower-like structures; tuned liquid gas damper; semi-active; elastic membrane; gas spring; gas volume; SA-TLGD; TLCD; TMD

Citation: Reiterer, M.; Schellander, J. A Novel Single Tube Semi-Active Tuned Liquid Gas Damper for Suppressing Horizontal Vibrations of Tower-like Structures. *Appl. Sci.* **2022**, *12*, 3301. <https://doi.org/10.3390/app12073301>

Academic Editor: Felix Weber

Received: 23 February 2022

Accepted: 22 March 2022

Published: 24 March 2022

Publisher's Note: MDPI stays neutral with regard to jurisdictional claims in published maps and institutional affiliations.



Copyright: © 2022 by the authors. Licensee MDPI, Basel, Switzerland. This article is an open access article distributed under the terms and conditions of the Creative Commons Attribution (CC BY) license (<https://creativecommons.org/licenses/by/4.0/>).

1. Introduction

Tower-like structures, e.g., high-rise buildings, chimneys, and wind turbines, are prone to vibrations when subjected to wind, sea waves, and earthquake loads, which may cause structural failure, discomfort to occupants, and malfunction of the installed equipment. Hence, the mitigation of structural vibrations has always been a major concern amongst structural engineers. One of the effective means to reduce the dynamic response of tower-like structures is the application of dynamic vibration absorbers. The Tuned Mass Damper (TMD) is one of the most popular passive control systems and has been broadly studied and applied to many engineering structures [1–9]. TMDs make use of a moving secondary mass capable of counteracting the dynamic motion of the vibrating structure.

Amongst the widely recognized application of TMDs, Tuned Liquid Dampers (TLDs) have also become very popular for vibration suppression of tower-like structures in recent decades. In civil engineering applications, the following two types of TLDs are commonly utilized: Tuned Sloshing Dampers (TSDs) and Tuned Liquid Column Dampers (TLCDs). TSDs are typically constructed by a tank partially filled with water and they can be either based upon a deep or a shallow water configuration. TSDs absorb and dissipate kinetic energy through boundary layer friction, wave breaking, and free surface rupture during the

interaction with the vibrating structure [10–14]. Pandey et al. [15] studied a compliant tuned liquid damper for controlling seismic vibrations of short period structures by mounting a TLD on an array of compliant elastomeric pads and in [16] the authors propose to implement a tuned liquid mass damper in a deep liquid storage tank by flexibly attaching the tank to the structure to allow tuning of vibration of the impulsive mass to short period structures.

TLCDs are a special type of TLDs that rely on the motion of a liquid mass in a rigid U-shaped tube to counteract the action of external forces acting on the structure, with the inherent damping being introduced in the oscillating liquid column through friction and built-in orifices. The tank consists of two vertical columns and a single horizontal connecting tank. TLCDs are partially filled with a Newtonian fluid until the liquid reaches a certain level in the two vertical columns. Due to its cost-effectiveness, simplicity in installation, and low maintenance costs, TLCDs have attracted significant interest for researchers and engineers [17–21]. The applicability of passive TLCDs is limited to civil engineering structures with extremely low vibrating frequencies up to around 0.5 Hz. However, this detrimental property of TLCDs is conquered through some innovative ideas such as utilizing an air spring (gas spring) in the vertical tubes, to extend the range of applicability to structural vibration frequencies up to 5.0 Hz [22,23]. The resulting beneficial frequency increase and tuning effects due to the gas spring are reflected by the so-called Tuned Liquid Column Gas Damper (TLCGD). The application of TLCGDs offers a quite simple tuning mechanism since the natural frequency can be adjusted by pressurizing the gas chambers or adjusting the size of the gas volume inside the vertical sealed tubes [24,25]. Further developments of TLDs and TLCDs were studied by Zhao et al. [26] who presented a novel tuned liquid inerter system by employing the synergy benefits of an inerter-based subsystem and a tuned liquid element to achieve the lightweight-based improved control performance and by Di Matteo et al. [27] who studied a tuned liquid column damper inerter to control the seismic response of structural systems.

For a passive vibration absorber, designed with optimal tuned frequency and damping ratio, these optimum parameters are valid only for a given level of wind, sea waves, or seismic excitation with a specific frequency content. In fact, wind, sea waves, and earthquake forces acting on tower-like structures are random in nature, with their extent and frequency content being different at different times. Likewise, the dynamic properties of a tall building structure, including the natural frequencies and damping ratios, are response-amplitude-dependent during strong winds [28]. It is therefore highly desirable, to develop frequency- and damping-variable or parameter-adjustable vibration absorbers to achieve optimal control performance for a wide range of loading conditions and therefore to be able to consider structural uncertainties [29,30]. Structures also show a significant change in their natural frequencies and damping ratios with increasing age and due to temperature effects. Hence, Yalla et al. [31] proposed a semi-active TLCD which achieves variable fluid damping by using a controllable valve to adjust the orifice opening and Haroun et al. [32] presented a concept of a hybrid liquid column damper that can actively control the orifice opening ratio. Altay and Klinkel [33] presented a semi-active TLCD that provides mechanisms for a continuous adaptation of both its natural frequency and damping behavior in real time. Further relevant research in the field of semi-active TLCDS has been performed by Wang et al. [34] and Sarkar and Chakraborty [35]. They presented a semi-active TLCD with the use of magneto-rheological (MR) fluids to generate controllable fluid damping. The MR fluids are smart materials that can reversibly change from a free-flowing, linear viscous fluid to a semi-solid with a controllable yield strength in milliseconds when exposed to a magnetic field [36]. Thus, they are used as damping fluids to devise semi-active MR-TLCDs with alterable fluid viscosity. The strongly modifiable fluid viscosity results in adjustable and controllable damping forces in the MR-TLCD for structural vibration control under a wide range of loading conditions.

Regarding existing installations of TLDs onto civil engineering structures, their sizes can vary, depending on the kinetic equivalent moving mass of the structure, from relatively compact units to much larger devices of several hundred tonnes (e.g., the two TLCDS

installed at the top of the 52-storey Random House Tower in New York City of, respectively, 265,000 and 379,000 kg [37]). In the case of TLDs, the apparent low density of the moving damper mass (e.g., water $\rho = 1000 \text{ kg/m}^3$) compared to classical tuned mass dampers (e.g., steel $\rho = 7850 \text{ kg/m}^3$) results in a considerable disadvantage in terms of the space required at the installation site of the damper. Especially slender vibration-prone structures, e.g., wind turbines, only provide a very small installation space at the tower head and, hence, the practical application of TLDs is a quite challenging task. For instance, a 5 MW offshore wind turbine with a 112 m steel tube length has a diameter of just 5.5 m at the tower head [38]. To achieve the desired bidirectional damping effect, at least two TLDs must be installed in the two relevant vibration directions, resulting in a very large space requirement at the tower head. In the case of installation of TLCDs, the two vertical columns of the U-shaped tank, which are arranged at a distance from each other and communicate through the horizontal passage, also need an enormous installation space inside of the structure. Thus, it is evident that although TLDs offer several advantages compared to TMDs, their application to real structures often fails because of the limited available installation space in the case of vibration-prone slender tower-like structures, e.g., wind turbines. Compared to the liquid dampers, the installation space required for the moving mass of pendulum dampers is significantly smaller due to the density of steel. However, the very low fundamental natural frequency in the range of approx. 0.20 Hz usually found in wind turbines and high-rise structures requires a very large pendulum length of approx. 6.21 m. Hence, the space gained by the small steel pendulum mass compared to the fluid mass of liquid dampers is compensated by the very long pendulum lengths.

In this paper, a novel single tube semi-active tuned liquid gas damper (SA-TLGD) for suppressing horizontal vibrations of tower-like structures is presented and its damping effectiveness is studied computationally considering a SDOF- and MDOF-main system. The novelty of the damper lies in the lack of any vertical columns and the design of a single tube only which is partially filled with a fluid, e.g., water (Figure 1). A large deformable elastic membrane with neglectable stiffness is used as an interface between the fluid and the air. The SA-TLGD can be interpreted as a TLCGD, but without any vertical columns, i.e., the restoring force from gravity is not present anymore. Both ends of the horizontally orientated tube are sealed and the resulting gas spring is used as the restoring force and frequency tuning parameter, respectively. To adjust the SA-TLGD vibrating frequency, the bulk gas volume V_0 is separated into a series of gas chambers V_{0i} that are connected via controllable valves. Depending on the desired optimal vibrating frequency, a specific size of gas volume is initiated through the utilized control software, running on the microcontroller (MC), which opens or closes the appropriate number of valves. It is noted that the valves are either in a completely closed or opened position, i.e., they do not work as damping-increasing throttling valves. The magnitude of the fluid damping is properly adjusted by varying the diameter of several controllable orifices.

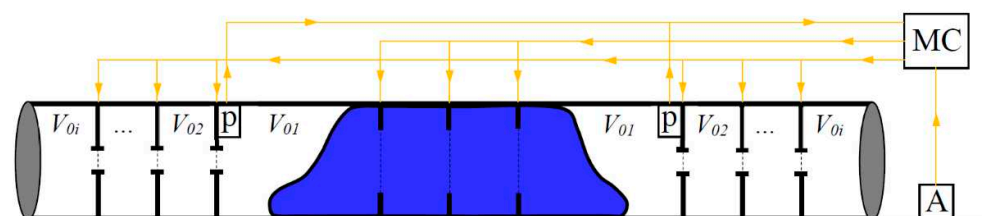


Figure 1. Novel single tube semi-active Tuned Liquid Gas Damper (SA-TLGD).

The semi-active control logic of the SA-TLGD is based on measuring the present resonance frequency of the vibration-prone main system with properly installed accelerometers (A). Hence, the input parameter for the control algorithm is the actual resonance frequency calculated from the recorded acceleration response in the time domain by application of FFT. Based on this resonance frequency information, the microcontroller (MC) sets the optimal number of opened or closed valves and the optimal diameter of the orifices to

achieve the optimal absorber parameters. The actual vibration response and vibrating frequency, respectively, of the fluid mass is measured with pressure sensors (p). Hence, the developed SA-TLGD is a semi-active vibration damping device, where its natural frequency and magnitude of energy dissipation can be re-adjusted during the operation of the damper at any time. However, the adjustment of the damper parameters to the optimal values is not performed in real time immediately after detecting slight changes in the main system resonance frequency, but after detecting significant changes during the structural lifetime and, therefore, it is not necessary to adjust the damper parameters in real time during the state of fluid mass vibration. Due to the lack of any vertical tubes, this new type of vibration absorber requires significantly less installation space compared to classical TLCs and its semi-active functionality ensures an optimal performance over the total operating life of vibration-prone structures. It is noted that the studied SA-TLGD has no fixed direction and, hence, it can act in arbitrary planes. Regarding the long-term durability of the SA-TLGD, it is important that all construction elements of the damper are designed for both the static and dynamic loading conditions that occur during the total operating lifetime.

2. Mechanical Model

Tower-like structures with low inherent damping are, in general, forced to couple bending and torsional vibrations. In this study, it is assumed that the vibration modes of the considered structure are well separated and, hence, modal tuning of SA-TLGD is applicable to a selected vibration mode. The mechanical model is developed in steps, starting with the free body diagram of the SA-TLGD (Figure 2a) and the formulation of in-plane rigid body motions of a seismic $w_g(t)$ and force $F(t)$ excited SDOF-shear frame structure with a single SA-TLGD attached (Figure 2b). The substructure synthesis method is applied to derive the coupled equations of motion.

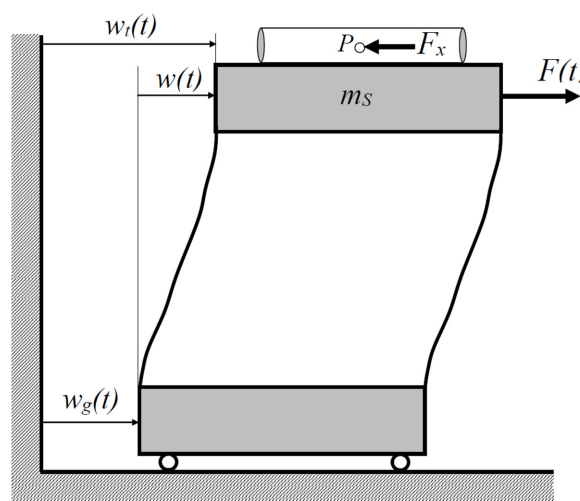
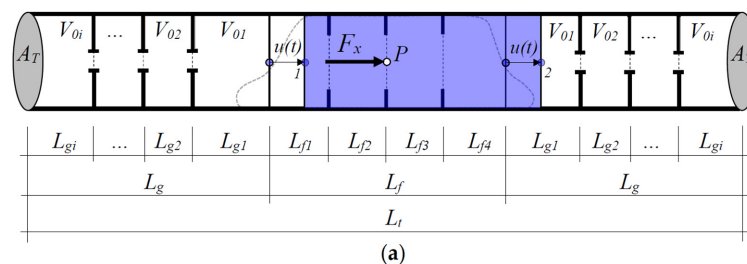


Figure 2. Free body diagrams of the mechanical model: (a) single tube SA-TLGD under horizontal floor excitation; (b) SDOF-main system under combined seismic $w_g(t)$ and force excitation $F(t)$ with horizontal interaction force F_x from the SA-TLGD dynamics.

2.1. Free Body Diagram of SA-TLGD

The single tube SA-TLGD is considered in a deflected position separated from the floor of the SDOF-main system under horizontal floor excitations $w_t = w_g + w$ (Figure 2). The horizontal orientated tube with diameter A_T is sealed at both ends and filled with a fluid (density ρ_f) over the length L_f , i.e., the total fluid mass yields to $m_f = \rho_f A_T L_f$. The relative motion of the fluid interface to gas is described by the displacement $u_1 = u_2 = u(t)$. A large deformable elastomeric membrane with neglectable stiffness is used as the interface. To formulate the SA-TLGDs dynamic, the shape of the membrane in static equilibrium is approximated as a pure vertically orientated surface. During the vibration process, the gas inside the air chambers V_{0i} is quasi-statically compressed and released by the moving fluid interface in relatively slow motion. A pressure difference $\Delta p = p_2 - p_1$ is created between the left and right gas chambers and it changes the undamped circular natural frequency of the SA-TLGD defined in Equation (8). The absolute acceleration of the chosen reference Point P in the prescribed rigid body motion is given by

$$\ddot{w}_t = \ddot{w}_g + \ddot{w}. \tag{1}$$

To derive the nonlinear equation of motion, the floor excited SA-TLGD is transformed into an equivalent single-mass oscillator [39]. Thereby, the fluid mass $m_f = \rho_f A_T L_f$ represents the equivalent mass M^* of the harmonic oscillator. Neglecting the stiffness contribution of the elastic membranes, the equivalent spring stiffness K^* results solely from the gas spring effect. It is assumed that the gas pressure p_0 is present in both gas chambers in the static equilibrium position of the fluid. p_0 can either be chosen equal to the atmospheric pressure ($p_0 \cong 10^5$ Pa) or to any other arbitrary desired value (negative or positive pressure). The initial size of the gas volume V_0 enclosed on the left and right sides of the fluid in the static equilibrium position is exposed to a constant change in compression and expansion, i.e., the size of V_0 fluctuates as a function of the horizontal dynamic deformation $u(t)$ of the fluid mass. Hence, the time varying size of V_0 leads to a change in the pressure state of the gas volume and in consequence of a restoring effect of the deflected fluid mass. The resulting gas pressure difference $\Delta p = p_2 - p_1$ approximately follows the quasistatic polytropic law [39] (ρ_0 is the gas density in the static equilibrium position of the fluid mass),

$$\Delta p = p_0 \left(\frac{\Delta \rho}{\rho_0} \right)^n = p_0 \left(\frac{V_0}{\Delta V} \right)^n, \Delta V = V_2 - V_1, V_0 = \sum_{i=1}^k V_i. \tag{2}$$

where n denotes the polytropic coefficient and k is the number of conducted separated gas chambers V_i . In the case of very slow fluid velocities (low eigenfrequency) the gas spring acts approximately under isothermal conditions $n = 1.0$, while in the case of higher velocities an adiabatic condition occurs and the coefficient changes to a value of $n = 1.4$. In any other circumstances, n takes a value in the range between 1.0 and 1.4 [25]. During the state of fluid mass vibration, the actual size of gas volume at the left and right gas chambers is defined as (Figure 2a),

$$V_1 = V_0 + A_T u, V_2 = V_0 - A_T u. \tag{3}$$

Inserting the expressions for the gas volumes V_1 and V_2 into Equation (2) yields the nonlinear gas pressure difference,

$$\Delta p(u) = p_0 \left[\left(\frac{V_0}{V_0 - A_T u} \right)^n - \left(\frac{V_0}{V_0 + A_T u} \right)^n \right]. \tag{4}$$

A linearization of Equation (4) is obtained using a Taylor series expansion of the nonlinear function with respect to the equilibrium pressure p_0 while neglecting the higher order terms,

$$\Delta p(u) = \frac{2 n p_0 A_T}{V_0} u + O(u^3) \approx \frac{2 n p_0}{L_g} u, \tag{5}$$

where $L_g = V_0/A_T$ defines the horizontal length of the gas spring at the left and right gas chambers of the SA-TLGD (Figure 2a). From Equation (5) and the relation $K^* u = \Delta p A_T$ the single-mass oscillator equivalent spring stiffness K^* results as

$$K^* = \frac{2 n p_0 A_T}{L_g}. \tag{6}$$

The deviation of the exact solution for the nonlinear relative pressure difference $\Delta p/p_0$ (Equation (4)) from the linearized solution (Equation (5)) is illustrated in Figure 3 as a function of the dimensionless relative displacement $u(t)/L_g$. The polytropic coefficient was chosen with $n = 1.2$, i.e., mean value of isotherm and adiabatic state change. It is indicated that up to $u(t)/L_g \leq 0.30$ the deviation to the exact nonlinear solution is insignificantly small, i.e., linearization is permissible in this range of the vibration amplitude. In the case of very large vibration amplitudes $u(t)/L_g > 0.50$, the restoring force of the nonlinear gas spring differs significantly from the linear solution and, therefore, leads to a disadvantageous detuning of the SA-TLGD eigenfrequency. Hence, when designing the SA-TLGD the relation of the maximum fluid mass displacement $u(t)$ to the chosen gas spring length L_g is an important tuning parameter to achieve the optimum vibration damping effect. For this reason, the maximum amplitude of gas compression is limited to $\max |u(t)| = U_{max} < 0.30 L_g$ to keep the eigenfrequency of the SA-TLGD approximately constant.

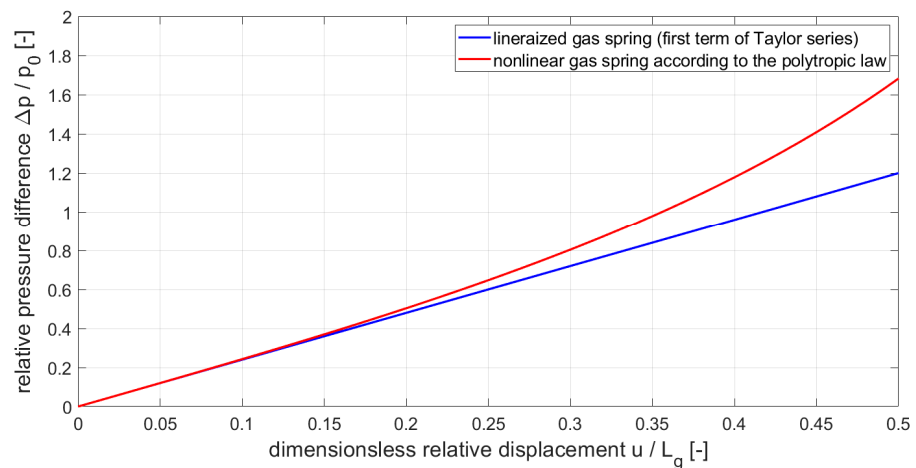


Figure 3. Comparison of linear and nonlinear gas spring stiffness function $\Delta p/p_0$.

After derivation of the equivalent mass $M^* = m_f = \rho_f A_T L_f$ and stiffness K^* given in Equation (6) of a single-mass oscillator, the nonlinear equation of motion for the floor excited SA-TLGD yields to,

$$\ddot{u} + \delta_L |\dot{u}| \dot{u} + \omega_A^2 u = -\ddot{w}_t, \tag{7}$$

where an averaged turbulent damping term, that must be experimentally verified, has been added. The head loss coefficient δ_L can be increased by properly selecting the diameter of the built-in orifice plate (Figure 2a). In the case of stationary flow, δ_L is tabulated for

relevant pipe elements and cross-sectional areas in [40]. In Equation (7), the undamped circular natural frequency ω_A of the both side sealed SA-TLGD is defined as,

$$\omega_A = \sqrt{\frac{2 n p_0 A_T}{m_f L_g}}. \tag{8}$$

In Equation (8) $n, p_0, A_T, m_f,$ and L_g denote the polytropic coefficient ($1.0 \leq n \leq 1.4$), the initial equilibrium pressure in the gas chambers, the cross-sectional area of the tube, the fluid mass, and the total gas spring length. $L_g = V_0/A_T$ is an important design variable of the SA-TLGD, defining the volume of the gas chamber in terms of the cross-sectional area. The re-optimization of the damper eigenfrequency is performed during the state of operation by semi-actively controlling the appropriate number of either closed or open valves, i.e., adjusting the size of the gas volume V_0 . Equation (8) rewritten into a more general form leads to,

$$\omega_A = \sqrt{\frac{2 n p_0 A_T^2}{m_f \sum_{i=1}^k V_{0i}}}. \tag{9}$$

Linearization of the Fluid Flow Equation of Motion

Regarding the application of the absorber optimization procedure in Section 3, the nonlinear turbulent damping term $\delta_L |\dot{u}| \dot{u}$ in Equation (7) must be transformed into its equivalent linear one, $2\zeta_A \omega_A \dot{u}$. Demanding equally dissipated energy during one cycle, over a vibration period T , for the nonlinear and the linear SA-TLGD results in the relation,

$$\int_0^T |(\delta_L |\dot{u}| \dot{u} + \omega_A^2 u) \dot{u}| dt = \int_0^T |2\zeta_A \omega_A \dot{u} + \omega_A^2 u) \dot{u}| dt, \tag{10}$$

and, when substituting the time harmonic displacement function, $u(t) = U_0 \cos \omega_A t$, the equivalent linear viscous damping coefficient can be written proportional to the absorber vibration amplitude as follows,

$$\zeta_A = \frac{4 U_0 \delta_L}{3 \pi}. \tag{11}$$

Under these conditions, Equation (7) takes on its linearized form with,

$$\ddot{u} + 2 \zeta_A \omega_A \dot{u} + \omega_A^2 u = -\ddot{w}_t, |u| \leq U_0 \approx U_{max}. \tag{12}$$

The value for U_0 , used in Equation (11) for general forced vibrations of the fluid mass, is determined by means of numerical simulations of the linear coupled main system with the SA-TLGD attached and commonly chosen as $U_0 = U_{max}$.

Applying the conservation of momentum to the fluid mass in the free body diagram of the SA-TLGD (Figure 2a) determines the resultant horizontal interaction force,

$$F_x = m_f (\ddot{w}_t + \ddot{u}), m_f = \rho_f A_T L_f. \tag{13}$$

2.2. Substructure Synthesis of a SDOF-Main System with SA-TLGD Attached

The SDOF-main system with the assigned interaction force F_x from the SA-TLGD dynamics under combined seismic \ddot{w}_g and force excitation $F(t)$, is considered in the next step of the substructure synthesis method (Figure 2b). The external dynamic force $F(t)$ is interpreted as a wind load. The main system floor deformation is given by the displacement $w(t)$, whereby the time variant P - Δ effect is neglected. The moving floor mass m_H includes the dead weight $m_{D,A}$ of the SA-TLGD and the modal masses of the vertical columns. The field stiffness of the columns is denoted with k , and it includes the geometric correction

of prestressing by the dead weight considered for the columns according to [39,41]. Light structural damping is assumed by the damping coefficient b .

Conservation of momentum of the floor mass m_S yields the relevant linear equation of motion of the SDOF-main system with the attached SA-TLGD (Figure 2b),

$$\ddot{w} + 2 \zeta_S \Omega_S \dot{w} + \Omega_S^2 w = -\ddot{w}_g + \frac{F(t)}{m_S} - \frac{F_x}{m_S}, \zeta_S = \frac{b}{2 m_S \Omega_S}, \Omega_S^2 = \frac{k_S}{m_S}, \quad (14)$$

where Ω_S and ζ_S represent the undamped circular natural frequency of the SDOF-main system, and the linear viscous damping ratio. Inserting the coupling force F_x from Equation (13) into Equation (14) leads together with Equation (12) to the coupled system of linearized equations of motion for the seismic and force excited 2-DOF system,

$$\begin{aligned} \ddot{w} + 2 \zeta_S \Omega_S \dot{w} + \Omega_S^2 w &= -\ddot{w}_g + \frac{F(t)}{m_S} - \mu \ddot{w}_t - \mu \ddot{u}, \\ \ddot{u} + 2 \zeta_A \omega_A \dot{u} + \omega_A^2 u &= -\ddot{w}_t, \\ w_t &= w_g + w. \end{aligned} \quad (15)$$

The ratio of fluid mass to the moving mass of the SDOF-main system is defined by,

$$\mu = \frac{m_f}{m_S}. \quad (16)$$

To provide highest possible vibration suppression of the main system the mass ratio μ should be maximized. However, from a practical point of view, i.e., limited installation space and avoidance of detrimental frequency shifts of the main system, the mass ratio μ is typically chosen in range of 0.5–5%.

To prepare for the equations of motion of a MDOF-main system with multiple, differently tuned SA-TLGDs attached, Equation (15) is rewritten in its linearized matrix form,

$$\begin{aligned} \mathbf{M}_S \begin{bmatrix} \ddot{w} \\ \ddot{u} \end{bmatrix} + \mathbf{C}_S \begin{bmatrix} \dot{w} \\ \dot{u} \end{bmatrix} + \mathbf{K}_S \begin{bmatrix} w \\ u \end{bmatrix} &= - \begin{bmatrix} m_S + m_f \\ 1 \end{bmatrix} \ddot{w}_g + \begin{bmatrix} F(t) \\ 0 \end{bmatrix}, \\ \mathbf{M}_S &= \begin{bmatrix} m_S + m_f & m_f \\ 1 & 1 \end{bmatrix}, \quad \mathbf{C}_S = \begin{bmatrix} 2\zeta_S \Omega_S m_S & 0 \\ 0 & 2\zeta_A \omega_A \end{bmatrix}, \quad \mathbf{K}_S = \begin{bmatrix} k_S & 0 \\ 0 & \omega_A^2 \end{bmatrix}. \end{aligned} \quad (17)$$

2.3. Substructure Synthesis of a MDOF-Main System with Multiple SA-TLGD Attached

Based on Equation (17), the coupled linearized equations of motion of a seismic and forced excited MDOF-main system with multiple SA-TLGDs attached are described by the following set of matrix equations, in a hyper matrix formulation,

$$\begin{aligned} \mathbf{M}_S \begin{bmatrix} \ddot{\vec{w}} \\ \ddot{\vec{u}} \end{bmatrix} + \begin{bmatrix} \mathbf{C} & 0 \\ 0 & \mathbf{C}_f \end{bmatrix} \begin{bmatrix} \dot{\vec{w}} \\ \dot{\vec{u}} \end{bmatrix} + \begin{bmatrix} \mathbf{K} & 0 \\ 0 & \mathbf{K}_f \end{bmatrix} \begin{bmatrix} \vec{w} \\ \vec{u} \end{bmatrix} \\ = - \begin{bmatrix} \mathbf{M} \vec{r}_S + \mathbf{L} \mathbf{M}_f \vec{i} \\ \vec{i} \end{bmatrix} \ddot{w}_g + \begin{bmatrix} \vec{F}(t) \\ 0 \end{bmatrix}. \end{aligned} \quad (18)$$

where \vec{r}_S denotes the static influence vector, which for the single point base excitation renders to $\vec{r}_S = \vec{i} = [1 \ 1 \ 1 \ \dots \ 1]^T$. In Equation (18) the sparse SA-TLGD position matrix

\mathbf{L} with dimension $N \times n_A$, where N and n_A define the main system degree of freedom (DOF) and the number of installed SA-TLGDs,

$$\mathbf{L} = \begin{bmatrix} 1 & 0 & 1 \\ \vdots & \vdots & \vdots \\ 0 & 1 & 0 \\ \vdots & \vdots & \vdots \\ 0 & 0 & 0 \end{bmatrix} \leftarrow \text{DOF to be influenced, } N \tag{19}$$

\uparrow
 number of SA – TLGD, n_A

is included into the generalized mass matrix \mathbf{M}_S as well,

$$\mathbf{M}_S = \begin{bmatrix} \mathbf{M} + \mathbf{L} \mathbf{M}_f \mathbf{L}^T & \mathbf{L} \mathbf{M}_f \\ \mathbf{L} & \mathbf{I} \end{bmatrix}. \tag{20}$$

\mathbf{M} , \mathbf{C} , and \mathbf{K} are the mass, damping, and stiffness matrices of the MDOF-main system and the SA-TLGD parameter-related diagonal matrices \mathbf{M}_f , \mathbf{C}_f , and \mathbf{K}_f are defined as follows,

$$\begin{aligned} \mathbf{M}_f &= \text{diag} [m_{f1}, \dots, m_{fn_A}], \\ \mathbf{C}_f &= \text{diag} [2\zeta_{A1}\omega_{A1}, \dots, 2\zeta_{An_A}\omega_{An_A}], \\ \mathbf{K}_f &= \text{diag} [\omega_{A1}^2, \dots, \omega_{An_A}^2]. \end{aligned} \tag{21}$$

3. Optimal Tuning of SA-TLGDs

3.1. Optimal Tuning of a Single SA-TLGD Attached to a SDOF-Main System

For optimal modal tuning of a single SA-TLGD attached to a SDOF-main system, the two design parameters $\delta = \omega_A/\omega_S$ and ζ_A must be selected appropriately. Here, δ defines the ratio between the natural frequency of the vibration absorber and the natural frequency of the SDOF-main system, and ζ_A defines the linearized viscous damping ratio of the SA-TLGD. The analytical formulas for determining the optimal design parameters for the classical TMD attached to a SDOF-main system were first presented by Den Hartog [1], for a time harmonic force excitation and an undamped main system $\zeta_S = 0$,

$$\delta_{opt} = \frac{\omega_A}{\omega_S} = \frac{1}{1 + \mu}, \zeta_{A,opt} = \sqrt{\frac{3\mu}{8(1 + \mu)}}, \mu = \frac{m_f}{m_S}. \tag{22}$$

Equation (22) is applicable for determining the optimal design parameters to minimize the displacement $w(t)$ of a harmonic force excited main system $F(t) = F_0 e^{i\nu t}$, ν is the excitation frequency, and it remains unchanged when minimizing the acceleration $\ddot{w}(t)$ of a harmonic base excited main system [7]. Slightly different parameters result for a harmonic base excited main system $w_g(t) = w_0 e^{i\nu t}$ when minimizing the displacement $w(t)$ [7],

$$\delta_{opt} = \sqrt{\frac{2 - \mu}{2(1 + \mu)^2}}, \zeta_{A,opt} = \sqrt{\frac{3\mu}{4(1 + \mu)(2 - \mu)}}. \tag{23}$$

The Equations (22) and (23) indicate that the optimum design parameters of the single SA-TLGD attached to a SDOF-main system depend solely on the mass ratio $\mu = m_A/m_S$. In practical applications, the mass ratio is usually chosen in range of 0.5–5%. It is noted that the optimal design parameters given in Equations (22) and (23) are derived under the assumption of an undamped main system, i.e., the optimal performance of the vibration absorber is present for $\zeta_S = 0$. However, Pocanschi and Phocas [42] give the following

analytical equations for the correction of the optimal design parameters considering the structural damping of the main system $\zeta_S > 0$ when optimizing the vibration damper,

$$\begin{aligned} \tilde{\delta}_{opt} &= \delta_{opt} - (0,241 + 1,7 \mu - 2,6 \mu^2) \zeta_S - (1 - 1,9 \mu + \mu^2) \zeta_S^2, \\ \tilde{\zeta}_{A,opt} &= \zeta_{A,opt} + (0,13 + 0,12 \mu + 0,4 \mu^2) \zeta_S - (0,01 + 0,9 \mu + 3 \mu^2) \zeta_S^2. \end{aligned} \tag{24}$$

3.2. State Space Optimal Tuning of Multiple SA-TLGDs Attached to a MDOF-Main System

In the case of multiple SA-TLGD attached to a MDOF-system, the tuning process is best performed in two steps. At first, the linearized model is tuned with respect to a selected vibration mode of the main system using the classical Den Hartog formulas, presented in Section 3.1. Fine tuning of the absorber parameters for MDOF-systems is best achieved by also considering adjacent vibration modes in a state space representation, by minimizing the weighted squared area of the frequency response function (FRF). Hence, the coupled linearized equations of motion of the seismic and force excited MDOF-main system with multiple SA-TLGDs attached (Equation (18)), are transformed into the state space. Introducing the state space hypervector $\vec{z} = \begin{bmatrix} \vec{w} & \vec{u} & \dot{\vec{w}} & \dot{\vec{u}} \end{bmatrix}$ and its time derivative $\dot{\vec{z}}$, renders the first order matrix equation in state space,

$$\begin{aligned} \dot{\vec{z}} &= (\mathbf{A} + \mathbf{B} \mathbf{R}) \vec{z} - \vec{e}_g \ddot{w}_g + \vec{b}, \\ \vec{e}_g &= \begin{bmatrix} \vec{0} & \vec{0} & \mathbf{M}_S^{-1} \begin{pmatrix} \mathbf{M} \vec{r}_S + \mathbf{L} \mathbf{M}_f \vec{i} \\ \vec{i} \end{pmatrix} \end{bmatrix}, \\ \vec{b} &= \mathbf{E}_F \vec{F}, \mathbf{E}_F = \begin{bmatrix} \mathbf{0} & \mathbf{0} & \mathbf{M}_S^{-1} \begin{pmatrix} \mathbf{I} \\ \mathbf{0} \end{pmatrix} \end{bmatrix}. \end{aligned} \tag{25}$$

The forcing hypervector contains the horizontal excitation forces $\vec{F}(t)$. Since only the matrix elements \mathbf{A} and \mathbf{B} from Equation (25) contain the known main system parameters, the state space matrix $\mathbf{A} + \mathbf{B} \mathbf{R}$ should be kept separated,

$$\begin{aligned} \mathbf{A} &= \begin{bmatrix} \mathbf{0} & \mathbf{0} & \mathbf{I} & \mathbf{0} \\ \mathbf{0} & \mathbf{0} & \mathbf{0} & \mathbf{I} \\ -\mathbf{M}_S^{-1} \begin{pmatrix} \mathbf{K} & \mathbf{0} \\ \mathbf{0} & \mathbf{0} \end{pmatrix} & -\mathbf{M}_S^{-1} \begin{pmatrix} \mathbf{C} & \mathbf{0} \\ \mathbf{0} & \mathbf{0} \end{pmatrix} \end{bmatrix}, \\ \mathbf{B} &= \begin{bmatrix} \mathbf{0} & \mathbf{0} & \mathbf{I} & \mathbf{0} \\ \mathbf{0} & \mathbf{0} & \mathbf{0} & \mathbf{I} \\ -\mathbf{M}_S^{-1} \begin{pmatrix} \mathbf{I} & \mathbf{0} \\ \mathbf{0} & \mathbf{I} \end{pmatrix} & -\mathbf{M}_S^{-1} \begin{pmatrix} \mathbf{I} & \mathbf{0} \\ \mathbf{0} & \mathbf{I} \end{pmatrix} \end{bmatrix}, \end{aligned} \tag{26}$$

and the matrix \mathbf{R} contains the unknown SA-TLGD design parameters,

$$\mathbf{R} = \begin{bmatrix} \mathbf{0} & \mathbf{0} & \mathbf{0} & \mathbf{0} \\ \mathbf{0} & \mathbf{K}_f & \mathbf{0} & \mathbf{0} \\ \mathbf{0} & \mathbf{0} & \mathbf{0} & \mathbf{0} \\ \mathbf{0} & \mathbf{0} & \mathbf{0} & \mathbf{C}_f \end{bmatrix}. \tag{27}$$

For the seismic excited MDOF-main system with multiple SA-TLGDs attached, the steady-state solution in the frequency domain results as,

$$\vec{z}(v) = [iv \mathbf{I} - (\mathbf{A} + \mathbf{B} \mathbf{R})]^{-1} \vec{e}_g. \tag{28}$$

For the force excited coupled MDOF-main system the steady state solution is given by,

$$\vec{z}(v) = [iv \mathbf{I} - (\mathbf{A} + \mathbf{B} \mathbf{R})]^{-1} \vec{b}_0. \tag{29}$$

To determine the optimal design parameters of the SA-TLGD it is common practice to minimize an appropriate performance index, e.g., defined by the infinite integral of the weighted sum of quadratic state variables of the MDOF-main system \vec{z}_S , in the frequency domain, see, e.g., Müller and Schiehlen [43], for the seismic excited coupled system

$$J(\nu) = \int_{-\infty}^{\infty} \vec{z}_S^T(\nu) \mathbf{S} \vec{z}_S(\nu) d\nu = 2\pi \vec{e}_g^T \mathbf{P} \vec{e}_g \rightarrow \min, \tag{30}$$

and for the force excited coupled system,

$$J(\nu) = \int_{-\infty}^{\infty} \vec{z}_S^T(\nu) \mathbf{S} \vec{z}_S(\nu) d\nu = 2\pi \vec{b}_0^T \mathbf{P} \vec{b}_g \rightarrow \min. \tag{31}$$

where the matrix \mathbf{P} is the solution of the algebraic Lypanuov matrix equation,

$$(\mathbf{A} + \mathbf{B} \mathbf{R})^T \mathbf{P} + \mathbf{P} (\mathbf{A} + \mathbf{B} \mathbf{R}) = -\mathbf{S}. \tag{32}$$

The matrix \mathbf{S} is a symmetric, positive semi-definite weighing matrix, which offers the opportunity to emphasize the importance of selected components of the state space vector. The matrix solution for \mathbf{P} is numerically evaluated by means of the software MATLAB. The minimum search is best performed by the MATLAB optimization toolbox, substituting Den Hartog’s modal design parameters for the SA-TLGDs as start values.

4. Numerical Studies on the Effectiveness of SA-TLGDs

4.1. SDOF-Wind Turbine with Single SA-TLGD Attached

The effectiveness of a single SA-TLGD regarding vibration reduction is demonstrated by considering a slender vibration-prone wind turbine with a flat gravity basement (Figure 4a) under severe wind-induced forcing by a time harmonic excitation force $F(t)$. The wind turbine is modeled as a clamped continuous Bernoulli–Euler beam with the height h and the head mass m_p on top (Figure 4b). Further ρA and EI denote the tower mass per unit length as well as the bending stiffness. The mass m_p is composed of the mass of the rotor blades, the hub, the nacelle including all internals, and the dead weight of the installed SA-TLGD. The first natural bending frequency f_1 with its corresponding mode shape ϕ_1 is selected as most critical resonance frequency regarding wind-induced vortex shedding, and hence the continuous beam model with an infinite number of DOF can be reduced to a simple SDOF system. The position of the installed single SA-TLGD is assumed at hub height h . The damping ratio of the wind turbine consists of structural damping and aerodynamic damping. Light modal damping is assumed with $\zeta_S = 1.4\%$ according to [44] for steel towers.

The parameters chosen in this numerical study for the considered wind turbine are listed in Table 1.

Table 1. Parameters chosen for the considered wind turbine.

Parameter of the Wind Turbine	Variable	Value	Unit
Hub height	h	60	m
Tower diameter	D	5.5	m
Tower mass per unit length	ρA	3330	kg/m
Bending stiffness	EI	2.9×10^{11}	Nm ²
Head mass	m_p	300,000	kg
Modal damping ratio	ζ_S	1.4	%

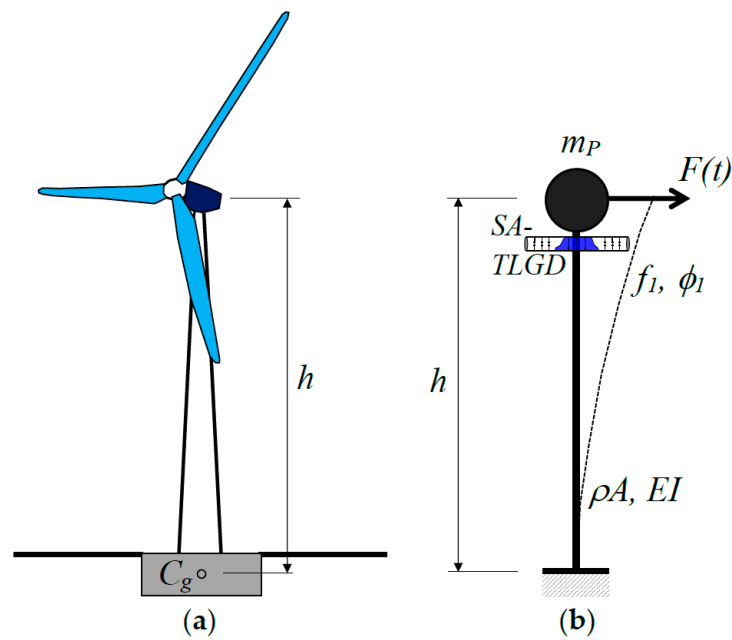


Figure 4. Wind turbine considered in the numerical study: (a) principal drawing of a wind turbine with a flat gravity basement, C_g is the center of gravity; (b) mechanical model of the harmonic force excited wind turbine with a single SA-TLGD attached.

By applying the single-unit Ritz approach for the approximated solution of the dynamic deflection along the height of the considered wind turbine tower,

$$w(x, t) = q(t) \cdot \phi_1(x), \tag{33}$$

with the properly chosen shape function for the relevant fundamental vibration mode (Figure 2b), which fulfills the kinematic boundary conditions,

$$\phi_1(x) = 1 - \cos \frac{\pi x}{2h}, \tag{34}$$

yield the following formulas for the (kinetic equivalent) modal mass and stiffness of the SDOF-main system just from an energy comparison to the equivalent single-mass oscillator [39],

$$m_S = 0.227 \rho A h + m_P, k_S = \frac{\pi^4 EI}{32 h^3}. \tag{35}$$

Subsequently, the fundamental circular natural frequency of the SDOF-main system can be written as follows,

$$\omega_1 = \sqrt{\frac{k_S}{m_S}} = \frac{\pi^2}{h^2} \sqrt{\frac{EI}{32 \cdot (0.227 \rho A + m_P/h)}}. \tag{36}$$

Inserting the assumed wind turbine parameters listed in Table 1 into Equation (36) results in the circular natural frequency of the considered first vibration mode of the wind turbine to $\omega_1 = 3.44$ rad/s ($f_1 = \omega_1/2\pi = 0.55$ Hz). The comparison with the measured fundamental frequencies of existing onshore wind turbines shows a very good agreement [45,46]. While Equation (36) is simple to use, it is noted that it does not consider the flexibility of the foundation and stiffness softening effects due to the axial vertical load arising from the mass m_P . The influence of these in practice relevant effects on the resulting natural frequencies of wind turbines was studied in [45,46].

Optimal tuning of the single SA-TLGD with respect to the relevant fundamental frequency of the force excited SDOF-main system, $f_1 = 0.55$ Hz, is performed by the

application of Den Hartog’s formulas (Section 3.1). The ratio of fluid mass to the modal mass of the SDOF-main system is chosen with $\mu = 1\%$. Inserting this mass ratio into Equation (22) and applying the correction formulas given in Equation (24) to account for the available light structural damping of the main system ($\zeta_S = 1.4\%$) renders the following optimal parameters for the SA-TLGD: $\omega_{A,opt} = 3.39$ rad/s ($f_{A,opt} = \omega_{A,opt}/2\pi = 0.54$ Hz) and $\zeta_{A,opt} = 6.28\%$. To realize the optimal natural frequency $f_{A,opt}$ in the practical application of the considered wind turbine, the dimensions of the SA-TLGD must be chosen appropriately. The optimal damping ratio $\zeta_{A,opt}$ is achieved by properly adjusting the diameter of the controllable orifices in the fluid stream. Table 2 lists both the calculated optimal parameters and the chosen dimensions of the SA-TLGD attached to the SDOF-wind turbine.

Table 2. Parameters and dimensions of the optimized SA-TLGD attached to the SDOF-wind turbine.

Parameter of SA-TLGD	Variable	Value	Unit
Optimal natural frequency	$f_{A,opt}$	0.54	Hz
Optimal damping ratio	$\zeta_{A,opt}$	6.28	%
Mass ratio	$\mu = m_f/m_S$	1.0	%
Fluid mass	m_f	3454	kg
Fluid density	ρ_f	1000	kg/m ³
Fluid volume	V_f	3.454	m ³
Fluid horizontal length	L_f	4.40	m
Polytropic coefficient	n	1.2	-
Initial atmospheric pressure	p_0	10 ⁵	Pa
Tube diameter	d	1.0	m
Tube cross-sectional area	A_T	0.79	m ²
Gas spring length	L_g	4.75	m
Initial gas volume	V_0	3.73	m ³

Assuming the time harmonic horizontal excitation force with $F(t) = F_0 e^{i\nu t}$, where ν is the excitation frequency, inserting the already chosen parameters for the considered wind turbine (Table 1) and for the optimally tuned SA-TLGD (Table 2) into Equation (17), yield the linearized matrix equations of the coupled system with now known mass, stiffness, and damping matrix elements. The steady state solutions for the tower head and fluid mass displacements $w(\nu)$ and $u(\nu)$ are determined in the frequency domain after inserting the exponential functions $w(\nu) = w_0 e^{i\nu t}$ and $u(\nu) = u_0 e^{i\nu t}$ as well as their derivatives into the matrix equation of the coupled system [7].

Figure 5 shows the gained results for the frequency response functions (FRF) of the SDOF-wind turbine with and without activated optimally tuned SA-TLGD. The force amplitude is chosen with $F_0 = 20,000$ N and the equivalent stiffness parameter of the wind turbine tower is defined by $k_S = m_S \omega_S^2 = 4.09$ MN/m, i.e., the static displacement of the tower head is given by $w_{st} = F_0/k_S = 0.0049$ m. It is seen that the activated optimally tuned SA-TLGD reduces the maximum horizontal displacement amplitude of the SDOF-wind turbine over the total frequency range of interest more than 70% (from 0.17 m without any vibration absorber to 0.05 m with activated SA-TLGD). The gained reduction in the maximum dynamic wind turbine head displacement corresponds to an effective structural damping ratio of $\zeta_{S,eff} = 4.9\%$ and this equates to an increase in the light structural damping of the wind turbine ($\zeta_S = 1.4\%$) of more than three times. Figure 6 illustrates the steady state response of the fluid mass displacement amplitude u for the case of the activated SA-TLGD. It is indicated that the maximum fluid mass amplitude results in $u_{max} = 0.37$ m over the total frequency range of interest.

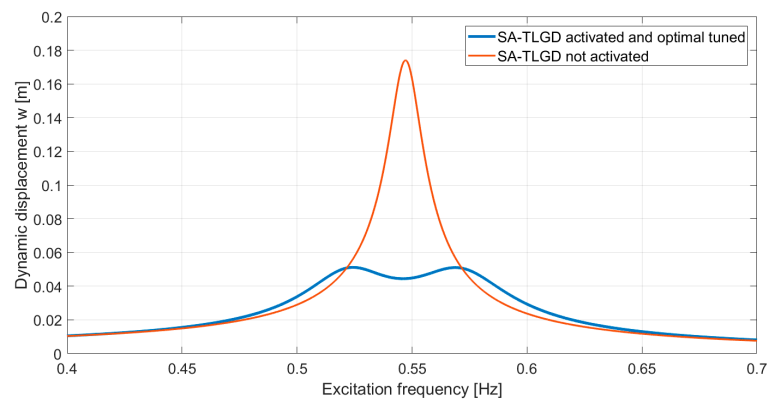


Figure 5. Frequency response functions (FRF) of the SDOF-wind turbine with and without activated optimally tuned SA-TLGD (steady state response of the horizontal tower head displacement w).

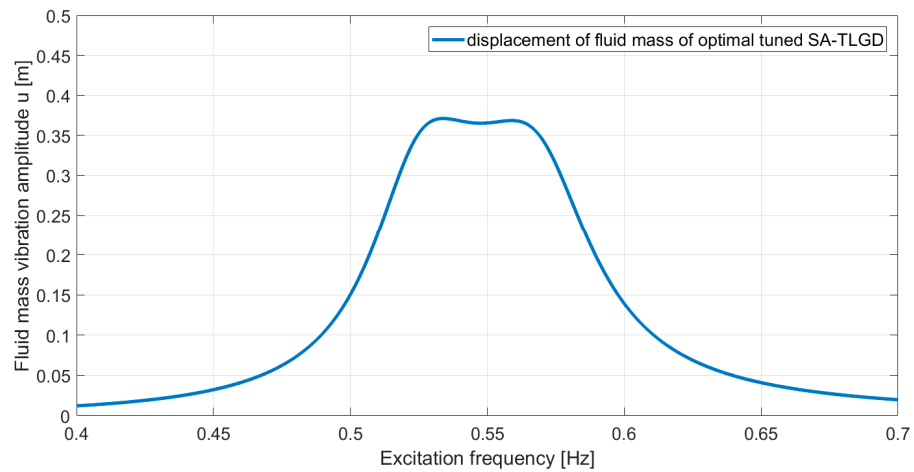


Figure 6. Frequency response function (FRF) of the activated optimally tuned SA-TLGD (steady state response of the fluid mass displacement amplitude u).

In the next step it is assumed that the natural frequency of the wind turbine $f_S = 0.55$ Hz varies $\pm 5\%$, i.e., $f_S^{+5\%} = 0.58$ Hz and $f_S^{-5\%} = 0.52$ Hz, and hence detuning of the SA-TLGD occurs, which obviously influences the achievable damping effect negatively. The assumed magnitude for the frequency shift is quite common in real structures and caused, for instance, by temperature effects and stiffness variations within the operating life of structures. Figure 7 clearly indicates that due to the assumed shifts in the fundamental frequency the maximum head displacement w increases from the minimum value 0.05 m for the optimally tuned SA-TLGD, to around 0.08 m.

To account for the expected frequency shifts that occur in real structures and that lead to a detrimental detuning of the installed vibration absorber, the SA-TLGD is equipped with a total of three gas volumes V_{01} , V_{02} , and V_{03} at each side of the tube (cf. illustration in Figure 1). Beside the optimal eigenfrequency of the SA-TLGD, $f_{A,opt} = 0.54$ Hz listed in Table 2, that corresponds to the unchanged natural frequency $f_S = 0.55$ Hz, the optimal eigenfrequencies that correspond to the shifted natural frequencies yield from Equations (22) and (24) to $f_{A,opt}^{-5\%} = 0.51$ Hz and $f_{A,opt}^{+5\%} = 0.57$ Hz. Subsequently, the required sizes of the gas volumes are calculated, based on the chosen SA-TLGD dimensions listed in Table 2, from Equation (9) to $V_{01} = 3.34$ m³ ($L_{g1} = 4.26$ m), $V_{02} = 0.39$ m³ ($L_{g2} = 0.49$ m), and $V_{03} = 0.35$ m³ ($L_{g3} = 0.45$ m) to achieve the corresponding vibration frequency of the SA-TLGD. It is noted that the separated gas chambers are connected via controllable valves (cf. again Figure 1) and that, for instance, the required gas volume to achieve the lowest eigenfrequency $f_{A,opt}^{-5\%} = 0.51$ Hz relates to the gas volume size of $V_{01} + V_{02} + V_{03} = 4.08$ m³.

In practical applications, the air chamber volumes V_{0i} can be redesigned with a smaller or larger cross-sectional area than A_T , i.e., basically the geometric shape of the air chambers is arbitrary and therefore adjustable to the available installation space of the structure. Obviously, the cross-sectional area of the tube A_T must be kept constant at least up to the maximum dynamic vibration amplitude $u = U_{max}$ of the fluid mass.

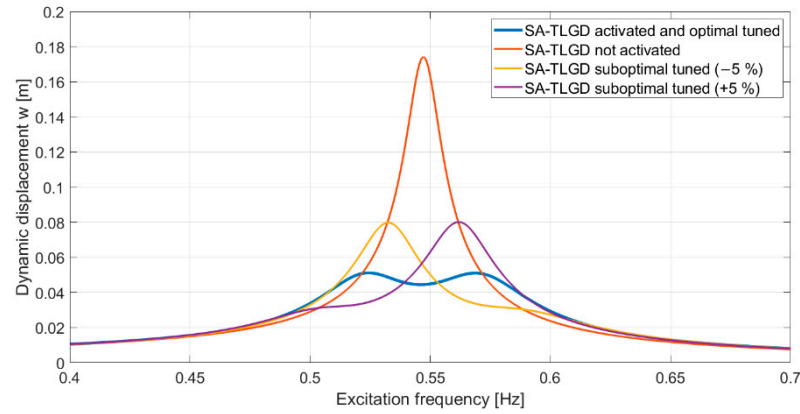


Figure 7. Frequency response functions (FRF) of the SDOF-wind turbine with sub-optimal tuned SA-TLGD (frequency shift of the wind turbine fundamental mode $f_S = 0.55$ Hz to $f_S^{+5\%} = 0.58$ Hz and $f_S^{-5\%} = 0.52$ Hz assumed).

4.2. MDOF-Shear Frame Structure with Multiple SA-TLGDs Attached

The effectiveness of multiple SA-TLGDs in vibration reduction is demonstrated for a plane three-DOF-shear frame structure under horizontal force excitation, e.g., caused by wind gusts. Based on a benchmark definition paper from Spencer et al. [47], a scale model of the original structure was built at the Multidisciplinary Center for Earthquake Engineering Research (MCEER) at Buffalo. In the following numerical study, the considered force excited MDOF-shear frame model with a total mass of 2943 kg and a total height of 2.55 m is equipped with two SA-TLGDs in parallel connection on the 3rd floor (see Figure 8). The optimization procedure of multiple vibration absorbers that are supposed to be tuned to the most critical resonance frequency of the structure, requires fine-tuning in the state space (see Section 3.2). Modal (SDOF) tuning as discussed in Section 3.1 is performed in a first step.

The mass- and stiffness matrix of the scale MDOF-shear frame model are provided in [48],

$$\mathbf{M} = \begin{bmatrix} 981 & 0 & 0 \\ 0 & 981 & 0 \\ 0 & 0 & 981 \end{bmatrix} [\text{kg}], \mathbf{K} = \begin{bmatrix} 650.3 & -183.4 & 33.2 \\ -183.4 & 574.7 & -148.9 \\ 33.2 & -148.9 & 387.2 \end{bmatrix} [\text{N/m}], \quad (37)$$

and the orthonormalized eigenvectors and well-separated undamped natural frequencies are yielded after solving the eigen value problem [39],

$$\vec{\phi}_1 = \begin{bmatrix} 0.2015 \\ 0.5472 \\ 0.8123 \end{bmatrix}, \vec{\phi}_2 = \begin{bmatrix} 0.6782 \\ 0.5204 \\ -0.5189 \end{bmatrix}, \vec{\phi}_3 = \begin{bmatrix} -0.7067 \\ 0.6555 \\ -0.2662 \end{bmatrix}, \quad (38)$$

$$f_{S1} = 2.38 \text{ Hz}, f_{S2} = 7.44 \text{ Hz}, f_{S3} = 12.29 \text{ Hz}.$$

The light modal damping ratios are set to $\zeta_{S1} = 1\%$, $\zeta_{S2} = 2\%$, and $\zeta_{S3} = 3\%$, respectively. Both attached SA-TLGD are tuned with respect to the most critical fundamental natural frequency $f_{S1} = 2.38$ Hz choosing the mass ratio $\mu = 4\%$ with respect to the moving modal mass $M_1 = 1531$ kg of the fundamental vibration mode. Thereby, the modal mass is determined by calculating the kinetic energy of the vibrating MDOF-main system in the first mode and comparing it with the kinetic energy of an equivalent single-mass oscillator [39].

With $\mu = 4\%$, the fluid mass of each attached SA-TLGD results in $m_{f1} = m_{f2} = 30$ kg, i.e., the total fluid mass is $m_{f,total} = 60$ kg.

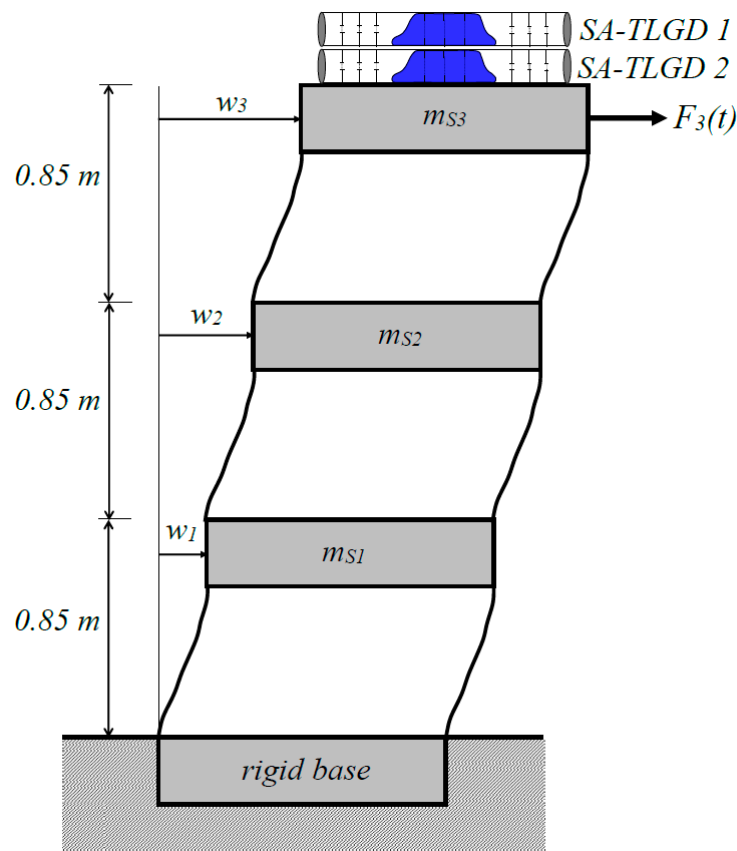


Figure 8. Scaled three-DOF-shear frame structure under horizontal force excitation $F_3(t)$ with two SA-TLGDs in parallel connection attached to the 3rd floor.

In a first step, the optimal absorber eigenfrequencies $f_{A1,opt}$, $f_{A2,opt}$, and optimal linearized viscous damping ratios $\zeta_{A1,opt}$, $\zeta_{A2,opt}$ of the two attached SA-TLGDs are determined by the application of Den Hartog’s formulas. Inserting $\mu = 4\%$ into Equation (22) yields identical optimal design parameters for both SA-TLGDs: $f_{A1,opt} = f_{A2,opt} = 2.29$ Hz, $\zeta_{A1,opt} = \zeta_{A2,opt} = 12.01\%$. Improvements in their performance are achieved by minimizing the frequency domain-based quadratic performance index $J(v)$ in the state space representation (see Section 3.2). The state vector of the MDOF-shear frame structure, $\vec{z}_S = [w_1, w_2, w_3, \dot{w}_1, \dot{w}_2, \dot{w}_3]^T$, to be substituted in Equation (31), does not contain the SA-TLGD quantities explicitly. However, the vibration damping effects of the attached SA-TLGDs are hidden in the system’s dynamics, Equation (29), and thus in the structural response state vector \vec{z}_S . The relevant system’s matrices **A**, **B**, and **R** are defined in Equations (26) and (27) and they contain both, the MDOF-main system’s parameters and the quantities of the two attached SA-TLGDs.

Having chosen the weighing matrix, $S = \text{diag}[10, 10, 10, 1, 1, 1]$ in Equation (32), the numerical minimization of the performance index $J(v)$ is started with Den Hartog’s modal tuning parameters as initial values. Calling the command *fminsearch* within the MATLAB optimization toolbox renders the final improved optimal tuning parameters for the two attached SA-TLGDs, significantly changed to: $f_{A1,opt} = 2.18$ Hz, $f_{A2,opt} = 2.49$ Hz, and $\zeta_{A1,opt} = 6.08\%$, $\zeta_{A2,opt} = 6.72\%$. It is noticed that the eigenfrequencies $f_{A1,opt}$ and $f_{A2,opt}$ are significantly smaller and larger, respectively, than the considered fundamental natural frequency of the MDOF-shear frame structure $f_{S1} = 2.38$ Hz. This gained properties regarding the eigenfrequencies of the two SA-TLGDs to increase the robustness of the

damping absorbers with respect to the expected changes of the fundamental natural frequency during the operating life. Based on the determined optimal tuning parameters the dimensions of the two SA-TLGDs must be chosen with respect to the available space at the 3rd floor of the MDOF-shear frame structure. The optimal damping ratios $\zeta_{Ai,opt}$ are achieved by properly adjusting the diameters of the controllable orifices in the fluid stream. The calculated optimal parameters and chosen dimensions of the installed two SA-TLGDs are listed in Table 3.

Assuming a time harmonic excitation force $F_3(t)$ with the force amplitude $F_{03} = 1000$ N acting on the 3rd floor of the MDOF-shear frame structure with the two optimally tuned SA-TLGDs attached (Figure 8) results in the frequency response function (FRF) for the horizontal floor displacement $w_3(t)$ illustrated in Figure 9. The two installed, activated, and optimally tuned SA-TLGDs reduce the maximum floor displacement from 0.143 m to just 0.017 m around the most critical fundamental mode of the MDOF-shear frame structure, i.e., the percentage of vibration reduction is almost 90%. In the case of the activated SA-TLGDs the FRF of the floor displacement indicates three peaks in the vicinity of the fundamental mode and obviously, these peaks arise due to the determined different optimal tuning parameters for both attached SA-TLGDs. Because the two SA-TLGDs are optimally tuned to the fundamental frequency of the MDOF-shear frame structure $f_{S1} = 2.38$ Hz, the higher modes $f_{S2} = 7.44$ Hz and $f_{S3} = 12.29$ Hz are not affected by the installed vibration absorbers. The modal stiffness parameter of the fundamental mode is defined by $K_1 = M_1 \omega_{S1}^2 = 4.09$ MN/m, i.e., the static displacement of the 3rd floor results in $w_{3,st} = F_{03}/K_1 = 0.0029$ m. Hence, the gained reduction in the maximum floor displacement w_3 corresponds to an effective structural damping ratio of $\zeta_{S1,eff} = 8.6\%$ and this equates to an increase in the assumed light structural damping for the fundamental mode ($\zeta_{S1} = 1\%$) of almost nine times.

Table 3. Parameters and dimensions of the two optimized SA-TLGDs attached to the 3rd floor of the MDOF-shear frame structure.

Parameter of SA-TLGD	Variable	TLGD 1	TLGD 2	Unit
Optimal natural frequency	$f_{Ai,opt}$	2.18	2.49	Hz
Optimal damping ratio	$\zeta_{Ai,opt}$	6.08	6.72	%
Total fluid mass	$m_{f,total}$		60	kg
Total mass ratio	$\mu_{total} = m_{f,total}/M_1$		4.0	%
Mass ratio of each SA-TLGD	$\mu_i = m_{fi}/M_1$		2.0	%
Fluid mass of each SA-TLGD	m_{fi}		30	kg
Fluid density	ρ_f		1000	kg/m ³
Fluid volume	V_f		0.031	m ³
Fluid horizontal length	L_f		0.624	m
Polytropic coefficient	n		1.2	-
Initial atmospheric pressure	p_0		10 ⁵	Pa
Tube diameter	d		0.25	m
Tube cross-sectional area	A_T		0.049	m ²
Gas spring length	L_g	2.05	1.57	m
Initial gas volume	V_0	0.1007	0.0772	m ³

To investigate the detrimental influence of an expected frequency shift of the MDOF-shear frame fundamental frequency $f_{S1} = 2.38$ Hz during the operating life on the vibration damping effectiveness gained through the two optimally tuned SA-TLGDs the following assumptions are made: $f_{S1}^{+5\%} = 2.50$ Hz and $f_{S1}^{-5\%} = 2.26$ Hz. The FRF of the detuned force excited MDOF-shear frame structure with the two sub-optimal tuned SA-TLGDs in parallel connection is illustrated in Figure 10. Note that the FRF of the activated and optimally tuned SA-TLGD is also illustrated in Figure 10. It is seen that due to the assumed frequency shift of the fundamental mode of the MDOF-shear frame structure the maximum floor displacement w_3 increases from the minimum value 0.018 m for the two optimally tuned SA-TLGDs, to around 0.023 m.

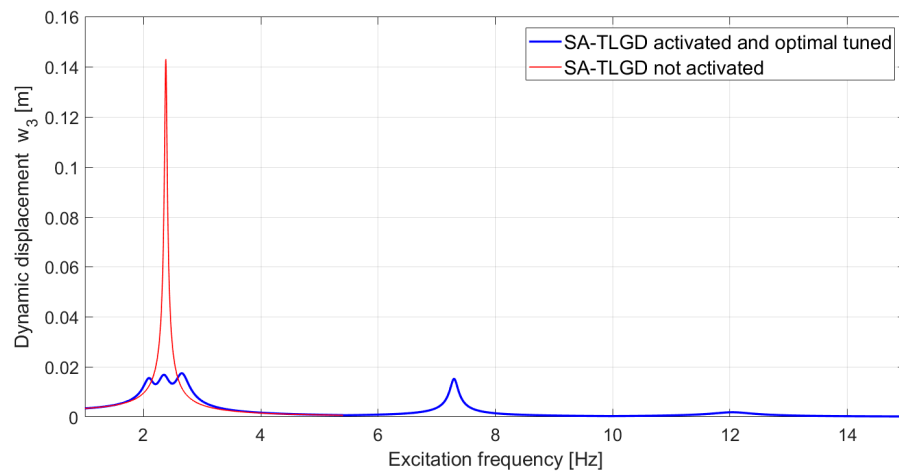


Figure 9. Frequency response functions (FRF) of the force excited MDOF-shear frame structure with and without the two activated optimally tuned SA-TLGDs (steady state response of floor displacement w_3).

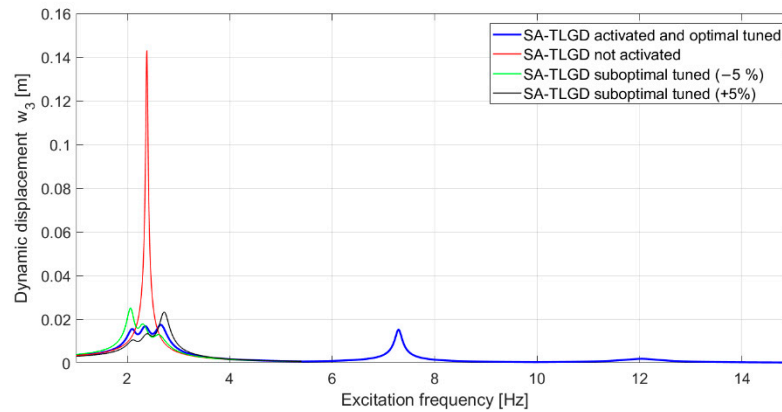


Figure 10. Frequency response functions (FRF) of the force excited MDOF-shear frame structure with two sub-optimal tuned SA-TLGDs in parallel connection (steady state response of floor displacement w_3 ; frequency shift of the fundamental natural frequency $f_{S1} = 2.38$ Hz to $f_{S1}^{+5\%} = 2.50$ Hz and $f_{S1}^{-5\%} = 2.26$ Hz assumed).

To account for the above-mentioned shift of the fundamental frequency of the MDOF-main system, the two SA-TLGDs are equipped with a total of three gas volumes V_{01} , V_{02} , and V_{03} at each side of the tube. The optimal eigenfrequencies of the SA-TLGDs that correspond to the shifted natural frequencies yield again by minimizing the frequency domain based quadratic performance index $J(\nu)$ in the state space representation (see Section 3.2): $f_{A1,opt} = 2.07$ Hz, $f_{A2,opt} = 2.36$ Hz in the case of $f_{S1}^{-5\%} = 2.26$ Hz and $f_{A1,opt} = 2.29$ Hz, $f_{A2,opt} = 2.61$ Hz in the case of $f_{S1}^{+5\%} = 2.50$ Hz. The linearized viscous damping ratios of the two SA-TLGDs remain unchanged. Subsequently, the required sizes of the gas volumes for the two installed SA-TLGDs, based on the chosen absorber dimensions listed in Table 3, from Equation (9) are: $V_{01,A1} = 0.0912$ m³ ($L_{g1,A1} = 1.86$ m), $V_{02,A1} = 0.0095$ m³ ($L_{g2,A1} = 0.19$ m), $V_{03,A1} = 0.0110$ m³ ($L_{g3,A1} = 0.22$ m) for the first installed SA-TLGD and $V_{01,A2} = 0.0702$ m³ ($L_{g1,A2} = 1.43$ m), $V_{02,A2} = 0.0069$ m³ ($L_{g2,A2} = 0.14$ m), $V_{03,A2} = 0.0087$ m³ ($L_{g3,A2} = 0.18$ m) for the second installed SA-TLGD.

The separated gas chambers are connected via controllable valves (cf. again Figure 1). To achieve the optimal absorber tuning frequency the appropriate number of valves must be opened or closed. In practical applications, the air chamber volumes V_{0i} can be redesigned with a smaller or larger cross-sectional area than A_T , i.e., basically the geometric shape of the air chambers is arbitrary and therefore adjustable to the available installation space of

the structure. Obviously, the cross-sectional area of the tube A_T must be kept constant at least up to the maximum dynamic vibration amplitude $u = U_{max}$ of the fluid mass.

5. Conclusions

This paper introduced a novel single tube semi-active tuned liquid gas damper (SA-TLGD) for suppressing horizontal vibrations of tower-like structures. The special feature of the presented SA-TLGD is its lack of any vertical tube sections, which lead to a great advantage regarding the required installation space in slender vibration-prone structures, e.g., wind turbines. The horizontal orientated single tube is partially filled with a fluid and sealed at both ends. A large deformable elastic membrane with neglectable stiffness is used as the interface between fluid and air, and the resulting gas spring provides the restoring force and frequency tuning parameter, respectively.

The equations of motion were derived for both a SDOF-main system with a single SA-TLGD and a MDOF-main system with multiple SA-TLGDs attached. Modal tuning of the single SA-TLGD attached to a SDOF-main system was presented by the application of Den Hartog's formulas considering a harmonic force and seismic excitation. Optimal tuning of multiple SA-TLGDs attached to a MDOF-main system was achieved by minimizing the frequency domain-based quadratic performance index in state space representation.

It was shown that the adjustment of the SA-TLGDs vibration frequency is simply achieved by separating the bulk gas volume V_0 at the left and right tube sections into a series of gas chambers V_{0i} all connected via controllable valves. Depending on the desired optimal vibrating frequency a specific size of gas volume is initiated through the utilized control software, which opens or closes the appropriate number of valves. In addition, the magnitude of the fluid damping is properly adjusted by varying the diameter of several controllable orifices that are built into the fluid stream.

The achievable damping effectiveness of the introduced SA-TLGDs were evaluated considering two different application examples. The first example was a SDOF-wind turbine with a single optimally tuned SA-TLGD attached. In this example, the vibration absorber was optimally tuned to the most critical fundamental mode of the force excited SDOF-main system and a frequency shift of $\pm 5\%$ of the main systems' fundamental frequency was assumed. The mass ratio was chosen with $\mu = 1\%$. It was shown that the achievable reduction in the maximum tower head displacement resulted as almost 70% and that the assumed light structural damping ratio of $\zeta_S = 1.4\%$ could be increased to the effective damping ratio of $\zeta_{S,eff} = 4.9\%$ by the installed optimally tuned SA-TLGD. To avoid detuning due to the assumed frequency shift the SA-TLGD was equipped with a total of three gas volumes V_{01} , V_{02} , and V_{03} at each side of the sealed tube and optimal tuning was achieved by setting the appropriate size of the gas volume via controllable valves.

The second example was a scaled MDOF-shear frame structure with two optimally tuned SA-TLGDs in parallel connection installed on the top floor of the structure. The mass ratio was chosen with $\mu = 4\%$ (includes the total fluid mass of both installed SA-TLGDs). The two vibration absorbers were tuned to the most critical fundamental vibration mode of the MDOF-main system, and it was shown that a vibration reduction in the maximum horizontal 3rd floor displacement of almost 90% could be achieved. The assumed light structural damping ratio of $\zeta_{S1} = 1\%$ of the fundamental mode could be increased to the effective damping ratio $\zeta_{S1,eff} = 8.6\%$ by the installed optimally tuned SA-TLGDs.

It is concluded that the presented SA-TLGDs achieve a high reduction in the maximum force vibration amplitudes of tower-like structures and that its semi-active functionality enables the possibility of re-adjustment any time during the operation of the damper. Hence, SA-TLGDs can best account for the expected frequency shifts that occur in real structures and, thus, provide the favored optimal performance over the total operation life of vibration-prone structures. Furthermore, the lack of any vertical tube sections of the presented SA-TLGD makes it easier to implement the vibration absorber into slender vibration-prone structures and, thus, opens a whole new field of possible applications.

In the next step of the research work we plan to set up a laboratory tests with the SA-TLGD on a small scale using a uniaxial shaking table and to study the achievable effectiveness as well as the practical implementation of the presented vibration absorber.

Author Contributions: Conceptualization, M.R.; introduction, M.R. and J.S.; mechanical model, M.R.; optimization, M.R. and J.S.; numerical studies, M.R.; writing—original draft preparation, M.R.; writing—review and editing, J.S.; visualization, M.R.; supervision, M.R.; project administration, M.R.; funding acquisition, M.R. All authors have read and agreed to the published version of the manuscript.

Funding: This research was funded by the Austrian Research Promotion Agency (Österreichische Forschungsförderungsgesellschaft, FFG) under the grant number 887996.

Institutional Review Board Statement: Not applicable.

Informed Consent Statement: Not applicable.

Data Availability Statement: The data presented in this article is available on request from the corresponding author.

Acknowledgments: The authors appreciate the financial support of this study by the Austrian Research Promotion Agency (FFG).

Conflicts of Interest: The authors declare no conflict of interest. The funders had no role in the design of the study; in the collection, analyses, or interpretation of data; in the writing of the manuscript, or in the decision to publish the results.

Abbreviations

The following abbreviations are used in this manuscript:

FRF	Frequency Response Function
MDOF	Multiple Degrees Of Freedom
MR-TLCD	Magneto-Rheological Tuned Liquid Column Damper
MW	Megawatt
SA-TLGD	Semi-Active Tuned Liquid Gas Damper
SDOF	Single Degree Of Freedom
TMD	Tuned Mass Damper
TLCD	Tuned Liquid Column Damper
TLCGD	Tuned Liquid Column Gas Damper
TLD	Tuned Liquid Damper
TSD	Tuned Sloshing Damper

References

- Den Hartog, J.P. *Mechanische Schwingungen*; Verlag von Julius Springer: Berlin, Germany, 1936. (In German)
- Ormondroyd, J.; Den Hartog, J.P. Theory of the Dynamic Vibration Absorber. *Appl. Mech.* **1928**, *50*, 9–22.
- Brock, J.E. Theory of the Damped Dynamic Vibration Absorber for Inertial Disturbance. *Appl. Mech.* **1949**, *16*, 86–92. [CrossRef]
- McNamara, R.J. Tuned mass dampers for buildings. *Struct. Div.* **1977**, *103*, 1785–1798. [CrossRef]
- Kwok, K.C.S. Damping increase in building with tuned mass damper. *Eng. Mech.* **1984**, *110*, 1645–1649. [CrossRef]
- Soong, T.T.; Dargush, G.F. *Passive Energy Dissipation Systems in Structural Engineering*; John Wiley & Sons: New York, NY, USA, 1997.
- Petersen, C. *Schwingungsdämpfer im Ingenieurbau*; Maurer Söhne GmbH & Co. KG: München, Germany, 2001. (In German)
- Spencer, B.F.; Nagarajaiah, S. State of the art of structural control. *Struct. Eng.* **2003**, *129*, 845–856. [CrossRef]
- Bernuzzi, C.; Crespi, P.; Montuori, R.; Natri, E.; Simoncelli, M.; Stochino, F.; Zucca, M. Resonance of steel wind turbine: Problems and Solutions. *Structures* **2021**, *32*, 65–75. [CrossRef]
- Fujii, K.; Tamura, Y.; Sato, T.; Wakahara, T. Wind induced vibration of tower and practical applications of tuned sloshing damper. *J. Wind Eng. Ind. Aerodyn.* **1988**, *37*, 537–546.
- Fujino, Y.; Pacheco, B.M.; Chaiseri, P.; Sun, L.M. Parametric studies on tuned liquid damper (TLD) using circular containers by free-oscillation experiment. *J. Struct. Eng. Earthqu. Eng.* **1988**, *5*, 381–391.
- Fujino, Y.; Sun, L.; Pacheco, B.M.; Chaiseri, P. Tuned Liquid Damper (TLD) for Suppressing Horizontal Motion of Structures. *Eng. Mech.* **1992**, *118*, 2017–2030. [CrossRef]
- Kareem, A. Reduction of Wind Induced Motion Utilizing a Tuned Sloshing Damper. *J. Wind Eng. Ind. Aerodyn.* **1990**, *36*, 725–737. [CrossRef]

14. Cavalagli, N.; Agresta, A.; Biscarini, C.; Ubertini, F.; Ubertini, S. Enhanced energy dissipation through 3D printed bottom geometry in Tuned Sloshing Dampers. *J. Fluids Struct.* **2021**, *106*. [CrossRef]
15. Pandey, D.K.; Sharma, M.K.; Mishra, S.K. A compliant tuned liquid damper for controlling seismic vibration of short period structures. *Mech. Syst. Signal Process.* **2019**, *132*, 405–428. [CrossRef]
16. Pandey, D.K.; Mishra, S.K.; Chakraborty, S. A tuned liquid mass damper implemented in a deep liquid storage tank for seismic vibration control of short period structures. *Struct. Des. Tall Spec. Build.* **2022**, e1928. [CrossRef]
17. Sakai, F.; Takaeda, S.; Tamaki, T. Tuned liquid column damper—new type device for suppression of building vibrations. In Proceedings of the International Conference on Highrise Buildings, Nanjing, China, 25–27 March 1989; pp. 926–931.
18. Balendra, T.; Wang, C.M.; Cheong, H.F. Effectiveness of tuned liquid column damper for vibration control of towers. *Eng. Struct.* **1995**, *17*, 668–675. [CrossRef]
19. Hitchcock, P.A.; Kwok, K.C.S.; Watkins, R.D.; Samali, B. Characteristics of Liquid Column Vibration Absorbers (LCVA)-I. *Eng. Struct.* **1997**, *19*, 126–134. [CrossRef]
20. Hitchcock, P.A.; Kwok, K.C.S.; Watkins, R.D.; Samali, B. Characteristics of Liquid Column Vibration Absorbers (LCVA)-II. *Eng. Struct.* **1997**, *19*, 135–144. [CrossRef]
21. Reiterer, M.; Ziegler, F. Control of Pedestrian-Induced Vibrations of Long Span Bridges. *Struct. Control Health Monit.* **2006**, *13*, 1003–1027. [CrossRef]
22. Hochrainer, M.J.; Ziegler, F. Control of tall building vibrations by sealed tuned liquid column dampers. *Struct. Control Health Monit.* **2006**, *13*, 980–1002. [CrossRef]
23. Hochrainer, M.J.; Fotiu, P.A. Design of coupled tuned liquid column gas dampers for multi-mode reduction in vibrating structures. *Acta Mech.* **2018**, *229*, 911–928. [CrossRef]
24. Mousavi, S.A.; Bargi, K.; Zahrai, S.M. Optimum geometry of tuned liquid column gas damper for control of offshore jacket platform vibrations under seismic excitation. *Earthq. Eng. Eng. Vib.* **2012**, *11*, 579–592. [CrossRef]
25. Mousavi, S.A.; Bargi, K.; Zahrai, S.M. Optimum parameters of tuned liquid column—gas damper for mitigation of seismic-induced vibrations of offshore jacket platforms. *Struct. Control Health Monit.* **2013**, *20*, 422–444. [CrossRef]
26. Zhao, Z.; Zhang, R.; Jiang, Y.; Pan, C. A tuned liquid inerter system for vibration control. *Mech. Sci.* **2019**, *164*. [CrossRef]
27. Di Matteo, A.; Masnata, C.; Adam, C.; Pirrotta, A. Optimal design of tuned liquid column damper inerter for vibration control. *Mech. Mech. Syst. Signal Proc.* **2022**, *167*, 1–18. [CrossRef]
28. Tamura, Y.; Suganuma, S. Evaluation of amplitude-dependent damping and natural frequency of building during strong winds. *J. Wind. Eng. Ind. Aerodyn.* **1996**, *59*, 115–130. [CrossRef]
29. Caterino, N.; Georgakis, C.T.; Trinchillo, F.; Occhiuzzi, A. *A Semi-Active Control System for Wind Turbines*; Springer International Publishing: Basel, Switzerland, 2014.
30. Karimi, H.R.; Zapateiro, M.; Luo, N. Semiactive vibration control of offshore wind turbine towers with tuned liquid column dampers using H_∞ output feedback control. In Proceedings of the IEEE International Conference on Control Applications, Yokohama, Japan, 8–10 September 2010; pp. 2245–2249.
31. Yalla, S.K.; Kareem, A.; Kantor, J.C. Semi-active tuned liquid column dampers for vibration control of structures. *Eng. Struct.* **2001**, *23*, 1469–1479. [CrossRef]
32. Haroun, M.A.; Pires, J.A.; Won, A.Y.J. Effectiveness of hybrid liquid column dampers for suppressing structural vibrations. In Proceedings of the 13th International Modal Analysis Conference, Nashville, TN, USA, 13–16 February 1995; pp. 525–531.
33. Altay, O.; Klinkel, S. A semi-active tuned liquid column damper for lateral vibration control of high-rise structures: Theory and experimental verification. *Struct. Control Health Monit.* **2018**, *25*, 422–444. [CrossRef]
34. Wang, J.Y.; Ni, Y.Q.; Ko, J.M.; Spencer, B.F. Magneto-rheological tuned liquid column dampers (MR-TLCDs) for vibration mitigation of tall buildings: Modelling and analysis of open-loop control. *Comp. Struct.* **2005**, *83*, 2023–2034. [CrossRef]
35. Sarkar, S.; Chakraborty, A. Optimal design of semiactive MR-TLCD for along-wind vibration control of horizontal axis wind turbine tower. *Struct. Control Health Monit.* **2018**, *25*. [CrossRef]
36. Jolly, M.R.; Bender, J.W.; Carlson, J.D. Properties and applications of commercial magnetorheological fluids. *Intell. Mater. Syst. Struct.* **1999**, *10*, 5–13. [CrossRef]
37. Tamboli, A. Manhattan’s mixed construction skyscrapers with tuned liquid and mass. In Proceedings of the CTBUH 7th World Congress, New York, NY, USA, 16–19 October 2005.
38. Seidel, M. Tragstruktur und Installation der Offshore-Windenergieanlage REpower 5M in 45m Wassertiefe. *Stahlbau* **2007**, *76*, 650–656. (In German) [CrossRef]
39. Ziegler, F. *Mechanics of Solids and Fluids*, 2nd ed.; Springer: New York, NY, USA, 1998.
40. Idelchick, I.E. *Handbook of Hydraulic Resistance, Coefficient of Local Resistance and of Friction*; U.S. Department of Commerce Springfield: Washington, DC, USA, 1960.
41. Clough, R.W.; Penzien, J. *Dynamic of Structures*; McGraw-Hill: New York, NY, USA, 1975.
42. Pocanschi, A.; Phocas, M. *Kräfte in Bewegung: Die Techniken des Erdbebensicheren Bauens*; Vieweg: Berlin, Germany, 2003. (In German)
43. Müller, P.C.; Schiehlen, W.O. *Lineare Schwingungen. Theoretische Behandlung von Mehrfachen Schwingern*; Akademische Verlagsgesellschaft: Wiesbaden, Germany, 1976. (In German)
44. Deutsches Institut für Bautechnik. *Richtlinie für Windenergieanlagen—Einwirkungen und Standsicherheitsnachweise für Turm und Gründung*; Reihe B, Heft 8; DIBT: Berlin, Germany, 2004. (In German)

45. Schaumann, P.; Seidel, M. Eigenschwingverhalten von Windenergieanlagen—Berechnungen und Messungen. In Proceedings of the 10th German Wind Energy Conference (DEWEK), Wilhelmshaven, Germany, 7–8 June 2000.
46. Adhikaria, S.; Bhattacharyab, S. Dynamic analysis of wind turbine towers on flexible foundations. *Shock. Vib.* **2012**, *19*, 37–56. [CrossRef]
47. Spencer, B.F.; Dyke, S.J.; Deoskar, H.S. Benchmark Problems in Structural Control, Part II: Active Tendon System. In Proceedings of the 1997 ASCE Structures Congress, Portland, OR, USA, 16 April 1997.
48. Reiterer, M. Damping of Vibration Prone Engineering Structures with Emphasis on Bridges. Ph.D. Thesis, Vienna University of Technology, Vienna, Austria, 2001. (In German)

Article

Development of Vibration Control Structure on Suspended Ceiling Using Pulley Mechanism

Ryo Majima ¹, Shigeki Sakai ² and Taiki Saito ^{1,*}

¹ Department of Architecture and Civil Engineering, Toyohashi University of Technology, Toyohashi 441-8580, Aichi, Japan; majima.ryo.bk@tut.jp

² Building Research Department of Research Institute, Hazama Ando Corporation, Tsukuba 305-0822, Ibaraki, Japan; sakai.shigeki@ad-hzm.co.jp

* Correspondence: saito.taiki.bv@tut.jp

Abstract: A suspended ceiling system (SCS) is one of the most fragile and non-structural elements during earthquakes. However, effective seismic protection technologies for enhancing the suspended ceiling system have not been developed other than the steel bracing system. An innovative passive vibration control system is proposed in this paper, which equipped a damper-employed pulley amplification mechanism into the indirect suspended ceiling system, named the pulley–damper ceiling system (PDCS). Theoretical formulation and the detailed information on the system were presented first. In addition, a new rotational damper composition consisting of a non-linear viscous damper was developed to follow the large wire-cable stroke. Six types of the full-scale ceiling specimens of a 15.6-square meter area with different configurations were constructed for the preliminary experiments to evaluate the seismic performance and feasibility of PDCS under simulated earthquake motions. The comparative results of the shake table test demonstrated that the application of PDCS is capable of controlling both displacement and acceleration of the ceiling panels. This study also presents the nonlinear time history analyses by modeling a wire-cable as an equivalent truss element to transmit the relative displacement of the ceiling system to the damper. The analytical model accurately simulated the dynamic behavior of PDCS.

Keywords: suspended ceiling systems; passively controlled structure; pulley tackle mechanism; shake table test; simulation analysis

Citation: Majima, R.; Sakai, S.; Saito, T. Development of Vibration Control Structure on Suspended Ceiling Using Pulley Mechanism. *Appl. Sci.* **2022**, *12*, 3069. <https://doi.org/10.3390/app12063069>

Academic Editor: Felix Weber

Received: 1 March 2022

Accepted: 15 March 2022

Published: 17 March 2022

Publisher's Note: MDPI stays neutral with regard to jurisdictional claims in published maps and institutional affiliations.



Copyright: © 2022 by the authors. Licensee MDPI, Basel, Switzerland. This article is an open access article distributed under the terms and conditions of the Creative Commons Attribution (CC BY) license (<https://creativecommons.org/licenses/by/4.0/>).

1. Introduction

The experience of countless earthquake events accelerated the development of seismic protection technologies for main structural frames, such as base isolation structures and vibration control devices. These systems are widely applied in structural design in Japan, especially after the 1995 Kobe earthquake, and their effectiveness in reducing the shaking was verified during the 2011 Great East Japan Earthquake [1]. Meanwhile, only a little attention has been paid to the seismic performance of nonstructural elements and/or secondary structures, including, for example, suspended ceilings, exterior walls, fire extinguishing equipment (fire door and sprinkler), piping installation, and lighting equipment [2,3].

During the consideration of nonstructural elements, a suspended ceiling system (hereinafter referred to as SCS), which is one of the most commonly used in large indoor public spaces, is fragile to the shaking during earthquake events [4]. The vulnerability of SCS in past earthquakes has been extensively documented. For instance, in Japan, the ceiling falls in indoor sports facilities, including a gymnasium in school, shopping mall, and airports terminal, were previously reported in the 2003 Tokachi-Oki earthquake [5] and the 2016 Kumamoto earthquake [6]. Moreover, the damage to the SCS has been reported in various countries, namely, in the 1994 Northridge earthquake in the United States [7], the 2010 Chile earthquake [8], the 2016 Gyeongju earthquake, and the 2017 Pohang earthquake

in Korea [9]. In addition, the failure and collapse of ceiling panels would cause, not only blocking evacuation paths and impending continuous operation of the building, but also human damage. During the 2011 Great East Japan Earthquake, there were more than 75 casualties caused by the collapsing of approximately 2000 SCSs [10,11].

The SCS is composed mainly of hanger elements, carrying ceiling runners, and ceiling panels. Based on the structure of the ceiling runner, the SCS can be classified into two types [12]: the direct-hung suspended ceiling system (direct-SCS) and indirect-hung suspended ceiling system (indirect-SCS). Figure 1 shows the schematic diagram of the SCS. The key difference between them is the connection of the cross runner and hanger elements. In the direct-SCS (Figure 1a), the primary runners are directly suspended from wires attached to the structural system above, and cross joints are applied to the secondary runners to insert between the span of the primary runners. Meanwhile, the indirect-SCS (Figure 1b,c) uses hanger bolts to suspend primary runners from the above floor, and primary runners and secondary runners are connected using clips.

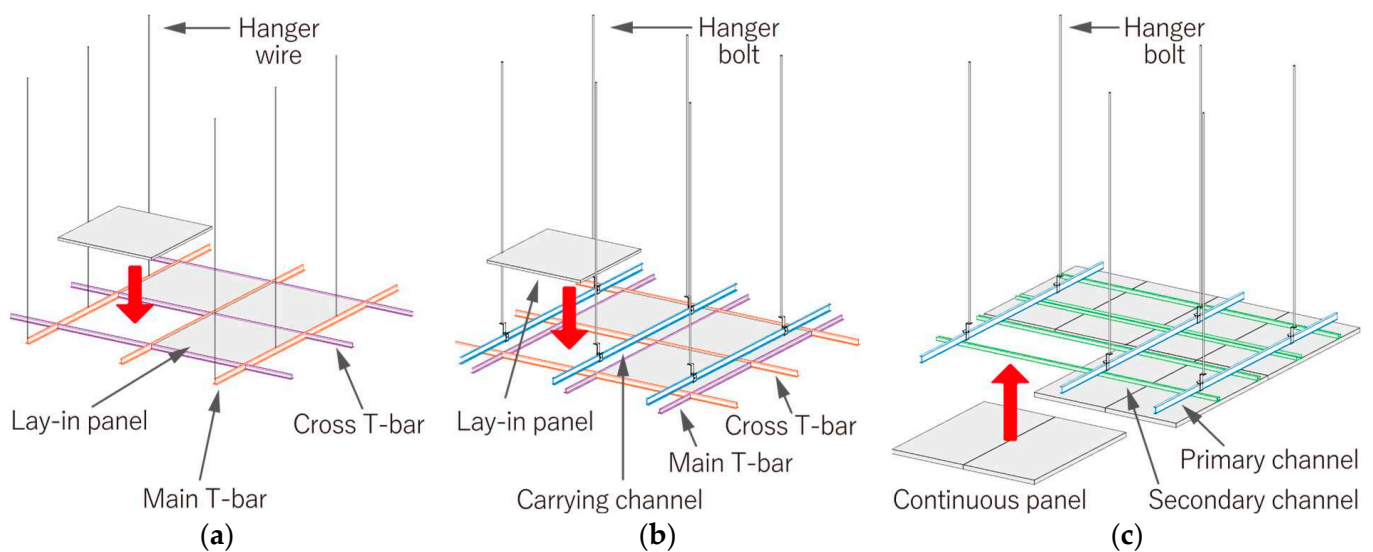


Figure 1. Type of suspended ceiling systems: (a) Direct-hung suspended ceiling system; (b) indirect-hung suspended ceiling system with lay-in panel; (c) indirect-hung suspended ceiling system with continuous panel.

On the one hand, as the direct-SCS is widely used because of its convenience when changing the ceiling panels, relocating the attached air conditioner unit, and the lighting equipment in the practice, most of the previous studies focused on evaluating and understanding the seismic response of the direct-SCS by using a shake table for more than two decades. The main finding from those experiments was about the connection failure of the ceiling grid members due to the collision between ceiling panels and the surrounding structures, including walls. To overcome this issue and improve the seismic performance, several studies were performed on the hanger connection [12,13], the perimeter [14–16], retainer clip [17], and the cross joint [18,19]. In addition to these studies, few researchers proposed and investigated the feasibility of a pendulum-type ceiling system that does not use any rigid elements and is completely separated from the surrounding wall, with an aim to reduce ceiling damage in the earthquake [20,21]. Similarly, Fiorino [22] presented the application of flexible braces (lightweight steel) integrated into the SCS to absorb the input energy.

On the other hand, research on the indirect-SCS is recently becoming active. Based on their response behavior in the earthquake, the indirect-SCS can be divided into two types [23]: a continuous panel ceiling and a lay-in panel type (Figure 1). In the case of the lay-in panel SCS, the seismic performance decreases rapidly, owing to the lack of lateral stiffness when one panel falls, which is due to the unfastening of the ceiling runner.

Therefore, the continuous panel SCS has been certified to perform low fragility because the larger area panels are fixed on the bottom surface of runners and the entire ceiling moves together [24]. The superiority of the continuous ceiling panel was also verified based on the seven types of direct and indirect SCSs using an array of two shaking tables [9].

In August 2013, a new technical bulletin of the suspended ceilings system “Determining a Safe Structural Method for Specific Ceilings and Specific Ceiling Structural Strengths” Notice No. 771 was established by the Ministry of Land, Infrastructure, Transport and Tourism (MLIT). According to this report, when the SCS is installed with more than 200 square meters with the end clearance and the mass per unit area is over 2 kg including the attached equipment, the required number of steel braces should be placed. The effect of damage reduction of the SCS with braces following the technical bulletin has been verified through a full-scale shaking table experiment of a school gym with approximately 550 square meters conducted at the E-Defense earthquake simulator in Japan [25]. However, Lee et al. [12] investigated the arrangement and the location of braces on the entire ceiling system through a shaking table test and indicated the necessity for consideration that the relative displacement occurs between the installed brace part and may cause the panel to fall out. Despite this, the separation distance of the braces for the installation is not explained in detail in the technical bulletin. Moreover, the installation of many braces greatly disturbs the facility design above the ceiling panel and decreases the advantage to adopt it. In addition, a rigid-brace-based ceiling design amplifies the acceleration from the above hanging structure and causes great influence on the interactions between SCS and other nonstructural elements [26–28]. Liangjie et al. [29] investigated the mechanism of the dynamic behavior between ceiling panels and suspended equipment, and revealed that the restriction by friction force between them is very limited and the air conditioner unit would collide even under a Level 1 earthquake. Furthermore, during a full-scale shaking table test of a five-story steel building using the E-Defense shake table, additional concern arose that the use of the bracing system increases the damage of SCS when subjected to the strong vertical excitation over about 1.0 G [30]. The rigid elements constrain the ceiling movement, so the acceleration difference between the fixed ceiling grid and the unfixed part makes the ceiling unstable and drop off.

In this study, an innovative passive control system employing pulley mechanisms into the SCS (hereinafter referred to as the pulley–damper ceiling system: PDCS) is proposed and the feasibility is evaluated through a full-scale shaking table test and simulation analysis. The proposed ceiling vibration control system is aimed to mitigate both the acceleration response and displacement response of the SCS and eliminate the possibilities of a ceiling system collapse even during a Level 2 earthquake. The concept of the pulley–damper system is to amplify the wire movement stretched between the SCS and surrounding structure as well as the force of the viscous damper device connected to the wire. Three types of full-scale ceiling system specimens: conventional-SC, braced-SCS, and damped-SCS, were designed for the shaking table tests.

2. Pulley–Damper Ceiling System

2.1. Mechanism of the System

Figure 2 explains the fundamental concept of PDCS, which consists of pulley tackle mechanisms, one energy-dissipating device (damper), and the SCS. A wire is reciprocally stretched n times with bilateral symmetry between Pulley P_{L1} , P_{R1} (attached on the SCS) and Pulley P_{L2} , P_{R2} (attached on the primary structure). Thus, according to the response displacement “ D ” of the SCS, the amount of damper deformation should be enlarged to $n \times D$ [31,32]. That is, the pulley tackle mechanism is employed in the proposed system to amplify the wire-cable movement and transmit it to significantly increase the energy absorption of the damper installed at the middle of the wire movement path.

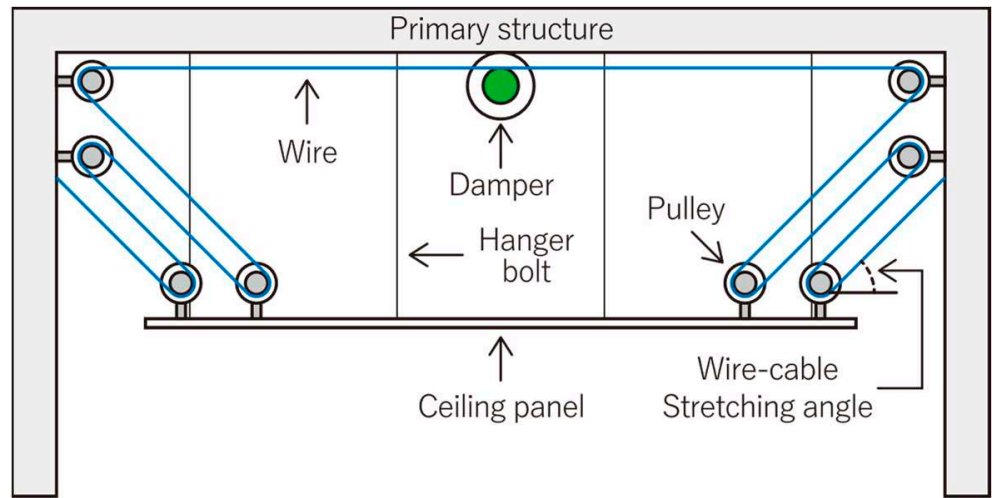


Figure 2. Concept schematic for the proposed pulley–damper ceiling system (PDCS).

2.2. Derivation of the Constitutive Equation

Constitutive equations were established for the proposed pulley–damper system considering wire–cable deformation under the static condition. Hence, the friction force, thermal changes, and the wire mass are not included in the equation. Figure 3 illustrates a schematic diagram for the PDCS. A continuous wire–cable is reciprocated n times between the movable pulley, P_{L1} , and the fixed pulley, P_{L2} , and similarly between the movable pulley, P_{R1} , and the fixed pulley, P_{R2} . When the SCS deformed displacement D in the horizontal direction and force, f_L and f_R act on the wire–cable each side (use plus for tension); the force–deformation relationship of the wire–cable in the diagonal part and horizontal part can be expressed both in the left-hand side of Equation (1) and the right-hand side of Equation (2), as follows:

$$f_L = \frac{K_{L1}}{n} \delta_{L1} \cdots \text{Diagonal part} \tag{1a}$$

$$f_L = K_{L2} \delta_{L2} \cdots \text{Horizontal part} \tag{1b}$$

$$f_R = \frac{K_{R1}}{n} \delta_{R1} \cdots \text{Diagonal part} \tag{2a}$$

$$f_R = K_{R2} \delta_{R2} \cdots \text{Horizontal part} \tag{2b}$$

where L_1 and δ_1 are the wire–cable length and deformation in the diagonal part, respectively; L_2 and δ_2 are the wire–cable length and deformation in the horizontal part, respectively; E is the Young’s module of wire–cable; A is the cross-sectional area of wire–cable; K is the axial stiffness of the wire–cable ($= EA/L$).

In this derivation, the wire–cable is modeled as equivalent truss–elements. Thus, the force–deformation relationship can be converted into the axial force, N , and the deformation, δ , as follows for each side:

$$N_L = n f_L \tag{3a}$$

$$\delta_L = \frac{(\delta_{R1} + \delta_{R2} + x)}{n} = \frac{(\alpha_L f_L + x)}{n} \tag{3b}$$

$$N_R = n f_R \tag{4a}$$

$$\delta_R = \frac{(\delta_{R1} + \delta_{R2} - x)}{n} = \frac{(\alpha_R f_R - x)}{n} \tag{4b}$$

where $\alpha = n/K_1 + 1/K_2$

As the PDCS consists of one continuous wire, if one side gets shorter, the other side must grow longer. Thus, the following relation should hold:

$$(\delta_{L1} + \delta_{L2} + x) + (\delta_{R1} + \delta_{R2} - x) = \alpha_L f_L + \alpha_R f_R = 0 \tag{5}$$

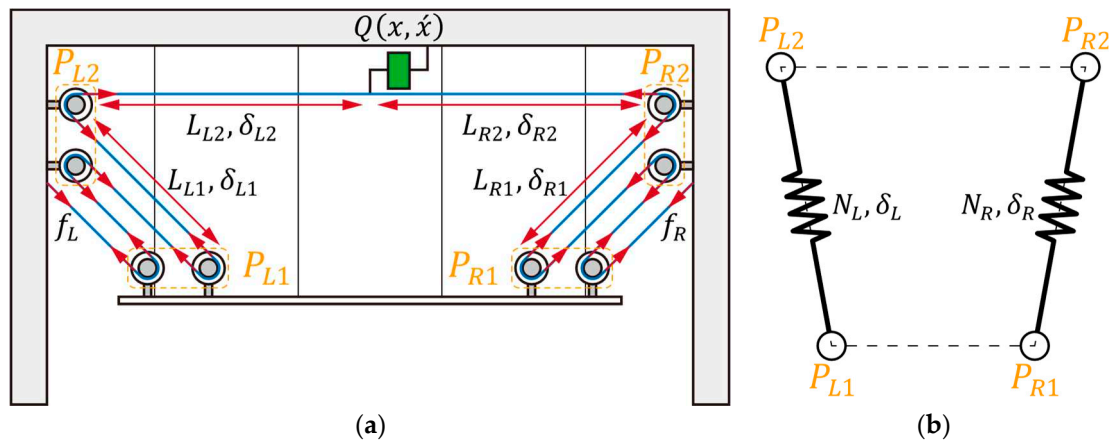


Figure 3. (a) Configuration model; (b) equivalent truss model.

In addition, the damper force can be obtained from the difference in the tensile force of both wire sides. Therefore, by substituting Equation (5) into Equation (6), the damper force and the displacement can be established as Equation (7):

$$Q(x, \dot{x}) = f_L - f_R \tag{6}$$

$$Q(x, \dot{x}) = \Omega(f - f') = \left(\frac{\alpha_L + \alpha_R}{\alpha_R}\right) f_L = -\left(\frac{\alpha_L + \alpha_R}{\alpha_L}\right) f_R \tag{7}$$

Utilizing Equations (3a), (4a), and (7), the axial force of the truss elements can be finally written, as follows:

$$N_L = n\left(\frac{\alpha_R}{\alpha_L + \alpha_R}\right) Q(x, \dot{x}), N_R = n\left(\frac{\alpha_L}{\alpha_L + \alpha_R}\right) Q(x, \dot{x}) \tag{8}$$

The deformation of the damper is given by:

$$x = -n\delta_L + \delta_{L1} + \delta_{L2} = -n\delta_1 + \frac{\alpha_L N_L}{n} \tag{9}$$

Therefore, the simulation analysis can be implemented by the following procedures:

- Step 1: Calculate the damper displacement using truss force and displacement from Equation (9);
- Step 2: Determine the damper force $Q(x, \dot{x})$;
- Step 3: Update the truss axial forces using Equation (8).

3. Component Details of the Pulley–Damper System

3.1. Friction Test of the Pulley Sheaves

A friction test was conducted to evaluate the friction coefficient of pulley sheaves. A stainless wire-cable comprises 7×19 strands with 2.75 kN braking force, and 2.0 mm in nominal diameter was selected. The tensile force of the wire-cable during excitations was monitored through strain gauges placed on either side of a copper plate after the calibration in Figure 4. A triple pulley was used in this study as a deviator of wire-cable to smoothly transmit the ceiling displacement to the damper (Figure 5a). The pulley consists of three sets of a sheave of 30 mm in internal diameter, with a ball bearing inside.

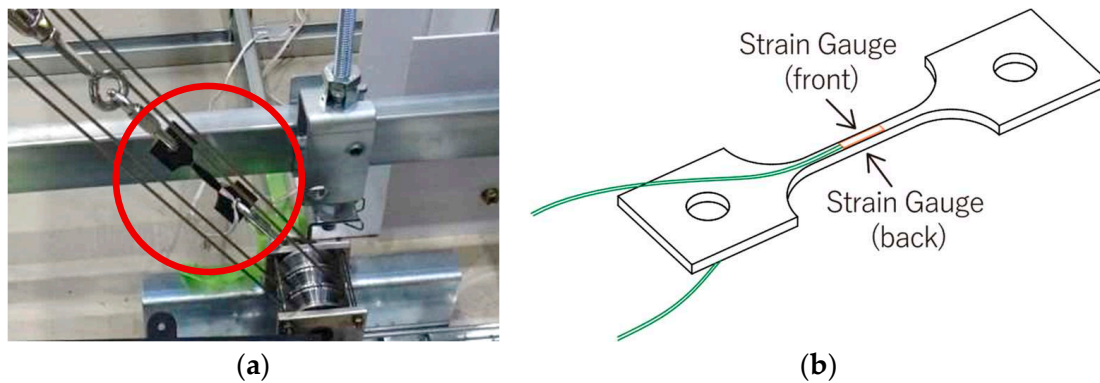


Figure 4. (a) Installation of the tension measuring plate at the end of the wire in the specimen; (b) details of the tension measuring plate.

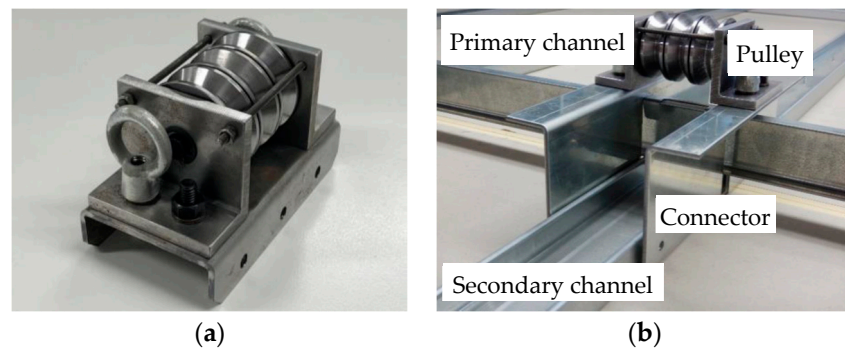


Figure 5. (a) Overview of the pulley; (b) details of the fixture between pulley and ceiling runners.

The purpose of this test is to discover the friction coefficient per sheave to predict friction force in the following shake table test and simulate it in the following simulation analysis. In this study, the friction coefficient μ per sheave was estimated by dividing the mean friction force, F_f , by the number of touched sheaves, N , and pre-tension force, T , as follows:

$$\mu = \frac{F_f}{N \times T} \tag{10}$$

Table 1 summarizes the three test cases for the friction test. The parameter in this friction test is the pre-tension force of the wire-cable and the number of wire-cable loops. Figure 6 shows the specimen view for the friction test. A steel test frame was prepared, and a movable pulley is hung from the top. The generated friction force when the movable pulley went up and down was calculated from the difference of the tensile force between the two strain gauges.

Table 1. Information on the friction test.

Test Case	Number of Loops (Activated Sheaves)	Pre-Tension Force
No.1	2 (5)	30 N
No.2	3 (7)	40 N
No.3	4 (9)	50 N

Figure 7a–c shows the force–displacement loop. The horizontal axis represents the movable pulley displacement, and the vertical axis represents the friction force, which comprises the overall activated sheaves. In all cases, if the number of loops stayed constant, the maximum friction force got larger as the initial tension increased. The friction coefficient was calculated from the displacement range as ± 5 mm, using Equation (10). As Figure 7d shows the relation of the friction coefficient and the pre-tension force on the wire-cable,

the coefficient stays constant and the results of the average friction coefficient in this test were 0.014.

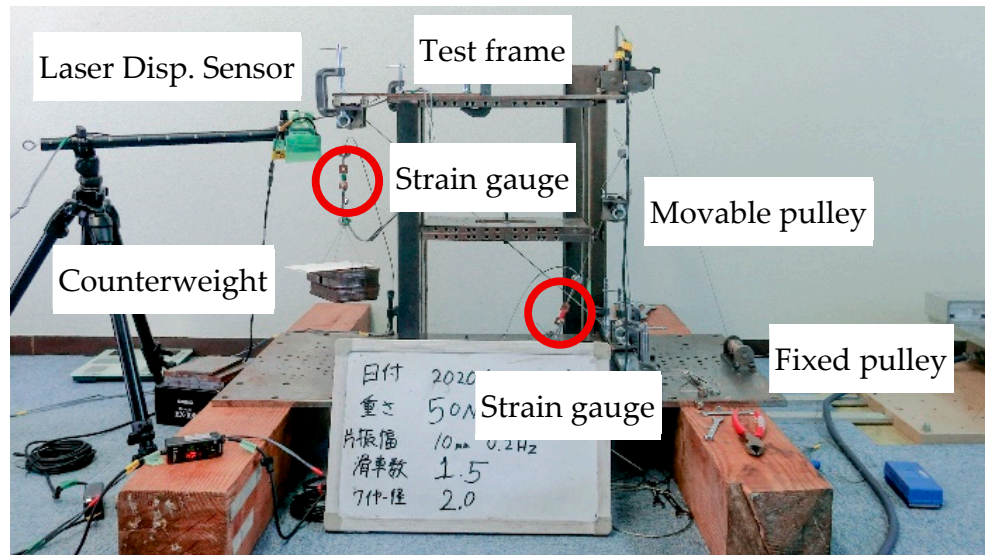


Figure 6. Test setup for characterizing friction behavior under sinusoidal wave excitation.

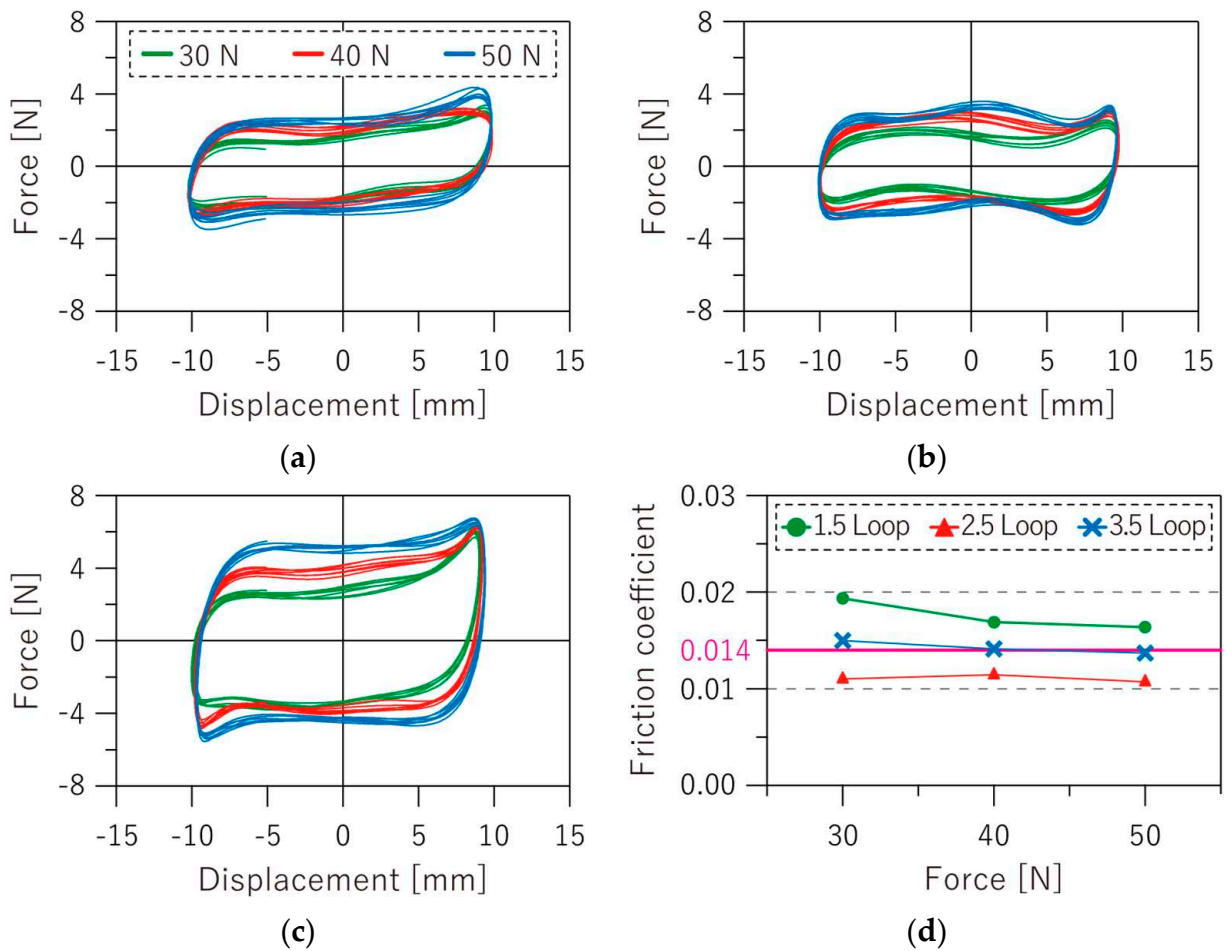


Figure 7. Experimental results of the pulley-friction test: (a–c) Force–displacement relationship under different number of the wire-cable loop and (d) friction coefficient with the average value.

3.2. Dynamic Test of the Viscous Damper

Figure 8 explains an assembly of the rotational non-linear viscous damper using silicon oil, which was specially developed to enhance the potential damping performance of the pulley–damper system. The component consists of two rotary dampers of 60 mNm-rated torque, two ball bearings, and other fixtures. Wire-cable should be wrapped around the spool several times to allow for a large stroke of the amplified wire-cable movement. As the velocity–force relationship can be expressed by Equation (11), and to quantify the velocity dependence, the sinusoidal excitation test and the frequency range between 0.1 Hz and 1.0 Hz were conducted to understand the variable of the equation:

$$F = CV^\alpha \tag{11}$$

where F is the damping force, C is the coefficient of the fluid inside the damper, V is the velocity of the damper, and α is the exponent ($0.0 < \alpha \leq 1.0$).

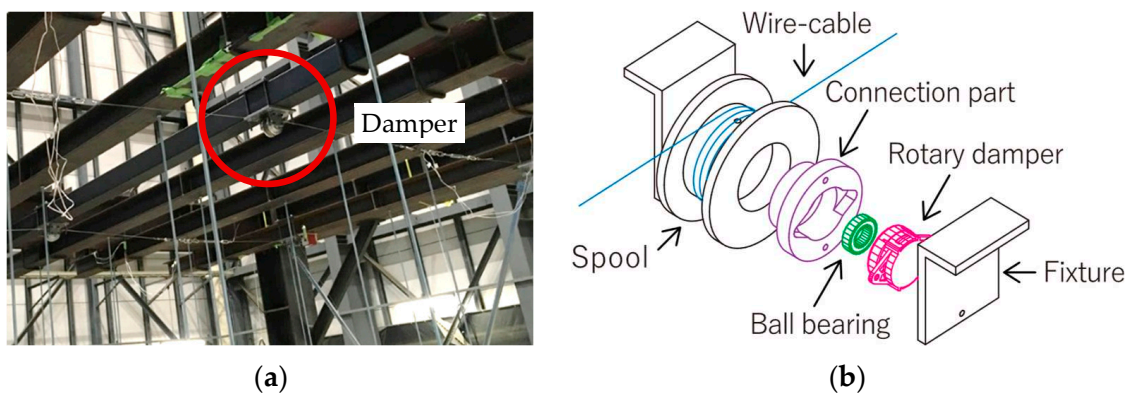


Figure 8. (a) Overview of the damper attached to the supporting beam in the specimen; (b) details of the damper components.

Figure 9 presents the test specimen for the sinusoidal wave excitation of the proposed rotational viscous damper. The damper is connected to actuator by the wire-cable to convert the horizontal movement of actuator to the rotational motion in damper. Besides, the counterweight was set at the other side of wire end to provide initial wire tension to avoid the cable being slack during the excitations.

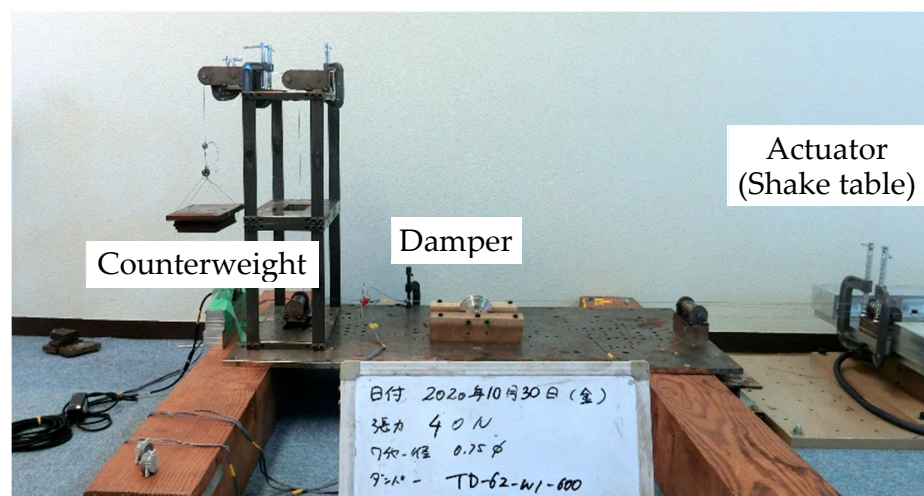


Figure 9. Test setup for characterizing the dynamic behavior of viscous damper under sinusoidal wave excitation.

The hysteresis loop of the force–displacement relationship and force–velocity relationship under the sinusoidal frequency test of the non-linear viscous damper is presented in Figure 10. The damping force gradually grows up as the input frequency increased. While the energy absorption of the viscous damper is relatively limited at approximately 25 N, the velocity power coefficient of $\alpha = 0.9$ and the damping coefficient $C = 0.06 \text{ N}\cdot(\text{s}/\text{mm})\alpha$ was decided based on the SRSS (square root of the sum of squares) of all the test results and modeled in the following simulation analysis.

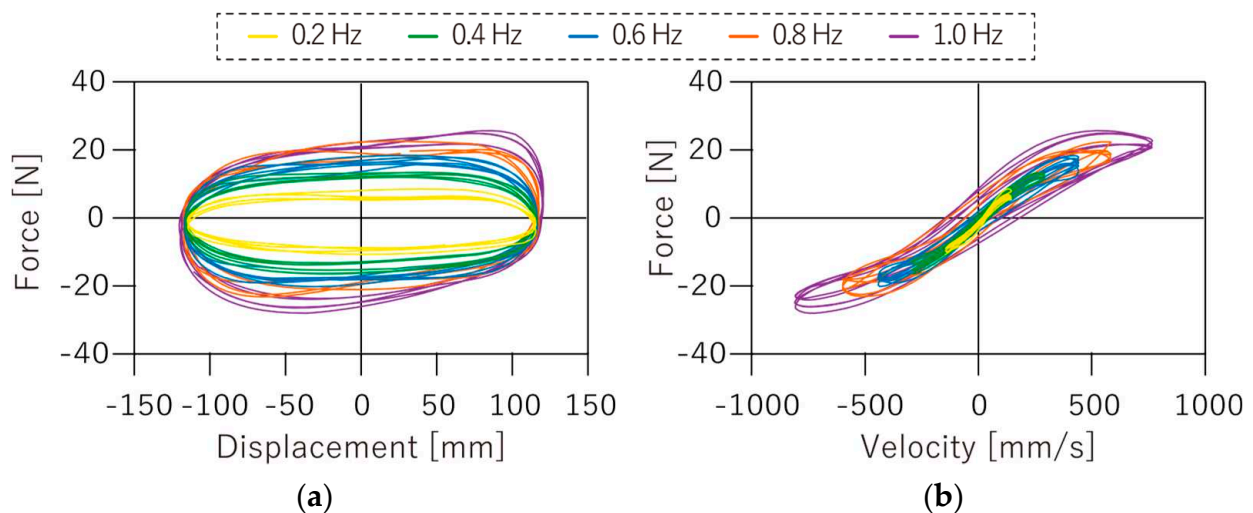


Figure 10. Hysteresis loop of viscous damper measured under sin wave excitation test at different frequencies: (a) Force–displacement loops; (b) force–velocity loops.

4. Full-Scale Shake Table Test

4.1. Shake Table and Test Specimens

The unidirectional dynamic tests were performed using the earthquake simulator at the structural engineering laboratory of the Hazama Ando Technical Research Institute to evaluate and qualify the ceiling vibration control system in January 2020 and 2021. The performance envelopes of the simulator are a ± 300 mm displacement and 3.0 g acceleration at a payload of 35 tf in the horizontal direction.

An overall 5800 mm (length) \times 3500 mm (width) \times 3200 mm (height) rigid steel test frame was properly designed and built to hang the SCS specimens test (Figure 11) At the ceiling level, 1500 mm from the top, steel beams were fixed to the columns on two sides in a Y-direction to provide support for the pulley installation.

The ceiling specimen assemblies consisted of ceiling panels, hanger bolts, carrying channels, and seismic clips. The ceiling system, 4020 mm \times 3200 mm in size, was suspended 1500 mm by the hanger bolt (9 mm diameter) under the beams attached to the structural frame (Figure 12). In the specimens, the primary runners were arranged along the Y-direction with a spacing of 900 or 600 mm. The secondary runners were placed under primary runners along the X-direction with a spacing of 364 mm. The interaction points of the ceiling runner were tightly connected by seismic clips. Then, plasterboard (1820 mm \times 910 mm) was fixed on the bottom surface of secondary runners. Here, in order to avoid the torsion of the entire system, V-braces were placed in the Y-direction for all the test cases.

4.2. Test Cases for the Shaking Table Tests

In this study, four types of indirect-SCSs with continuous panels were designed to understand the dynamic behavior of the proposed system: conventional SCS (Case C), braced SCS (Case CB), wired SCS (Case CW), and damped SCS (Case CWD), which places the proposed damper in Section 3.1. Moreover, to investigate the influence of

the wire stretching angle on seismic performance, two types of system arrangement, the horizontally stretched case (0-degree angle) and diagonally stretched case (60-degree angle), were prepared. The list of specimens is summarized in Table 2. The wire was symmetrically reciprocated 2.5 times between pulleys on the left and right sides, with 50 N of initial tensile force.

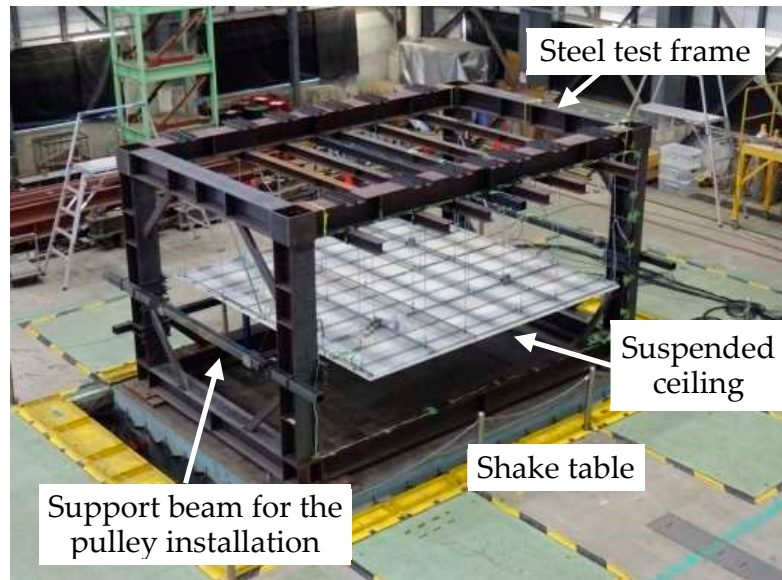


Figure 11. Overall view of the SCS specimen on the shake table.

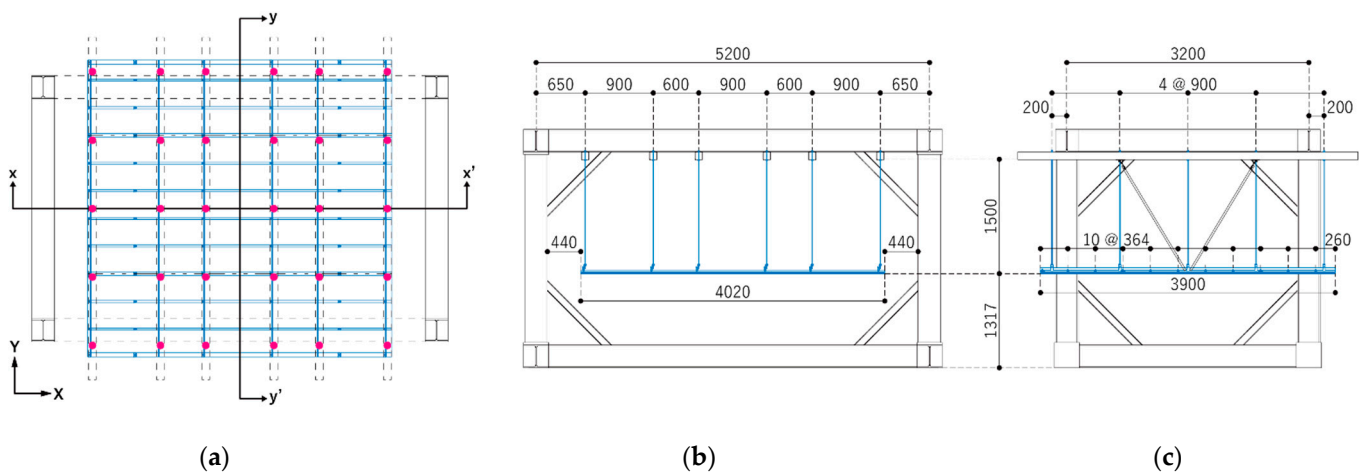


Figure 12. Schematic view of overall specimen: (a) Plan view; (b) cross-section view in X-direction; (c) cross-section view in Y-direction.

4.3. Measurement Plan and Input Excitations

A total of 27 accelerometers, in a triaxial direction and with 9 locations (four of each on the specimen top and ceiling panel, and the shake table surface), and 4 laser displacement sensors (two of each in the X-direction and Y-direction) were used for monitoring the outputs in the tests with 500 Hz sampling frequency. During the excitation with the damper system, one draw-wire displacement sensor, and four tension measuring plates with strain gauges were installed for each pulley–damper system. The location and details of these instruments are shown in Figure 13.

Table 2. Information on the SCS specimen.

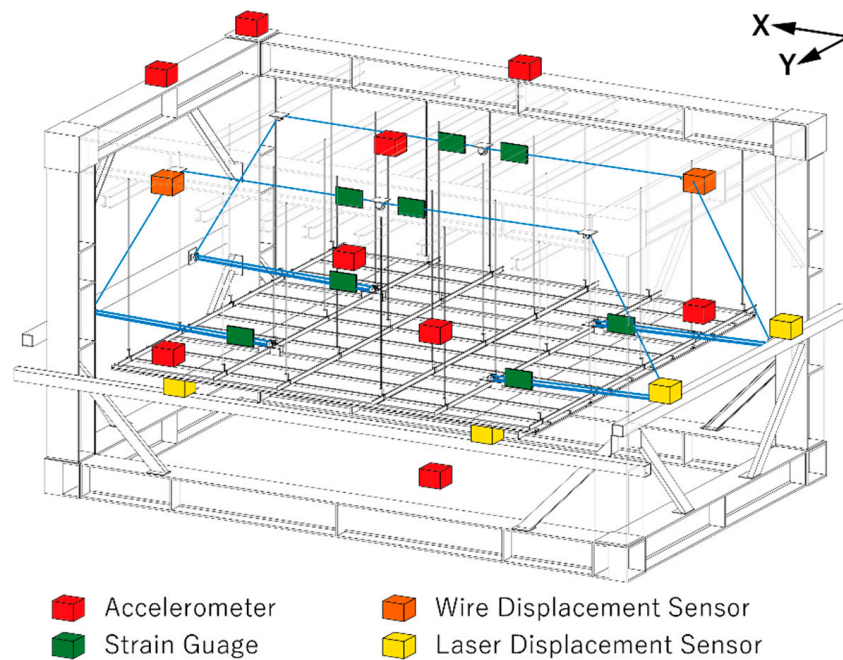
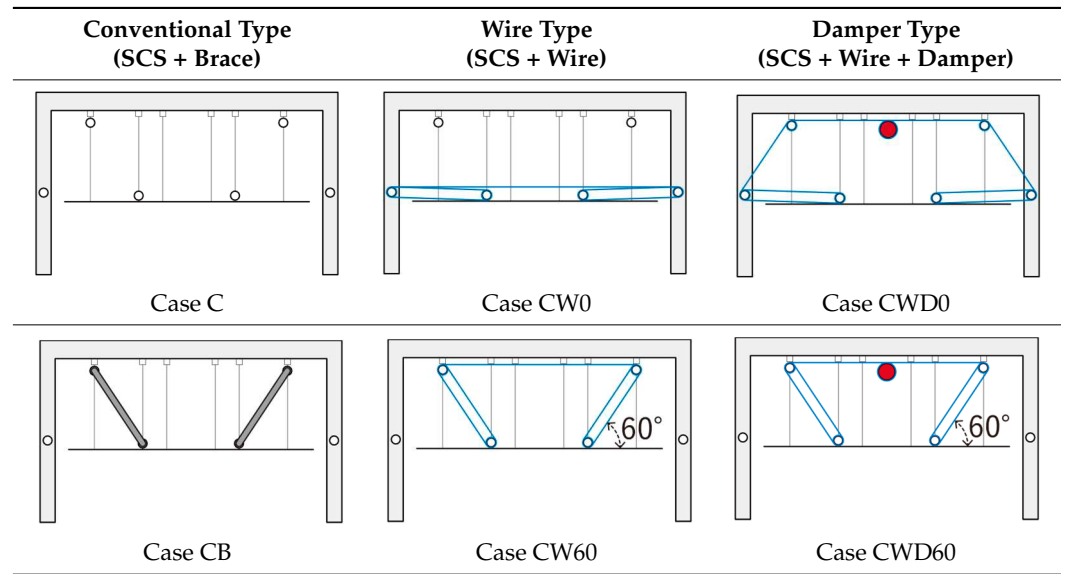


Figure 13. Measurement instrument location for the full-scale suspended ceiling system.

White noise with random phase tests (frequency range: 0.1 Hz to 49 Hz) were conducted for the initial tests to analyze the dynamic properties of the SCS and the test steel frame. Then, earthquake excitation tests using a simulated earthquake ground motion with random phases, based on the design spectrum specified in the Building Standards Law of Japan, were carried out. The amplitude was gradually scaled according to the condition of the specimens. Figures 14 and 15 show the acceleration time histories and spectrum of the input motions given to the shake table.

4.4. Full-Scale Shake Table Test Results

Figure 16 displays the amplitude of acceleration transfer functions from the shake table surface to the ceiling panel surface under random waves for a better understanding of the dynamic response of six specimens and to estimate the natural periods. The first natural periods of Case C and Case CB were 1.37 and 0.14 s, respectively. In other cases,

for example, Case CW and Case CWD, a distinct peak point was not confirmed. That is, the implementation of PDCS into the SCS provides a great effect to suppress vibration and prevent resonance damage to the ceiling.

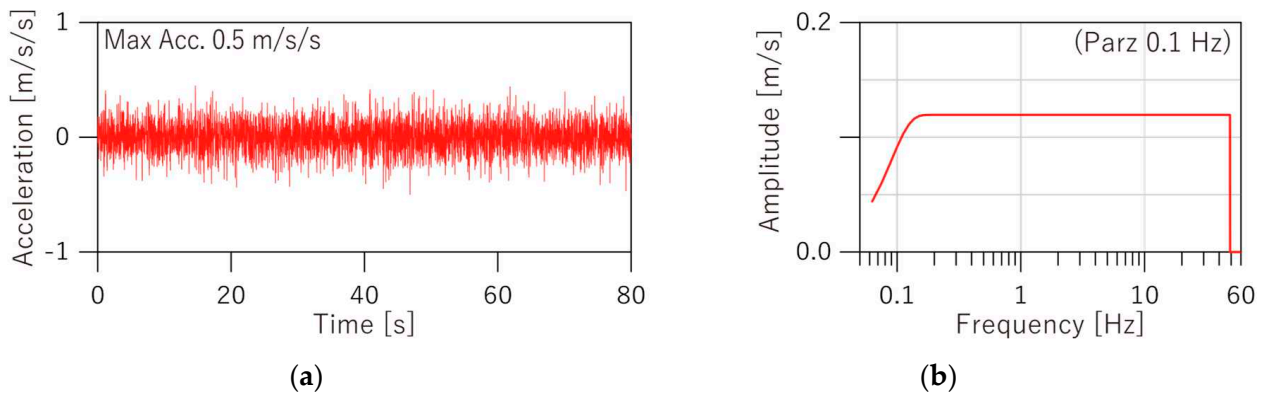


Figure 14. White noise wave used in shake table test: (a) Acceleration time histories; (b) Fourier amplitude spectrum.

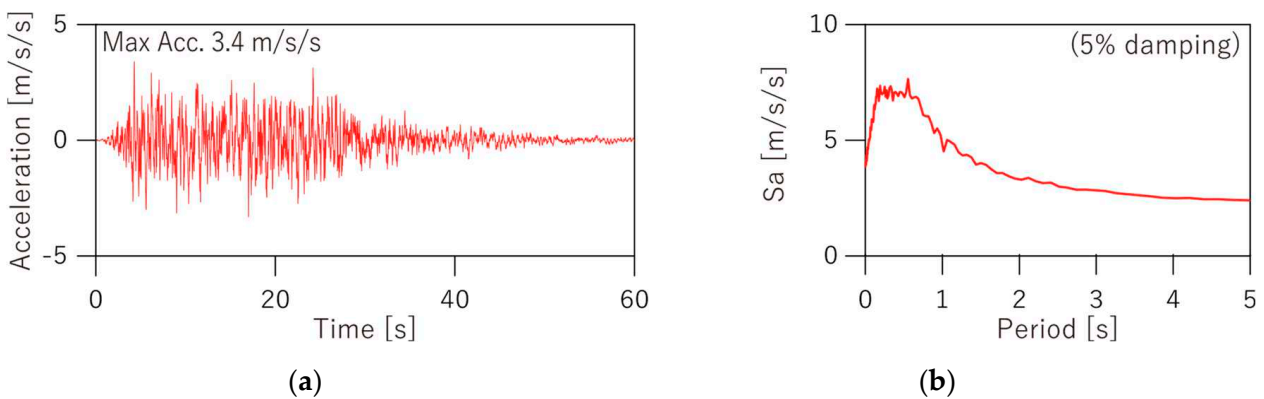


Figure 15. Simulated earthquake wave used in shake table test: (a) Acceleration time histories; (b) spectral acceleration.

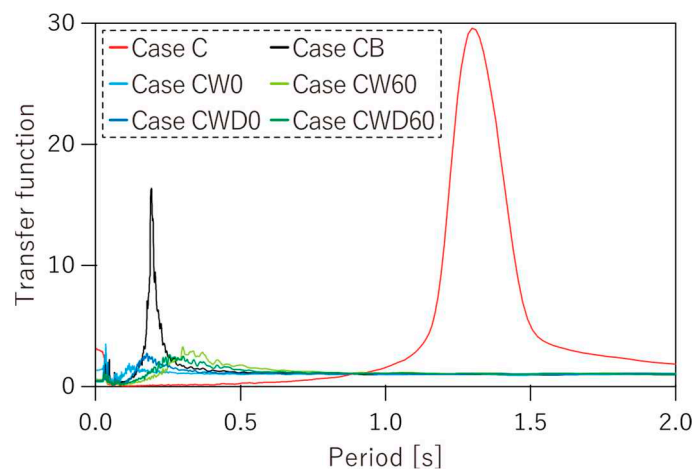


Figure 16. Amplitude of acceleration transfer function under white noise wave.

Figure 17a depicts the relationship between the maximum displacement response of the ceiling panel and the peak ground acceleration (PGA) at the shake table surface for simulated earthquake waves up to PGA 5 m/s/s. Table 3 summarizes the ratio of the maximum displacement response for each test case to Case C under major PGAs.

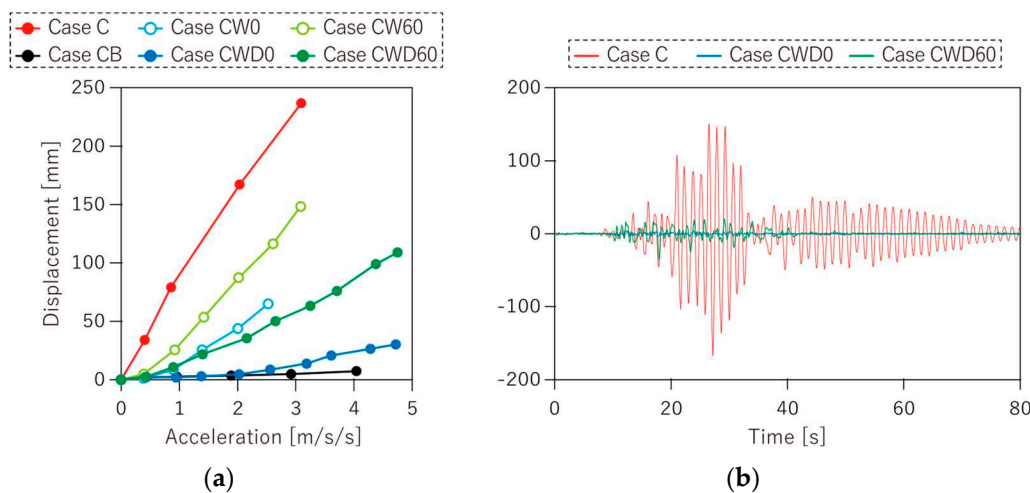


Figure 17. Displacement response of the SCS surface under simulated wave: (a) Maximum displacement for different PGAs; (b) displacement time histories under PGA 2 m/s/s.

Table 3. The response ratio of maximum displacement to the Case C under major PGAs.

PGA	Case CB	Case CW0	Case CW60	Case CWD0	Case CWD60
1 m/s/s	0.03	0.11	0.32	0.02	0.14
2 m/s/s	0.02	0.26	0.52	0.03	0.21
3 m/s/s	0.02	—	0.63	0.06	0.27
Average	0.03	0.18	0.49	0.04	0.21

As shown in Figure 17a and Table 3, Case CB, which was rigidly fixed to the floor above by the steel brace, exhibited the largest response reduction, of an average of 3% for the unreinforced Case C. Similarly, the specimens applying the proposed system, Case CWD0 and Case CWD60, effectively reduced the displacement response to 6% in Case CWD0 and 27% in Case CWD60, respectively, compared to Case C. Case CW0 mitigated the displacement response more than Case CW60, because the horizontal stiffness given by the stretched wire of Case CW0 is larger than that of Case CW60.

Figure 17b compares the displacement time history of the ceiling panel for each case under the simulated earthquake motion at PGA 2 m/s/s. As the displacement time history demonstrates, the displacements in Case CWD0 and CWD60 were much smaller than Case C, between 20 to 40 s, and they suppressed the shaking faster than Case C.

Figure 18a displays the relationship between the maximum acceleration response at the ceiling panel and the peak ground acceleration (PGA) at the shake table surface for simulated earthquake waves up to PGA 5 m/s/s. The ratio of the maximum acceleration response for each test case to Case CB under major PGAs is presented in Table 4.

As shown in Figure 18a and Table 4, the acceleration response of Case CB was amplified twice as compared with Case C; meanwhile, the Case CB provided great displacement reduction effect. Moreover, in the Case CB, the buckling of the hanger bolts after the excitation of the simulated earthquake motion at PGA 6 m/s/s was observed due to the large acceleration response. The accelerations in other cases were reduced to almost 20% of Case CB, and there were no significant differences at the maximum acceleration response between Case CWD0 and Case CWD60.

Figure 19 displays the amplification factor of PDCS under the simulated ground motion at different PGAs. This amplification factor is the ratio of the maximum damper displacement to the maximum ceiling panel displacement. The theoretical amplification factor for Case CW0/CWD0 and Case CW60/CWD60 are 5.0 and 2.5, respectively. While little fluctuation of the factor can be observed, especially in Case CWD0 when PGAs are small, the mean values of the experimental results are close to the theoretical values.

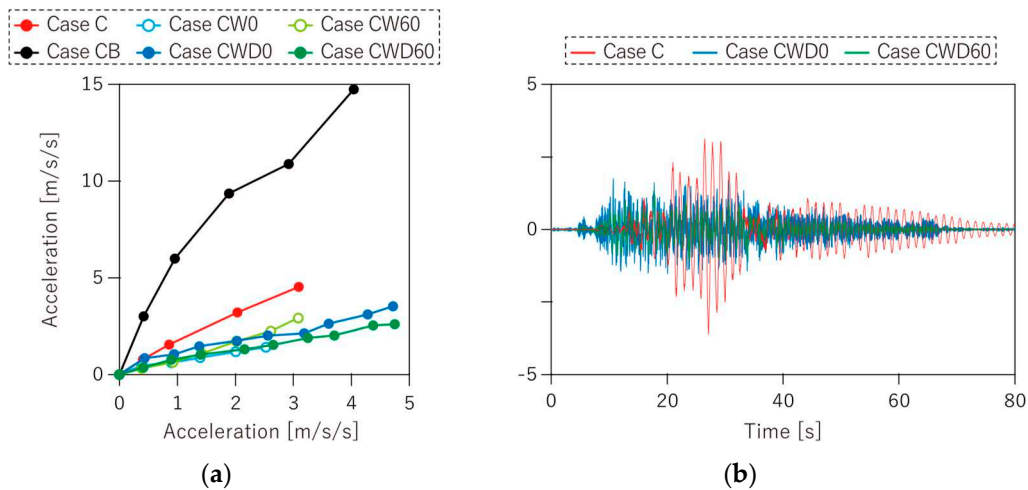


Figure 18. Acceleration response of the SCS surface under simulated wave: (a) Maximum acceleration for different PGAs; (b) acceleration time histories under PGA 2 m/s/s.

Table 4. The response ratio of maximum acceleration to the Case CB under major PGAs.

PGA	Case C	Case CW0	Case CW60	Case CWD0	Case CWD60
1 m/s/s	0.29	0.1	0.11	0.17	0.13
2 m/s/s	0.39	0.13	0.18	0.19	0.14
3 m/s/s	0.46	—	0.27	0.2	0.17
Average	0.38	0.11	0.19	0.19	0.15

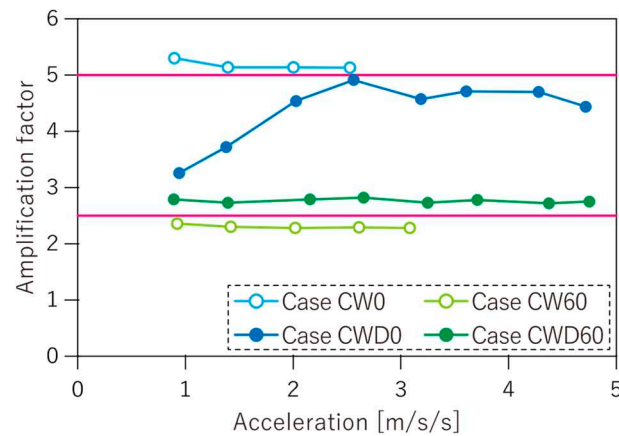


Figure 19. Amplification factor for different PGAs.

5. Simulation Analysis

5.1. Simulation Model

With the aim of observing the verification of the structural modeling using equivalent truss elements for the wire-cable, a simulation analysis was carried out and the modeling results were compared with the experimental results. The 3D-frame simulation model of the experimental test specimen was constructed by using the SStructural Earthquake Response Analysis 3D (STERA 3D Version 10.8) software, which is a finite element-based program developed by one of the authors considering the material and geometric nonlinearities [33]. In the model, as illustrated in Figure 20, the steel beam element is presented by a line element and two nonlinear flexural springs at both ends. The steel column element is presented by a line element with nonlinear vertical springs in both end sections to consider nonlinear axial-moment interaction.

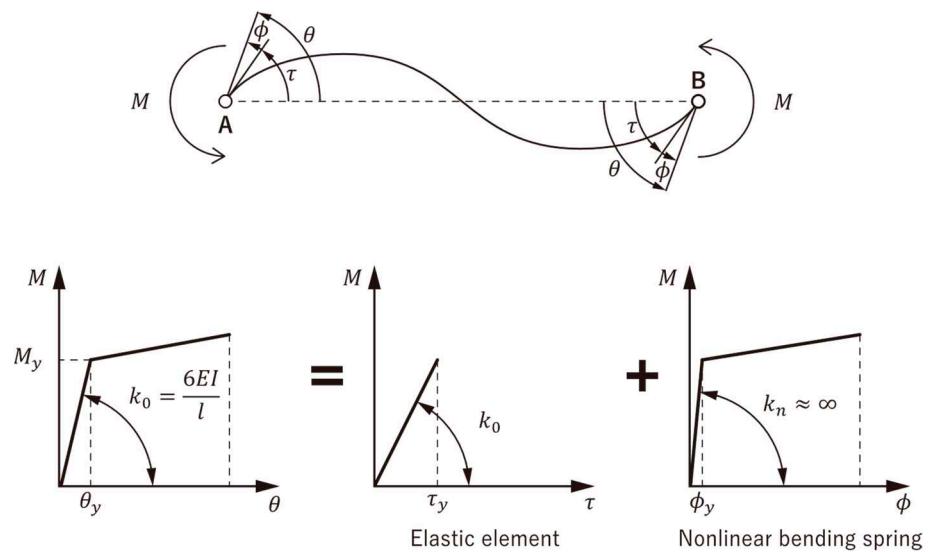


Figure 20. Moment-rotation relationship for bending spring.

Figure 21 shows the simulation model in the STERA 3D. The ceiling panel is suspended 1500 mm from the supporting beams, and the model was analyzed applying the fixed-ended connection to all the joints. In addition, recorded acceleration data at the shake table surface during the excitation were used as the input seismic motions.

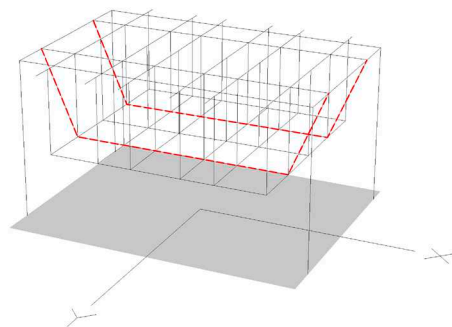


Figure 21. Analytical model in the STERA 3D.

Figure 22 shows the mechanical model of the bilinear and non-linear viscous damper. The friction force, F_f , generated on pulley-wire contacts, was modeled as one bilinear model, and the yield strength, F_{fy} , was estimated by multiplying the number of pulleys and the friction coefficient, using Equation (10). The initial and second stiffnesses of the bilinear hysteresis are K_0 and K_1 , respectively. The hysteresis behavior of the fluid viscous damper is modeled based on the element test results in Figure 10. The damping force F_d is quantified in proportion to an exponential α of the velocity \dot{d} (Equation (11)).

The technical parameters for the one set of the pulley-damper system in the simulation model are summarized in Table 5. The damping factor in the SCS was predicted using a free-vibration range during shake table excitation, and 1.5% was selected for the inherent damping of the SCS by the logarithmic attenuation method.

5.2. Simulation Results

In Figure 23, the experimental results of maximum response values and time history data in displacement and acceleration at the SCS panel are compared with the analytical results for all the experimental cases under simulated earthquake waves. During the comparison of the maximum response value, while the experimental results are relatively larger than the analytical results, the experimental and numerical models' responses are in good agreement.

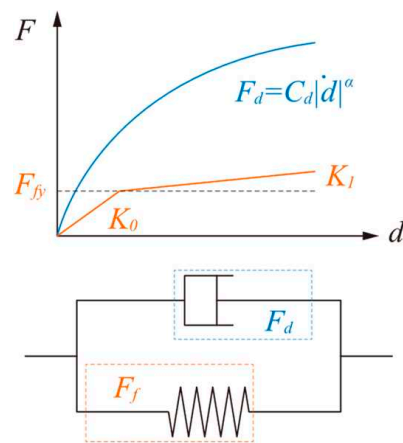


Figure 22. Restoring force characteristics of damper in the simulation model.

Table 5. Damper parameter in the analytical model.

Damper Type	Parameter	
Bilinear model	Initial stiffness K_0 [N/mm]	110
	Stiffness ratio K_1 / K_0	0.0001
	Yield force F_{fy} [N]	6
Nonlinear viscous dashpot model	Damping coefficient C_d [N·(s/mm) ^α] *	0.06
	Velocity exponent α	0.9

* the unit of the damping coefficient C_d changes with velocity exponent α (i.e., when $\alpha = 1$ is N·s/mm, and when $\alpha = 0.9$ is N·(s/mm)^{0.9}).

It is considered that the repeated earthquake excitation to the specimen decreased the pre-tension force of the stay cable, and the joint rigidness caused the differences between the experimental and analytical results. The shake table test of Case CW60 was carried out after the Case CW0 in 2020. Therefore, due to the cumulative of the previous test case damage, the error in Case CW60 was made to become larger than Case CW0.

The coefficient of determination, R^2 , is selected to quantitatively measure the accuracy of the simulation model in this study, and it is defined as Equation (12). In addition, Table 6 shows the R^2 for the validation of each simulation model. The R^2 value for all cases of the maximum acceleration and displacement response are 0.83 and 0.91, respectively. In particular, the minimum R^2 value was 0.69 in the Case CW60. Besides, the simulation model accurately reproduced the time histories responses of the accelerations and displacements, including the frequency and the location of the wave crest.

$$R^2 = 1 - \frac{\sum_{i=1}^n (Exp_i - Ana_i)^2}{\sum_{i=1}^n (Exp_i - \overline{Exp})^2} \tag{12}$$

where Exp_i is the output by the shake table test, Ana_i is the output by the simulation analysis, and \overline{Exp} is the mean of Exp_i .

The results of the force–velocity relationship of the damper device in the shake table tests and simulation analyses are contrasted in Figure 24. The gaps in the hysteresis loop shape were confirmed; however, the error between the experimental and analytical results of the time histories are reproduced well. Thereby, the effect of displacement amplification was successfully simulated in the analytical model.

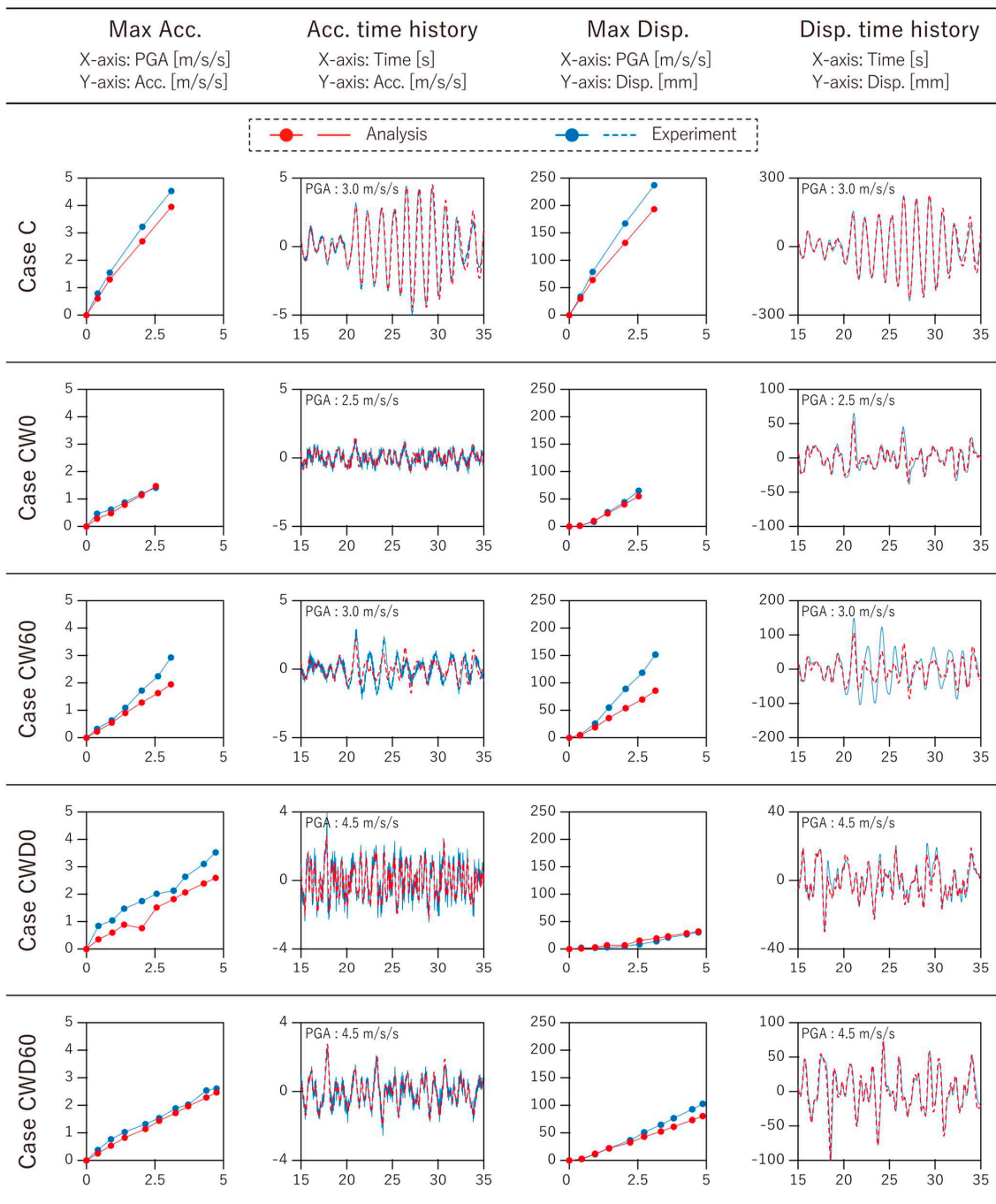


Figure 23. Results comparison of the SCS response between shake table test and simulation analysis.

Table 6. Coefficient of correlation for the validation of simulation model.

Case Name	Acceleration Response	Displacement Response
Case C	0.86	0.93
Case CW0	0.98	0.97
Case CW60	0.69	0.79
Case CWD0	0.70	0.99
Case CWD60	0.94	0.82
All cases	0.83	0.91

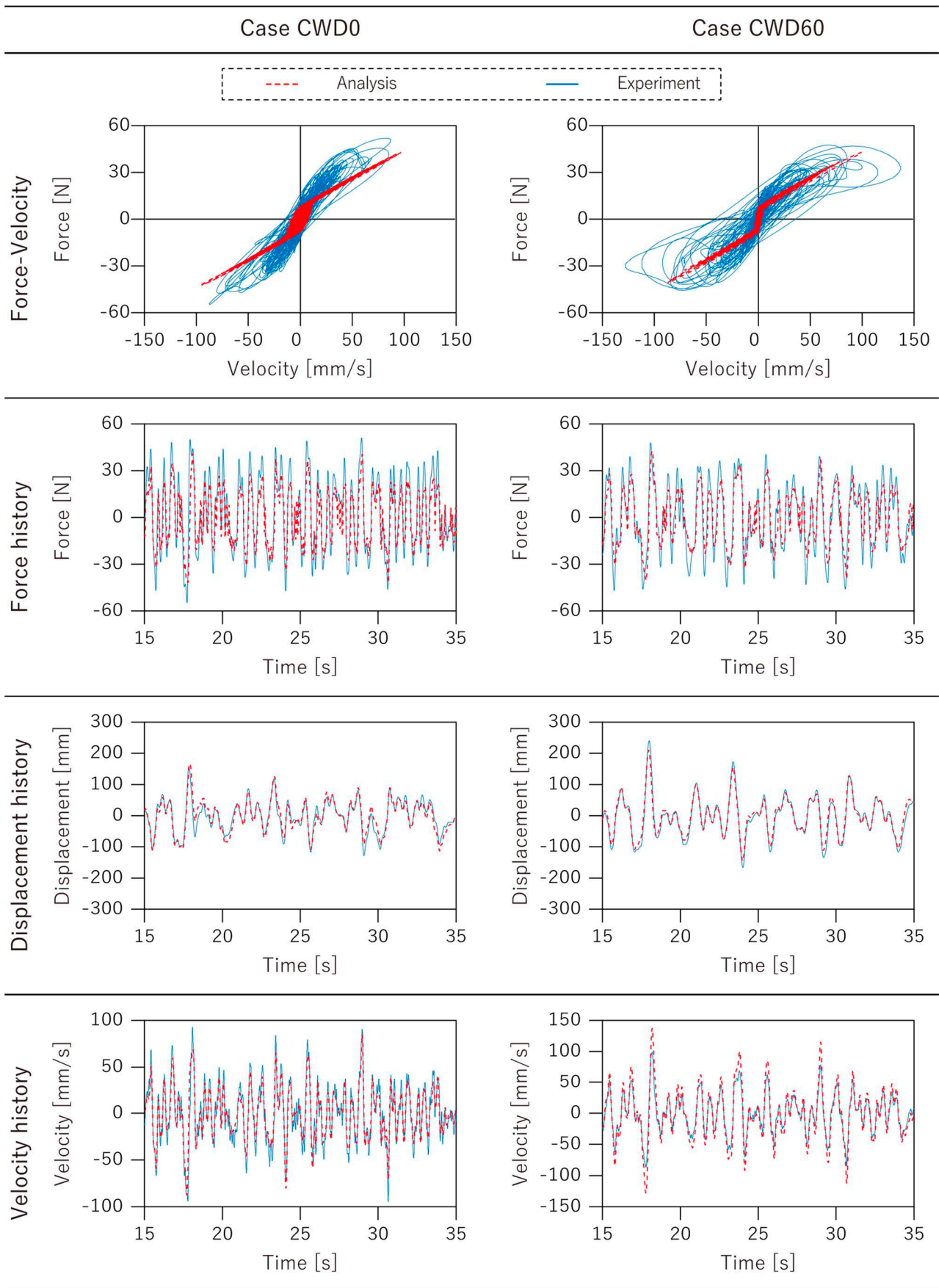


Figure 24. Results comparison of the damper response between shake table test and simulation analysis.

6. Conclusions

This paper proposed an innovative passive vibration control structure for an indirect suspended ceiling system using pulley tackle mechanisms, named the pulley–damper ceiling system (PDCS), and provided detailed information on the system configuration. A preliminary experimental investigation of the dynamic characteristics of the proposed system was conducted. A main goal was to understand the behavior of the entire system under seismic motion and evaluate the feasibility. The results obtained in this study are summarized below:

- The fundamental concept to integrate passive damper system-employed pulley tackle mechanisms into a SCS was presented, which amplifies the SCS displacement in proportion to the number of stretched wire and its installing angle, and transmits to the damper. Moreover, theoretical formulation, considering the amplification mechanism and the elasticity of the wire-cable by modeling as equivalent truss elements, was established.
- Shake table tests using a full-scale SCS specimen of 4020 mm × 3200 mm in area were demonstrated using simulated earthquake ground motion to evaluate the vibration reduction effect of the PDCS. Conventional SCS (Case C), reinforced SCS with the steel brace (Case CB), and damped SCS using PDCS (Case CWD) were constructed. In addition, in the case of Case CWD, two configurations were prepared to investigate the influence of the system installing angle (horizontal: Case CWD0 and diagonal: Case CWD60) to the response reduction effect. The average response ratio of the maximum displacement in Case CWD0 and Case CWD60 to Case C were 0.04 and 0.21, respectively. Additionally, the average response ratio of the maximum displacement in Case CWD0 and Case CWD60 to Case CB were 0.19 and 0.15, respectively. It was confirmed that both acceleration and displacement could be controlled with high efficiency compared to the unbraced SCS and braced SCS.
- A non-linear rotational damper comprises of two fluid viscous dampers, and the cable bobbin was developed for the proposed system to follow up the large wire stroke. The damper successfully worked during shake table excitations and the theoretical amplification effect was observed.
- The analytical model of the full SCS specimens and formulation of the constitute equation in the DPDS were verified by comparing the experimental and analytical results. The friction force on the pulley was equivalently converted as a bilinear hysteresis model. The analytical model accurately simulated the experimental time history responses of both displacements with 0.83 R^2 and acceleration with 0.91 R^2 , including the dynamic behavior of the damper.

Author Contributions: Conceptualization, T.S.; methodology, S.S.; software, T.S.; validation, R.M. and S.S.; formal analysis, R.M.; investigation, R.M.; data curation, R.M.; writing—original draft preparation, R.M.; writing—review and editing, T.S.; visualization, R.M.; supervision, T.S.; project administration, S.S.; funding acquisition, T.S. All authors have read and agreed to the published version of the manuscript.

Funding: This research received no external funding.

Institutional Review Board Statement: Not applicable.

Informed Consent Statement: Not applicable.

Data Availability Statement: The data presented in this study are available on request from the corresponding author.

Acknowledgments: The authors gratefully thank the practice committee of the development of the ceiling vibration control system: M. Uchikawa (Sato Kogyo Co., Ltd.), E. Nishimura (Toda Corp.), Y. Yamasaki (Nishimatsu Construction Co., Ltd.), H. Ryujin (Maeda Co., Ltd.), and R. Doi (Kumagai Gumi Co., Ltd.).

Conflicts of Interest: The authors declare no conflict of interest.

References

1. Kasai, K.; Mita, A.; Kitamura, H.; Matsuda, K.; Morgan, T.A.; Taylor, A.W. Performance of Seismic Protection Technologies during the 2011 Tohoku-Oki Earthquake. *Earthq. Spectra* **2013**, *29*, 265–293. [CrossRef]
2. Villaverde, R. Seismic Design of Secondary Structures: State of the Art. *J. Struct. Eng.* **1997**, *123*, 1011–1019. [CrossRef]
3. Soroushian, S.; Zaghi, A.E.; Maragakis, M.; Echevarria, A.; Tian, Y.; Filiatrault, A. Analytical Seismic Fragility Analyses of Fire Sprinkler Piping Systems with Threaded Joints. *Earthq. Spectra* **2015**, *31*, 1125–1155. [CrossRef]
4. Xu, Z.; Zhang, H.; Wei, W.; Yang, Z. Virtual Scene Construction for Seismic Damage of Building Ceilings and Furniture. *Appl. Sci.* **2019**, *9*, 3465. [CrossRef]
5. Building Research Institute National Research and Development Agency, Japan. *Report on the Field Survey of Damage to Ceilings in Airport Terminal Buildings during the 2003 Tokachi-Oki Earthquake*; Building Research Institute National Research and Development Agency: Ibaraki, Japan, 2003. (In Japanese)
6. Building Research Institute National Research and Development Agency, Japan. *Quick Report of the Field Survey and the Building Damage by the 2016 Kumamoto Earthquake*; Building Research Institute National Research and Development Agency: Ibaraki, Japan, 2016. (In Japanese)
7. Reitherman, R.; Sabol, T. Nonstructural Damage. *Earthq. Spectra* **1995**, *11*, 453–514. [CrossRef]
8. Miranda, E.; Mosqueda, G.; Retamales, R.; Pekcan, G. Performance of Nonstructural Components during the 27 February 2010 Chile Earthquake. *Earthq. Spectra* **2012**, *28*, 453–471. [CrossRef]
9. Jun, S.C.; Lee, C.H.; Bae, C.J.; Lee, K.J. Shake-Table Seismic Performance Evaluation of Direct- and Indirect-Hung Suspended Ceiling Systems. *J. Earthq. Eng.* **2020**. [CrossRef]
10. Motosaka, M.; Mitsuji, K. Building Damage during the 2011 off the Pacific Coast of Tohoku Earthquake. *Soils Found.* **2012**, *52*, 929–944. [CrossRef]
11. Architectural Institute of Japan. *Guidelines for Preventing Falling Accidents of Nonstructural Elements Such as Ceilings*; Special Investigation Committee on Safety Evaluation and Fall Accident Prevention of Nonstructural Elements, Architectural Institute of Japan: Tokyo, Japan, 2013. (In Japanese)
12. Lee, J.-S.; Jung, D.-I.; Lee, D.-Y.; Cho, B.-H. Performance Evaluation of Rigid Braced Indirect Suspended Ceiling with Steel Panels. *Appl. Sci.* **2021**, *11*, 1986. [CrossRef]
13. Lu, Y.; Mosqueda, G.; Han, Q.; Zhao, Y. Shaking Table Tests Examining Seismic Response of Suspended Ceilings Attached to Large-Span Spatial Structures. *J. Struct. Eng.* **2018**, *144*, 04018152. [CrossRef]
14. Luo, Z.; Xue, J.; Zhou, T.; Qi, L.; Zhao, X. Shaking Table Tests and Seismic Design Suggestions for Innovative Suspended Ceiling Systems with Detachable Metal Panels. *Eng. Struct.* **2021**, *232*, 111830. [CrossRef]
15. Ryu, K.P.; Reinhorn, A.M. Experimental Study of Large Area Suspended Ceilings. *J. Earthq. Eng.* **2019**, *23*, 1001–1032. [CrossRef]
16. Soroushian, S.; Maragakis, M.; Jenkins, C. Capacity Evaluation of Suspended Ceiling-Perimeter Attachments. *J. Struct. Eng.* **2016**, *142*, 04015124. [CrossRef]
17. Badillo-Almaraz, H.; Whittaker, A.S.; Reinhorn, A.M. Seismic Fragility of Suspended Ceiling Systems. *Earthq. Spectra* **2007**, *23*, 21–40. [CrossRef]
18. Dhakal, R.P.; Macrae, G.A.; Pourali, A.; Paganotti, G. Seismic Fragility of Suspended Ceiling Systems used in NZ Based on Component Tests. *Bull. N. Z. Soc. Earthq. Eng.* **2016**, *49*, 45–63. [CrossRef]
19. Fiorin, L.; Brandolese, S.; Scotta, R. Experimental and Numerical Assessment of Suspended Ceiling Joints. *Bull. Earthq. Eng.* **2021**, *19*, 919–962. [CrossRef]
20. Yao, G.C. Seismic Performance of Direct Hung Suspended Ceiling Systems. *J. Archit. Eng.* **2000**, *6*, 6–11. [CrossRef]
21. Pourali, A.; Dhakal, R.P.; Macrae, G.; Tasligedik, A.S. Fully Floating Suspended Ceiling System: Experimental Evaluation of Structural Feasibility and Challenges. *Earthq. Spectra* **2017**, *33*, 1627–1654. [CrossRef]
22. Fiorino, L.; Shakeel, S.; Landolfo, R. Seismic Behaviour of a Bracing System for LWS Suspended Ceilings: Preliminary Experimental Evaluation through Cyclic Tests. *Thin-Walled Struct.* **2020**, *155*, 106956. [CrossRef]
23. Fiorino, L.; Bucciero, B.; Landolfo, R. Evaluation of Seismic Dynamic Behaviors of Drywall Partitions, Façades and Ceilings through Shake Table Testing. *Eng. Struct.* **2019**, *180*, 103–123. [CrossRef]
24. Magliulo, G.; Pentangelo, V.; Maddaloni, G.; Capozzi, V.; Petrone, C.; Lopez, P.; Talamonti, R.; Manfredi, G. Shake Table Tests for Seismic Assessment of Suspended Continuous Ceilings. *Bull. Earthq. Eng.* **2012**, *10*, 1819–1832. [CrossRef]
25. National research Institute for Earth Science and Disaster Prevention, Japan. *Collapse Mechanism of Wide-Area Suspended Ceiling System Based on E-Defense Full-Scale Shake Table Experiments*; National Research Institute for Earth Science and Disaster Prevention: Ibaraki, Japan, 2015. (In Japanese)
26. Soroushian, S.; Rahmanishamsi, E.; Ryu, K.P.; Maragakis, M.; Reinhorn, A.M. Experimental Fragility Analysis of Suspension Ceiling Systems. *Earthq. Spectra* **2016**, *32*, 881–908. [CrossRef]
27. Soroushian, S.; Maragakis, E.; Zaghi, A.E.; Rahmanishamsi, E.; Itani, A.M.; Pekcan, G. Response of a 2-Story Test-Bed Structure for the Seismic Evaluation of Nonstructural Systems. *Earthq. Eng. Eng. Vib.* **2016**, *15*, 19–29. [CrossRef]
28. Soroushian, S.; Rahmanishamsi, E.; Jenkins, C.; Maragakis, E.M. Fragility Analysis of Suspended Ceiling Systems in a Full-Scale Experiment. *J. Struct. Eng.* **2019**, *145*, 4019005. [CrossRef]
29. Qi, L.; Kurata, M.; Ikeda, Y.; Kunitomo, K.; Takaoka, M. Seismic Evaluation of Two-Elevation Ceiling System by Shake Table Tests. *Earthq. Eng. Struct. Dyn.* **2021**, *50*, 1147–1166. [CrossRef]

30. Soroushian, S.; Maragakis, E.; Ryan, K.L.; Sato, E.; Sasaki, T.; Okazaki, T.; Mosqueda, G. Seismic Simulation of an Integrated Ceiling-Partition Wall-Piping System at E-Defense. II: Evaluation of Nonstructural Damage and Fragilities. *J. Struct. Eng.* **2016**, *142*, 04015131. [CrossRef]
31. Saito, T.; Maegawa, T.; Denno, S.; Sakai, S.; Uchikawa, M.; Kanagawa, M.; Ryujin, H. New Seismic Response Control System Using Block and Tackle. In Proceedings of the 16th World Conference on Earthquake Engineering (WCEE), Santiago, Chile, 9–13 January 2017; Chilean Association on Seismology and Earthquake Engineering (ACHISINA): Santiago, Chile, 2017.
32. Saito, T.; Morita, K.; Hamada, M.; Maegawa, T.; Kikuta, S.; Denno, S.; Demizu, T.; Kanagawa, M.; Makita, T.; Sasaki, H.; et al. Basic Performance of Seismic Control Structure Using Block and Tackle System. *J. Struct. Eng. B* **2013**, *59B*, 349–355. (In Japanese)
33. Saito, T. Structural Earthquake Response Analysis, STERA_3D Version 10.8 and STERA_WAVE Version 1.0. Available online: <http://www.rc.ace.tut.ac.jp/saito/software-e.html> (accessed on 24 October 2021).

Effect of MetaFoundation on the Seismic Responses of Liquid Storage Tanks

Mostafa Farajian ^{1,2}, Mohammad Iman Khodakarami ^{1,*}  and Pejman Sharafi ² 

¹ Faculty of Civil Engineering, Semnan University, Semnan 35131-19111, Iran; m_farajian@semnan.ac.ir

² School of Engineering, Design and Built Environment, Western Sydney University, Sydney, NSW 2747, Australia; p.sharafi@westernsydney.edu.au

* Correspondence: khodakarami@semnan.ac.ir

Abstract: Cylindrical liquid storage tanks are vital lifeline structures, playing a critical role in industry and human life. Damages to these structures during previous earthquakes indicate their vulnerability against seismic events. A novel strategy to reduce the seismic demands in the structures is the use of metamaterials, being periodically placed in the foundation, called MetaFoundation (MF). The periodic configuration of metamaterials can create a stop band, leading to a decrease in wave propagation in the foundation. The aim of this paper is to study the effect of MF on the dynamic behaviour of liquid storage tanks. To that end, the governing equations of motion of the liquid storage tank equipped with MF are derived and solved in the time domain to obtain the time history of the responses under a set of ground motions. Then, the peak responses of tanks, mounted on MF, are compared with the corresponding responses in the fixed base condition. Besides, a parametric study is performed to assess the effect of the predominant frequency of earthquakes, the number of layers of metamaterials, the thickness of soft material, and the damping ratios of soft material on the performance of the MF. The obtained results indicate that the MF improves the dynamic behaviour of the squat tank, in which the mean ratio of responses using MF to the ones in the fixed base conditions equals 0.551 for impulsive displacement, overturning moment, and base shear.

Keywords: liquid storage tank; MetaFoundation; time domain analysis; earthquake; passive control; stop band

Citation: Farajian, M.; Khodakarami, M.I.; Sharafi, P. Effect of MetaFoundation on the Seismic Responses of Liquid Storage Tanks. *Appl. Sci.* **2022**, *12*, 2514. <https://doi.org/10.3390/app12052514>

Academic Editor: Felix Weber

Received: 28 January 2022

Accepted: 22 February 2022

Published: 28 February 2022

Publisher's Note: MDPI stays neutral with regard to jurisdictional claims in published maps and institutional affiliations.



Copyright: © 2022 by the authors. Licensee MDPI, Basel, Switzerland. This article is an open access article distributed under the terms and conditions of the Creative Commons Attribution (CC BY) license (<https://creativecommons.org/licenses/by/4.0/>).

1. Introduction

Cylindrical liquid storage tanks made of steel or concrete materials are strategic structures, having been employed to store water for drinking or firefighting, oil and chemical products in urban areas, and industrial plants. Damages to these structures may have catastrophic consequences such as economic losses, fire due to flammable materials, environmental pollution, and disruption of human lives. The reported failure modes of these structures during past earthquakes indicate their inappropriate seismic performance [1,2] and the need for a safeguard against seismic events. The seismic behaviour of liquid storage tanks has been studied extensively (e.g., [3–6]). Generally, two approaches can be followed to improve the performance of liquid containers against seismic events. The first approach is the strengthening of tanks by increasing their wall thickness. However, increasing the thickness of the wall will increase the input seismic energy. The second approach, aiming to decrease and dissipate the input seismic energy, is exploiting the advantages of control devices, such as base isolation systems, dampers, or other innovative control devices [7].

For more than four decades, a wide variety of studies have been conducted to develop various base isolation devices and to study their effects on the improvement of the seismic performance of steel tanks [8–14]. However, several factors influence the seismic responses of structures [15,16], and in the case of base-isolated liquid storage tanks, they may have adverse effects leading to an increase in seismic demands compared to the fixed base

condition [17–19]. For example, Bagheri and Farajian [17] showed that the base isolation may experience an excessive displacement when the system is subjected to near-fault excitations with severe pulses, resulting in a dramatic increase in the displacement of the impulsive mass and, consequently, base shear and overturning moment. The same results were observed through experimental tests conducted on the seismic response of scaled structures isolated by highly efficient, low-cost PVC-Rollers Sandwich seismic isolation [20,21]. Besides, the traditional base isolation devices are less capable of improving the seismic performance of structures built on soft soil and cannot isolate structures from the vertical component of ground motions. Therefore, it would be beneficial to mitigate the seismic demands through other control systems without the shortages mentioned above.

In recent years, the progress in the area of solid-state physics showed that the structures being placed periodically display distinctive properties called frequency stop band, which can be explained as a wave is blocked to propagate through a continuum model if its frequency falls in the stop band frequency and can propagate to the model for the frequencies other than the frequencies of stop band [22–24]. This fascinating feature attracted considerable attention, stimulating researchers to construct materials with periodic structures to block the propagation of waves. Locally resonant metamaterials (LRMs) and phononic crystals (PCs) have been known as two types of periodic structures which are employed to avoid the propagation of waves [25]. Compared to PCs, LRMs have a more suitable performance to diminish vibrations with low frequency because the local resonances have the ability to create the stop band. LRMs, made from heavy materials (metamaterials) coated with a soft layer in a stiff matrix [26] (usually concrete), have been employed as foundations and barriers to decrease the propagation of seismic waves into structures and to protect them against the harmful consequences of earthquakes. The benefits of such a foundation would be magnified in the case of different structures, such as liquid storage tanks as well as modular structures, in which their performance under seismic actions is still a big question [27,28]. Jia and Shi [29] investigated the effect of physical as well as geometrical properties of periodic foundation on the stop band. They concluded that a lower band gap can be achieved by considering a higher mass density for the core. Bao et al. [24] compared the seismic behaviour of a seven-story building mounted on a periodic foundation with the traditional foundation and base isolation system. They observed that the periodic foundation has a better performance compared to base isolation systems in attenuating the seismic responses when the predominant frequency of the wave incident lies in the stop band. Mitchell et al. [30] proposed metaconcrete in which spherical metal cores coated with soft material are used instead of standard concrete. The coated metal core behaved as a resonator, activating when a dynamic blast load is applied with the frequency at or near the resonator frequency. Hence, the overall system exhibits negative effective mass, leading to the reduction of the amplitude of the applied blast wave. Dertimanis et al. [31] used mass-in-mass barriers being placed periodically to investigate the effect of locally resonant metamaterials. They connected internal mass to the outer mass by tendons and found that the input energy is filtered if the frequency falls in the stop band. Maleki and Khodakarami [32] conducted numerical analyses to evaluate the effect of MetaSoil on the amplification of in-plane waves due to topography irregularities. More recently, Basone et al. [33] employed the concept of LRMs to alleviate the demand in liquid tanks due to seismic actions. The foundation was made of steel columns, and the concrete-type resonators were connected to these columns. They conducted an optimization procedure to obtain the optimized damping and frequency corresponding to the resonators. The obtained results demonstrated that the proposed system could decrease the base shear in a slender tank up to 30%. Aguzzi et al. [34] investigated the propagation of flexural waves in a thin reticulated plate augmented with two classes of metastructures for wave mitigation. Despite all the research on metamaterials, no study has been conducted on the performance of MetaFoundation, composed of concrete matrix and steel core, in liquid storage tanks. Moreover, it is vital to investigate the effect of various parameters influencing the performance of MF on the seismic behaviour of the superstructure. Particularly, due to

the fact that the MF works in a range of frequencies, it is essential to investigate the effect of earthquake frequency on the seismic behaviour of MF.

This paper aims to investigate the efficiency of a foundation made by concrete and locally resonant materials coated with a soft layer called MetaFoundation (MF) on the dynamic behaviour of cylindrical tanks made from steel materials. To that end, the theory and background of the MF based on Bloch’s theorem are studied, and a simplified mass–spring model is suggested for the dynamic analysis of the coupled MF–tank system. Then, the governing equations of motion of the system are derived and solved in the time domain. For the numerical study, two types of tanks, namely squat and slender, are subjected to a set of ground motions with far-field characteristics to compare the seismic responses of the tanks mounted on MF with corresponding responses in the fixed base condition. Besides, a parametric study is performed to investigate the influence of different parameters on seismic responses of considered tanks with MF. These parameters are the predominant frequency of ground motions, the number of layers of metamaterials, the thickness of the soft material, and the damping of the soft material.

2. Simplified Model of MF

The 3D view of an MF is illustrated in Figure 1. Compared to the traditional foundation, which is made of concrete and longitudinal and transversal rebars, the MF contains heavy cores with cubic shapes that are coated with soft material in addition to the concrete and rebars. It is assumed that the MF is subjected to dynamic excitations in X and Y directions. Therefore, it can be divided into N unit cells in X, Y, and N -layers in Z directions.

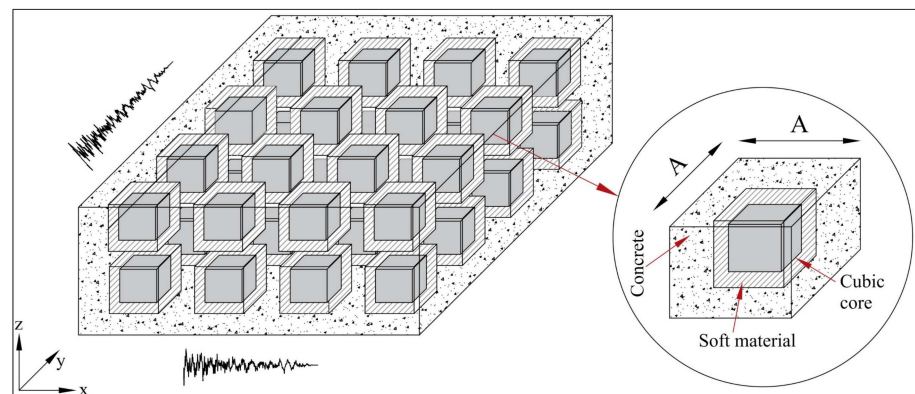


Figure 1. Three-dimensional view of the proposed MetaFoundation.

Assuming that the model is continuous, isotropic, made by materials with perfectly plastic behaviour, small deformation and insignificant damping, the governing equation of an inhomogeneous solid is written as [35]:

$$\rho(\mathbf{r}) \frac{\partial^2 \mathbf{u}}{\partial t^2} = \nabla \{ [\lambda(\mathbf{r}) + 2\mu(\mathbf{r})](\nabla \cdot \mathbf{u}) \} - \nabla \times [\mu(\mathbf{r}) \nabla \times \mathbf{u}] \tag{1}$$

where ρ is the mass density, $\mathbf{u} = (u_x, u_y, u_z)$ is the displacement vector, t is the time parameter, $\mathbf{r} = (x, y, z)$ the coordinate vector, λ and μ are Lamé’s constants and ∇ is the Laplace operator. Decoupling the out-of-plane modes from those of in-plane ones, Equation (1) is rewritten as [35]:

$$\rho(\mathbf{r}) \frac{\partial^2 u_j}{\partial t^2} = \frac{\partial}{\partial x_j} \left[\lambda(\mathbf{r}) \frac{\partial u_l}{\partial x_j} \right] + \frac{\partial}{\partial x_l} \left[\mu(r) \left(\frac{\partial u_l}{\partial x_j} + \frac{\partial u_j}{\partial x_l} \right) \right] \tag{2}$$

where $u_j = u_j(x, y)$ is the in-plane displacement vector, $j, l = 1, 2$ and $\mathbf{r} = (x, y)$. Using the Floquet–Bloch theorem for the periodic configuration of unit cells in uniaxial direction, the solution of Equation (2) is given as:

$$u(x, t) = e^{i(qx - \omega t)} u \tag{3}$$

where q is the wave vector in reciprocal space, ω is the circular frequency. The wave amplitude is shown by u , which is a periodic function and is expressed as:

$$u(x) = u(x + A) \tag{4}$$

where A is the unit cell size (shown in Figure 1). The stop band can be calculated through the dispersion analysis of the periodic structure. Two different approaches can be employed to conduct the dispersion analysis and obtain the stop band. The first approach is the 3D finite element modelling of the MF, which requires potential workload and high computational effort due to the complexity in modelling. The second approach is the use of the simple model of MF, which is represented by a set of masses and springs. Since the unit cells of each layer operate in parallel under seismic excitation, they can be represented by an equivalent unit cell through dynamic condensation. Figure 2 shows the simplified mass–spring model of an MF with N -layers in the Z direction.

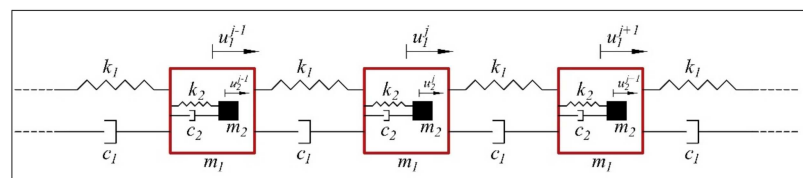


Figure 2. Simplified mass–spring model of an MF.

The total mass of the concrete in each layer is shown by the external mass (m_1), and the total mass of the metamaterials in each layer is shown by the internal mass (m_2). The stiffness corresponding to each layer of foundation and soft material is represented by springs whose stiffnesses are shown by k_1 and k_2 , respectively. The stiffness corresponding to the soft material for each unit cell is obtained by:

$$k_2 = \frac{E_{SM} A_{SM}}{t_{SM} - (|u_2 - u_1|)} \tag{5}$$

where E_{SM} and t_{SM} are the modulus of elasticity and thickness of the soft material, respectively. The area of the soft material perpendicular to the applied wave direction is represented by A_{sm} ; u_1 and u_2 are displacements of external and internal masses. Note that, in this study, the stiffness corresponding to the soft material will be updated during the analysis based on the relative displacement of the internal and external masses. Therefore, more accurate seismic responses will be obtained. The damping associated with the external and internal masses are shown by c_1 and c_2 and expressed by

$$c_1 = 2\zeta_{con} \sqrt{k_1(m_1 + m_2)} \tag{6}$$

$$c_2 = 2\zeta_{SM} \sqrt{k_2 m_2} \tag{7}$$

where ζ_{con} and ζ_{SM} are the damping ratios of concrete and soft material, respectively. Due to the periodicity, it is possible to reduce the dispersion analysis of the infinite structure to the dispersion analysis of a single unit cell with the same boundary condition. The response of boundary conditions is calculated by substituting Equation (4) into Equation (3) as follows:

$$u(x + A, t) = e^{iqA} u(x, t) \tag{8}$$

The stop band is estimated by conducting the Eigen-frequency analysis of an undamped unit cell for a considered Bloch wave vector (q). The governing equations of motion of j -th unit cell are written as:

$$m_1^j \ddot{u}_1^j + k_1(2u_1^j - u_1^{j-1} - u_1^{j+1}) + k_2(u_1^j - u_2^j) = 0 \tag{9}$$

$$m_1^j \ddot{u}_1^j + k_2(u_2^j - u_1^j) = 0 \tag{10}$$

Equations (9) and (10) are rewritten by substituting Equation (8) into Equation (9) and under the consideration of the trigonometric relationship of $e^{iqA} = \cos(qA) + i \sin(qA)$, as follows:

$$m_1^j \ddot{u}_1^j + (2k_1 - 2k_1 \cos(qA) + k_2)u_1^j - k_2u_2^j = 0 \tag{11}$$

$$m_2^j \ddot{u}_2^j - k_2u_1^j + k_2u_2^j = 0 \tag{12}$$

Equations (11) and (12) are formulated by Equation (13) to obtain the dispersion relation of the considered MetaFoundation.

$$[\mathbf{K}(q) - \omega^2 \mathbf{M}] \mathbf{u} = 0 \tag{13}$$

where $\mathbf{K}(q)$ and \mathbf{M} are the stiffness and mass matrices of the unit cell, respectively. Equation (13) shows that the stiffness of the unit cell is dependent on the Bloch wave vector (q). The nontrivial solution of the eigenvalue problem is

$$m_1 m_2 \omega^4 - [(m_1 + m_2)k_2 + 2m_2 k_1 (1 - \cos(qA))] \omega^2 + 2k_1 k_2 (1 - \cos(qA)) = 0 \tag{14}$$

Equation (14) has two responses corresponding to two dispersion curves, known as acoustic and optical. The lower response is related to the acoustic branch, and the higher response is associated with the optical branch. The stop band gap falls between these two dispersion curves.

3. Structural Model of the Liquid Storage Tank

The three-dimensional finite element modelling and analysis of a cylindrical liquid tank is a complicated process and requires computational effort mainly due to the interaction of tank and fluid. Besides, the MF, which is made of different materials, increases its modelling and analysing complexity. Therefore, the use of a simple and accurate model with the capability to determine the response of a liquid storage tank under seismic ground motions is of interest. As an alternative approach of finite element modelling, the simplified mass–spring model, which is accepted by standard codes such as API 650 [36], ASCE 7-16 [37], and Eurocode 8 [38] can be employed to model and analyse of tank containers. This simplified mass–spring model is generally based on the work conducted by Housner [39]. He evaluated the effect of hydrodynamic actions in liquid storage tanks, assuming that the tank wall has a rigid behaviour. According to Housner’s model, the hydrodynamic response of a fluid tank system is determined by the superposition of two components, namely convective and impulsive components. The convective component is generated by convective mass (m_c), and the impulsive component is produced by impulsive mass (m_i). The convective mass refers to the portion of the liquid in the upper part of the tank near the free surface, which experiences a long period of sloshing motion during dynamic loading. Conversely, the portion of the filling liquid near the base of the liquid storage tank accelerating in unison with the tank wall is represented by impulsive mass. Haroun and Housner [40] modified the simplified mass–spring model of Housner to consider the tank wall flexibility. Malhotra et al. [41] offered a simple and accurate procedure to assess the seismic responses of liquid storage tanks. They combined the first impulsive modal mass with the higher impulsive modal mass and the first convective modal mass with the higher convective modal mass. As a result of such a combination, the tank liquid system was represented by two modes only. Figure 3 demonstrates a cylindrical liquid tank mounted

on an N -layer MF. The geometrical properties of the tank are the height of the liquid (H), the thickness of the wall of the tank (t_w) and the radius of the tank (R).

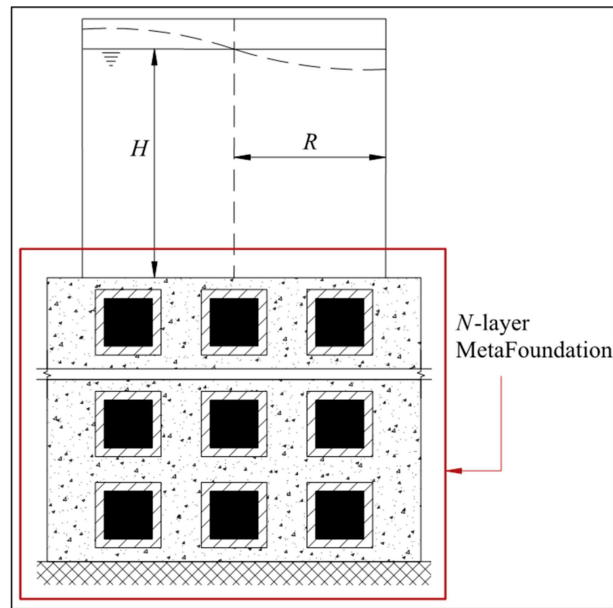


Figure 3. A liquid storage tank mounted on an MF.

In this paper, the mass–spring model suggested by Malhotra et al. is used for the dynamic time history analysis of the liquid storage tank (Figure 4).

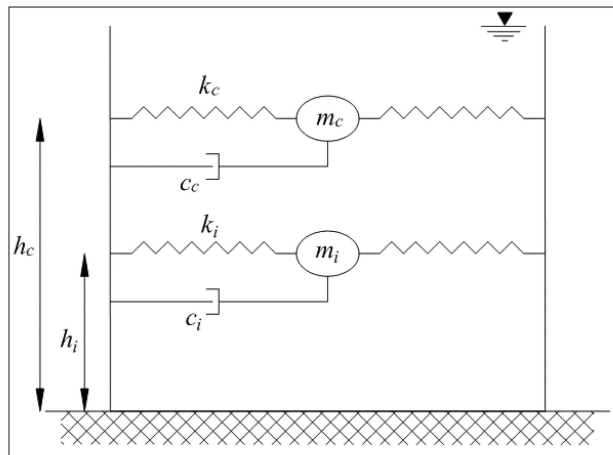


Figure 4. Simplified model of the liquid storage tank.

The impulsive and convective masses (m_i and m_c) are connected to the wall of the tank by linear springs whose stiffnesses are k_i and k_c , respectively. The stiffness of springs is influenced by the properties of the filling fluid, the tank material, and the geometric properties of the tank. The damping coefficients corresponding to the impulsive and convective masses are shown by c_i and c_c , respectively.

The damping coefficient and stiffness corresponding to impulsive and convective masses are expressed as follows:

$$c_i = 2\zeta_i m_i \times \frac{2\pi}{T_i} \tag{15}$$

$$c_c = 2\zeta_c m_c \times \frac{2\pi}{T_c} \tag{16}$$

$$k_i = m_i \times \frac{4\pi^2}{T_i^2} \tag{17}$$

$$k_c = m_c \times \frac{4\pi^2}{T_c^2} \tag{18}$$

where ζ_i and ζ_c are the damping ratios of the impulsive and convective masses. T_i and T_c are natural periods corresponding to impulsive and convective responses, given by [41]:

$$T_i = C_i \frac{H\sqrt{R}}{\sqrt{t_w/R} \times \sqrt{E_s}} \tag{19}$$

$$T_c = C_c \sqrt{R} \tag{20}$$

where E_s is the modulus of elasticity of the tank material and ρ_w is the mass density of filling fluid, respectively. The ratio of impulsive and convective masses to the total mass (m_i/m) and (m_c/m), relative heights of impulsive and convective masses (h_i/H) and (h_c/H), and the coefficients C_i and C_c are suggested by Malhotra et al. [41]. The filling fluid mass (m) equals to $\pi R^2 H \rho_w$.

4. Governing Equations of Motion MF-Tank System

The simplified mass–spring model of an N -layer MF-tank system is depicted in Figure 5.

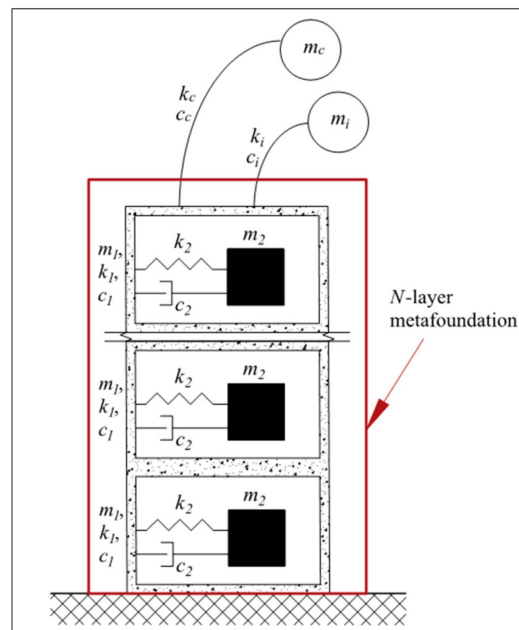


Figure 5. Simplified mass–spring model of the liquid storage tank mounted on an N -layer MF.

The whole system comprises $2N$ degrees of freedom representing the MetaFoundation and two degrees of freedom demonstrating the convective and impulsive masses, respectively.

The governing equations of motion of the MF tank system can be written in matrix form:

$$M_T \ddot{u} + C_T \dot{u} + K_T u = -M_T \ddot{r}_g \tag{21}$$

where M_T , K_T , and C_T are the mass, stiffness, and damping matrices of the coupled tank system mounted on the MetaFoundation, respectively expressed by

$$M_T = \begin{bmatrix} M_{MF} & 0 \\ 0 & M_{Tank} \end{bmatrix} \tag{22}$$

$$C_T = \begin{bmatrix} C_{MF} + C_{Tank} & -C_{Tank} \\ -C_{Tank} & C_{Tank} \end{bmatrix} \tag{23}$$

$$K_T = \begin{bmatrix} K_{MF} + K_{Tank} & -K_{Tank} \\ -K_{Tank} & K_{Tank} \end{bmatrix} \tag{24}$$

$$M_{MF} = \text{diagonal } (m_1, m_2 \dots m_1, m_2)_{2N \times 2N}; M_{Tank} = \text{diagonal } (m_i, m_c)_{2 \times 2}; \tag{25}$$

$$C_{MF} = \begin{bmatrix} 2c_1 + c_2 & -c_2 & -c_1 & \dots & 0 \\ -c_2 & c_2 & 0 & \dots & 0 \\ -c_1 & 0 & \ddots & \dots & \vdots \\ \vdots & \vdots & \vdots & c_1 + c_2 & -c_2 \\ 0 & 0 & \dots & -c_2 & c_2 \end{bmatrix} \tag{26}$$

$$C_{Tank} = \text{diagonal } (c_i, c_c)_{2 \times 2} \tag{27}$$

$$K_{MF} = \begin{bmatrix} 2k_1 + k_2 & -k_2 & -k_1 & \dots & 0 \\ -k_2 & k_2 & 0 & \dots & 0 \\ -k_1 & 0 & \ddots & \dots & \vdots \\ \vdots & \vdots & \vdots & k_1 + k_2 & -k_2 \\ 0 & 0 & \dots & -k_2 & k_2 \end{bmatrix} \tag{28}$$

$$K_{Tank} = \text{diagonal } (k_i, k_c)_{2 \times 2} \tag{29}$$

$$u = [u_1, u_2 \dots u_1, u_2, u_i, u_c]^T \tag{30}$$

The superscript *MF* and *Tank* stand for MetaFoundation and tank system, respectively; *u* is the displacement of the system relative to the ground; $x_2 = (u_2 - u_1)$, $x_i = (u_i - u_1)$, $x_c = (u_c - u_1)$ are displacement of internal, impulsive, and convective masses relative to the external mass, respectively. In Equation (21), the earthquake acceleration is shown by $\ddot{u}g$, and *r* is a column vector of one.

To obtain the time history of responses of the liquid storage tanks with MF, the governing equations of motion are derived and transferred to the first-order differential equations. Then, these equations are solved in each time step using the state-space representation and ODE15s in MATLAB programming language. The response quantities of interest are vertical displacement of the surface of the fluid (d_v), impulsive displacement (x_i), overturning moment (*M*) at the top of the MF, and structural base shear of the tank (F_s). While the impulsive displacement can be obtained directly through the solving of equations of motion, the vertical displacement of the free surface, the overturning moment at the top of the foundation, and structural base shear are calculated according to Equations (31)–(33), respectively [8]. The overturning moment determines the generated hydrodynamic forces in the tank wall, which is proportional to the axial compressive force. The axial compressive force is the main reason of buckling of the tank walls, either in the form of elephant foot buckling or diamond shape buckling. Conversely, the vertical displacement of the free surface caused by the convective component controls the required freeboard. In the case of lack of sufficient freeboard, the tank may experience a leak of fluid, tear of the shell or break of the shell–roof connection.

$$d_v = 0.837R \frac{\omega_c^2 x_c}{g} \tag{31}$$

$$M = -\{m_c h_c (\ddot{u}_c + \ddot{u}_g) + m_i h_i (\ddot{u}_i + \ddot{u}_g)\} \tag{32}$$

$$F_s = -\{m_c (\ddot{u}_c + \ddot{u}_g) + m_i (\ddot{u}_i + \ddot{u}_g)\} \tag{33}$$

where ω_c is the frequency of the convective mass ($\omega_c = 2\pi/T_c$). For simplicity and better comparison of the results, the performance index of vertical displacement of the surface of the liquid (PI d_v), the displacement of impulsive mass (PI x_i), overturning moment on

the foundation (PI M), and structural base shear (PI F_s) are defined as the ratio of seismic responses of the liquid storage tank mounted on the MF (d_v^{MF} , x_i^{MF} , M^{MF} and F_s^{MF}) to the corresponding responses of the tank in fixed base condition (d_v^F , x_i^F , M^F and F_s^F), according to Equations (34)–(37). Therefore, a PI of less than one indicates that the MF is an efficient solution to improve the dynamic behaviour of liquid storage tanks. However, the performance index of more than one shows that the response is amplified due to the implementation of MF. Therefore, the MF has an adverse effect.

$$PI\ d_v = \frac{d_v^{MF}}{d_v^F} \tag{34}$$

$$PI\ x_i = \frac{x_i^{MF}}{x_i^F} \tag{35}$$

$$PI\ M = \frac{M^{MF}}{M^F} \tag{36}$$

$$PI\ F_s = \frac{F_s^{MF}}{F_s^F} \tag{37}$$

In addition to the time history of responses, it is interesting to evaluate the efficiency of the proposed MetaFoundation in the frequency domain through the transmission ratio (TR) of displacement above the MF against different frequencies (f). The transmission ratio is expressed as

$$TR(f) = 20 \log_{10} \left(\frac{u_t(f)}{u_0(f)} \right) \tag{38}$$

In Equation (38), the amplitude of the input displacement at the bottom of the MF is shown by $u_0(f)$, and the amplitude of the displacement measured at the top of the MF is shown by $u_t(f)$, respectively. In detail, in order to obtain the displacement transmission ratio, a harmonic displacement at various frequencies is imposed at the bottom of the foundation with amplitude u_0 , and the displacement response u_t on the top of the foundation is observed.

5. Numerical Study

For practical applications, the periodic MetaFoundation must be constructed by available materials. In this paper, it is assumed that the foundation is made of concrete, and the heavy cores are made of steel coated by rubber. The material properties of different parts of unit cells, including modulus of elasticity and density, are listed in Table 1.

Table 1. Material properties of a unit cell.

Part Name	Material	Modulus of Elasticity, E (GPa)	Density, ρ (kg/m ³)
matrix	concrete	24.85	2400
soft material	rubber	0.000137	1300
core	steel	210	7850

For the preliminary time history analysis, it is assumed that the MetaFoundation comprises unit cells with dimensions of $0.305 \times 0.305 \times 2.0$ m corresponding to the length, width, and height, respectively. In addition, the cores of unit cells have a dimension of 0.10 m. The thickness of the rubber is assumed to be 0.05 m. The damping ratios corresponding to concrete and rubber are assumed to be 5% and 30%, respectively. A dispersion analysis has been conducted to calculate the dispersion relation and stop band corresponding to an infinite unit cell. The optical and acoustic branches obtained from the dispersion analysis are illustrated in Figure 6.

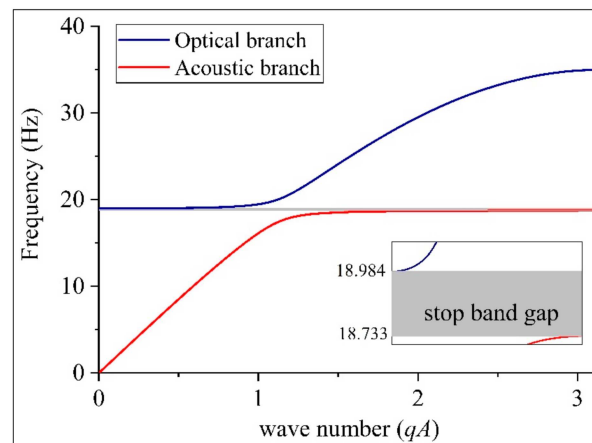


Figure 6. Dispersion analysis of considered unit cell.

The results show that the stop band forms in the frequency range of 18.733 to 18.984 Hz, where the elastic waves cannot propagate through the MF according to the Floquet–Bloch theory. However, the obtained stop band is valid for an infinite number of unit cells. For the case of the foundation comprising finite unit cells, additional modal analysis is required to calculate the stop band.

Two different types of cylindrical tanks have been considered as case studies from [8]. The considered tanks have different aspect ratios (height to radius). The ratio of height to the radius of the assumed tanks ($S = H/R$) is 0.6 and 1.85, corresponding to squat and slender tanks, respectively. The filling fluid is assumed to be water, with a mass density of $\rho_w = 1000 \text{ kg/m}^3$. Table 2 shows the geometrical properties of considered tanks. A foundation that has a square shape is considered for both squat and slender tanks. The dimension of the MF for the squat tank is assumed to be $50.0 \times 50.0 \text{ m}$, corresponding to its width and length, respectively; for the slender tank, a MetaFoundation with 15.0 m length and width is considered. As mentioned above, the height of each layer of MF is assumed to be 2.0 m.

Table 2. Geometrical properties of the selected tanks used as case studies.

Tank Type	H (m)	R (m)	t_w (m)
Squat	14.6	24.4	0.0203
Slender	11.3	6.1	0.0058

The natural period, relative masses, and relative heights of the simplified mass–spring model depend on the geometrical properties of the cylindrical tanks. The parameters of the equivalent mechanical model of the tank have been calculated and tabulated in Table 3. The damping ratios of the convective (ζ_c) and impulsive masses (ζ_i) are assumed to be 0.5% and 2%, respectively, as suggested by [8].

Table 3. Resultant parameters of the equivalent mechanical model for the selected squat and slender tanks.

Tank Type	m_c/m	m_i/m	h_c/H	h_i/H	C_c (s/m ^{0.5})	C_i	T_c (s)	T_i (s)
Squat	0.608	0.392	0.557	0.400	1.65	7.08	8.15	0.253
Slender	0.245	0.755	0.727	0.444	1.48	6.07	3.66	0.157

An adequate number of earthquakes should be considered for the required time history analysis to assess the efficacy of the proposed MF on the seismic responses of liquid storage tanks. Federal Emergency Management Agency (FEMA) [42] suggested three sets of ground motions for quantifying seismic performance factors of buildings. The three sets

include far-field (FF), near-fault without pulse (NF-WO Pulse), and near-fault with pulse (NF-W Pulse) ground motions. In this paper, the FF set, which comprises twenty-two pairs of records with an average moment magnitude of $M_w = 7.0$, has been used. Each record has two horizontal components; therefore, the system is subjected to forty-four ground motions. All of the considered earthquakes with a distance from the fault rupture of more than 10 km were recorded on site classes C or D based on the NEHRP classification, and they do not reveal any pulse in their velocity time history. Besides, the selected excitations cover different intensities in terms of their PGA. The ground motions were downloaded from the strong ground motion database of the PEER NGA-West2 (pacific earthquake engineering research) centre. The properties of the considered earthquakes, including the station name, M_w , PGA, and PGV, have been listed in detail in Table 4. Figure 7 a,b depicts the pseudo-acceleration and spectral displacement of the selected earthquake ground motions for 2% and 0.5% damping ratios corresponding to the impulsive and convective masses, along with median as well as 2.5% and 97.5% percentile.

Table 4. Selected earthquakes for time history analysis.

Record Pair	Earthquake	Year	Station	M_w	Component 1	Component 2	PGA (g)	PGV (cm/s)
1	Northridge	1994	Beverly Hills-Mulhol	6.7	MUL009	MUL279	0.52	63
2	Northridge	1994	Canyon Country-WLC	6.7	LOS000	LOS270	0.48	45
3	Duzce, Turkey	1999	Bolu	7.1	BOL000	BOL090	0.82	62
4	Hector Mine	1999	Hector	7.1	HEC000	HEC090	0.34	42
5	Imperial Valley	1979	Delta	6.5	H-DLT262	H-DLT352	0.35	33
6	Imperial Valley	1979	El Centro Array # 11	6.5	H-E11140	H-E11230	0.38	42
7	Kobe, Japan	1995	Nishi-Akashi	6.9	INIS000	NIS090	0.51	37
8	Kobe, Japan	1995	Shin-Osaka	6.9	SHI000	SHI090	0.24	38
9	Kocaeli, Turkey	1999	Duzce	7.5	DZC180	DZC270	0.36	59
10	Kocaeli, Turkey	1999	Acrelik	7.5	ARC000	ARC090	0.22	40
11	Landers	1992	Yermo Fire Station	7.3	YER270	YER360	0.24	52
12	Landers	1992	Coolwater	7.3	CLW-LN	CLW-TR	0.42	42
13	Loma Prieta	1989	Capitola	6.9	CAP000	CAP090	0.53	35
14	Loma Prieta	1989	Gilroy Array #3	6.9	G03000	G03090	0.56	45
15	Manjil, Iran	1990	Abbar	7.4	ABBAR-L	ABBAR-T	0.51	65
16	Superstition Hills	1987	El Centro Imp. Co.	6.5	B-ICC000	B-ICC090	0.36	46
17	Superstition Hills	1987	Poe Road (temp)	6.5	B-POE270	B-POE360	0.45	36
18	Cape Mendocino	1992	Rio Dell Overpass	7.0	RIO270	RIO360	0.55	44
19	Chi-Chi, Taiwan	1999	CHY101	7.6	CHY101-E	CHY101-N	0.44	115
20	Chi-Chi, Taiwan	1999	TCU045	7.6	TCU045-E	TCU045-N	0.51	39
21	San Fernando	1971	LA-Hollywood stor	6.6	PEL090	PEL180	0.21	19
22	Friuli, Italy	1976	Tolmezzo	6.5	A-TMZ000	A-TMZ270	0.35	31

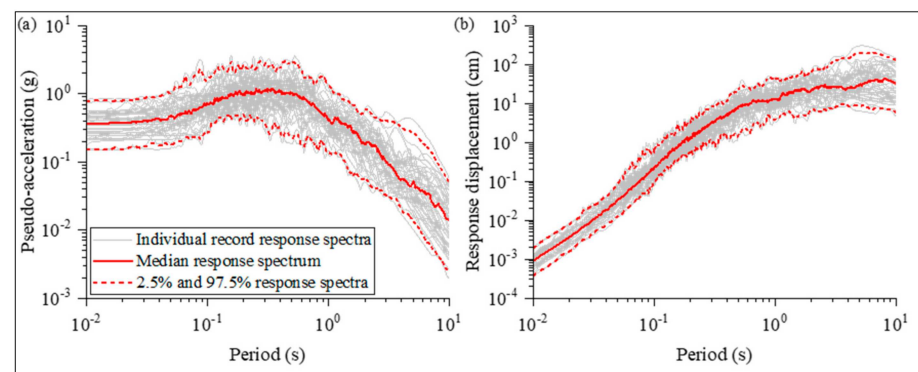


Figure 7. (a) Pseudo-acceleration and (b) response displacement spectra of considered earthquake ground motions.

6. Verification

In order to verify the obtained governing equations of motion, the vertical displacement of free surface (d_v) and impulsive mass displacement (x_i) of both squat and slender tanks mounted on an MF with a small dimension of the core are compared with corresponding responses in fixed base conditions. To that end, it is assumed that the core has a dimension of 0.001, 0.001, and 0.001 m corresponding to width, length, and height, respectively, and the thickness of the soft layer is 0.001 m. These small dimensions have been assigned to the core and the soft layer to avoid difficulties during solving of the governing equations of motion. It is expected that this MetaFoundation behaves as a traditional foundation made by concrete, and the resonators have no significant influence on the seismic responses of tanks.

Figure 8 compares the time history of the vertical displacement of the free surface as well as the impulsive displacement of both squat and slender tanks subjected to the Friuli, A-TMZ270 earthquake. The obtained responses verify the governing equations of motion and the accuracy of responses of liquid storage tanks with MF. The maximum difference between the responses is found to be less than 1%.

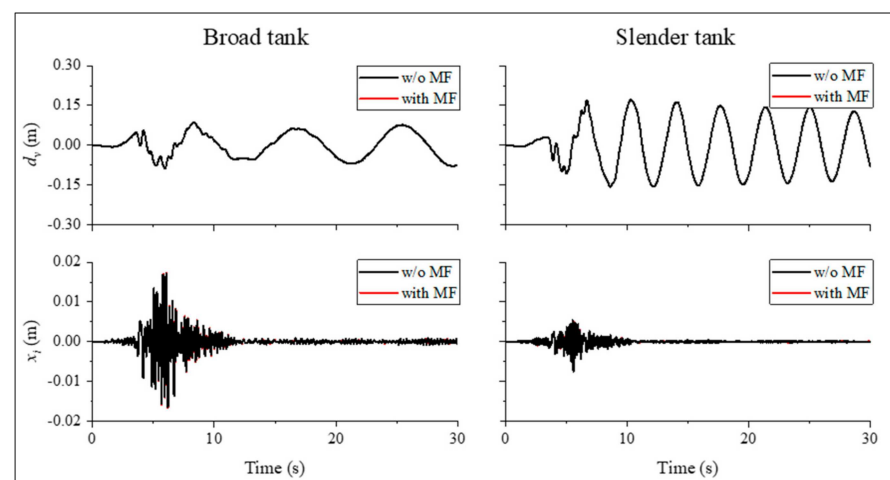


Figure 8. Verification of the obtained responses subjected to the Friuli, A-TMZ270 earthquake.

7. Results and Discussions

7.1. Effect of MetaFoundation

To evaluate the influence of the proposed MetaFoundation in the time domain, the time transient analysis is performed under selected ground motions. The seismic responses of liquid storage tanks mounted on MF are compared with the corresponding responses in fixed base condition. The parameters of the MF are described in the previous section.

Figure 9 shows the time history of seismic responses of considered tanks under ABBAR—L, Manjil earthquake.

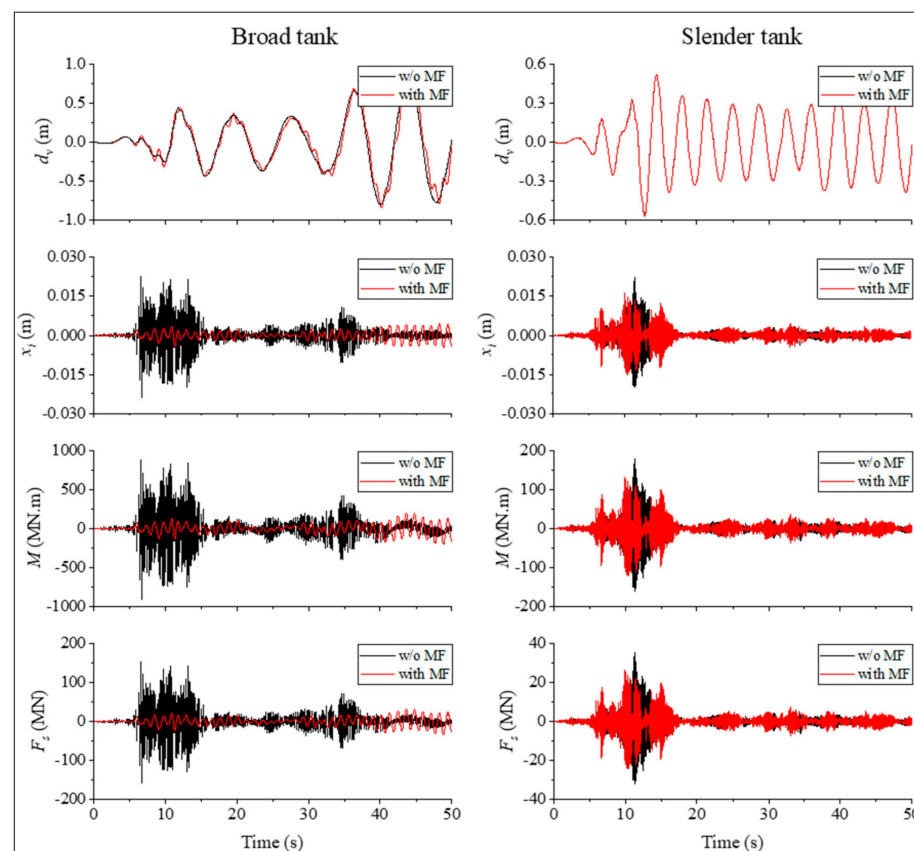


Figure 9. Time history of responses of squat and slender tank subjected to ABBAR—L, Manjil ground motion for w/o and w MF.

The seismic responses are depicted for both squat and slender tanks in fixed base condition and mounted on MF, respectively. The performance index of seismic responses of the selected liquid storage tank tanks subjected to various ground motions is depicted in Figure 10. According to the obtained responses, two different trends were observed for the performance of the MF on the seismic responses of squat and slender tanks.

First, in the squat tanks, it is observed that the displacement of the impulsive mass, overturning moment on top of the foundation, and base shear have been reduced in most cases due to the implementation of the MF. The mean performance index of the displacement of impulsive mass, overturning moment on the foundation, and base shear are 0.551, 0.551, and 0.551, illustrating that the MF reduces the input excitation. Therefore, the use of the MF in the squat tank is an effective solution to improve its dynamic behaviour. The best performance of the MF was observed when the system was subjected to G03000, Loma Prieta ground motion in which the PI of the displacement of the impulsive mass, overturning moment on the MF, and base shear equalled 0.091, 0.09, and 0.091, respectively. However, a performance index of more than one is seen in some cases. For example, a PI equal to 1.491, 1.480, and 1.476 for the displacement of impulsive mass, the overturning moment on the foundation and base shear was observed when the system was excited by HEC090, showing that the MF increases the responses compared to fixed base condition. This is attributed to the fact that the performance of MF highly depends on the frequency content of input earthquake ground motion as well as the stop band. According to Figure 11, it is seen that in some frequency ranges, the TR is magnified. This illustrates that the amplitude of the input wave will be intensified, and therefore, the responses of liquid storage tanks are increased compared to the fixed base condition. The reduction of the

overturning moment leads to a decrease in the axial demand in the tank wall, which is the main reason for the buckling of the tank wall. Hence, the more economical and reliable design of the tank is achievable by the use of MF.

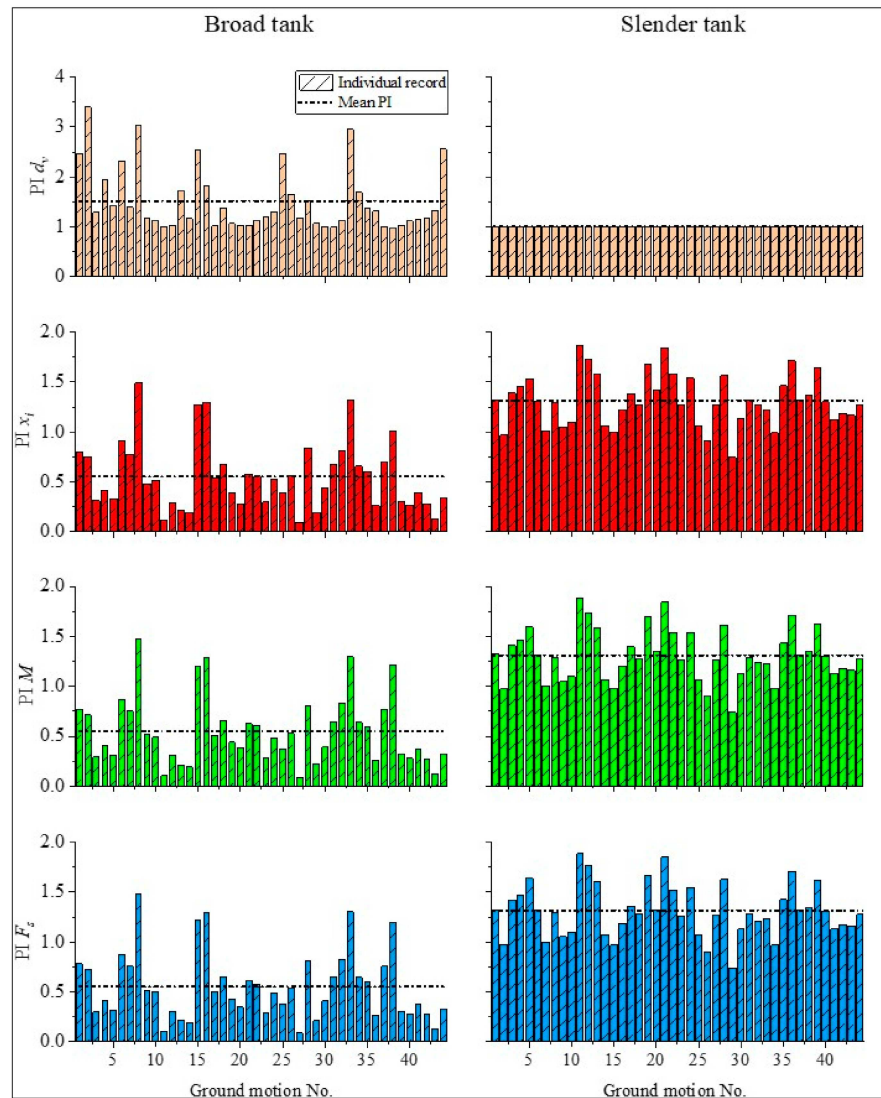


Figure 10. Performance index (PI) of various seismic responses of squat and slender tanks.

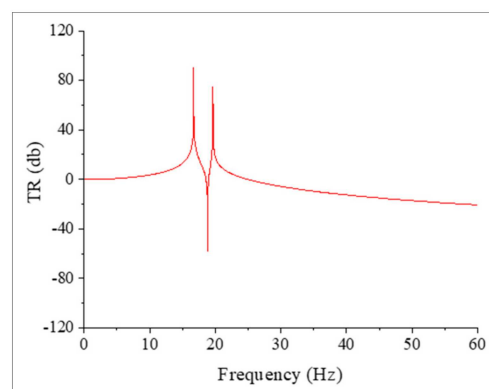


Figure 11. TR of the displacement above the MF.

Conversely, it is seen that the MF increases the vertical displacement of the free surface of the liquid. The mean performance index of the vertical free surface displacement is 1.5. Therefore, it is vital to consider a more freeboard to avoid the disrupting consequences corresponding to vertical displacement of the free surface.

Second, with reference to Figure 10, one can conclude that the displacement of impulsive mass, overturning moment on the foundation, and base shear in the slender tank are magnified in most cases. The mean PI of the impulsive displacement, overturning moment, and base shear in the slender tank are 1.315, 1.315, and 1.35, respectively. Therefore, it can be concluded that the MF has an adverse effect on the seismic responses of the slender liquid storage tank. The best performance of the MF is observed under the ABBAR—L, Manjil earthquake in which the PI corresponding to the displacement of impulsive mass, overturning moment on top of foundation, and base shear are 0.742, 0.742, and 0.740, respectively. In terms of the vertical displacement of the free surface, it is seen that the MF has no significant effect. As is seen in Figure 10, the PI of the vertical displacement of the free surface approximately equals one for all of the earthquake ground motions.

To demonstrate the filtering effect of the MF, the TR above the MF in the absence of the liquid storage tank is demonstrated in Figure 11.

A TF equal to zero implies that the displacement output on the top of the foundation equals the input displacement induced at the bottom of the foundation. After that, the TR corresponding to the regions of less than zero indicates that the amplitude of the output displacement is less than the amplitude of the input displacement. This is due to the fact that the incident wave is blocked and cannot pass through the MF. Conversely, when the amplitude of the input displacement increases, the value of TR becomes more than zero; hence, the MF has an adverse effect. With reference to Figure 11, an amplification area is seen for the frequency region below 18.733 Hz, followed by an attenuation region from 18.733 to 18.984 Hz where the wave cannot propagate throughout the MF. The second attenuation zone is seen for frequencies over 22.4 Hz. Based on the obtained responses, the MF reduces the amplitude of waves with frequencies falling in the stop band. Since an earthquake is a random phenomenon with a wide range of frequencies, and its frequency content cannot be predetermined, the effectiveness of MF is limited to those ranges of frequencies which it is designed for.

7.2. Effect of the Frequency Content of the Excitation

To evaluate the influence of the characteristics of the input excitation, the PI of the seismic responses of both squat and slender tanks are depicted in Figure 12 against the predominant frequency of the considered earthquake. The predominant frequency is determined through the signal processing of considered earthquake ground motions and by selecting the maximum spectral acceleration occurring in their acceleration response spectra.

Besides, a linear regression line is plotted to observe the overall trend of the responses over the frequencies of the considered earthquake ground motions. Generally, it is seen that the PI of the displacement of the impulsive mass, overturning moment, and base shear of the squat tank is less than one for all of the ground motions with the predominant frequency higher than the frequency corresponding to impulsive mass. Conversely, both a PI of less and more than one were observed for the aforementioned responses when the system was subjected to ground motions with the predominant frequency lower than the frequency of the impulsive mass. In the case of the slender tank, the PI of more than one was observed for the impulsive displacement, overturning moment, and base shear when the system was subjected to excitations with the predominate frequency lower than the impulsive frequency. Besides, for those earthquakes with a predominant frequency higher than the impulsive mass frequency, a PI of less and more than one can be observed.

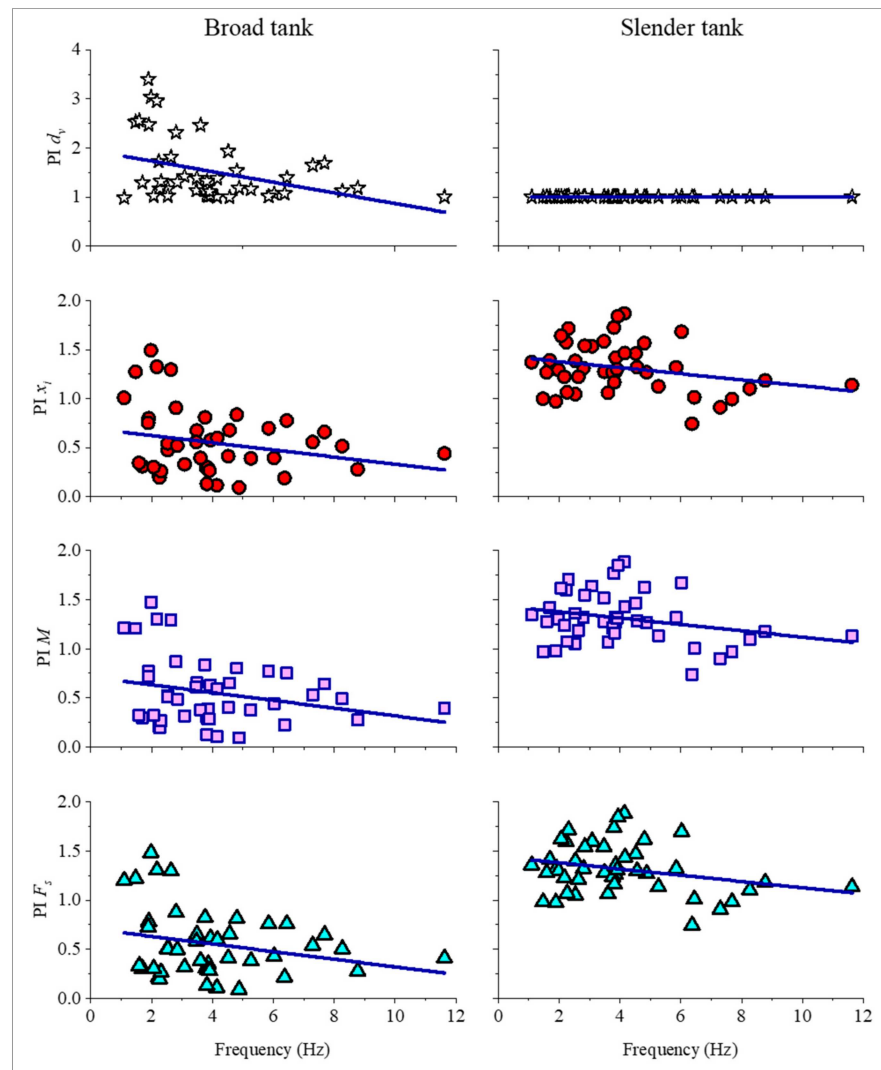


Figure 12. Effect of the frequency content of input earthquake on performance index of seismic responses of squat and slender tanks.

7.3. Effect of Number of Layers

In this section, the effect of the number of layers of MetaFoundation on the seismic responses of squat and slender liquid storage tanks is investigated. The height of each layer is kept constant at 2.0 m, and the properties of unit cells are the same as those mentioned in the previous sections. For the required analysis, five types of MF with one, two, three, four, and five layers are considered. For a better comparison of the obtained results, the numerical results provided in terms of performance index under various considered ground motions are shown in Figure 13.

In the case of the squat tank, one can see that the performance index of the displacement of impulsive mass, overturning moment on the foundation, and structural base shear decreases as the number of layers. Therefore, the more layers there are, the more reduction in the responses. Conversely, for the slender tank, it is seen that as the number of layers of MetaFoundation increases, the displacement of the impulsive mass, overturning moment on the MF, and base shear significantly increase. According to the TR shown in Figure 14, the boundary of the stop band becomes steeper when the number of layers of MF increases, leading to more attenuation of the input energy in this region. Conversely, for other regions other than the stop band, the TR increases, causing the intensify of the input energy. Therefore, the seismic responses of the squat tank are decreased, and those of the slender tank are magnified.

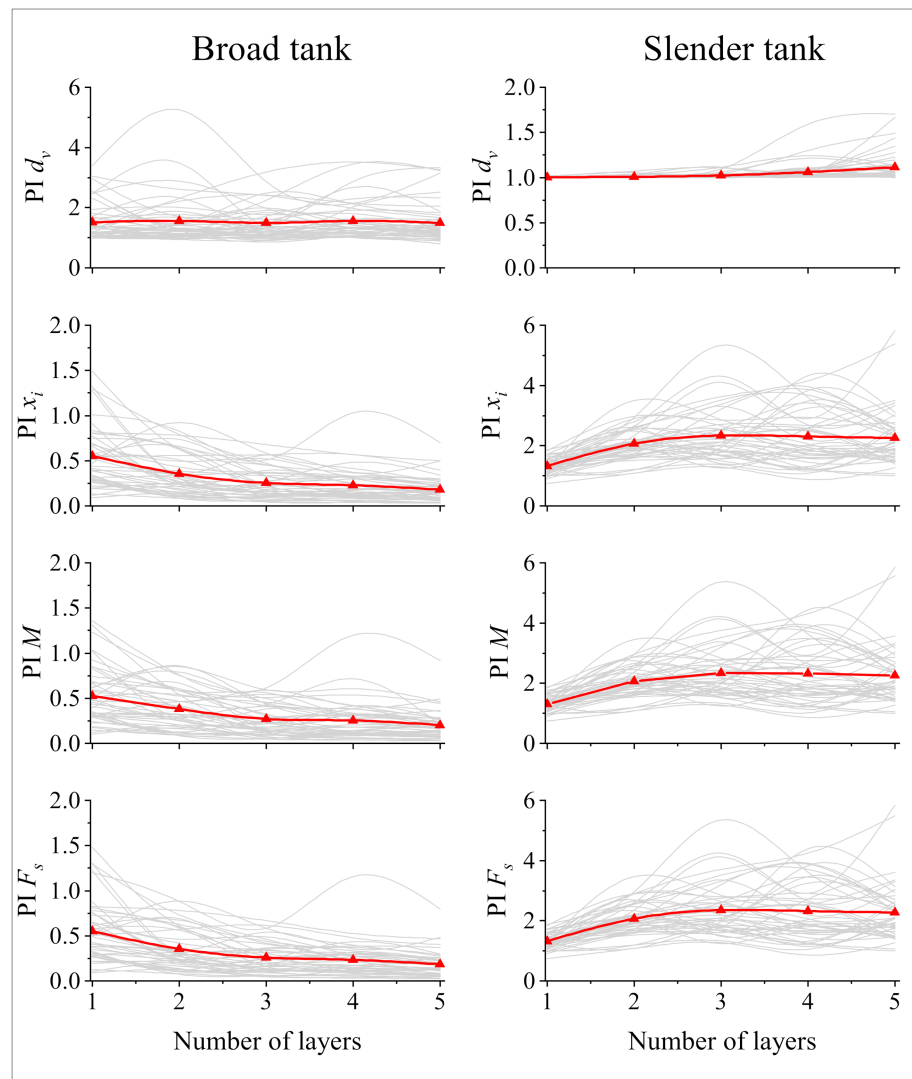


Figure 13. Effect of the number of layers on various seismic responses of squat and slender liquid storage tanks.

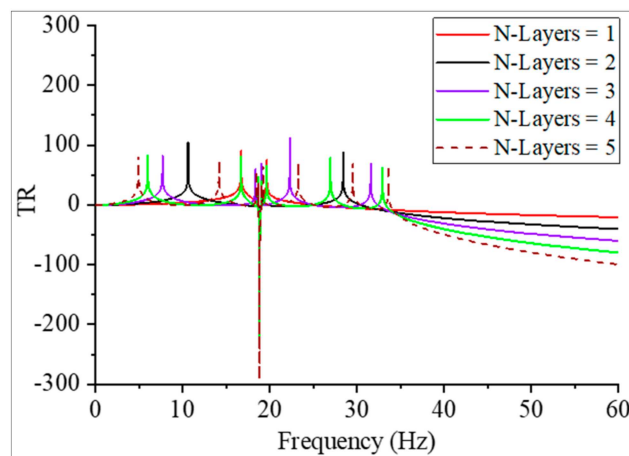


Figure 14. Effect of the number of layers on the TR on top of the foundation.

In terms of the vertical displacement of the free surface, it is observed that the mean PI of vertical displacement of the free surface remains constant for the different number of layers in the squat tank. However, a slight increase is observed in the slender tank.

7.4. Effect of Rubber Thickness (t_r)

The effect of rubber thickness on the seismic responses of liquid storage tanks is investigated here. Five different rubber thicknesses, $t_r = 0.01, 0.02, 0.03, 0.04, 0.05$ m were considered for the models. The dimension of the unit cell and the heavy core is the same with other sections. The obtained responses of squat and slender tanks subjected to various ground motions are illustrated in Figure 15.

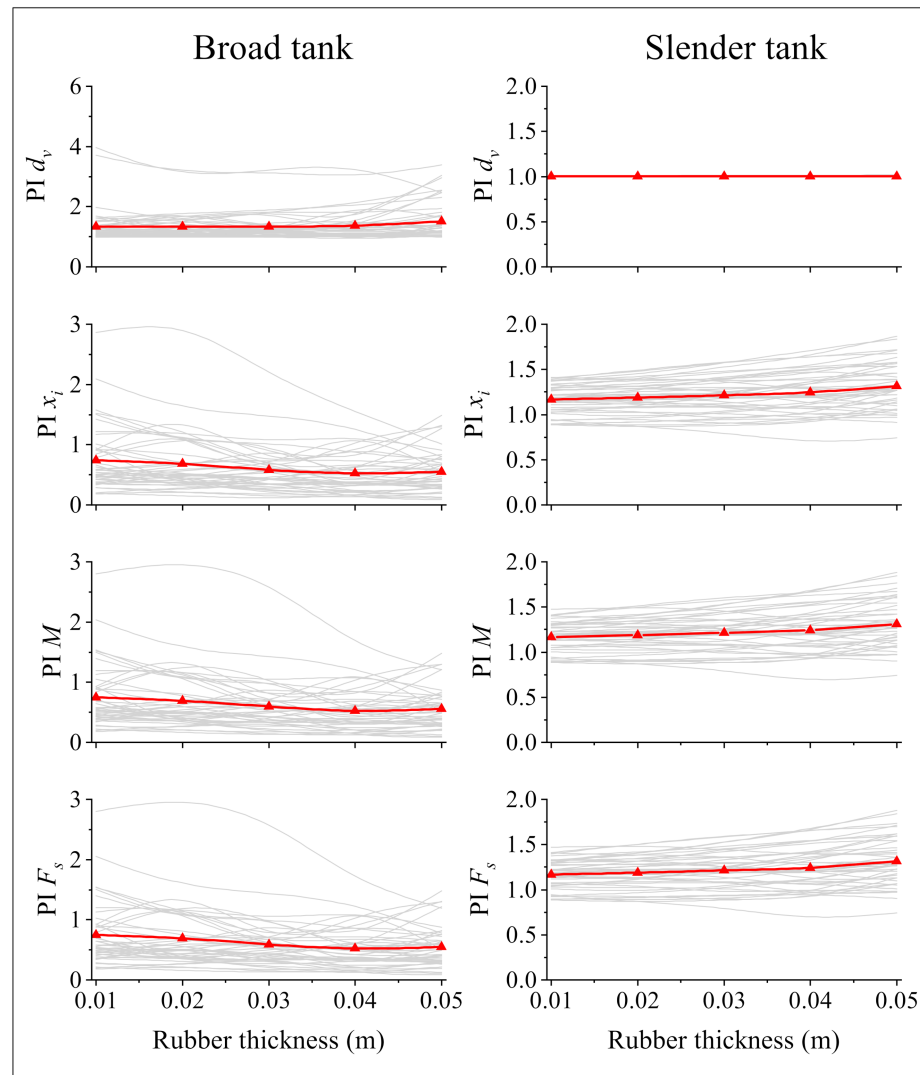


Figure 15. Effect of thickness of rubber (t_r) on various seismic responses of squat and slender liquid storage tanks.

From the obtained response, one can observe that the free vertical surface displacement (d_v) is not sensitive to rubber thickness (t_r), and these responses are almost constant for various values of rubber thickness. Conversely, other seismic responses are changed with the change in rubber thickness. The obtained results show that as the thickness of rubber increases, the displacement of the impulsive mass (x_i), overturning moment on the MF, and base shear (M and F_s) decreases in the squat tank, leading to the improvement in the performance of the liquid storage tank. Conversely, a slight increase is observed in the impulsive mass displacement, overturning moment, and base shear of the slender tank. However, a fluctuation trend is seen for some earthquakes in both squat and slender tanks. This is attributed to the frequency content of earthquake ground motion, which affects the performance of MF.

7.5. Effect of Damping of Soft Material

In this section, the effect of damping of soft material on the seismic response of considered liquid storage tanks is investigated. In order to study the effect of damping, five different damping ratios of ζ_{SM} are considered as 0.05, 0.1, 0.15, 0.2, 0.25 and 0.3, respectively. The dimension of unit cell, heavy core, and thickness of soft material are assumed to be the same with the previous sections. Figure 16 illustrates the effect of damping ratios on the maximum responses of both liquid storage tanks.

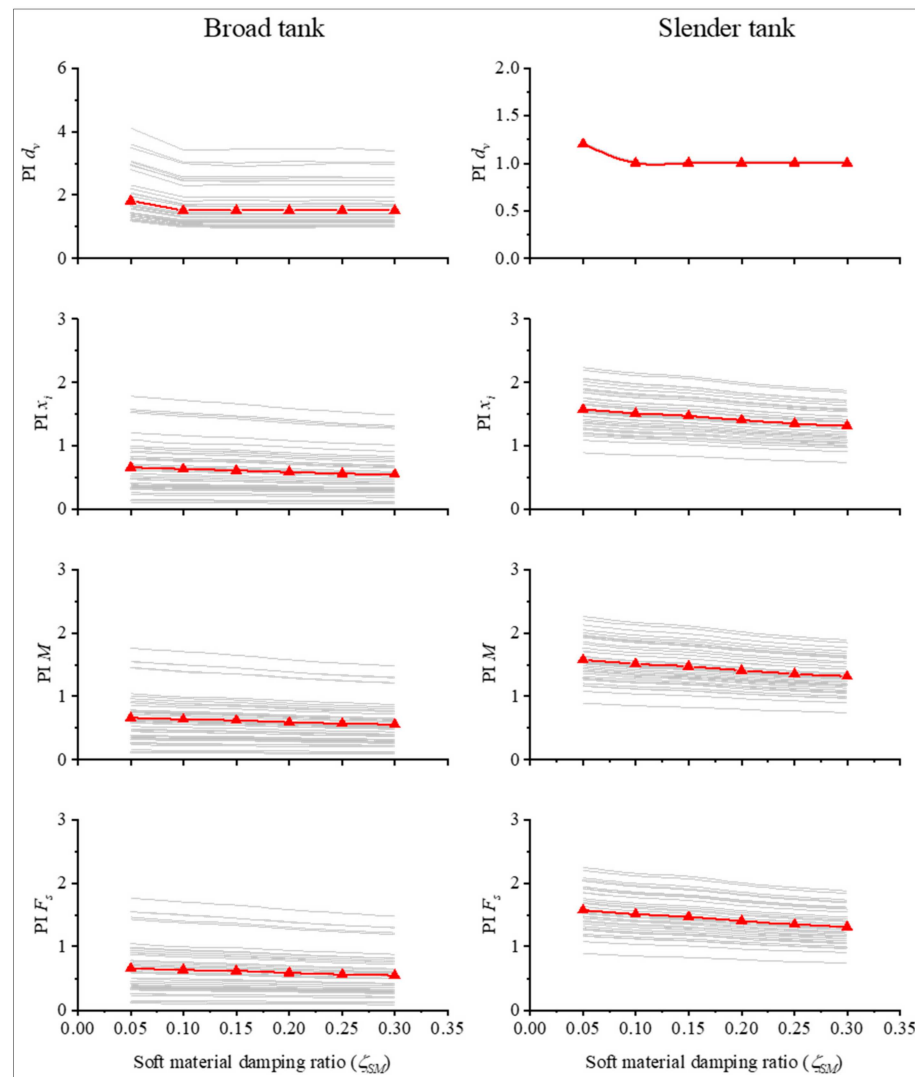


Figure 16. Effect of soft material damping ratio on the seismic response of squat and slender liquid storage tanks.

The results obtained from time history analysis indicate that the damping ratios of soft material affects the maximum responses of structures. The more damping ratios there are, the more the impulsive mass displacement (x_i) becomes reduced. As a result of such reduction, the overturning moment (M) recorded on the MF and the structural base shear (F_s) are decreased. However, it is seen that the damping ratio of soft material has no significant effect on the vertical displacement of free surface (d_v).

8. Conclusions

This paper evaluates the effectiveness of a novel foundation called MetaFoundation (MF) on the seismic response of liquid storage tanks. The MF comprises concrete and cubic shape steel coated with rubber as a soft layer. The concept of the MF is based on the finite

locally resonant metamaterials, which produce a stop band to avoid the propagation of waves. The obtained results indicate that the MF has the capability to reduce the seismic response of squat liquid storage tanks, such as displacement of the impulsive mass, overturning moment, and base shear. Conversely, the obtained performance indexes indicate that the use of MF will lead to an increase in the seismic responses of the slender tank.

The effects predominant frequency of earthquakes, the number of layers of metamaterial, rubber thickness, and damping ratios of soft material were studied. The results confirm that as the number of metamaterials increases, more reductions can be observed in the TR of the stop band; therefore, the displacement of the impulsive mass, overturning moment on the top of the foundation, and base shear of squat tank decreases. However, the displacement of free vertical surface displacement was not significantly affected. Besides, the obtained responses show that the rubber thickness has an insignificant effect on the vertical displacement of the free surface of the squat tank, while other responses such as impulsive mass displacement, overturning moment, and structural base shear reduce when the rubber thickness increases. Furthermore, it was observed that the use of MF amplified the seismic responses of the slender tank. The results indicated that as the number of layers of metamaterial increases, the results become more reduced.

Author Contributions: Conceptualization, M.F. and M.I.K.; methodology, M.F. and M.I.K.; software, M.F.; validation, M.F., M.I.K. and P.S.; formal analysis, M.F.; investigation, M.F.; resources, P.S.; data curation, M.F.; writing—original draft preparation, M.F.; writing—review and editing, P.S.; visualization, M.I.K.; supervision, M.I.K.; project administration, M.I.K.; funding acquisition, P.S. All authors have read and agreed to the published version of the manuscript.

Funding: No specific funding was received for this article.

Institutional Review Board Statement: Not applicable.

Informed Consent Statement: Not applicable.

Data Availability Statement: The data presented in this study are available on request from the corresponding author. The data are not publicly available.

Conflicts of Interest: The authors declare no conflict of interest.

References

- Cooper, T.W. *A Study of the Performance of Petroleum Storage Tanks during Earthquakes, 1933–1995*; US National Institute of Standards and Technology: Gaithersburg, MD, USA, 1997.
- Hamdan, F. Seismic behaviour of cylindrical steel liquid storage tanks. *J. Constr. Steel Res.* **2000**, *53*, 307–333. [CrossRef]
- Lee, C.-B.; Lee, J.-H. Nonlinear Dynamic Response of a Concrete Rectangular Liquid Storage Tank on Rigid Soil Subjected to Three-Directional Ground Motion. *Appl. Sci.* **2021**, *11*, 4688. [CrossRef]
- Zhao, Y.; Li, H.-N.; Zhang, S.; Mercan, O.; Zhang, C. Seismic Analysis of a Large LNG Tank Considering Different Site Conditions. *Appl. Sci.* **2020**, *10*, 8121. [CrossRef]
- Zhang, R.; Chu, S.; Sun, K.; Zhang, Z.; Wang, H. Effect of the Directional Components of Earthquakes on the Seismic Behavior of an Unanchored Steel Tank. *Appl. Sci.* **2020**, *10*, 5489. [CrossRef]
- Jing, W.; Feng, H.; Cheng, X. Dynamic responses of liquid storage tanks caused by wind and earthquake in special environment. *Appl. Sci.* **2019**, *9*, 2376. [CrossRef]
- Zhang, S.; Zhang, R.; Zhao, Z. Demand-Based Optimal Design of Storage Tank with Inerter System. *Shock. Vib.* **2017**, *2017*, 2956153. [CrossRef]
- Malhotra, P.K. New method for seismic isolation of liquid-storage tanks. *Earthq. Eng. Struct. Dyn.* **1997**, *26*, 839–847. [CrossRef]
- Shrimali, M.; Jangid, R. A comparative study of performance of various isolation systems for liquid storage tanks. *Int. J. Struct. Stab. Dyn.* **2002**, *2*, 573–591. [CrossRef]
- Shrimali, M.; Jangid, R. Seismic response of liquid storage tanks isolated by sliding bearings. *Eng. Struct.* **2002**, *24*, 909–921. [CrossRef]
- Shekari, M.; Khaji, N.; Ahmadi, M. A coupled BE–FE study for evaluation of seismically isolated cylindrical liquid storage tanks considering fluid–structure interaction. *J. Fluids Struct.* **2009**, *25*, 567–585. [CrossRef]
- Shekari, M.; Khaji, N.; Ahmadi, M. On the seismic behavior of cylindrical base-isolated liquid storage tanks excited by long-period ground motions. *Soil Dyn. Earthq. Eng.* **2010**, *30*, 968–980. [CrossRef]
- Abali, E.; Uckan, E. Parametric analysis of liquid storage tanks base isolated by curved surface sliding bearings. *Soil Dyn. Earthq. Eng.* **2010**, *30*, 21–31. [CrossRef]

14. Jadhav, M.B.; Jangid, R.S. Response of Base-Isolated Liquid Storage Tanks. *Shock. Vib.* **2004**, *11*, 276030. [CrossRef]
15. Farajian, M.; Khodakarami, M.I.; Kontoni, D.-P.N. Evaluation of Soil-Structure Interaction on the Seismic Response of Liquid Storage Tanks under Earthquake Ground Motions. *Computation* **2017**, *5*, 17. [CrossRef]
16. Karkabadi, A.; Khodakarami, M.I.; Farajian, M. Seismic Response of Steel Frame by Considering Soil-Structure Interaction under Seismic Sequence. *J. Struct. Constr. Eng.* **2021**, *8*, 66–86.
17. Bagheri, S.; Farajian, M. The effects of input earthquake characteristics on the nonlinear dynamic behavior of FPS isolated liquid storage tanks. *J. Vib. Control* **2018**, *24*, 1264–1282. [CrossRef]
18. Cheng, X.; Jing, W.; Chen, J.; Zhang, X. Pounding Dynamic Responses of Sliding Base-Isolated Rectangular Liquid-Storage Structure considering Soil-Structure Interactions. *Shock. Vib.* **2017**, *2017*, 8594051. [CrossRef]
19. Bagheri, S.; Farajian, M. Seismic Response of Base Isolated Liquid Storage Tanks under Near Fault Ground Motions. *Athens J. Technol. Eng.* **2016**, *3*, 153–161. [CrossRef]
20. Tsiavos, A.; Sextos, A.; Stavridis, A.; Dietz, M.; Dihoru, L.; Alexander, N.A. Experimental investigation of a highly efficient, low-cost PVC-Rollers Sandwich (PVC-RS) seismic isolation. *Structures* **2021**, *33*, 1590–1602. [CrossRef]
21. Tsiavos, A.; Markic, T.; Schlatter, D.; Stojadinovic, B. Shaking table investigation of inelastic deformation demand for a structure isolated using friction-pendulum sliding bearings. *Structures* **2021**, *31*, 1041–1052. [CrossRef]
22. Mead, D. Wave propagation in continuous periodic structures: Research contributions from Southampton, 1964–1995. *J. Sound Vib.* **1996**, *190*, 495–524. [CrossRef]
23. Sigalas, M.; Kushwaha, M.S.; Economou, E.N.; Kafesaki, M.; Psarobas, I.E.; Steurer, W. Classical vibrational modes in phononic lattices: Theory and experiment. *Z. Krist.-Cryst. Mater.* **2005**, *220*, 765–809. [CrossRef]
24. Bao, J.; Shi, Z.; Xiang, H. Dynamic responses of a structure with periodic foundations. *J. Eng. Mech.* **2011**, *138*, 761–769. [CrossRef]
25. Sun, F.; Xiao, L.; Bursi, O.S. Optimal design and novel configuration of a locally resonant periodic foundation (LRPF) for seismic protection of fuel storage tanks. *Eng. Struct.* **2019**, *189*, 147–156. [CrossRef]
26. Sun, F.; Xiao, L. Bandgap characteristics and seismic applications of inerter-in-lattice metamaterials. *J. Eng. Mech.* **2019**, *145*, 04019067. [CrossRef]
27. Farajian, M.; Sharafi, P.; Kildashti, K. The influence of inter-module connections on the effective length of columns in multi-story modular steel frames. *J. Constr. Steel Res.* **2021**, *177*, 106450. [CrossRef]
28. Alembagheri, M.; Sharafi, P.; Rashidi, M.; Bigdeli, A.; Farajian, M. Natural dynamic characteristics of volumetric steel modules with gypsum sheathed LSF walls: Experimental study. *Structures* **2021**, *33*, 272–282. [CrossRef]
29. Jia, G.; Shi, Z. A new seismic isolation system and its feasibility study. *Earthq. Eng. Eng. Vib.* **2010**, *9*, 75–82. [CrossRef]
30. Mitchell, S.J.; Pandolfi, A.; Ortiz, M. Metaconcrete: Designed aggregates to enhance dynamic performance. *J. Mech. Phys. Solids* **2010**, *65*, 69–81. [CrossRef]
31. Dertimanis, V.K.; Antoniadis, I.A.; Chatzi, E.N. Feasibility analysis on the attenuation of strong ground motions using finite periodic lattices of mass-in-mass barriers. *J. Eng. Mech.* **2016**, *142*, 04016060. [CrossRef]
32. Maleki, M.; Khodakarami, M. Feasibility analysis of using MetaSoil scatterers on the attenuation of seismic amplification in a site with triangular hill due to SV-waves. *Soil Dyn. Earthq. Eng.* **2017**, *100*, 169–182. [CrossRef]
33. Basone, F.; Wenzel, M.; Bursi, O.S.; Fossetti, M. Finite locally resonant Metafoundations for the seismic protection of fuel storage tanks. *Earthq. Eng. Struct. Dyn.* **2019**, *48*, 232–252. [CrossRef]
34. Aguzzi, G.; Kanellopoulos, C.; Wiltshaw, R.; Craster, R.V.; Chatzi, E.N.; Colombi, A. Octet lattice-based plate for elastic wave control. *Sci. Rep.* **2022**, *12*, 1088. [CrossRef]
35. Cheng, Z.; Shi, Z. Novel composite periodic structures with attenuation zones. *Eng. Struct.* **2013**, *56*, 1271–1282. [CrossRef]
36. Institute, A.P. *Seismic Design of Storage Tanks-Appendix E, Welded Steel Tanks for Oil Storage*; API Publishing Services: Washington, DC, USA, 2007.
37. American Society of Civil Engineers. *Minimum Design Loads and Associated Criteria for Buildings and Other Structures*; American Society of Civil Engineering & Structural Engineering Institute: Reston, VA, USA, 2016.
38. European Committee for Standardization. *Eurocode 8: Design of Structures for Earthquake Resistance-Part 4: Silos, Tanks and Pipelines*; European Committee for Standardization: Brussels, Belgium, 2006.
39. Housner, G.W. The dynamic behavior of water tanks. *Bull. Seismol. Soc. Am.* **1963**, *53*, 381–387. [CrossRef]
40. Haroun, M.A.; Housner, G.W. Seismic design of liquid storage tanks. *J. Tech. Counc. ASCE* **1981**, *107*, 191–207. [CrossRef]
41. Malhotra, P.K.; Wenk, T.; Wieland, M. Simple procedure for seismic analysis of liquid-storage tanks. *Struct. Eng. Int.* **2000**, *10*, 197–201. [CrossRef]
42. FEMA. *Quantification of Building Seismic Performance Factors*; US Department of Homeland Security, FEMA: Washington, DC, USA, 2009.

Article

Semi-Active Cable Damping to Compensate for Damping Losses Due to Reduced Cable Motion Close to Cable Anchor

Felix Weber ^{1,*} , Simon Spensberger ², Florian Obholzer ², Johann Distl ³ and Christian Braun ²¹ Maurer Switzerland GmbH, Grossplatzstrasse 24, 8118 Pfaffhausen, Switzerland² Maurer SE, Frankfurter Ring 193, 80807 Munich, Germany; s.spensberger@maurer.eu (S.S.); f.obholzer@maurer.eu (F.O.); c.braun@maurer.eu (C.B.)³ Maurer Engineering GmbH, Frankfurter Ring 193, 80807 Munich, Germany; j.distl@maurer.eu

* Correspondence: f.weber@maurer.eu

Abstract: The relative motion of transverse cable dampers is smaller than predicted by the taut string model because of the effects of bending stiffness and fixed support conditions. As a result of the reduced damper motion, the dissipated energy per cycle is reduced as well, which may explain why damping measurements on real stay cables with transverse dampers often show lower cable damping ratios than expected from the taut string theory. To compensate for the reduced damper motion and damper efficiency, respectively, a semi-active cable damper is proposed. The controllable damper is realized by a hydraulic oil damper with real-time controlled bypass valve whereby the resulting damper force is purely dissipative. The proposed control law is clipped viscous damping with negative stiffness. The viscous coefficient is adjusted in real time to the actual frequency of vibration to generate optimum modal damping while the negative stiffness component partially compensates for the reduced damper motion due to the flexural rigidity and fixed support conditions of the cable. The measurements of the prototype semi-active hydraulic damper are used to derive a precise model of the semi-active damper force including the control force constraints due to the fully open and fully closed bypass valve. This model is used to compute the cable damping ratios of the first four cable modes, for typical damper positions, for a taut string model and for a cable model with flexural rigidity and fixed supported ends. The obtained cable damping ratios are compared to those resulting from the passive linear viscous damper being optimized to the first four cable modes. The results demonstrate that the proposed semi-active cable damper with the consideration of the minimum and maximum control force constraints significantly enhances the cable damping of the first four modes compared to the linear viscous damper.

Citation: Weber, F.; Spensberger, S.; Obholzer, F.; Distl, J.; Braun, C. Semi-Active Cable Damping to Compensate for Damping Losses Due to Reduced Cable Motion Close to Cable Anchor. *Appl. Sci.* **2022**, *12*, 1909. <https://doi.org/10.3390/app12041909>

Academic Editor: Elsa Caetano

Received: 2 December 2021

Accepted: 7 February 2022

Published: 11 February 2022

Publisher's Note: MDPI stays neutral with regard to jurisdictional claims in published maps and institutional affiliations.



Copyright: © 2022 by the authors. Licensee MDPI, Basel, Switzerland. This article is an open access article distributed under the terms and conditions of the Creative Commons Attribution (CC BY) license (<https://creativecommons.org/licenses/by/4.0/>).

Keywords: cable; control; damping; semi-active; negative stiffness; vibration

1. Introduction

Stay cables are susceptible to vibrations because of their low inherent damping [1,2]. The transverse cable amplitude may become unacceptably large when the excitation frequency due to vertex-shedding matches one of the cable eigenfrequencies whereby the entire excitation energy is transmitted to one modal component [2–10]. Such cable vibrations with amplitudes in the range of 0.3 m to 0.6 m have been observed on several stay-cable bridges, e.g., the Dongting Lake Bridge in China [11], the Franjo Tudjman Bridge in Croatia [12] or the Alamillo Bridge in Spain [13].

The common countermeasure is to install transverse cable dampers close to the deck anchor [14–18]. The selection of the damper position relative to the cable length, which is often between 2% and 3%, is a critical issue. On the one hand, the damper position must be great enough to guarantee at least the required damping ratios in the targeted modes. On the other hand, the damper must not be positioned too far away from the deck anchor because of aesthetic reasons, additional costs of tall damper supports and

geometrical conflicts of the damper support with the anchor of the neighbour cable. The common procedure is to optimize the viscous damper coefficient to the targeted modes in order to guarantee at the required damping in lowest and highest targeted modes whereby the damper position is automatically minimized [19]. This analytical method is based on optimum modal damping, assuming that the cable can be modelled as a taut string, i.e., a cable without bending rigidity and with simply supported ends [14–16]. However, real cables show the effects due to bending rigidity and fixed support end conditions which necessitates a different design of the damper viscous coefficient and reduces the attainable cable damping ratio significantly as presented in [20–22]. The studies [20–22] estimate that the bending rigidity and fixed support end conditions reduce the attainable cable damping ratio in one target mode by approximately 20% compared to the attainable damping ratio assuming a taut string behaviour. However, the experimental investigations on a single strand with fixed support end conditions and bending rigidity described in [23,24] demonstrate that the cable motion at typical damper positions is reduced by 20% to 40% compared to the taut string model prediction. This means that the cable damping ratio due to a transverse damper is at least 20% to 40% smaller than expected from the closed-form solution $\frac{1}{2} a/L$ (a : damper position, L : cable length, valid for $a/L \approx 1$ %) being valid for a taut string behaviour. This estimation agrees well with the experiments reported in [25–31] which show that the measured additional cable damping ratio due to the transverse damper, i.e., the total cable damping ratio minus the inherent cable damping ratio, is often around 50% to 70% of the theoretical value $\frac{1}{2} a/L$ being valid for a taut string behaviour. Besides the effect of the reduced damper motion, other effects may also lead to reduced cable damping ratios such as insufficient damper activation due to manpower excitation of real stay cables with great modal mass [32], friction damping [33–35], excitation of higher order modes necessitating low pass filtering during post-processing of the measurement data [29,35], force tracking errors in case of controllable dampers [24–27,36–40] and the fact that the damping estimation $\frac{1}{2} a/L$ is valid for $a/L \approx 1$ % but transverse dampers are commonly positioned at 2% to 3% of the cable length.

This testimony of cable damper tests and even the development of other damper concepts [41–43] show that efficient and reliable stay cable dampers is a need to ensure the serviceability of cable-stayed bridges [44]. This paper therefore describes the damping efficiency of a prototype semi-active hydraulic damper whose actual force is controlled in real time by the controlled bypass between the minimum and maximum damping forces due to the fully open and fully closed bypass valve. The adopted control law is clipped viscous damping with negative stiffness whose viscous coefficient is adjusted to the actual frequency of motion in real time generating optimum modal damping and the negative stiffness force helps to increase the damper motion in order to dissipate more energy than the passive damper. The implementation of the control law in programmable logic control (PLC) is explained and the according control flow chart is presented. Furthermore, it is explained how the control force tracking task is solved without the use of a force feedback in order to save the costs of a force transducer for each semi-active cable damper. The cable damping ratios resulting from this adaptive damper with the consideration of the minimum and maximum damper force constraints are computed for the first four cable modes, for typical damper positions, for a taut string cable model and for a cable model with the effects of bending rigidity and fixed support conditions. The results are compared to those obtained from the passive linear viscous damper being optimized to one targeted mode and the passive linear viscous damper being optimized to the first four targeted modes. The former benchmark is a theoretical one because transverse dampers are never optimized to one modal component only while the latter benchmark represents the practical one. The comparative study demonstrates that the proposed prototype semi-active damper significantly enhances the cable damping ratios of the targeted modes even with the control force limitations due to the fully open and fully closed bypass valve.

2. Cable with Passive Transverse Damper

2.1. Cable without Bending Rigidity and Simply Supported Ends

The cable model without bending rigidity and with simply supported ends is given by the taut string model

$$T \frac{\partial^2 v(x, t)}{\partial x^2} - m \frac{\partial^2 v(x, t)}{\partial t^2} = f \delta(x - a) \tag{1}$$

where T denotes the cable force, m is the mass per unit length, $v(x, t)$ is the transverse cable motion, f describes the force of the transverse damper, $\delta(x - a)$ is the Dirac delta function that applies the damper force f at position $x = a$ where a is the damper position from the left anchor. For the real cable the left anchor corresponds to the anchor on the bridge deck (Figure 1a). The boundary conditions for the simply supported ends become

$$v(x = 0, t) = 0, \frac{\partial^2 v(x = 0, t)}{\partial x^2} = 0, v(x = L, t) = 0, \frac{\partial^2 v(x = L, t)}{\partial x^2} = 0 \tag{2}$$

where L is the cable length. This means that bending moments at both ends are zero whereby the modeshape functions are given by sine functions

$$V_n(x) = \sin\left(\frac{n \pi}{L} x\right) \tag{3}$$

where n is the mode number.

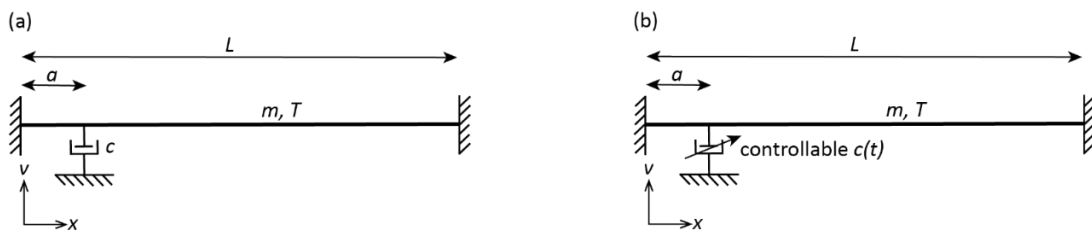


Figure 1. Schematic of cable with (a) passive transverse viscous damper and (b) with controllable transverse viscous damper.

2.2. Cable with Flexural Rigidity and Fixed Supported Ends

Modeshape measurements on a single steel strand with seven wires and fixed support ends were performed using a laser-based displacement sensor (Figure 2a). The length of the steel wire strand was approximately 15.5 m and the mass per unit length including the additional masses was approximately 1.17 kg/m and the pre-stressing force was approximately 33 kN. The measured modeshape, which can be described by sinus-hyperbolics and cosine-hyperbolics functions, clearly deviates from the sinusoidal modeshape function being valid for a taut string with simply supported ends and without flexural rigidity (Figure 2b). The measurements show that the transverse cable motion especially deviates from the sinusoidal modeshape between the anchor and approximately 5% of the cable length which is the range where transverse dampers are commonly positioned. If the cable model includes the fixed end conditions and the flexural rigidity, the cable can be modelled by the beam modelling approach

$$E I \frac{\partial^4 v(x, t)}{\partial x^4} + T \frac{\partial^2 v(x, t)}{\partial x^2} - m \frac{\partial^2 v(x, t)}{\partial t^2} = f \delta(x - a) \tag{4}$$

where E is the elastic modulus of the cable and I is the second moment of area. The boundary conditions for the case of the fixed supported ends are as follows:

$$v(x = 0, t) = 0, \frac{\partial v(x = 0, t)}{\partial x} = 0, v(x = L, t) = 0, \frac{\partial v(x = L, t)}{\partial x} = 0 \tag{5}$$

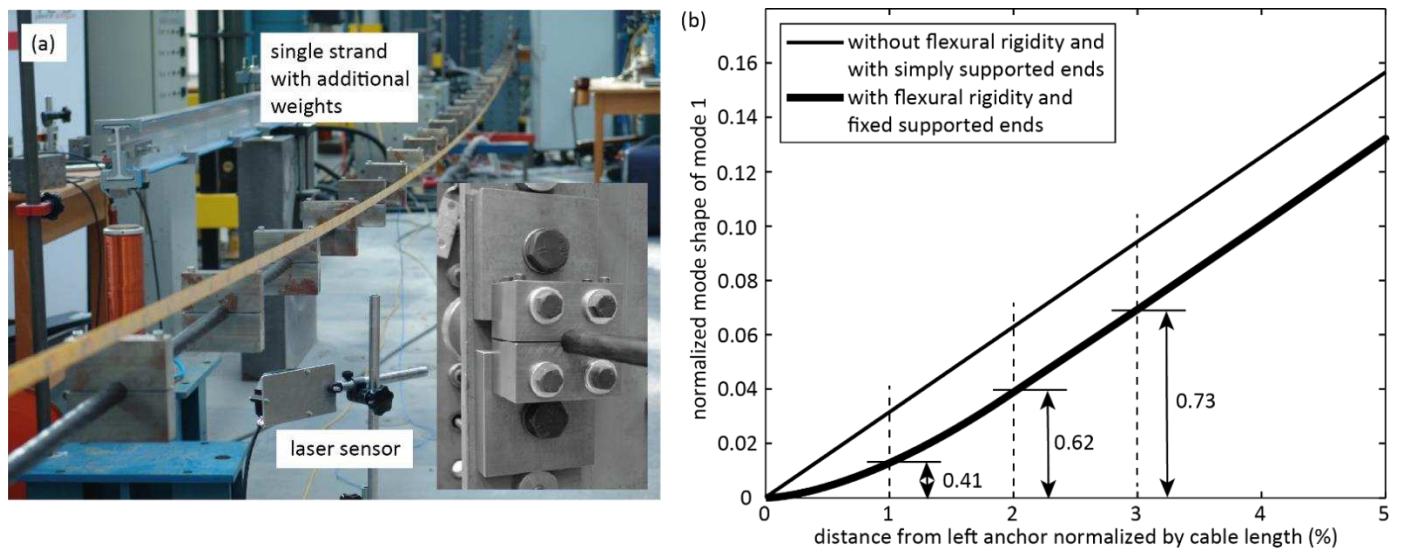


Figure 2. Measured modeshape of first cable mode: (a) single strand with additional masses and fixed support conditions (close-up) and (b) measured modeshape compared to theoretical modeshape due to simply supported ends.

These boundary conditions mean that the bending moments at both cable ends are not zero which leads to modeshape functions based on a linear combination of sine-hyperbolic, cosine-hyperbolic, sine and cosine functions

$$V_n(x) = -\frac{\alpha_n}{\beta_n} \sinh(\beta_n x) - \frac{1}{\theta_n} \cosh(\beta_n x) + \sin(\beta_n x) + \frac{1}{\theta_n} \cos(\beta_n x) \quad (6)$$

$$\theta_n = \frac{\beta_n \sinh(\beta_n L) + \alpha_n \sin(\alpha_n L)}{-\alpha_n \cosh(\beta_n L) + \alpha_n \cos(\alpha_n L)} \quad (7)$$

where $\alpha_1 L = 3.181$ and $\beta_1 L = 1.624$ etc., see [23]. This cable model is validated by adjusting $E I$ to obtain the measured modeshape.

2.3. Cable Model for Simulation

For the simulation of the cable model with transverse damper, the partial differential Equations (1) and (3) are discretized, adopting a finite truss element modelling approach with the spatial sampling interval $\Delta x \ll L$ that is selected small enough to ensure precise approximation of the partial differential Equations (1) and (3) [24,34,35,45]

$$M \ddot{v} + C \dot{v} + K v = \varphi f(t) + F_{ex} \quad (8)$$

where M , C and K denote the mass, damping and stiffness matrices, v is the vector of the transverse displacements, φ is the connectivity vector of the transverse damper force and the excitation force vector F_{ex} is introduced to excite the cable model harmonically at the eigenfrequencies of the considered modes. The inherent cable damping ratio ζ_{cable} is assumed to be 0.4% which is a typical value of the first few modes of stay cables [2,29,30].

2.4. Optimum Viscous Damper for One Targeted Mode and Taut String Behaviour

The force of the passive transverse damper is assumed to produce linear viscous damping

$$f(t) = -c \frac{\partial v(a, t)}{\partial t} \quad (9)$$

where c denotes the viscous damper coefficient in (Ns/m). According to the literature [14–16], the optimum value of c for maximum damping in mode n and assuming that the cable dynamics can be described by the taut string model is given as follows

$$c = c_n^{opt} = \frac{T}{a \omega_n} \tag{10}$$

where ω_n denotes the eigenfrequency in rad/s of mode n . The resulting damping ratio in mode n is given by the simple approximation

$$\zeta_n \approx \frac{1}{2} \frac{a}{L} \tag{11}$$

The expressions (10) and (11) are only valid for a taut string, i.e., a cable with simply supported ends and without flexural rigidity, and a transverse damper being optimized to one targeted mode and not to several modes as commonly specified for real stay cables.

2.5. Optimum Viscous Damper for Several Targeted Modes and Taut String Behaviour

Cable dampers are always specified to provide at least the required damping ratio in several targeted modes, e.g., the first four modes. Then, the solution (10), which maximizes the damping in one targeted mode, does not yield the optimum tuning of the transverse damper. As shown in [19], the optimum tuning of c targeting several modes is obtained by equating the damping ratios in the lowest (mode number i) and highest (mode number j) targeted modes and setting these damping ratios equal to the required damping ratio ζ_{req} . Then, the optimum of the viscous damper coefficient for maximum damping of modes i to j becomes

$$c = \left(c_{i-j}^{opt} \right)_{\min(a)} = \frac{T}{\zeta_{req} L \omega_1 (i + j)} \tag{12}$$

The according damper position is automatically minimized because the damping ratios of the lowest and highest targeted modes just meet ζ_{req} , that is

$$\left(\frac{a_{min}}{L} \right)_{i-j} = \frac{\zeta_{req} (i + j)}{\sqrt{i j}} \tag{13}$$

The resulting damping ratio in mode n then becomes

$$\left(\zeta_{i-j}^{\min(a)} \right)_n = \frac{\zeta_{req} n (i + j)}{n^2 + i j} \tag{14}$$

3. Semi-Active Cable Damper

3.1. System Description

The semi-active damper is realized using a conventional passive oil damper which is enriched by a controlled bypass with electromagnetic valve (Figure 3a). To limit the maximum viscous force at fully closed bypass valve, a small passive bypass is added. The oil volume stream of this passive bypass valve and therefore the maximum oil damper force is tuned by a passive throttle within the passive bypass. The controlled bypass valve in combination with the passive bypass generate quadratic viscous damping because both bypasses act as throttles. The controllable viscous coefficient as function of the applied electromagnetic valve current defines the control force range between the minimum and the maximum viscous coefficients; the according look-up table data is depicted in Figure 3b. The control law of clipped viscous damping with negative stiffness is computed based on the collocated relative damper motion, which is measured by the displacement sensor measuring the relative motion between damper cylinder and damper piston and which is equal to the transverse cable motion at damper position.

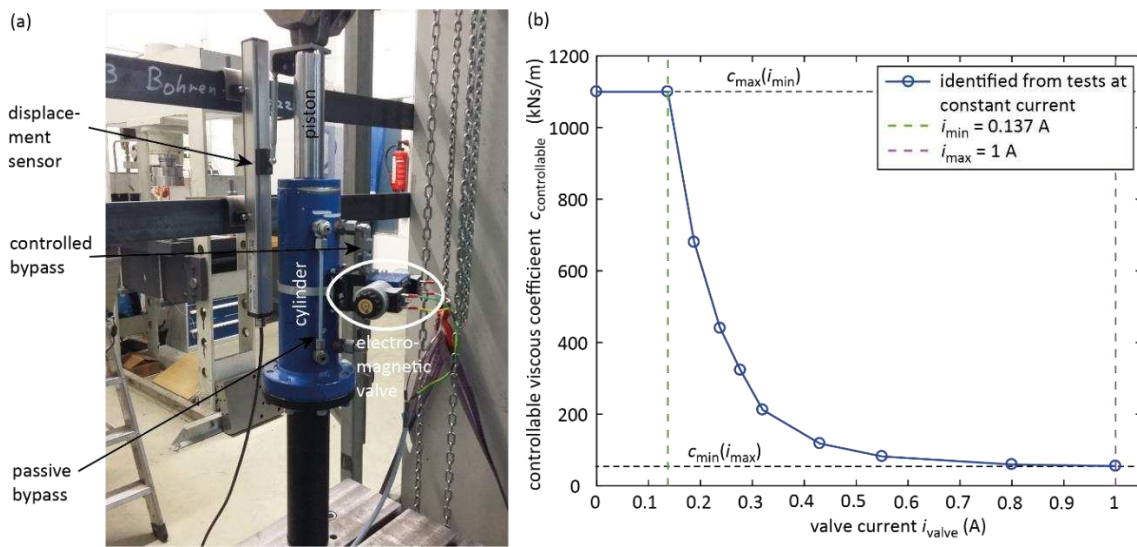


Figure 3. (a) Semi-active hydraulic damper; (b) measured steady-state relation between electromagnetic valve current and resulting controllable viscous coefficient.

3.2. Control Law

The control law is semi-active linear viscous damping with negative stiffness (clipped VDNS), which can be realized by collocated control and is proven to be a very efficient damping algorithm (Figures 1b and 5, [24,38,39]). The high damping efficiency of clipped VDNS is explained by the fact that VDNS combines energy dissipation by the viscous force while the negative stiffness force increases the relative motion of the damper which leads to increased cycle energy within the damper. In addition, the control force characteristics of VDNS are similar to those resulting from optimal control as shown in [24]. For these two reasons, i.e., enlarged damper relative motion due to the negative stiffness force and optimal control similarity, VDNS is a very effective damping strategy. Further benefits are that VDNS does not require a state observer as optimal control does and that it works for any type of excitation, i.e., for single harmonic, narrow and broad band excitations because the desired semi-active control force can be computed in real time based on the measured actual damper motion only. In the following, the most relevant steps of the control law computation are explained. The viscous damping coefficient $c_{\text{frequency}}^{\text{opt}}$ is adjusted in real time to the actual frequency of vibration in order to generate optimum modal damping (15). The negative stiffness coefficient k is formulated based on the known parameters T and a [46]. The two tuning parameters g_1 and g_2 are needed to compensate for the damping increase and stiffness loss due to the clipping of the active desired control force; more information on undesired damping increase and stiffness loss due to clipping can be found in [47]. Reasonable values for g_1 and g_2 are 0.80 and 1.20 [46]. The main modules of the control algorithm are shortly described here (Figure 5):

- Bandpass filtering of damper relative motion (displacement sensor signal, Figure 3a) to remove offset and noise in the displacement signal.
- Derivation of damper relative velocity by numeric differentiation with subsequent low pass filtering to attenuate noise due to the numeric differentiation.
- Frequency detection from the peaks of the displacement signal resulting in a maximum time delay of half a period. This time delay is more than acceptable considering that resonant vibrations are long standing vibrations, see cable vibration measurements presented in [30].
- Computing the desired active control force $f_{\text{des}}^{\text{active}}$ (17) and the desired semi-active control force $f_{\text{des}}^{\text{semi-active}}$ (18).
- The control force tracking task is solved in two steps. First, the desired viscous coefficient $c_{\text{des}}(t)$ of the controllable damper is computed based on the desired semi-

active control force (19) and the actual damper relative velocity, then the desired current of the electromagnetic valve is computed based on the steady state relation between valve current and viscous damper coefficient (Figure 3a, (20)). Equation (19) shows that the controllable damper exerts quadratic viscous damping at constant bypass valve position, i.e., at constant valve current, because both the controlled bypass valve and the passive bypass act as throttles resulting in quadratic viscous damping.

- The PID-based current controller including an anti-reset windup (ARW) due to the current limitations ensures that the actual valve current precisely tracks the desired current i_{des} .
- The state variables, which are given as function of time t in (15)–(20), are computed in real time at the controller frequency of 1000 Hz.
- The closed-loop structure consisting of hardware components, software components and cable damper dynamics is depicted in Figure 4.

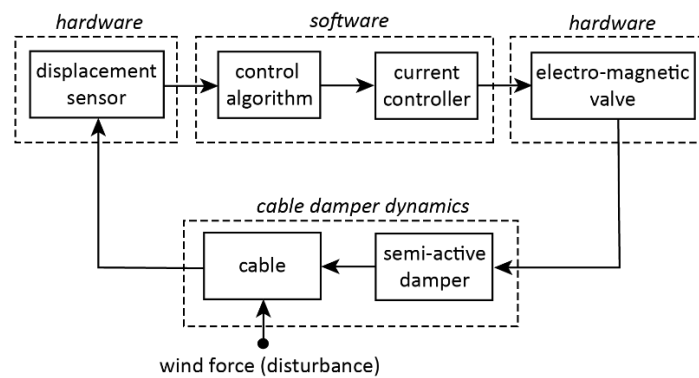


Figure 4. Closed-loop structure.

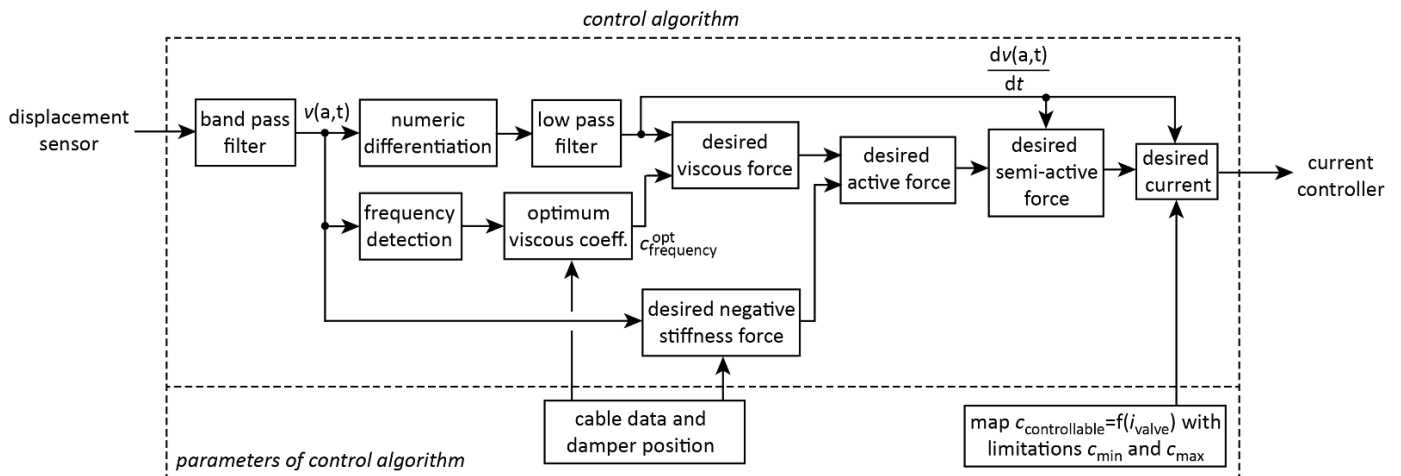


Figure 5. Structure of real-time control algorithm.

$$c_{frequency}^{opt}(t) = g_1 \frac{T}{a (2 \pi frequency(t))} \tag{15}$$

$$k = g_2 \frac{T}{a} \tag{16}$$

$$f_{des}^{active}(t) = - \left\{ c_{frequency}^{opt}(t) \frac{dv(a,t)}{dt} - k v(a,t) \right\} \tag{17}$$

$$f_{des}^{semi-active}(t) = \begin{cases} f_{des}^{active}(t) & : f_{des}^{active}(t) \frac{dv(a,t)}{dt} \leq 0 \\ 0 & : f_{des}^{active}(t) \frac{dv(a,t)}{dt} > 0 \end{cases} \quad (18)$$

$$c_{des}(t) = \frac{|f_{des}^{semi-active}(t)|}{\left(\frac{dv(a,t)}{dt}\right)^2} \quad (19)$$

$$i_{des}(t) = function(c_{des}(t), c_{min}, c_{max}) \quad (20)$$

3.3. Experimental Validation

The control algorithm described in 3.2 is experimentally validated with an active hydraulic damper imposing a displacement with defined frequency and amplitude into the semi-active damper, see Figure 3a. The goal of this experiment is to determine the real-time force tracking accuracy without using a force sensor (no force feedback in the algorithm) in order to save the costs of a load cell for each semi-active cable damper. The test results at the amplitude of 20 mm and the frequency of 0.27 Hz are depicted by the force displacement and force velocity curves of the desired semi-active control force and the actual force of the semi-active damper in Figure 6. The experimental results demonstrate that the force tracking error between the desired semi-active control force and the actual semi-active force are predominantly caused by the minimum and maximum viscous coefficients resulting from the fully open and fully closed electromagnetic valve. These force tracking errors cannot be avoided even with force feedback because the minimum and maximum viscous coefficients determine the force limitations of the controllable damper.

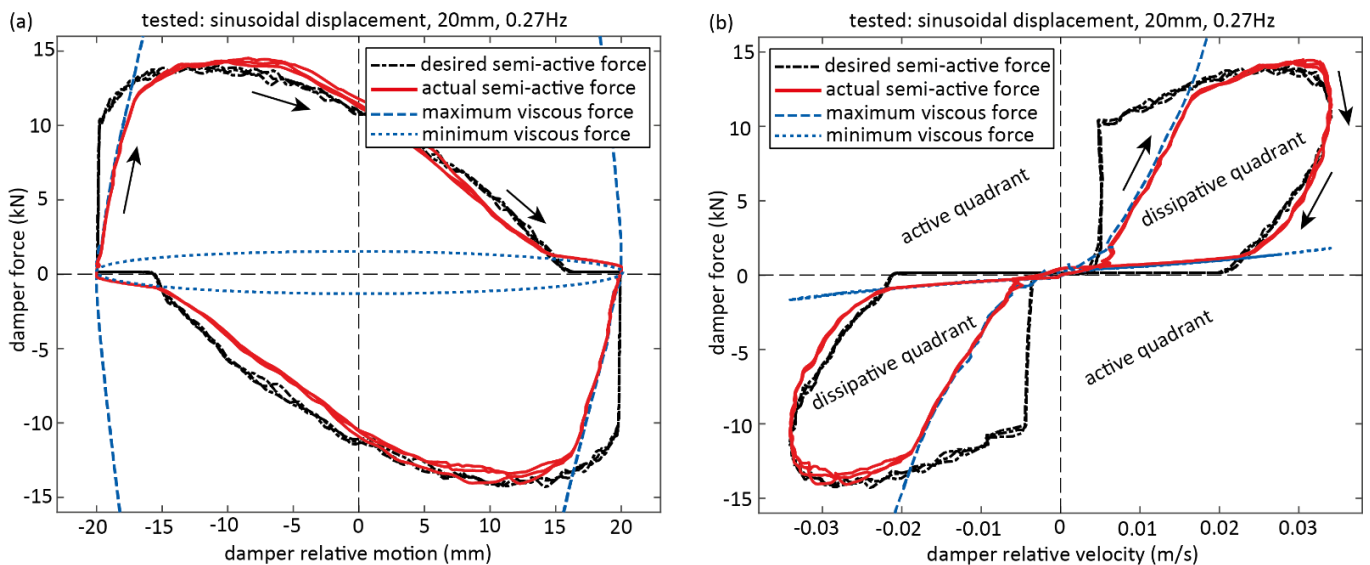


Figure 6. Experimental verification of clipped VDNS with hydraulic damper with real-time controlled bypass valve for sinusoidal displacement input (no cable damper interaction): (a) force displacement curves and (b) force velocity curves of desired and actual semi-active damper forces with according minimum and maximum control force constraints.

3.4. Modell of Semi-Active Damper Force including Force Limitations

For the simulations of the cable model with semi-active damper, the actual force of the semi-active damper is modelled by the actual semi-active control force that is equal to the desired semi-active control force, including the force limitations due to the minimum and

maximum viscous coefficients at fully open and fully closed bypass valve, i.e., at maximum and minimum valve currents, see Figure 3b (21).

$$f_{actual}^{semi-active}(t) = \begin{cases} \text{sign}\left(\frac{dv(a,t)}{dt}\right) c_{min}\left(\frac{dv(a,t)}{dt}\right)^2 & : |f_{des}^{semi-active}(t)| < c_{min}\left(\frac{dv(a,t)}{dt}\right)^2 \\ f_{des}^{semi-active}(t) & : c_{min}\left(\frac{dv(a,t)}{dt}\right)^2 \leq |f_{des}^{semi-active}(t)| \leq c_{max}\left(\frac{dv(a,t)}{dt}\right)^2 \\ \text{sign}\left(\frac{dv(a,t)}{dt}\right) c_{max}\left(\frac{dv(a,t)}{dt}\right)^2 & : |f_{des}^{semi-active}(t)| > c_{max}\left(\frac{dv(a,t)}{dt}\right)^2 \end{cases} \quad (21)$$

4. Simulation results

4.1. Assumptions, Cable Properties

The simulations with transverse damper are performed for the following damper types, assumptions, vibration modes, cable properties and damper positions:

- Damper types:
 - Passive linear viscous damper being optimized to one targeted mode, i.e., the excited mode, which represents a theoretical benchmark as passive dampers always need to mitigate several targeted modes.
 - Passive linear viscous damper being optimized to the targeted modes 1 to 4 describing the realistic benchmark.
 - Semi-active damper controlled by clipped VDNS including the control force constraints due to the minimum and maximum controllable viscous coefficients.
- The vibration mitigation of the considered transverse dampers are computed for the first four cable modes.
- Single mode vibrations are considered as resonant vibrations result in greatest cable displacement amplitudes.
- The excitation force due to vortex-shedding is modelled as harmonic excitation.
- The simulations are performed assuming typical cable properties and typical damper positions:
 - Cable length $L = 300$ m.
 - Cable tension force $T = 6700$ kN.
 - Mass per unit length $m = 100$ kg/m.
 - First eigenfrequency $f_1 = 0.431$ Hz (determined by L, T, m).
 - Inherent cable damping ratio $\zeta_{cable} = 0.4\%$.
 - Relative damper positions $a/L = 1\%, 1.67\%, 2\%, 2.5\%$ and 3% .

4.2. Excitation Force Amplitude

The excitation force amplitude is selected to obtain $L/1700$ anti-node displacement amplitude V_n during steady state conditions to ensure that the semi-active damper including control force constraints is operated in the typical range of damper relative velocities with associated typical semi-active damper forces. After reaching steady state vibrations, the excitation force is turned off to simulate the free decay response (Figure 7).

4.3. Damper Performance Assessment from Free Decay Response

The efficiencies of the passive damper and of the semi-active damper with control force constraints are assessed from simulated free decay responses adopting the logarithmic decrement method

$$\delta_i = \ln\left(\frac{V_i}{V_{i+1}}\right) \quad (22)$$

where V_i denotes the anti-node cable displacement amplitude of period i during the free decay response and V_{i+1} is the anti-node amplitude of the subsequent period. This yields the damping ratio as follows

$$\zeta_i = \frac{\delta_i}{\sqrt{4\pi^2 + \delta_i^2}} - \zeta_{cable} \quad (23)$$

where the cable inherent damping ratio is subtracted from the damping ratio obtained from the free decay response.

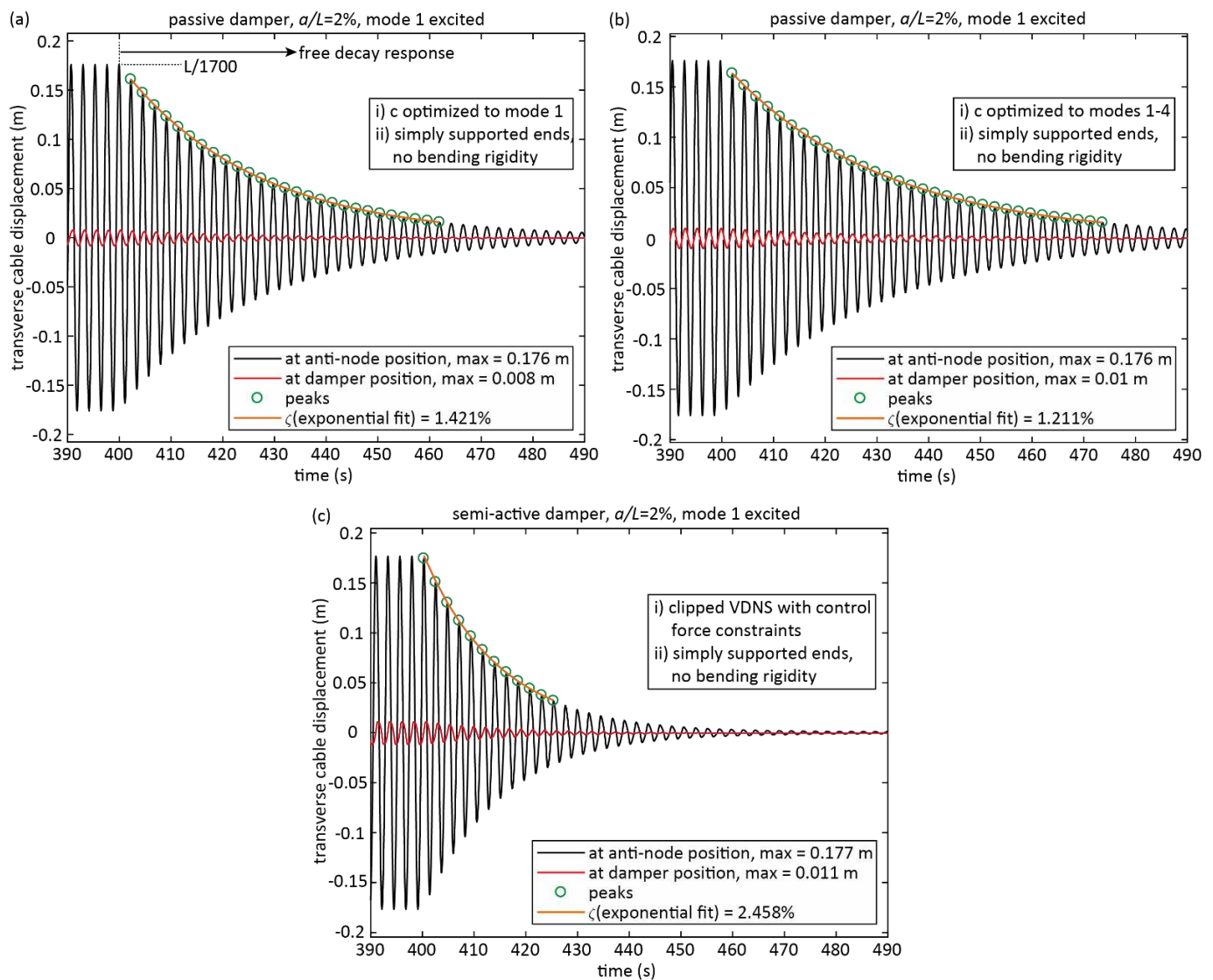


Figure 7. Simulated free decay responses of mode 1 for a cable with (a) passive viscous damper optimized to mode 1, (b) passive viscous damper optimized to modes 1 to 4, (c) clipped VDNS with control force constraints.

The damping assessment from the free decay response is selected because the cable damping due to the semi-active damper cannot be determined in a different way due to the nonlinearities of clipping and control force constraints. Because of these nonlinearities the peak-to-peak damping ratio is not fully constant as for linear transverse cable dampers. Therefore, the damping of the free decay response is assessed from the exponential fit of the free decay response between decay start and 10% of the steady state amplitude [29,30,34]. Figure 7 depicts examples of the exponential fits for a passive damper being optimized to the excited mode (10), a passive damper being optimized to the first four targeted modes (12) and for the semi-active damper with the consideration of the control force constraints. Figure 7c shows that the local peaks during the free decay response match well the exponential fit. Hence, the nonlinearities due to clipping and control force limitations of the semi-active damper are minor and therefore do not falsify the damping determination by the exponential fit method.

4.4. Damper Efficiency

The efficiency η of the transverse dampers is determined by comparing the damping ratio obtained from the exponential fit of the free decay response with the theoretical damping ratio due to linear viscous damping being optimized to one target mode

$$\eta = \frac{(\zeta_{fit} - \zeta_{cable}) - \zeta_{num}}{\frac{1}{2} \frac{a}{L}} \tag{24}$$

The numerical damping ζ_{num} , which is subtracted from $(\zeta_{fit} - \zeta_{cable})$, is determined for the simulation case of optimum modal linear viscous damping for which the resulting damping ratio is known by the analytical expression $L/(2a)$ where L denotes the half wavelength [14–16]. Note that the numerical damping of significantly less than 0.1% results from any integration algorithm and therefore cannot be avoided.

4.5. Results

The damping ratio due to the damper (including the numerical damping) and the according damper efficiency (24, without numerical damping) are given in Tables 1–4 for modes 1 to 4 as function of:

- Damper types:
 - Passive, tuned to mode X (1, 2, 3, 4): linear viscous damper being optimized to the excited mode (19); this is a theoretical benchmark because transverse cable dampers always need to provide the specified damping in several targeted modes; this computation is required to determine the numerical damping.
 - Passive, m1-m4: linear viscous damper being optimized to the targeted modes 1–4 (12).
 - Semi-active: clipped VDNS including control force constraints due to c_{min} and c_{max} (21).
- Cable model:
 - Taut string: cable without flexural rigidity and simply supported ends.
 - FR and FSC: cable with flexural rigidity and fixed support end conditions.
- Relative damper positions $a/L = 1\%, 1.67\%, 2\%, 2.5\%$ and 3% .

Table 1. Results for mode 1 excited.

Damper Type	Cable Model	a/L (%)	$\zeta_{fit} - \zeta_{cable}$ (%)	ζ_{num} (%)	$1/2 a/L$	η (%)
passive, tuned to mode 1	taut string	1%	0.505%	0.005% (*)	0.5%	100% (*)
	FR & FSC		0.354%			69.8%
passive, tuned to modes 1–4	taut string	1%	0.403%	0.005% (*)	0.5%	79.6%
	FR & FSC		0.198%			38.6%
semi-active	taut string	1%	1.036%	0.005% (*)	0.5%	206.2%
	FR & FSC		0.571%			113.2%
passive, tuned to mode 1	taut string	1.67%	0.848%	0.013% (*)	0.84%	100% (*)
	FR & FSC		0.716%			84.2%
passive, tuned to modes 1–4	taut string	1.67%	0.675%	0.013% (*)	0.84%	79.3%
	FR & FSC		0.431%			50.1%
semi-active	taut string	1.67%	1.723%	0.013% (*)	0.84%	204.8%
	FR & FSC		1.310%			155.3%
passive, tuned to mode 1	taut string	2%	1.021%	0.021% (*)	1%	100% (*)
	FR & FSC		0.912%			89.1%
passive, tuned to modes 1–4	taut string	2%	0.811%	0.021% (*)	1%	79.0%
	FR & FSC		0.570%			54.9%
semi-active	taut string	2%	2.058%	0.021% (*)	1%	203.7%
	FR & FSC		1.790%			176.9%

Table 1. Cont.

Damper Type	Cable Model	a/L (%)	$\zeta_{fit} - \zeta_{cable}$ (%)	ζ_{num} (%)	$1/2 a/L$	η (%)
passive, tuned to mode 1	taut string	2.5%	1.284%	0.034% (*)	1.25%	100% (*)
	FR & FSC		1.194%			92.8%
passive, tuned to modes 1–4	taut string	2.5%	1.017%	0.034% (*)	1.25%	78.6%
	FR & FSC		0.775%			59.3%
semi-active	taut string	2.5%	2.636%	0.034% (*)	1.25%	208.2%
	FR & FSC		2.395%			188.9%
passive, tuned to mode 1	taut string	3%	1.549%	0.049% (*)	1.5%	100% (*)
	FR & FSC		1.471%			94.8%
passive, tuned to modes 1–4	taut string	3%	1.224%	0.049% (*)	1.5%	78.3%
	FR & FSC		0.978%			61.9%
semi-active	taut string	3%	3.169%	0.049% (*)	1.5%	208.0%
	FR & FSC		3.014%			197.7%

(*) numerical damping determined from ζ_{fit} due to passive viscous damping optimized to excited mode to obtain $\eta = 100\%$.

Table 2. Results for mode 2 excited.

Damper Type	Cable Model	a/L (%)	$\zeta_{fit} - \zeta_{cable}$ (%)	ζ_{num} (%)	$1/2 a/L$	η (%)
passive, tuned to mode 2	taut string	1%	0.506%	0.006% (*)	0.5%	100% (*)
	FR & FSC		0.354%			69.6%
passive, tuned to modes 1–4	taut string	1%	0.506%	0.006% (*)	0.5%	100.0%
	FR & FSC		0.354%			69.6%
semi-active	taut string	1%	1.025%	0.006% (*)	0.5%	203.8%
	FR & FSC		0.571%			113.0%
passive, tuned to mode 2	taut string	1.67%	0.849%	0.014% (*)	0.84%	100% (*)
	FR & FSC		0.716%			84.1%
passive, tuned to modes 1–4	taut string	1.67%	0.849%	0.014% (*)	0.84%	100.0%
	FR & FSC		0.716%			84.1%
semi-active	taut string	1.67%	1.732%	0.014% (*)	0.84%	205.7%
	FR & FSC		1.342%			159.0%
passive, tuned to mode 2	taut string	2%	1.023%	0.023% (*)	1%	100% (*)
	FR & FSC		0.913%			89.0%
passive, tuned to modes 1–4	taut string	2%	1.023%	0.023% (*)	1%	100.0%
	FR & FSC		0.913%			89.0%
semi-active	taut string	2%	2.083%	0.023% (*)	1%	206.0%
	FR & FSC		1.807%			178.4%
passive, tuned to mode 2	taut string	2.5%	1.288%	0.038% (*)	1.25%	100% (*)
	FR & FSC		1.196%			92.6%
passive, tuned to modes 1–4	taut string	2.5%	1.288%	0.038% (*)	1.25%	100.0%
	FR & FSC		1.196%			92.6%
semi-active	taut string	2.5%	2.574%	0.038% (*)	1.25%	202.9%
	FR & FSC		2.461%			193.8%
passive, tuned to mode 2	taut string	3%	1.557%	0.057% (*)	1.5%	100% (*)
	FR & FSC		1.474%			94.5%
passive, tuned to modes 1–4	taut string	3%	1.557%	0.057% (*)	1.5%	100.0%
	FR & FSC		1.474%			94.5%
semi-active	taut string	3%	3.083%	0.057% (*)	1.5%	201.7%
	FR & FSC		3.081%			201.6%

(*) numerical damping determined from ζ_{fit} due to passive viscous damping optimized to excited mode to obtain $\eta = 100\%$.

Table 3. Results for mode 3 excited.

Damper Type	Cable Model	a/L (%)	$\zeta_{fit} - \zeta_{cable}$ (%)	ζ_{num} (%)	$1/2 a/L$	η (%)									
passive, tuned to mode 3	taut string	1%	0.506%	0.006% (*)	0.5%	100% (*)									
	FR & FSC		0.354%			69.6%									
passive, tuned to modes 1–4	taut string		0.465%			91.8%									
	FR & FSC		0.452%			89.2%									
semi-active	taut string		0.975%			193.8%									
	FR & FSC		0.567%			112.2%									
passive, tuned to mode 3	taut string		1.67%			0.851%	0.016% (*)	0.84%	100% (*)						
	FR & FSC					0.716%			83.8%						
passive, tuned to modes 1–4	taut string					0.782%			91.7%						
	FR & FSC					0.836%			98.2%						
semi-active	taut string					1.655%			196.3%						
	FR & FSC					1.318%			155.9%						
passive, tuned to mode 3	taut string					2%			1.028%	0.028% (*)	1%	100% (*)			
	FR & FSC								0.913%			88.5%			
passive, tuned to modes 1–4	taut string								0.944%			91.6%			
	FR & FSC								1.025%			99.7%			
semi-active	taut string								1.980%			195.2%			
	FR & FSC								1.761%			173.3%			
passive, tuned to mode 3	taut string								2.5%			1.296%	0.046% (*)	1.25%	100% (*)
	FR & FSC											1.199%			92.2%
passive, tuned to modes 1–4	taut string	1.190%		91.5%											
	FR & FSC	1.295%		99.9%											
semi-active	taut string	2.403%		188.6%											
	FR & FSC	2.319%		181.8%											
passive, tuned to mode 3	taut string	3%		1.569%	0.069% (*)							1.5%			100% (*)
	FR & FSC			1.481%											94.1%
passive, tuned to modes 1–4	taut string		1.442%	91.5%											
	FR & FSC		1.563%	99.6%											
semi-active	taut string		2.833%	184.3%											
	FR & FSC		2.924%	190.3%											

(*) numerical damping determined from ζ_{fit} due to passive viscous damping optimized to excited mode to obtain $\eta = 100\%$.

Table 4. Results for mode 4 excited.

Damper Type	Cable Model	a/L (%)	$\zeta_{fit} - \zeta_{cable}$ (%)	ζ_{num} (%)	$1/2 a/L$	η (%)			
passive, tuned to mode 4	taut string	1%	0.507%	0.007% (*)	0.5%	100% (*)			
	FR & FSC		0.354%			69.4%			
passive, tuned to modes 1–4	taut string		0.402%			79.0%			
	FR & FSC		0.497%			98.0%			
semi-active	taut string		0.949%			188.4%			
	FR & FSC		0.557%			110.0%			
passive, tuned to mode 4	taut string		1.67%			0.855%	0.020% (*)	0.84%	100% (*)
	FR & FSC					0.715%			83.2%
passive, tuned to modes 1–4	taut string					0.675%			78.4%
	FR & FSC					0.850%			99.4%
semi-active	taut string					1.647%			194.9%
	FR & FSC					1.290%			152.1%

Table 4. Cont.

Damper Type	Cable Model	a/L (%)	$\zeta_{fit} - \zeta_{cable}$ (%)	ζ_{num} (%)	$1/2 a/L$	η (%)						
passive, tuned to mode 4	taut string	2%	1.033%	0.033% (*)	1%	100% (*)						
	FR & FSC		0.914%			88.1%						
passive, tuned to modes 1–4	taut string		0.814%			0.058% (*)	1.25%	78.1%				
	FR & FSC		1.009%					97.6%				
semi-active	taut string		1.954%			0.090% (*)	1.5%	192.1%				
	FR & FSC		1.761%					172.8%				
passive, tuned to mode 4	taut string		2.5%			1.308%	0.090% (*)	1.5%	100% (*)			
	FR & FSC					1.204%			91.7%			
passive, tuned to modes 1–4	taut string					1.029%			0.090% (*)	1.5%	77.7%	
	FR & FSC					1.242%					94.7%	
semi-active	taut string					2.419%			0.090% (*)	1.5%	188.9%	
	FR & FSC					2.346%					183.0%	
passive, tuned to mode 4	taut string					3%			1.590%	0.090% (*)	1.5%	100% (*)
	FR & FSC								1.488%			93.2%
passive, tuned to modes 1–4	taut string	1.245%		0.090% (*)	1.5%				77.0%			
	FR & FSC	1.475%							92.3%			
semi-active	taut string	2.842%		0.090% (*)	1.5%				183.5%			
	FR & FSC	2.954%							190.9%			

(*) numerical damping determined from ζ_{fit} due to passive viscous damping optimized to excited mode to obtain $\eta = 100\%$.

The observation of Tables 1–4 reveals the following main findings:

- The reduced cable motion at damper position due to cable flexural rigidity and fixed supported ends has strong impact on the cable damping ratio due to passive dampers located at $a/L \leq 2\%$. This fact is explained by the associated reduced transverse damper motion, see Figure 2b, whereby less energy per cycle can be dissipated.
- The damper efficiencies obtained from the simulation case of a cable with flexural rigidity and fixed supported ends, mode 1 excited, typical damper positions around 2% to 2.5% and passive damper being optimized to modes 1–4 match well with the reported damper efficiencies [23–31]. The according results for mode 2 are greater because a damper being optimized to modes 1–4 generates optimum damping in mode 2 (14), see [19]. In this perspective the according simulation results for modes 3 and 4 of the cable model with bending stiffness and fixed support conditions (FR and FSC) seem to be unrealistically high. This irrational result is interpreted by the fact that the cable model FR and FSC is validated for the modeshape of mode 1 of the test steel wire strand depicted in Figure 2 but not for higher modes.
- For some simulation cases, the damping of the cable model with flexural rigidity and fixed supported ends is greater than for the taut string model. This unexpected result is observed for some simulations of modes 3 and 4 and mainly for the passive damper being optimized to modes 1 to 4. An explanation can be that the reduced cable motion at damper position reduces the damper velocity as well whereby the viscous coefficient being optimized for modes 1 to 4 (12) almost generates the optimum viscous force for modes 3 and 4.
- The damping results due to the semi-active damper with the consideration of the minimum and maximum force limitations due to fully open and fully closed bypass valve show the following picture:
 - Mode 1: The damping is approximately 2.5 . . . 2.6 (taut string) and approximately 2.8 . . . 3.2 (FR and FSC) times greater than the damping due to the passive damper being optimized to modes 1 to 4.

- Mode 2: The damping is approximately 2.0 ... 2.6 (taut string) and approximately 1.6 ... 2.1 (FR and FSC) times greater than the damping due to the passive damper being optimized to modes 1 to 4.
- Mode 3: The damping is approximately 2.0 ... 2.1 (taut string) and approximately 1.3 ... 1.9 (FR and FSC) times greater than the damping due to the passive damper being optimized to modes 1 to 4.
- Mode 4: The damping is approximately 2.3 ... 2.5 (taut string) and approximately 1.2 ... 2.1 (FR and FSC) times greater than the damping due to the passive damper being optimized to modes 1 to 4.
- The tracking of the desired semi-active force is limited by the minimum and maximum viscous coefficients of the controllable damper. The according force displacement curves due to the minimum and maximum quadratic viscous forces are depicted in Figures 8 and 9 for the simulations of mode 1 and 4. It is observed that c_{max} mainly constrains the force tracking accuracy for lower frequency modes while c_{min} mainly limits the force tracking accuracy for higher frequency modes. This is explained by the fact that the according limiting control forces are in proportion to the square of the damper relative velocity, see (21). Hence, how precisely the desired semi-active force can be tracked by the semi-active damper with control force limitations due to c_{min} and c_{max} depends on mode number, which makes the interpretation of the obtained cable damping results for modes 3 and 4 difficult.

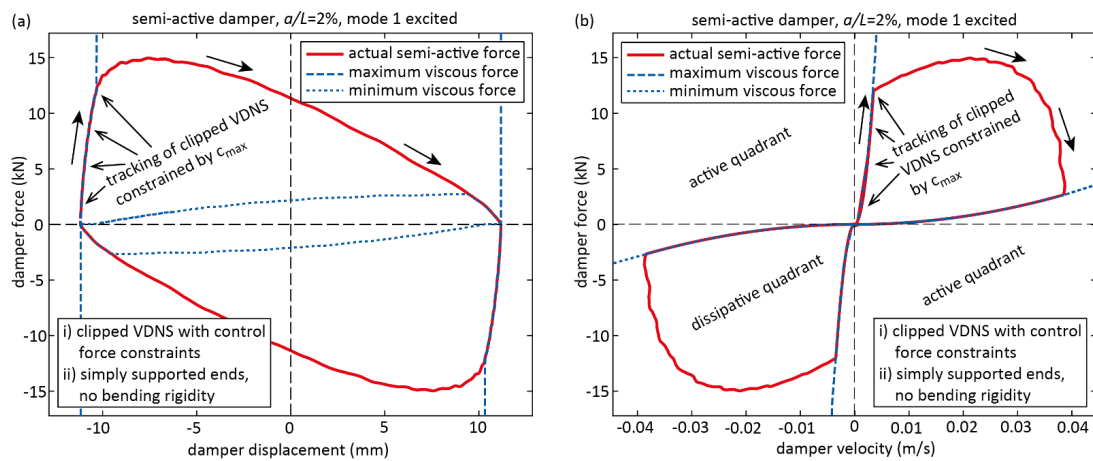


Figure 8. Simulated clipped VDNS with control force constraints for mode 1: (a) force displacement curves and (b) force velocity curves during steady state conditions (before simulated free decay response).

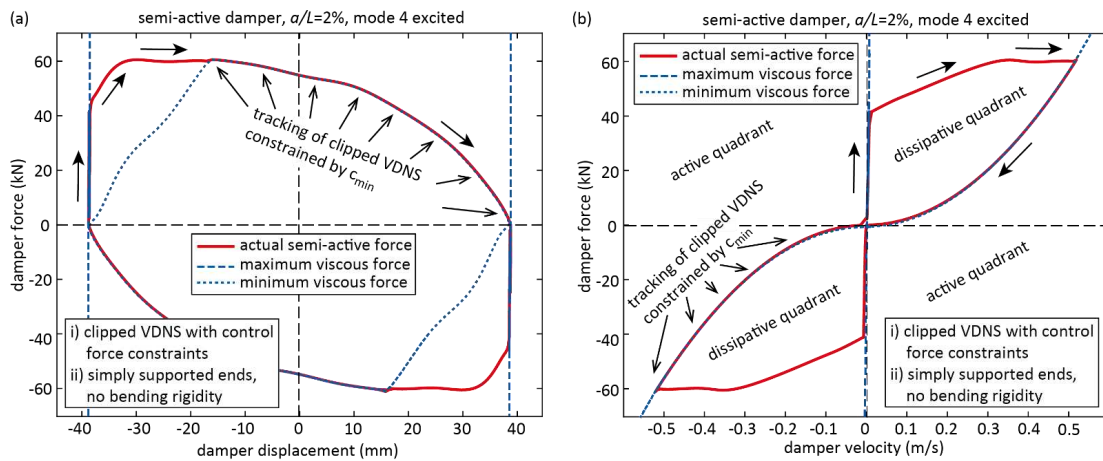


Figure 9. Simulated clipped VDNS with control force constraints for mode 4: (a) force displacement curves and (b) force velocity curves during steady state conditions (before simulated free decay response).

5. Conclusions

This study investigates the potential to use semi-active cable dampers controlled by clipped viscous damping with negative stiffness to compensate for the reduced cable motion at damper position due to cable flexural rigidity and fixed supported ends. For this a prototype hydraulic damper with real-time controlled bypass valve has been developed and experimentally tested. Based on the test results a model of the semi-active hydraulic damper is derived that includes the control force constraints resulting from the minimum and maximum viscous coefficients at fully open and fully closed bypass valve. This model is used to compute the cable damping ratios of the first four cable modes, typical damper positions and cable models without and with flexural rigidity and fixed supported ends. As benchmark, the passive damper being optimized to the first four cable modes is computed. The comparative study demonstrates that the presented semi-active cable damper leads to far greater cable damping ratios than the passive damper. This is explained by the facts that the viscous force is optimized in real time to the actual frequency of motion and the negative stiffness force increases the damper relative motion whereby the viscous force can dissipate more energy per cycle. Because of the dissipative nature of the semi-active damper force, stability issues as for active systems do not exist. In addition, power consumption is not critical because power is only needed to control the oil volume stream through the bypass valve but not to produce active forces. Therefore, the presented semi-active hydraulic damper represents an efficient, cost-effective and robust damping tool for stay cable damping.

Author Contributions: Conceptualization, F.W. and J.D.; methodology, F.W., S.S. and F.O.; software, F.W. and S.S.; formal analysis, F.W. and S.S.; writing—original draft preparation, F.W., S.S., F.O., J.D. and C.B.; writing—review and editing, F.W., S.S., F.O., J.D. and C.B.; project administration, F.W. and J.D. All authors have read and agreed to the published version of the manuscript.

Funding: This research received no external funding.

Institutional Review Board Statement: Not applicable.

Informed Consent Statement: Not applicable.

Data Availability Statement: The data presented in this study are available on request from the corresponding author.

Acknowledgments: The authors acknowledge the support of Maurer SE, Maurer Engineering GmbH and Maurer Switzerland GmbH.

Conflicts of Interest: The authors declare no conflict of interest.

References

1. Fib Bulletin 30. Acceptance of stay cable systems using prestressing steels. In *Bulletin 30*; International Federation for Structural Concrete Fib: Lausanne, Switzerland, 2005; ISBN 2-88394-070-3.
2. Jain, A.; Simsir, C.; Sarkar, P.P. Analysis, Measurement, and Mitigation of Stay Cable Vibrations. *Eighth Congr. Forensic Eng.* **2018**, 791–799. [CrossRef]
3. Matsumoto, M.; Saitoh, T.; Kitazawa, M.; Shirato, H.; Nishizaki, T. Response characteristics of rain-wind induced vibration of stay-cables of cable-stayed bridges. *J. Wind Eng. Ind. Aerodyn.* **1995**, *57*, 323–333. [CrossRef]
4. Zuo, D.; Jones, N.P. Interpretation of field observations of wind- and rain-wind-induced stay cable vibrations. *J. Wind Eng. Ind. Aerodyn.* **2010**, *98*, 73–87. [CrossRef]
5. Li, S.; Chen, Z.; Wu, T.; Kareem, A. Rain-wind-induced in-plane and out-of-plane vibrations of stay cables. *J. Eng. Mech.* **2013**, *139*, 1688–1698. [CrossRef]
6. Wang, H.; Li, A.; Niu, J.; Zong, Z.; Li, J. Long-term monitoring of wind characteristics at Sutong Bridge site. *J. Wind Eng. Ind. Aerodyn.* **2013**, *115*, 39–47. [CrossRef]
7. Guo, J.; Zhu, X. Field Monitoring and Analysis of the Vibration of Stay Cables under Typhoon Conditions. *Sensors* **2020**, *20*, 4520. [CrossRef] [PubMed]
8. Vo-Duy, H.; Nguyen, C.H. Vibration Control Techniques for Dynamic Response Mitigation of Civil Structures under Multiple Hazards. *Shock Vib.* **2020**, *2020*, 5845712. [CrossRef]
9. Daniottia, N.; Jakobsen, J.B.; Snæbjörnsson, J.; Cheynet, E.; Wang, J. Observations of bridge stay cable vibrations in dry and wet conditions: A case study. *J. Sound Vib.* **2021**, *503*, 116106. [CrossRef]

10. An, M.; Li, S.; Liu, Z.; Yan, B.; Li, L.; Chen, Z. Galloping vibration of stay cable installed with a rectangular lamp: Field observations and wind tunnel tests. *J. Wind Eng. Ind. Aerodyn.* **2021**, *215*, 104685.
11. Ni, Y.Q.; Wang, X.Y.; Chen, Z.Q.; Ko, J.M. Field observations of rain-wind-induced cable vibration in cable-stayed Dongting Lake Bridge. *J. Wind Eng. Ind. Aerodyn.* **2007**, *95*, 303–328. [CrossRef]
12. Savor, Z.; Radic, J.; Hrelja, G. Cable vibrations at Dubrovnik bridge. *Bridge Struct.* **2006**, *2*, 97–106. [CrossRef]
13. Casas, J.R.; Aparicio, A.C. Rain-wind-induced cable vibrations in the Alamillo cable-stayed bridge (Sevilla, Spain). Assessment and remedial action. *Struct. Infrastruct. Eng.* **2010**, *6*, 549–556. [CrossRef]
14. Pacheco, B.M.; Fujino, Y.; Sulekh, A. Estimation curve for modal damping in stay cables with viscous damper. *J. Struct. Eng.* **1993**, *119*, 1961–1979. [CrossRef]
15. Krenk, S. Vibrations of a taut cable with an external damper. *J. Appl. Mech.* **2000**, *67*, 772–776. [CrossRef]
16. Main, J.A.; Jones, N.P. Free vibrations of taut cable with attached damper. I: Linear viscous damper. *J. Eng. Mech.* **2002**, *128*, 1062–1071. [CrossRef]
17. Krenk, S.; Høgsberg, J.R. Damping of cables by a transverse force. *J. Eng. Mech.* **2005**, *131*, 340–348. [CrossRef]
18. Fujino, Y.; Siringoringo, D. Vibration Mechanisms and Controls of Long-Span Bridges: A Review. *Struct. Eng. Int.* **2013**, *23*, 248–268. [CrossRef]
19. Weber, F.; Feltrin, G.; Maślanka, M.; Fobo, W.; Distl, H. Design of viscous dampers targeting multiple cable modes. *Eng. Struct.* **2009**, *31*, 2797–2800. [CrossRef]
20. Hoang, N.; Fujino, Y. Analytical study on bending effects in a stay cable with a damper. *J. Eng. Mech.* **2007**, *133*, 1241–1246. [CrossRef]
21. Hammoudi, Z.S.; Abbas, A.L.; Mahmood, H.A. Free Vibration Analysis of Cable Stayed-Bridge by Finite Element Method. *Diyala J. Eng. Sci.* **2019**, *12*, 67–72.
22. Liu, M.; Zhang, G. Damping of Stay Cable-Passive Damper System with Effects of Cable Bending Stiffness and Damper Stiffness. *Appl. Mech. Mater.* **2021**, *204–208*, 4513–4517. [CrossRef]
23. Boston, C.; Weber, F.; Guzzella, L. Optimal semi-active damping of cables with bending stiffness. *Smart Mater. Struct.* **2011**, *20*, 055005. [CrossRef]
24. Weber, F.; Boston, C. Clipped viscous damping with negative stiffness for semi-active cable damping. *Smart Mater. Struct.* **2011**, *20*, 045007. [CrossRef]
25. Duan, Y.F.; Ni, Y.Q.; Ko, J.M. State-derivative feedback control of cable vibration using semiactive magnetorheological dampers. *Comput.-Aided Civ. Infrastruct. Eng.* **2005**, *20*, 431–449. [CrossRef]
26. Christenson, R.E.; Spencer, B.F., Jr.; Johnson, E.A. Experimental verification of smart cable damping. *J. Eng. Mech.* **2006**, *132*, 268–278. [CrossRef]
27. Duan, Y.F.; Ni, Y.Q.; Ko, J.M. Cable vibration control using magnetorheological dampers. *J. Intell. Mater. Syst. Struct.* **2006**, *17*, 321–325. [CrossRef]
28. Zhou, H.; Sun, L.; Xing, F. Damping of Full-Scale Stay Cable with Viscous Damper: Experiment and Analysis. *Adv. Struct. Eng.* **2014**, *17*, 265–274. [CrossRef]
29. Weber, F.; Distl, H. Amplitude and frequency independent cable damping of Sutong Bridge and Russky Bridge by MR dampers. *Struct. Control Health Monit.* **2015**, *22*, 237–254. [CrossRef]
30. Weber, F.; Distl, H. Damping estimation from free decay responses of cables with MR dampers. *Sci. World J. Spec. Issue Cable Struct. Dyn. Control Monit.* **2015**, *2015*, 861954. [CrossRef]
31. Zhou, H.; Xiang, N.; Huang, X.; Sun, L.; Xing, F.; Zhou, R. Full-scale test of dampers for stay cable vibration mitigation and improvement measures. *Struct. Monit. Maint.* **2018**, *5*, 489–506.
32. Lee, J.-J.; Kim, J.-M.; Ahn, S.-S.; Choi, J.-S. Development of a cable exciter to evaluate damping ratios of a stay cable. *KSCE J. Civ. Eng.* **2010**, *14*, 363–370. [CrossRef]
33. Bournand, Y.; Crigler, J. The VSL friction damper for cable-stayed bridges. Some results from maintenance and testing on long cables. In Proceedings of the 6th International Conference on Cable Dynamics 2005, Charleston, SC, USA, 19–22 September 2005; pp. 199–204.
34. Weber, F.; Høgsberg, J.; Krenk, S. Optimal tuning of amplitude proportional Coulomb friction damper for maximum cable damping. *J. Struct. Eng.* **2010**, *136*, 123–134. [CrossRef]
35. Weber, F.; Boston, C. Energy Based Optimization of Viscous-Friction Dampers on Cables. *Smart Mater. Struct.* **2010**, *19*, 045025. [CrossRef]
36. Maślanka, M.; Sapinski, B.; Snamina, J. Experimental study of vibration control of a cable with an attached MR damper. *J. Theor. Appl. Mech.* **2007**, *45*, 893–917.
37. Li, H.; Liu, M.; Ou, J. Negative stiffness characteristics of active and semi-active control systems for stay cables. *Struct. Control Health Monit.* **2008**, *15*, 120–142. [CrossRef]
38. Weber, F. Bouc-Wen model-based real-time force tracking scheme for MR dampers. *Smart Mater. Struct.* **2013**, *22*, 045012. [CrossRef]
39. Weber, F. Robust force tracking control scheme for MR dampers. *Struct. Control Health Monit.* **2015**, *22*, 1373–1395. [CrossRef]
40. Zhou, P.; Li, H. Modeling and control performance of a negative stiffness damper for suppressing stay cable vibrations. *Struct. Control Health Monit.* **2016**, *23*, 764–782. [CrossRef]

41. Wang, Z.H.; Xu, Y.W.; Gao, H.; Chen, Z.Q.; Xu, K.; Zhao, S.B. Vibration control of a stay cable with a rotary electromagnetic inertial mass damper. *Smart Struct. Syst* **2019**, *23*, 627–639.
42. Li, Y.; Shen, W.; Zhu, H. Vibration mitigation of stay cables using electromagnetic inertial mass dampers: Full-scale experiment and analysis. *Eng. Struct.* **2019**, *200*, 109693. [CrossRef]
43. Di, F.; Sun, L.; Chen, L. Cable vibration control with internal and external dampers: Theoretical analysis and field test validation. *Smart Struct. Syst.* **2020**, *26*, 575–589.
44. Jeong, S.; Lee, Y.-J.; Sim, S.-H. Serviceability Assessment Method of Stay Cables with Vibration Control Using First-Passage Probability. *Math. Probl. Eng.* **2019**, *2019*, 4138279. [CrossRef]
45. Bathe, K.-J. *Finite Element Procedures in Engineering Analysis*; Prentice-Hall: Englewood Cliffs, NJ, USA, 1982.
46. Weber, F.; Distl, H. Semi-active damping with negative stiffness for multi-mode cable vibration mitigation: Approximate collocated control solution. *Smart Mater. Struct.* **2015**, *24*, 115015. [CrossRef]
47. Weber, F.; Mašlanka, M. Precise Stiffness and Damping Emulation with MR Dampers and its Application to Semi-active Tuned Mass Dampers of Wolgograd Bridge. *Smart Mater. Struct.* **2014**, *23*, 015019. [CrossRef]

Article

Vertical Seismic Isolation Device for Three-Dimensional Seismic Isolation of Nuclear Power Plant Equipment—Case Study

Gyeong-Hoi Koo ^{1,*}, Jin-Young Jung ¹, Jong-Keun Hwang ², Tae-Myung Shin ³ and Min-Seok Lee ⁴ ¹ Korea Atomic Energy Research Institute, Daejeon 34057, Korea; jyoung@kaeri.re.kr² SMARTEK E&C, Daejeon 34013, Korea; jkhwang0@hanmail.net³ School of Mechanical, Automotive and Aeronautical Engineering, Korea National University of Transportation, Chungju 27469, Korea; tmshin@ut.ac.kr⁴ Nuclear Power Team & Structural Group, Korea Electric Association, Seoul 05718, Korea; lms536@kepic.org

* Correspondence: ghkoo@kaeri.re.kr

Abstract: The purpose of this study was to develop a vertical seismic isolation device essential for the three-dimensional seismic isolation design of nuclear power plant equipment. The vertical seismic isolation device in this study has a concept that can be integrally combined with a conventional laminated rubber bearing, a horizontal seismic isolator with a design vertical load of 10 kN. To develop the vertical seismic isolation device, the vertical spring and the seismic energy dissipation device capable of limiting the vertical displacement of the spring were designed and their performances were verified through actual tests. In this study, the target elevation of the floor is 136 ft, where safety-related nuclear equipment, such as cabinet and remote shutdown console, etc., is installed. The sensitivity studies were carried out to investigate the optimal design vertical isolation frequencies for the target building elevation. Based on the results of the sensitivity study, a disc spring and a helical coil spring were selected for the vertical stiffness design, and the steel damper was selected for the seismic energy dissipation, and their performance characteristics were tested to confirm the design performance. For the steel damper, three types were designed and their energy dissipation characteristics by hysteretic behavior were confirmed by the inelastic finite element analyses and the tests in static fully reversed cyclic conditions. Through the study of the vertical seismic isolation device, it was found that 2.5 Hz~3.0 Hz is appropriate for the optimal design vertical isolation. With results of the vertical seismic isolation performance analysis, the appropriate number of steel dampers are proposed to limit the vertical seismic displacement of the spring within the static displacement range by the design vertical load.

Citation: Koo, G.-H.; Jung, J.-Y.; Hwang, J.-K.; Shin, T.-M.; Lee, M.-S. Vertical Seismic Isolation Device for Three-Dimensional Seismic Isolation of Nuclear Power Plant Equipment—Case Study. *Appl. Sci.* **2022**, *12*, 320. <https://doi.org/10.3390/app12010320>

Academic Editors:
Giuseppe Lacidogna and José A.F.O. Correia

Received: 24 November 2021

Accepted: 24 December 2021

Published: 29 December 2021

Publisher's Note: MDPI stays neutral with regard to jurisdictional claims in published maps and institutional affiliations.



Copyright: © 2021 by the authors. Licensee MDPI, Basel, Switzerland. This article is an open access article distributed under the terms and conditions of the Creative Commons Attribution (CC BY) license (<https://creativecommons.org/licenses/by/4.0/>).

Keywords: three-dimensional (3D) seismic isolation; vertical seismic isolation device; disc spring; helical coil spring; steel damper; laminated rubber bearing; seismic energy dissipation; nuclear power plant equipment; seismic isolation frequency; hysteretic behavior

1. Introduction

After the Fukushima nuclear power plant accident, nuclear power plant safety improvement against earthquakes has emerged as a major issue. The current Safe Shutdown Earthquake (SSE) design basis required for nuclear power plant design is 0.3 g, which is 50% higher than the previous 0.2 g. In recent years, seismic design requirements are being strengthened to ensure the seismic safety of nuclear power plants in case of beyond-design-basis earthquakes, and various methods are being studied to solve this issue [1–3].

In general, it is true that the improvement of seismic capacity of nuclear power plants has been mainly focused on plant buildings and structures. To achieve this goal, the seismic base isolation design technology using laminated rubber bearings (LRBs) has been studied worldwide for a long time as one of the measures to ensure the safety of nuclear power

plants against large earthquake loads. In the development of seismic isolation design technology for nuclear power plant application, the entire major nuclear power plant buildings are constructed on one common mat, and this is supported by seismic isolators. Most of the future advanced nuclear power plants currently under development adopt seismic isolation design for nuclear power plant buildings [4–6].

So far, the development of seismic isolation design technology for nuclear power plant buildings has been mainly focused on LRBs that can support the heavy building weight stably and allow horizontally flexible deformation. These LRBs have been continuously developed as a seismic isolator only for horizontal seismic isolation of nuclear power plant buildings because the horizontal design earthquake level is much larger than the vertical design level. Recently, the vertical seismic design load is required to be equal to the horizontal load level. Therefore, the unavoidable disadvantage of the LRBs amplifying the vertical earthquake response by vertical earthquakes is a big issue to overcome [7–9]. In particular, as the vertical seismic load level has recently increased and the importance of nuclear power plant design covering this has become more of an issue, horizontal seismic isolation design using only LRBs may not be able to ensure the required seismic design goal.

To overcome the disadvantage of the horizontal seismic isolation with the LRBs, much research and development on three-dimensional (3D) seismic isolators has been carried out worldwide [10–15]. However, there are still not many practical cases applied to nuclear power plants. One of the design barriers of vertical seismic isolation for whole reactor buildings may be to construct a rigid upper mat supporting the reactor buildings to prevent local uneven settlement due to the flexibility of the vertical seismic isolation device.

The goal of this study is to develop a 3D seismic isolator for individual nuclear power plant facilities that are relatively easy to install and maintain when compared with the whole building seismic isolation design. For this purpose, a study was conducted on a vertical seismic isolation device having a spring and a steel damper that can be integrally combined with lead-inserted small LRBs for horizontal seismic isolation developed for individual facilities in nuclear power plants [16,17].

There are many studies for the supplemental seismic energy dissipation using the LRBs, such as ring-type steel [18], high damping rubber [19], friction pad [20], and viscous damper [21]. In this study, various dimensions and shapes of thin plate-type steel dampers integrated with the LRBs are investigated, and the capacity of their seismic energy dissipation is verified by the tests and simulations.

A disc spring or a helical coil spring was used for the vertical stiffness design that determines the vertical seismic isolation frequency (VIF) of the vertical seismic isolation device, and a steel damper was used for the vertical seismic energy dissipation that controls the vertical relative displacement. In this study, with the goal of 3D seismic isolation design for nuclear power plant facilities installed in 136 ft of an actual nuclear power plant building, a vertical spring design for determining the optimal VIF and an optimal steel damper that can accommodate relative vertical displacement were designed and verified. The feasibility of the design concept was confirmed by performing verification tests and simulations for spring and steel damper.

2. Concept of Vertical Seismic Isolation Device

2.1. Configurations and Dimensions

The 3D seismic isolator being developed in this study is intended to be applied to individual facilities of nuclear power plants where severe vertical earthquake response amplification is expected. To this end, the horizontal seismic isolator uses a lead-inserted small LRB with proven stability and seismic isolation performance [16,17], and a spring-damper-based vertical seismic isolator is mounted on the top of the LRB.

Figure 1 presents the conceptual configuration of the horizontal–vertical integrated 3D seismic isolator being developed in this study. As shown in the figure, the LRB with relatively high vertical stiffness supports vertical springs and dampers of the vertical seismic isolation device.

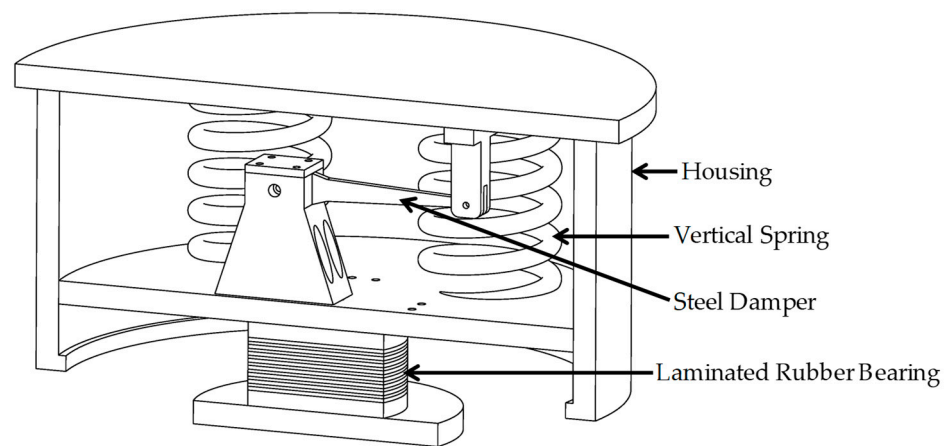


Figure 1. Overall design concept of integrated 3-dimensional seismic isolator (half-symmetric view).

The housing in Figure 1 has a function to transmit the horizontal seismic load, simultaneously guiding the vertical seismic motion of the spring due to the superstructure. Table 1 shows the specifications of the 3D seismic isolator based on the lead-inserted LRB used in this study.

Table 1. Summary of 3D seismic isolator design parameters [16].

Isolation Devices	Design Parameters	Design Value
Horizontal Seismic Isolation Device (LRB)	Outer diameter (mm)	100
	Lead plug diameter (mm)	21.5
	Total LRB height (mm)	34
	Shape factor (S_1, S_2)	9.9, 5.0
	Design vertical load (kN)	10
	Design shear disp. (mm)	35 (175%)
	Beyond design shear disp. (mm)	80 (400%)
Vertical Seismic Isolation Device	Housing diameter (mm)	450
	Total height (mm)	140~360
	Design vertical load (kN)	10

As shown in Table 1, the design vertical load of the 3D seismic isolator considered in this study is 10 kN, the total height of the LRB is 34 mm, and the design horizontal seismic frequency is 2.3 Hz. The vertical seismic isolation device mounted on the top of the LRB will maintain the vertical stiffness by a disc spring or a helical spring and dissipate the vertical seismic energy by steel dampers.

In the design of the vertical seismic isolation device, the vertical spring mainly controls the VIF, and the vertical damper controls the vertical displacement of the spring. The higher the vertical stiffness, the higher the vertical seismic isolation frequency, and the lower the vertical seismic isolation performance. The lower the vertical stiffness, the better the vertical seismic isolation performance, but the displacement of the vertical spring will significantly increase so that it may not meet the design concept of integral 3D seismic isolator presented in Figure 1. Therefore, a vertical spring design having an appropriate design VIF and a damping device design capable of properly suppressing the vertical spring displacement are required in a design stage.

2.2. Vertical Design Displacement Limit

Figure 2 presents the operation concept of the 3D seismic isolator. Figure 2b shows the schematics of static vertical displacement condition due to dead weight of the superstructure, and Figure 2c shows the horizontal and vertical displacement condition during earthquake events. The housing of the vertical seismic isolator transmits the horizontal load of the superstructure to the LRB and guides the vertical seismic movement. The dimension

design of such a housing is determined according to the shape and dimensions of the vertical spring and steel dampers, which are determined according to the determination of the design VIF. The most important aspect in this design concept is that the housing should be designed so that interference with the LRB does not occur during the beyond-design-basis earthquakes. To do this, the vertical seismic displacement of the spring should be properly limited by the determination of a design VIF and damper design.

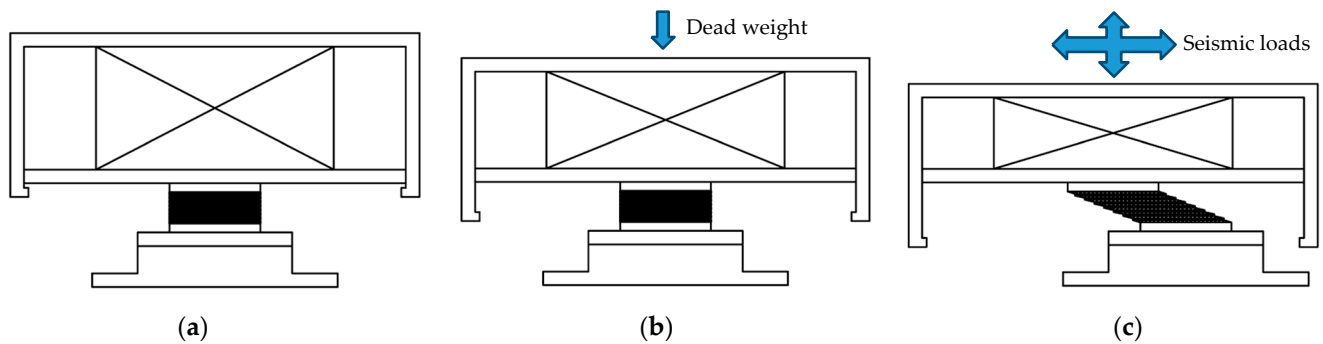


Figure 2. Schematics of 3D seismic isolator’s motions: (a) Without loads; (b) with vertical static load; (c) with horizontal and vertical seismic loads.

In this paper, the design target is established to limit the maximum vertical seismic displacement response within the static displacement of the spring by design vertical load of 10 kN. This will prevent detachment between the housing and the vertical spring.

Table 2 presents the required vertical stiffness of the spring according to the design VIF for a design vertical load of 10 kN and their static vertical displacement values.

Table 2. Parameter values for simple seismic analysis model.

Design VIF (Hz)	Required Vertical Stiffness (kN/m)	Static Disp. for 10 kN (mm)
1.0	39.5	253.3
2.0	157.9	63.3
2.5	246.7	40.5
3.0	355.3	28.1
3.5	483.6	20.7
4.0	631.7	15.8
5.0	987.0	10.1

3. Sensitivity Study on Vertical Seismic Isolation Performance with VIF

In principle, the basic concept of seismic isolation design is to design an appropriate seismic isolation frequency to avoid resonance with input earthquakes by moving the natural frequency of the superstructure in the frequency range of a strong earthquake to a sufficiently low frequency using a seismic isolator.

In general, the vertical natural frequency of a nuclear power plant building is around 10~20 Hz, which is out of the range of peak spectral frequency band, 3 Hz to 10 Hz in the US NRC RG-1.60 design ground-response spectrum [22]. However, there is possibility of resonance seismic response if the earthquake level increases enough to invoke severe cracks in the nuclear power plant building structures. In this case, the spectral peak frequencies of the response spectrum at the floor where the nuclear power plant equipment is seismically isolated may be shifted to a lower region due to the decrease of the structural stiffness of the nuclear power plant building. This situation can cause severe vertical seismic response amplification in nuclear power plants. Therefore, in the vertical seismic isolation design of nuclear power plants against a large earthquake, it is very important to determine the

design VIF that can deviate from the floor-response spectrum peak frequency band and the resonant frequency of the upper structure.

In this study, a remote shutdown console (RSC), which is installed at elevation of 136 ft of an actual nuclear power plant building, is chosen as one of the target 3D seismic isolation equipment. To investigate the sensitivity of the VIF, the vertical seismic isolation performance analyses are carried out with the preliminary specified design parameters of the vertical seismic isolation device, as shown in Table 3.

Table 3. Preliminary design parameter values for sensitivity analysis.

Parameters	Values
Superstructure mass (kg)	1000
Stiffness of vertical spring, K_{VS} (N/m)	Variable depending on VIF
Damping of vertical spring, C_{VS} (kg/s)	62.8
Elastic stiffness of steel damper, K_e (N/m)	621,700
Tangential stiffness of steel damper, K_t (N/m)	36,460
Characteristic strength, F_{slide} (N)	990
Struct. Damping of steel damper, C_{SD} (kg/s)	0

Figure 3 presents the input earthquake used in the design of the vertical seismic isolation device in this study. Figure 3a is the vertical floor-response spectrum at 136 ft of the auxiliary building, corresponding to the peak ground acceleration, $PGA = 0.5$ g, which is 1.67 times the Safe Shutdown Earthquake ($PGA = 0.3$ g). We can see that the peak spectral frequency band exists at 10 Hz to 16 Hz and the peak spectral acceleration is large at about 40 g. As shown in Figure 3b,c, the zero-period acceleration (ZPA) value is 1.2 g, and the peak/valley displacements are -211 mm/ $+176$ mm.

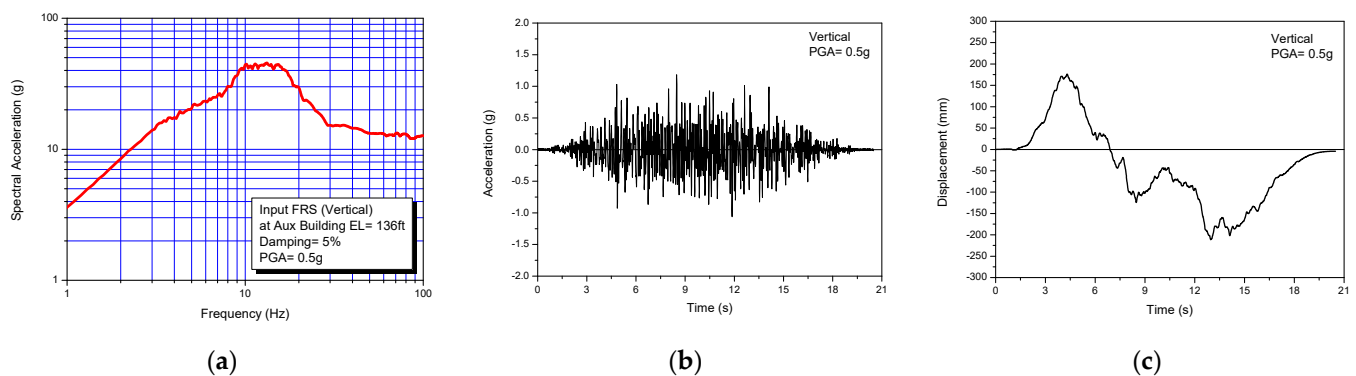


Figure 3. Used vertical seismic input motion ($PGA = 0.5$ g): (a) Floor response spectrum; (b) acceleration time history; (c) displacement time history.

Figure 4 presents the simple seismic analysis model used for the sensitivity of the vertical seismic isolation performance on the VIF. For the transient seismic time history analysis, a commercial finite element program ANSYS [23] was used. As shown in Figure 4a, the vertical spring is modeled by a simple stiffness–damping element (COMBIN14), and the vertical damper is model with a bilinear force–displacement element (COMBIN40), reflecting the hysteretic characteristics of the steel damper. It was assumed that the inertia mass of the superstructure acts as a concentrated mass (MASS21) at node 3. Figure 4b shows the concept of the bilinear model of the steel damper.

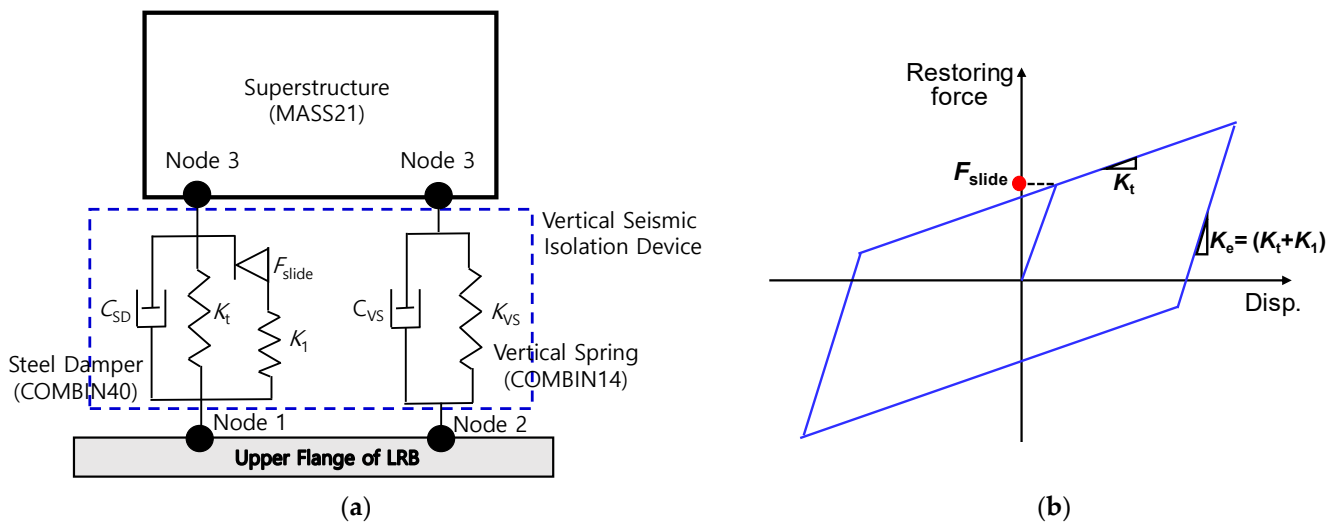


Figure 4. Schematics of simple seismic analysis model used for sensitivity analysis: (a) Finite element model of vertical seismic isolation device; (b) bilinear model of steel damper.

To investigate the sensitivity of the design VIF on the vertical seismic isolation performance, the design VIF was considered in the range of 1 Hz~5 Hz. The equivalent damping ratio and stiffness of the steel damper corresponding to the hysteretic bilinear model in Table 3 are 30.7% and 75,291 N/m, respectively. The equivalent stiffness of the steel damper has a corresponding natural frequency of about 1.38 Hz for a vertical design load of 10 kN. Therefore, the actual VIF will be determined by considering both spring and steel damper stiffness.

Figure 5 shows the result of the calculated vertical response spectrum for the superstructure according to the design VIF determined by the stiffness value of the vertical spring. As shown in the figure, it can be seen that the lower the design VIF, the higher the seismic isolation performance is due to the frequency shift effect. When the design VIF is 1.0 Hz, the spectral acceleration response of the superstructure is significantly reduced compared with the input response spectrum throughout frequencies. When the design VIF increases to 3 Hz, the superstructure exhibits the vertical seismic isolation effect in the range of about 6 Hz to 50 Hz, and the ZPA value is almost similar to that of the input earthquake without vertical seismic isolation effect. When the design VIF exceeds 3.0 Hz, the vertical seismic isolation effect is greatly reduced in the overall frequency range, and the ZPA value of the superstructure becomes larger than that of the input earthquake.

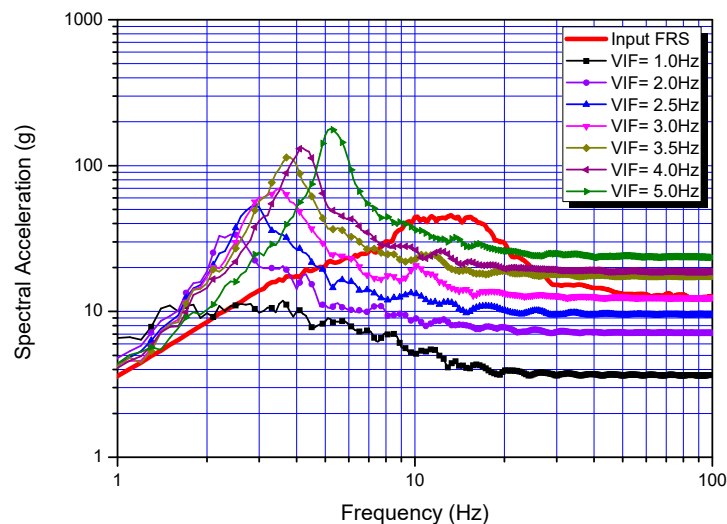


Figure 5. Spectral acceleration response of superstructure for various design VIF.

Figure 6 shows the maximum vertical spring displacement response according to the design VIF. As shown in Figure 6a, when only a vertical spring is used without using a steel damper, the vertical spring displacement becomes very large (e.g., 101.3 mm when VIF = 3 Hz). Therefore, it is not possible to design a vertical seismic isolation device actually accommodating the LRB dimensions in Table 1. When the steel damper with the design characteristics of Table 3 is used, the vertical spring displacement can be significantly reduced to 30 mm or less, as shown in Figure 6b.

In addition, it can be seen that the actual VIF is larger than the design value assumed for the vertical stiffness spring due to the stiffness effect of the steel damper, showing the hysteretic characteristic. The lower the design VIF, the larger the stiffness effect of the steel damper. When the design VIF is 1.0 Hz, the actual VIF increases by 80%.

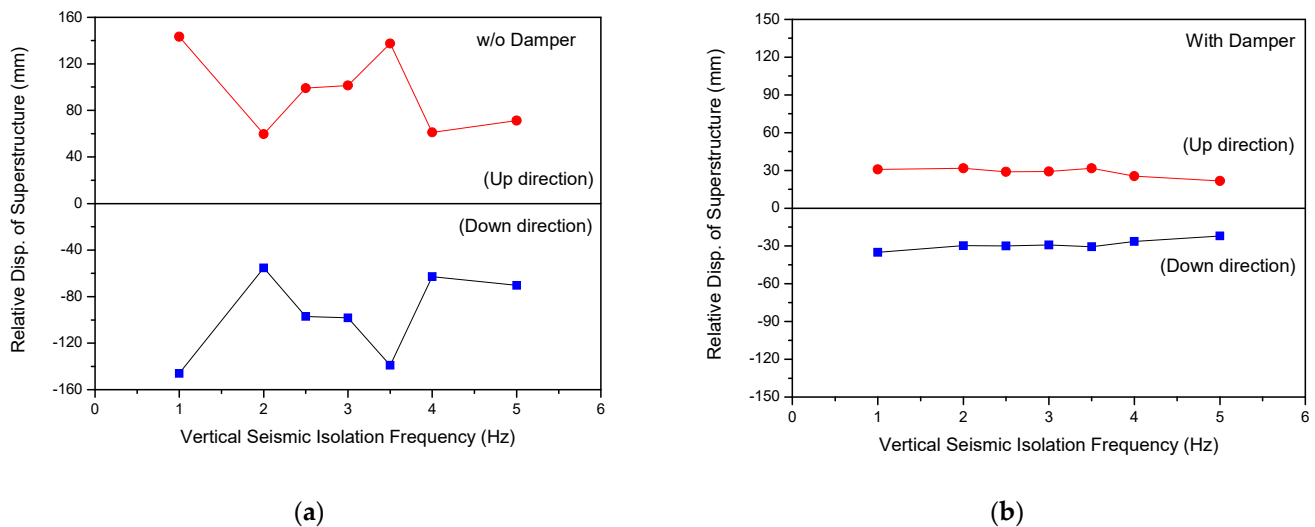


Figure 6. Maximum spring displacement response for various design VIF: (a) Without steel damper; (b) with steel damper.

Table 4 summarizes the sensitivity analysis results of the vertical seismic isolation performance according to the design VIF. As shown in the table, it can be seen that as the design VIF increases, the effective frequency range in which the actual seismic isolation effect can be obtained is rapidly reduced. When the design VIF is equal to or higher than 3.0 Hz, the ZPA response becomes larger than that of the input floor response spectrum, and then the vertical seismic isolator has the opposite effect of amplifying the vertical seismic response in the high-frequency region.

Table 4. Summary results of vertical seismic isolation performance with design VIF.

Design VIF (Hz)	Effective Frequency Range (Hz)	ZPA ¹ Response (g)	Max. Displacement (mm)		VIF with Damper (Hz)
			Without Damper	With Damper	
1.0	2.6<	0.37	+143.4/−146.0	+30.8/−35.1	1.8
2.0	4.2<	0.73	+59.7/−55.3	+31.7/−29.8	2.4
2.5	5.0<	0.97	+99.2/−97.0	+28.9/−30.0	2.9
3.0	6.2~80.0	1.27	+101.3/−98.3	+29.2/−29.3	3.5
3.5	7.5~26.0	1.78	+137.6/−139.0	+31.7/−30.7	3.8
4.0	8.0~24.0	1.91	+61.2/−62.9	+25.6/−26.5	4.2
5.0	9.5~20.0	2.40	+71.2/−70.4	+21.6/−22.1	5.2

¹ Note that ZPA of input floor response spectrum is 1.27 g.

4. Vertical Spring Design for Vertical Seismic Isolation Device

As shown in Figure 1 above, the spring for vertical stiffness is designed to be applied to a vertical seismic isolator that can be integrally mounted on a small-sized LRB with a vertical design load of 10 kN, which is a horizontal seismic isolator for individual facilities in a nuclear power plant. To substantiate the stiffness of the vertical seismic isolation device, the spring design was investigated in detail based on the sensitivity analysis results above.

In this study, two types, such as disc spring and helical coil spring, were chosen for a stiffness design of the vertical seismic isolation device.

4.1. Disc Spring Design

The disc spring used in this study is a cone-shaped, thin steel structure with outer diameter (D), inner diameter (d), thickness (t), and height (H) as shown in Figure 7. When a vertical force is applied, the disc spring stably undergoes compression deformation and has a constant stiffness value within the operating displacement. Once the design stiffness value is determined, it can be designed to have the appropriate load capacity and displacement range by stacking the required number of disc springs in series or in parallel.

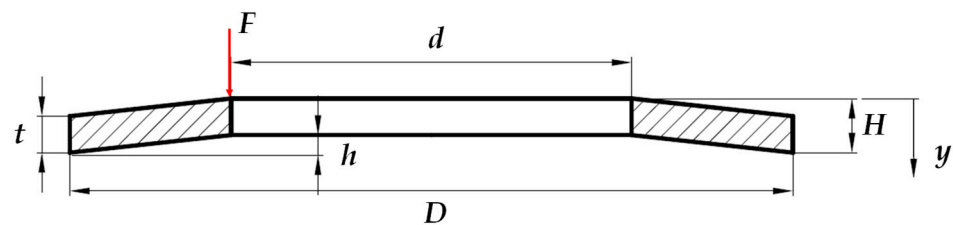


Figure 7. Schematics of the disc spring configurations and dimensional design parameters.

The relationship between the applied load (F) and the corresponding displacement (y) in the disc spring in Figure 7 can be described as the following equation [24]:

$$F = \frac{2Et}{(1 - \nu^2)ZD^2} \left[y^3 - 3hy^2 + 2y(h^2 - t^2) \right] \quad (1)$$

where

$$Z = \frac{1}{\pi} \left(\frac{C - 1}{C} \right)^2 \left[\left(\frac{C + 1}{C - 1} \right) - \ln \frac{2}{C} \right]^{-1} \quad (2)$$

$$C = \frac{D}{d} \quad (3)$$

In the above equation, E and ν represent the elastic modulus and Poisson’s ratio of the material, respectively. When the disc springs are stacked in series, the total displacement and equivalent stiffness are proportional to $1/n$ (n is number of disc springs). Therefore, when the design VIF is determined, it can be implemented by connecting an appropriate number of disc springs in series.

Table 5 presents the design parameters of the disc spring designed in this study. The plate spring material used in the design is JIS SUP10 spring steel.

In Table 5 above, the shut displacement (h) refers to the maximum displacement that the disc spring can accommodate. The disc spring is mounted on the upper flange of LRB, which functions as a horizontal seismic isolator. If the outer diameter of the disc spring is larger than the outer diameter of the LRB, bending deformation may occur in the upper flange of LRB due to the load reaction force applied to the disc spring by the seismic response of the superstructure. In this study, considering the outer diameter of 100 mm of the LRB, the outer diameter of the disc spring is determined to be 80 mm.

In general, the design-allowable displacement of the disc spring assumes 75% of the shut displacement. In this case, the design-allowable displacement for a single disc spring of Table 5 is 1.65 mm, considering the shut displacement ($h = 2.2$ mm). Therefore,

assuming that the relationship between displacement and reaction force is linear within the design-allowable displacement of the single disc spring, the load capacity of the single disc spring becomes 22.9 kN from Equation (1) above, and, accordingly, the spring stiffness is determined to be 13,879 kN/m.

Table 5. Design parameter values for a single disc spring.

Design Parameters of Disc Spring	Values
Outer diameter, D (mm)	80
Inner diameter, d (mm)	41
Thickness, t (mm)	4
Shut displacement, h (mm)	2.2
Height, $H(=t + h)$ (mm)	6.2
Design vertical load, F (kN)	10
Young's modulus, E (GPa)	190
Poisson ratio, ν	0.27

Figure 8 compares the stiffness test results for six single disc springs manufactured according to the design parameters in Table 5 and the stiffness values calculated from Equation (1). As shown in the figure, it was confirmed that the stiffness test results and calculation results were well matched up to the design-allowable displacement of 1.65 mm, and linearity was guaranteed.

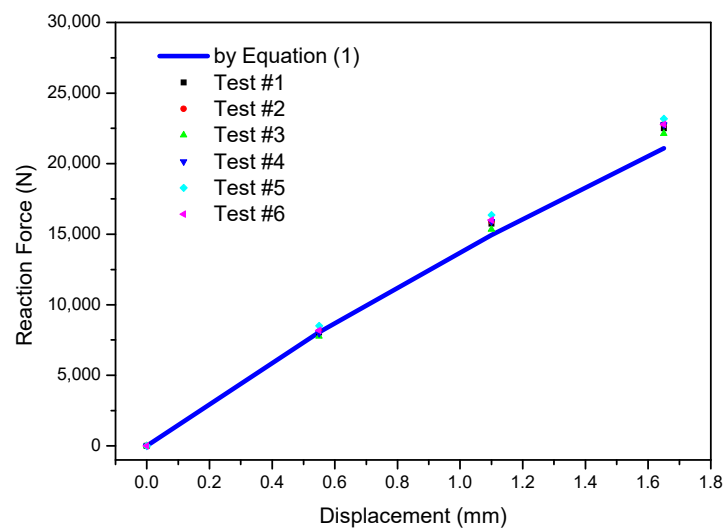


Figure 8. Comparison of the linearity characteristics between tests and calculation values by formula for a single disc spring.

Table 6 presents the results of design summary for the set of disc spring that satisfies the design VIF. As shown in the table, when the design VIF is lower, the required number of disc springs greatly increases. This results in a significant increase in the total height of the spring and acts as a burden in the housing design. When the design VIF is set to 2.0 Hz or less, the required housing height of the vertical seismic isolation device is more than 500 mm. Therefore, when using a disc spring, it is desirable to determine the design VIF at least larger than 2.5 Hz with consideration of an appropriate height.

Table 6. Design summary of stacked disc springs for various design VIF.

Design VIF (Hz)	Required Stiffness (kN/m)	Required Number of Disc Spring ¹	Total Height ¹ (mm)	Total Shut Disp. (mm)	Static Disp. for 10 kN (mm)
1.0	39.5	352	2182	1408	253.3
2.0	157.9	88	546	352	63.3
2.5	246.7	58	360	232	40.5
3.0	355.3	40	248	160	28.1
3.5	483.6	30	186	120	20.7
4.0	631.7	22	136	88	15.8
5.0	987.0	16	99	64	10.1

¹ In case of a serial stack.

4.2. Helical Coil Spring Design

In this study, a helical coil spring, which is widely used in industry, was selected as another spring type to provide vertical stiffness. The main design variables that determine the stiffness characteristics of a helical coil spring are the coil diameter, section diameter, and number of turns, as shown in Figure 9.

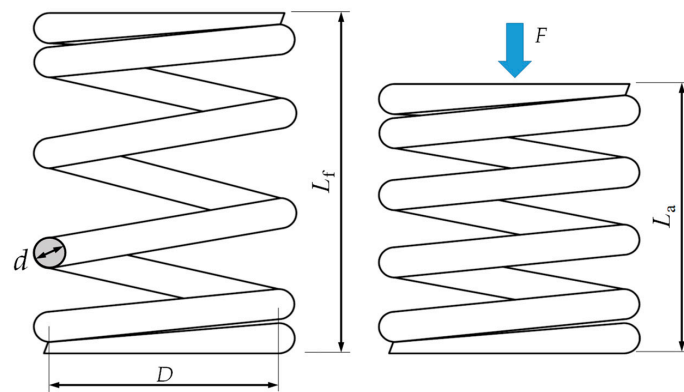


Figure 9. Configuration and dimensional parameters for helical coil spring.

In above figure, L_f and L_a indicate the free length and assembled length with compression force, respectively.

The relationship between the applied force (F) and the total stretch (y) of a helical coil spring in Figure 9 can be approximately described as follows [24]:

$$y = \frac{F(8D^3N_a)}{d^4G} \tag{4}$$

where D , d , N_a , and G represent the helical coil diameter measured from spring axis to center of section, diameter of circular section, number of active turns, and shear modulus of the material, respectively.

As the helical coil spring has relatively less rigidity than the disc spring, it is recommended to install the springs in parallel. In this study, four helical coil springs, which have a spring diameter $D = 88$ mm and coil section diameter $d = 12$ mm, are considered for a vertical stiffness design corresponding to vertical design load of 10 kN.

Table 7 presents the results of design summary for the set of helical coil springs that satisfies the design VIF.

As shown in the above table, as the design VIF decreases, the number of coil turns required for the spring stiffness increases rapidly, which leads to a great increase in the total height of the spring. In this study, the design VIF of 2.5 Hz~3.0 Hz was selected to be an appropriate total height of the helical coil spring for substantiation of the design.

Table 8 shows the detailed design parameter values for the helical coil spring that satisfies the selected design VIF of 2.5 Hz and 3.0 Hz.

Table 7. Design summary of helical coil spring system with design VIF.

Design VIF (Hz)	Required Stiffness (kN/m)	Number of Spring ¹	Required Number of Coil Turns	Total Height (mm)	Total Shut Displacement (mm)
1.0	39.5	4	29	880	368
2.0	157.9	4	7.5	230	110
2.5	246.7	4	5	160	78
3.0	355.3	4	3.5	135	60
3.5	483.6	4	2.5	100	50
4.0	631.7	4	1.8	90	45
5.0	987.0	4	-	-	-

¹ Parallel mounting.

Table 8. Summary results of final design parameter values for a single helical coil spring.

Design Parameters	Values	
	VIF = 2.5 Hz	VIF = 3.0 Hz
Outer diameter, D_o (mm)	100	100
Coil diameter, d (mm)	12	12
Mean spring diameter, $D = D_o - d$ (mm)	88	88
Number of coil turns, N_a	5	3.5
Pitch, p (mm)	27.20	31.71
Total height, L_f (mm)	160	135
Assembled height, L_a (mm)	119.47	106.86
Minimum height, $L_{m,}$ (mm)	78	60
Shear modulus, G (GPa)	75	75
Spring constant, K (kN/m)	61.69	88.83

To substantiate the actual stiffness design of the helical coil springs satisfying the design VIF of 2.5 Hz and 3.0 Hz in Table 8, the springs were fabricated, and static stiffness tests were performed with 16 specimens. Figure 10 presents the comparison results between tests and the design values calculated by Equation (4). As shown in the figure, the stiffness test results reveal a deviation of less than 1%, on average, when VIF = 2.5 Hz compared to the design value, and about 2%, on average, when VIF = 3.0 Hz.

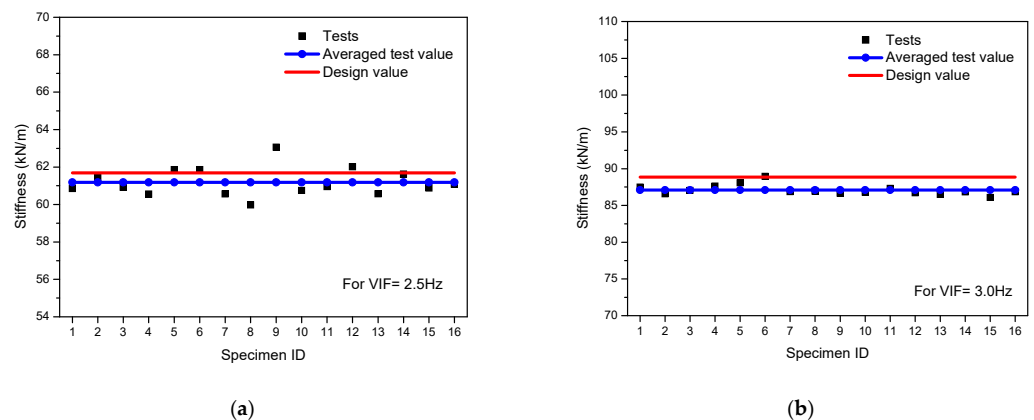


Figure 10. Comparison of stiffness between tests and design values of helical coil springs: (a) For VIF = 2.5 Hz; (b) for VIF = 3.0 Hz.

5. Design and Verification of Vertical Steel Damper

5.1. Design Configurations and Dimensions

The seismic energy dissipation performance of the steel damper reduces the vertical seismic displacement response of the spring with an appropriate size and configuration. As shown in the results of vertical seismic isolation performance in Table 4, the vertical damper should be designed enough to control the seismic displacement of the spring to avoid the interference with the LRB.

Figure 11 shows the configuration and dimensional parameters of the steel damper designed in this study. As shown in the figure, the steel damper is a thin beam plate having a tapered length. The steel damper is fixed by a specific jig mounted on the LRB upper flange, and its end is connected to the superstructure with pin joint.

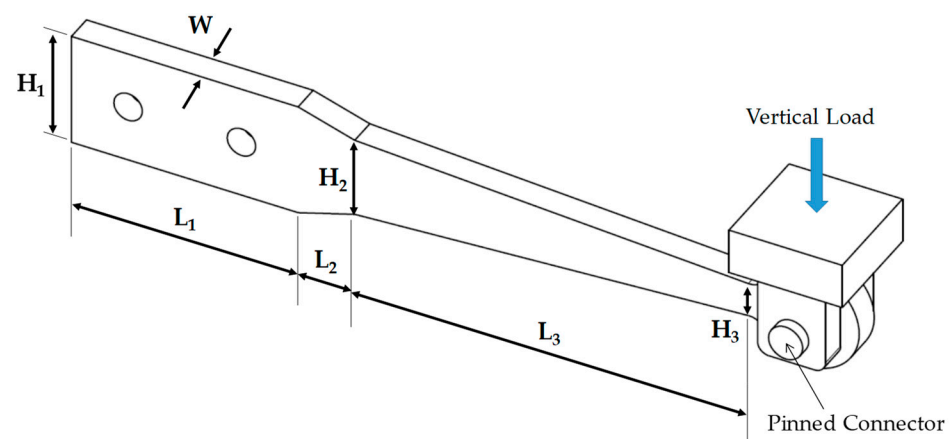


Figure 11. Configurations and dimensional parameters of steel damper.

In this study, the dimensions of three shapes were considered to investigate the hysteretic damping characteristics. Table 9 presents the design dimensions considered in this study.

Table 9. Dimensions for steel dampers (mm).

Steel Damper ID	L1	L2	L3	H1	H2	H3	W
SD1	40	40	80	20	8	5	5
SD2	40	35	75	15	10	5	4
SD3	40	10	70	20	14	6	5

5.2. Evaluations of Energy Dissipation Performance

To evaluate the damping performance of the considered steel dampers in Table 9, force–displacement analysis was performed for the cyclic displacement load. Figure 12 shows the detailed finite element analysis model for the steel damper. As shown in the figure, a three-dimensional solid element (SOLID181) was used for the steel damper model, and it was modeled to have a sufficient number of elements and aspect ratio to enable more accurate plastic deformation analysis. As a boundary condition, a virtual node that can transmit the load from the superstructure was set and modeled so that a cyclic displacement load could be applied to the end of the steel damper using the connecting element (MPC184). As shown in Figure 12, all displacements at two pin holes are assumed to be constrained as fixed conditions, and the displacement-controlled cyclic load is applied at the end of the pinned joint.

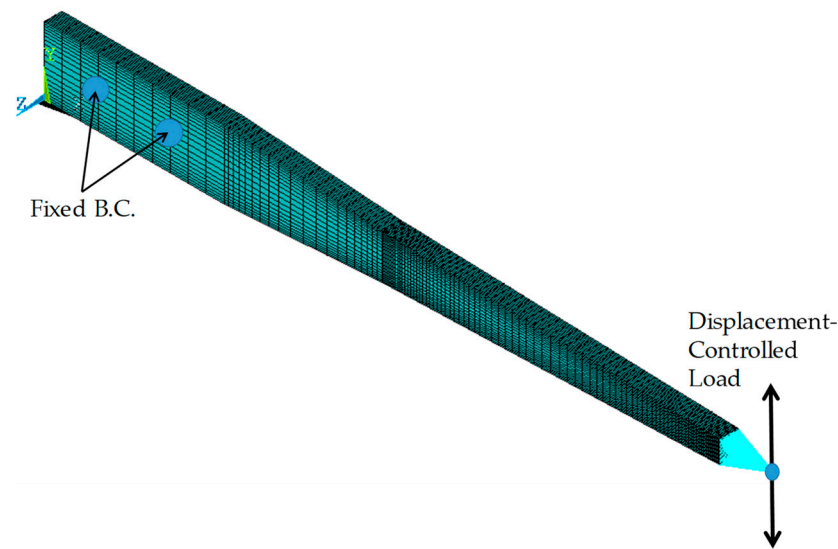


Figure 12. Finite element model of steel damper for energy dissipation analysis.

In order to accurately describe the plastic behavior of Type 316SS, the material of the steel damper used in this study, for the finite element analysis, the following Chaboche’s inelastic constitutive equations [25,26] were used for the kinematic hardening model:

$$\dot{\alpha}_{ij} = \sum_{k=1}^3 \left[\frac{2}{3} C_k \dot{\epsilon}_{ij}^p - \gamma_k (\alpha_{ij})_k \dot{p} \right] \quad (5)$$

where $\dot{\alpha}_{ij}$ and \dot{p} indicate the revolution of back stress and an accumulated plastic strain, respectively, and C_k and γ_k ($k = 1\sim 3$) are material constants to be used in the ANSYS program.

For the isotropic hardening model, the inelastic Voce model [27] is used as follows:

$$\dot{R} = b[Q - R]\dot{p} \quad (6)$$

where \dot{R} indicates the revolution of drag stress, and b and Q are material constants.

Table 10 is the material constants for Type 316 stainless steel used in the above inelastic material constitutive equations [28].

Table 10. Material constants for inelastic material models at room temperature.

Material	σ_{yo} (MPa)	E (GPa)	C_1 $\times 10^9$	C_2 $\times 10^9$	C_3 $\times 10^9$	γ_1 $\times 10^3$	γ_2 $\times 10^3$	γ_3	b	Q $\times 10^6$
Type 316SS	135	190	120	20.2	10.67	1.0	1.0	1.0	45.0	85

To evaluate the hysteretic damping performance of the steel damper, the vertical cyclic displacement range was set to ± 30 mm and inelastic finite element analysis was performed on the triangular waveform input.

Figure 13 shows the distribution of an equivalent plastic deformation for the steel damper of SD2 during five cycles. As shown in the figure, the maximum equivalent plastic strain occurs at the upper and lower surfaces of the middle part of the steel damper by about 2.5%, and after the final fifth cyclic load, the maximum residual plastic strain remains about 0.56% at the transition region.

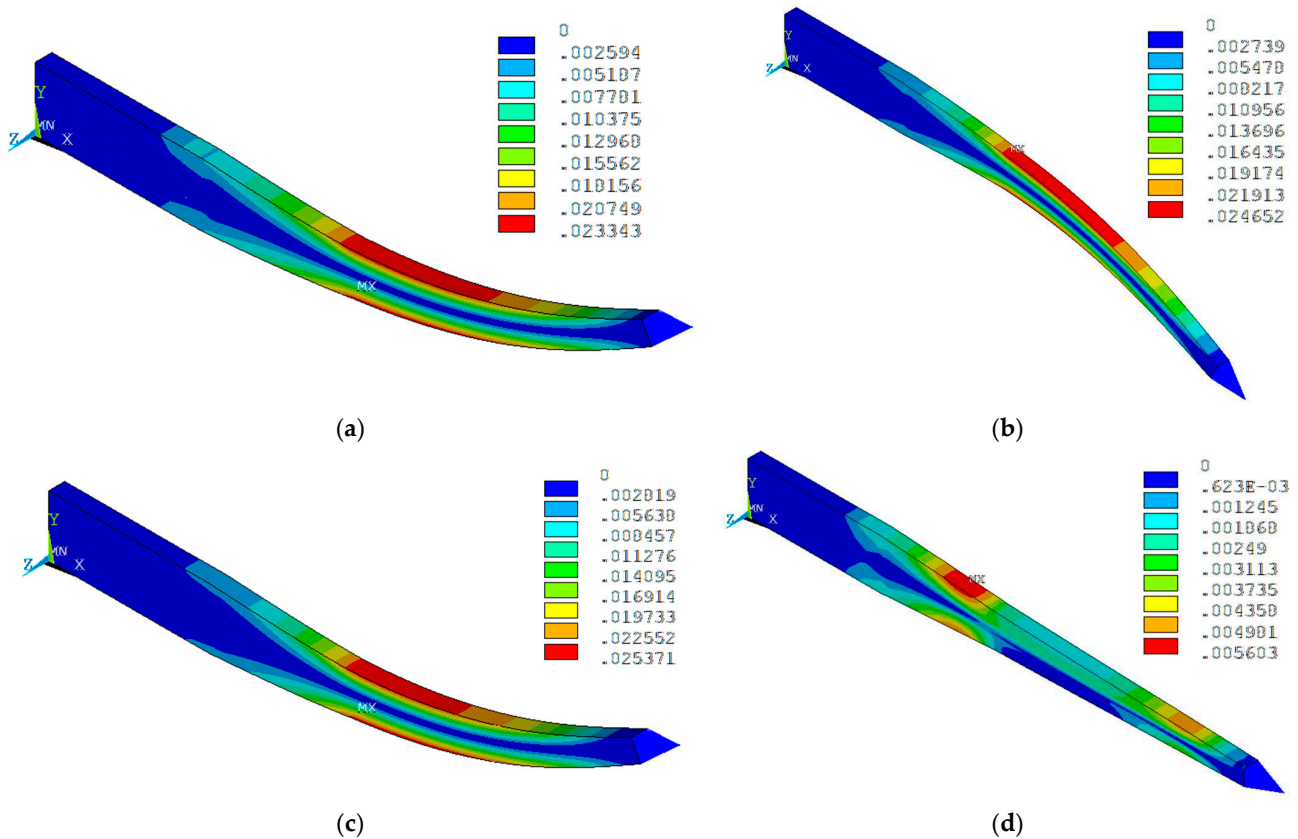


Figure 13. Analysis results of equivalent plastic strain distributions and deformation shapes of steel damper, SD2 during ± 30 mm stroke: (a) After 1/4 cycle; (b) after 1(3/4) cycles; (c) after 3(1/4); (d) after 5 cycles.

Figure 14 presents the analysis results of an equivalent plastic strain time history at the node where the maximum plastic strain occurs for SD2. As shown in the figure, the maximum equivalent plastic strain in the middle of the steel damper is about 2.6% at the time of the maximum and minimum cyclic displacement loads. Considering that Type 316 SS material used in this study has a total elongation of 40% or more, it is expected that sufficient plastic strain margin can secure the structural integrity of the steel damper without fracture during the strong vertical earthquakes.

Figure 15 presents the analysis results of hysteretic behavior for five cycles, which is the vertical displacement–reaction force relationship of the steel damper. As shown in the figure, the effective stiffness increases in order of SD1, SD2, and SD3, and energy dissipation area increases inversely, and it can be seen that all shapes of steel dampers exhibit hysteretic behavior in which all isotropic hardening properties are quickly stabilized after about three cycles.

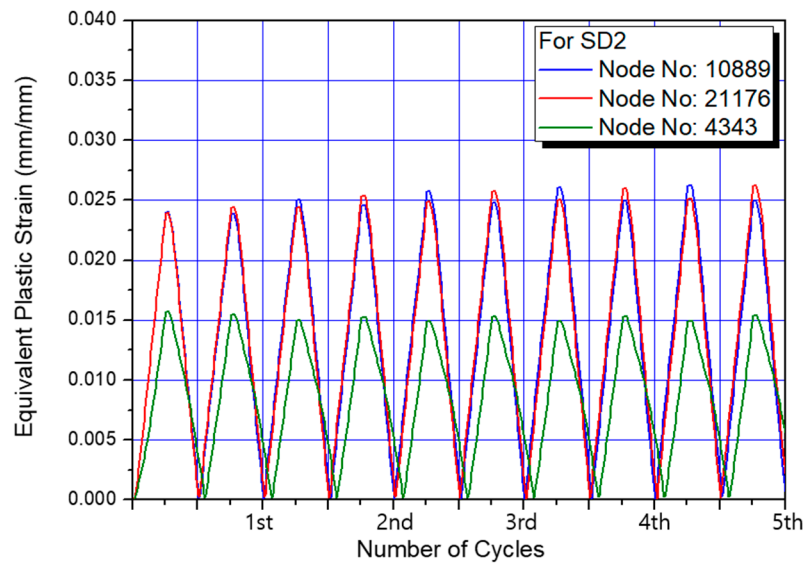


Figure 14. Analysis results of equivalent plastic strain time history during cyclic load for SD2.

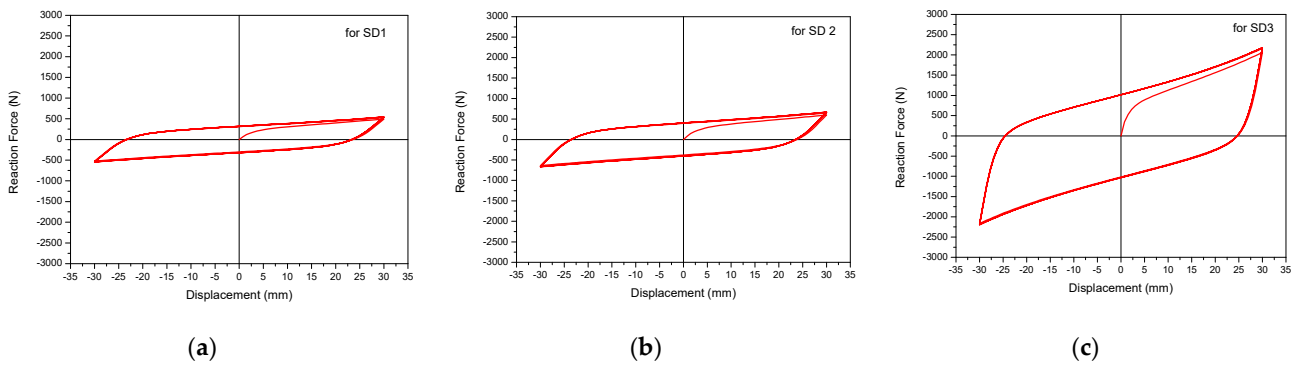


Figure 15. Analysis results of hysteretic response for steel dampers: (a) SD1; (b) SD2; (c) SD3.

Table 11 presents the results of calculating the energy dissipation performance of the steel dampers from the following relational expression [16], assuming idealized bilinear hysteretic behavior extracted from the third cycle.

$$\zeta_d = W / (2\pi K_{eff} D^2) \tag{7}$$

Table 11. Evaluation results of energy dissipation capacity of steel dampers.

Steel Damper ID	K_t (kN/m)	K_e (kN/m)	F_{slide} (N)	W^1 (N·m)	Critical Damping Ratio (%)
SD1	7.21	100.82	330.64	25.44	35.17
SD2	9.00	127.21	413.24	31.87	35.25
SD3	37.00	695.77	1064.61	90.60	31.70

¹ W is the area of hysteresis curve indicating the energy dissipation per cycle (EDC).

In the above equation, W , K_{eff} , and D represent the energy dissipation area per cyclic load, the effective stiffness, and the maximum displacement of the hysteresis curve, respectively. As shown in the table, all steel dampers designed in this study were evaluated to have damping performance with a critical damping ratio of 30% or more.

5.3. Verification Tests of Steel Damper Performance

The quasistatic test was performed to verify the hysteretic damping performance of the steel dampers in Table 11. In the verification test, three specimens were used for each steel damper ID. Figure 16 is a photograph of the steel damper specimen shapes and test facility with installation of the steel damper specimen. Table 12 shows the specifications of the DC motor-driven testing machine used in this test.

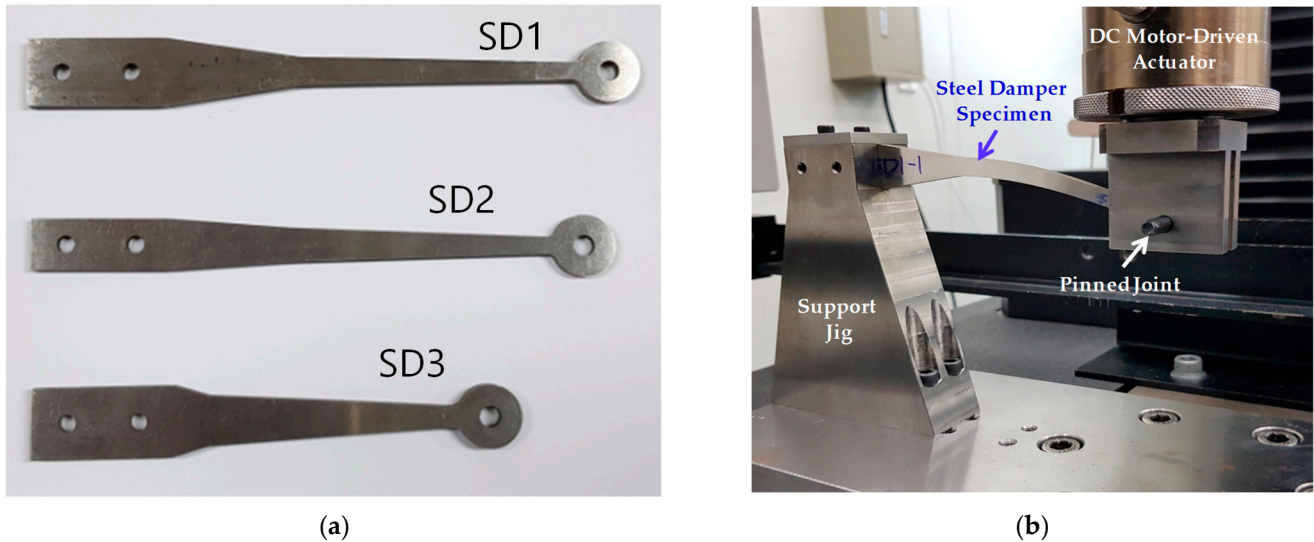


Figure 16. Photos of steel damper specimen and test facility: (a) Steel damper specimen; (b) test facility with specimen.

Table 12. Performance characteristics of test facility.

Item	Performance
Facility model name	INSTRON 5982
Max. loading (kN)	100
Footprint dimensions (mm)	1130 × 777
Height (mm)	2273
Control axes	1
Max. displacement (mm)	1330
Min. speed (mm/min)	0.0001
Max. speed (mm/min)	1016
Excitation mechanism	Brush DC Motor
Control software	INSTRON Bluehill 3

In order to verify the hysteretic energy dissipation performance, the test was carried out in five cycles for two ranges of maximum ± 24 mm and ± 30 mm, considering the target design displacement limit with quasistatic displacement control. The test speed applied to the quasistatic displacement control test is 5 mm/min. Figure 17 shows a photograph of the deformed shape under the maximum displacement load during the cyclic tests on the steel damper. Through visual inspection after the test, it was confirmed that there were no surface cracks on all steel damper specimens.



Figure 17. Deformed shapes of steel dampers after the maximum displacement loads.

Figures 18–20 present a comparison of the results of the hysteretic behavior of the steel dampers between the tests and inelastic analyses.

As shown in the figures above, we can see that the hysteretic behavior of the steel dampers by tests are in good agreement with the analysis results. In addition, the initial yield behavior and cyclic hardening characteristics are well matched, and all steel dampers are rapidly stabilized after three cycles. Therefore, it is expected that there is no significant change in the energy dissipation performance due to the increase in the yield strength according to the cyclic load. From the comparison results of these tests and analysis results, it is confirmed that the design of the steel damper presented in this study for application to the vertical seismic isolation device of the 3D seismic isolator can ensure the damping performance of 30% or more, which is the design target in terms of energy dissipation performance.

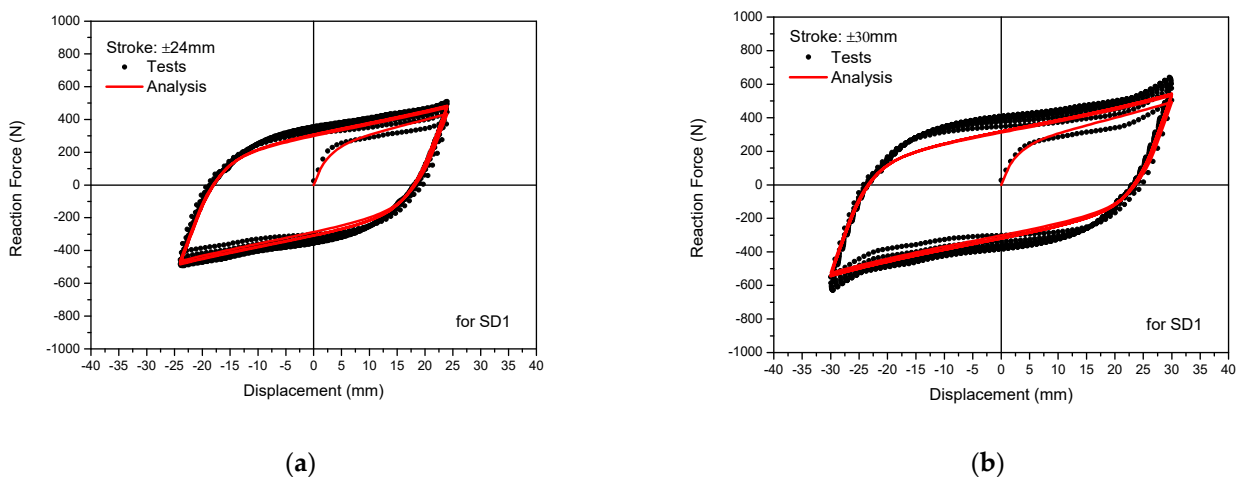


Figure 18. Comparison results of hysteretic behavior between tests and analyses for steel damper, SD1: (a) for ± 24 mm stroke; (b) for ± 30 mm stroke.

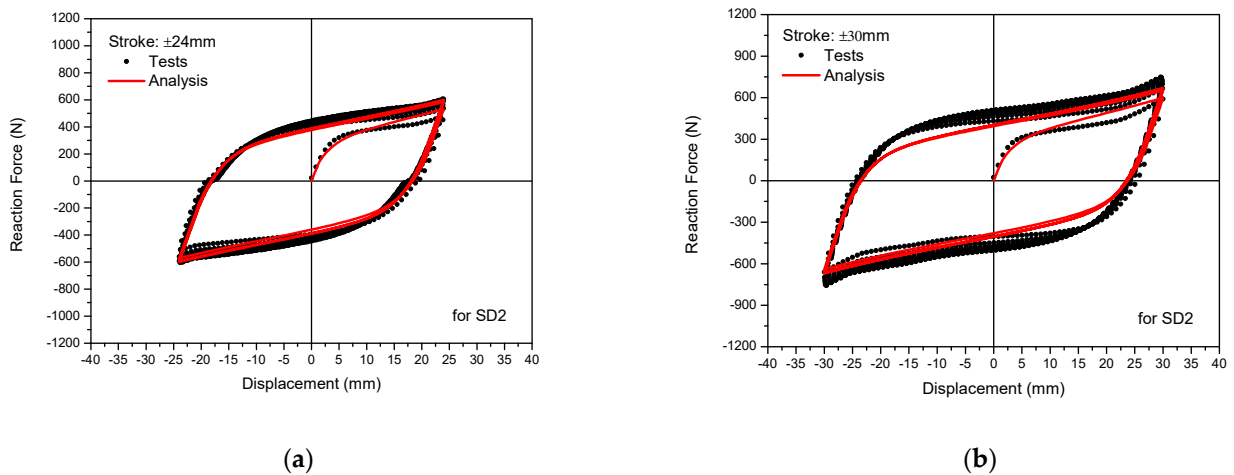


Figure 19. Comparison results of hysteretic behavior between tests and analyses for steel damper, SD2: (a) for ± 24 mm stroke; (b) for ± 30 mm stroke.

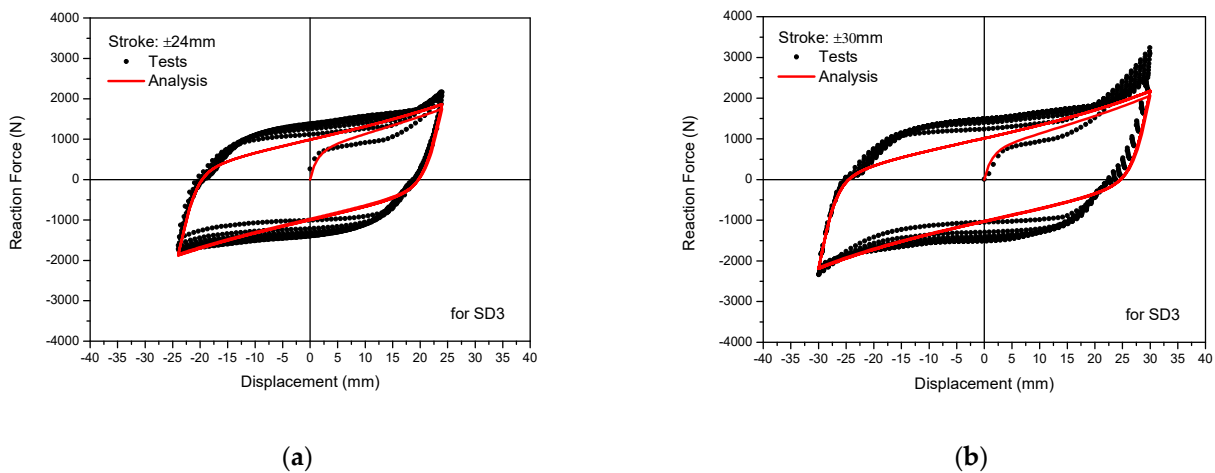
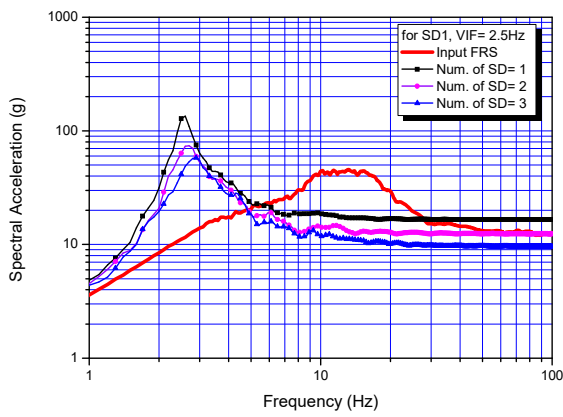


Figure 20. Comparison results of hysteretic behavior between tests and analyses for steel damper, SD3: (a) for ± 24 mm stroke; (b) for ± 30 mm stroke.

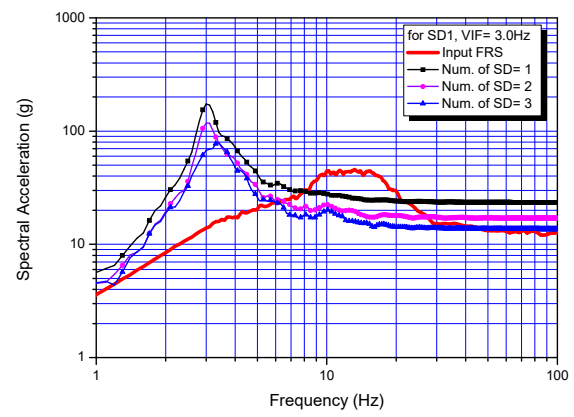
6. Evaluations of Vertical Seismic Isolation Performance

To investigate the seismic energy dissipation performance and find the adequate number of steel dampers required for the vertical displacement limits, the vertical seismic isolation performance evaluations are carried out for the chosen design VIF of 2.5 Hz and 3.0 Hz with three designed steel dampers of SD1, SD2, and SD3. The used finite element seismic analysis model is shown in Figure 4, and the steel damper is modeled by the bilinear stiffness, as identified in Table 11.

Figures 21–23 present the calculation results of the floor response spectrum according to the used number of steel dampers. As shown in Figure 21, in the case of the relatively flexible steel damper SD1, the variation of the actual VIF is not sensitive to the used number of steel dampers. However, in order to obtain effective vertical seismic isolation performance, it was found that two or more SD1 dampers should be used when VIF is 2.5 Hz, and three or more when design VIF is 3.0 Hz. From the results of Figure 22, it can be seen that the steel damper SD2 shows almost similar vertical seismic isolation performance characteristics to that of the steel damper SD1.

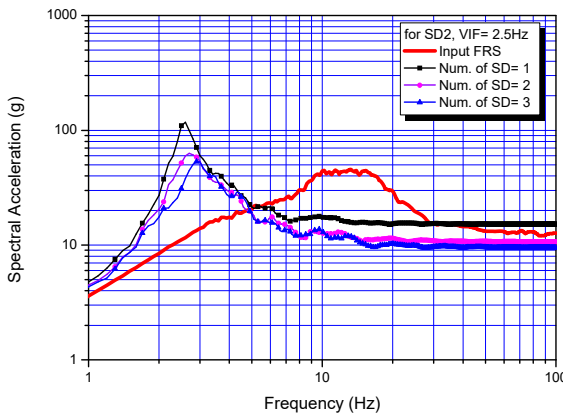


(a)

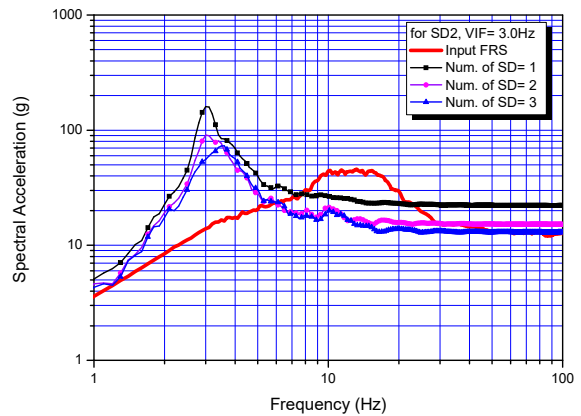


(b)

Figure 21. Results of vertical response spectrum for steel damper, SD1: (a) Design VIF = 2.5 Hz; (b) design VIF = 3.0 Hz.



(a)



(b)

Figure 22. Results of vertical response spectrum for steel damper, SD2: (a) Design VIF = 2.5 Hz; (b) design VIF = 3.0 Hz.

In the case of the SD3 steel damper, which has relatively strong rigidity, as the used number of steel dampers increases, the actual VIF significantly increases, and the effective frequency range in which the seismic isolation effects can be obtained is greatly reduced, especially at lower frequency less than 10 Hz as shown in Figure 23. However, in case of vertical seismic isolation design for nuclear power plant equipment designed with a vertical natural frequency of 10 Hz or higher, it can be seen that an effective vertical seismic isolating effect can be obtained even if three steel dampers are used.

To check the vertical displacement limits, as discussed in Section 2.2 above, the seismic displacement responses were investigated for each case of the disc spring and helical coil spring. Table 13 presents the summary analysis results of the maximum vertical seismic displacement response of the vertical seismic isolation device according to the used number of steel dampers. In the table, the values of column 4 and column 5 represent the accommodatable vertical seismic displacement by extracting the static displacement from the shut displacement. As shown in the table, when the steel damper SD1 is used, five or more steel dampers must be used to satisfy the vertical displacement limits, and four or more steel dampers are required for SD2 and one or more steel dampers for SD3.

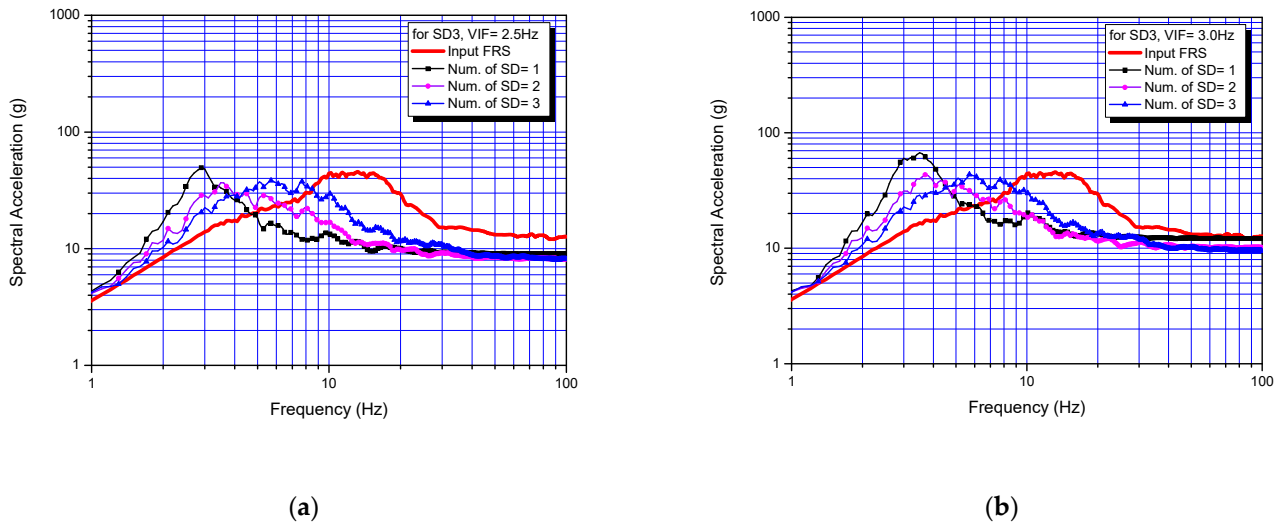


Figure 23. Results of vertical response spectrum for steel damper, SD3: (a) Design VIF = 2.5 Hz; (b) design VIF = 3.0 Hz.

Table 13. Results of vertical seismic displacement responses of vertical isolation device.

Steel Damper ID	# of Dampers	Peak Vertical Seismic Disp. Response (mm)		$(D_{sd} - D_{dw})^{(1)}$ for Disc Spring (mm)		$(D_{sd} - D_{dw})^{(1)}$ for Helical Coil Spring (mm)		Vertical Disp. Limits (mm)	
		VIF = 2.5 Hz	VIF = 3.0 Hz	2.5 Hz	3.0 Hz	2.5 Hz	3.0 Hz	2.5 Hz	3.0 Hz
SD1	1	-63.6/+62.1	-63.2/+63.7						
	2	-45.1/+41.8	-44.3/+42.7						
	3	-30.9/+32.1	-33.5/+33.6	86.5	59.9	37.5	32.0	40.5 ⁽²⁾	28.1
	4	-29.8/+28.2	-29.0/+30.5						
	5	-25.9/+25.7	-26.1/+27.9						
SD2	1	-57.8/+55.0	-59.8/+59.7						
	2	-37.2/+36.3	-38.6/+33.6						
	3	-30.2/+28.7	-29.7/+30.6	86.5	59.9	37.5	32.0	40.5 ⁽²⁾	28.1
	4	-25.8/+25.6	-26.0/+27.8						
SD3	1	-28.0/+27.9	-27.9/+28.3						
	2	-18.9/+17.8	-16.4/+18.7	86.5	59.9	37.5	32.0	40.5 ⁽²⁾	28.1
	3	-13.6/+9.9	-13.3/+10.5						

⁽¹⁾ D_{sd} : Shut displacement, D_{dw} : Static displacement due to design vertical load of 10 kN. ⁽²⁾ It will be 37.5 mm in the case of helical coil spring.

7. Conclusions

In this study, the design of a vertical seismic isolation device that can be integrally used combined with a lead-inserted small-sized laminated rubber bearing (LRB) was studied for three-dimensional seismic isolation of the nuclear power plant equipment. The overall study was based on the target equipment installed at 136 ft elevation of the typical nuclear power plant building, the input vertical seismic motions of Figure 3, and the rigid superstructure.

From the results of this study, some valuable conclusions are obtained, as follows:

1. The design VIF required for the design of the vertical seismic isolation device should be determined considering both seismic isolation performance and limitation of the vertical displacement of spring. In this study, the design VIF is recommended to be in the range of 2.5 Hz~3.0 Hz.
2. It is confirmed that the disc spring and the helical coil spring are useful for a stiffness design of the vertical seismic isolation device for equipment. The validation of the

design values obtained from the equation of a force and displacement relationship are verified by tests.

3. With an appropriate steel damper design, the vertical displacement response can be limited to the design value. In this study, the vertical displacement response is limited to 40.5 mm (disc spring) and 37.5 mm (helical coil spring) for the design VIF = 2.5 Hz and 28.1 mm for the design VIF = 3.0 Hz, which are based on the static displacement by the design vertical load of 10 kN.
4. It is verified that the designed three shapes of the steel dampers, SD1, SD2, and SD3 reveal the seismic energy dissipation performance over 30% critical damping ratio by tests and analyses.
5. From the vertical seismic isolation performance analyses to find an adequate number of steel dampers satisfying the vertical displacement limits, it is found that the required number of steel dampers are at least five for SD1, four for SD2, and one for SD3.
6. The optimal VIF should be determined with consideration of the frequency characteristics of the input design response spectrum at a specific floor where the equipment is seismically isolated and the vertical natural frequency characteristics of the superstructure.

Author Contributions: Conceptualization, G.-H.K. and J.-Y.J.; methodology, G.-H.K., J.-Y.J. and J.-K.H.; validation, G.-H.K. and J.-Y.J.; formal analysis, G.-H.K.; investigation, T.-M.S. and M.-S.L.; writing—original draft preparation, G.-H.K.; writing—review and editing, J.-Y.J., J.-K.H., T.-M.S. and M.-S.L.; funding acquisition, G.-H.K. All authors have read and agreed to the published version of the manuscript.

Funding: This study was funded by the Ministry of Trade, Industry and Energy through KETEP (Korea Institute of Energy Technology Evaluation Planning). (No. 20181510102380).

Institutional Review Board Statement: Not Applicable.

Informed Consent Statement: Not Applicable.

Data Availability Statement: Not Applicable.

Acknowledgments: This study was funded by the Ministry of Trade, Industry and Energy through KETEP (Korea Institute of Energy Technology Evaluation Planning). (No. 20181510102380).

Conflicts of Interest: The authors declare no conflict of interest.



References

1. Pierre, L. Pioneering actual use of seismic isolation for nuclear facilities. In Proceedings of the 1st Kashiwasaki International Symposium on Seismic Safety of Nuclear Installation, Kashiwasaki, Japan, 26 November 2010.
2. Kwag, S.Y.; Kwag, J.S.; Lee, H.H.; Oh, J.H.; Koo, G.H. Enhancement in the Seismic Performance of a Nuclear Piping System using Multiple Tuned Mass Dampers. *Energies* **2019**, *12*, 2077. [CrossRef]
3. Kostarev, V.; Petrenko, A.; Vasilev, P. A New Method for Essential Reduction of Seismic and External Loads on NPP's Structures, Systems and Components. In Proceedings of the 17th International Conference on SMiRT, Prague, Czech Republic, 17–22 August 2003.
4. Germane, L. Seismic Isolation of the Jules Horowitz Reactor. In Proceedings of the 1st Kashiwasaki International Symposium on Seismic Safety of Nuclear Installation, Kashiwasaki, Niigata, Japan, 26 November 2010.
5. Tajirian, F.F.; Schrag, M.R. Conceptual design of seismic isolation for the PRISM liquid metal reactor. In Proceedings of the Transactions of the 9th International Conference on Structural Mechanics in Reactor Technology, Switzerland, Lausanne, 17–21 August 1987; Volume K2, pp. 705–710.
6. Okamura, S.; Kamishima, Y.; Negishi, K.; Sakamoto, Y.; Kitamura, S.; Kotake, S. Seismic isolation design for JSFR. *J. Nucl. Sci. Technol.* **2011**, *48*, 688–692. [CrossRef]
7. Koo, G.H.; Kim, S.H.; Kim, J.B. Seismic Modeling and Analysis for Sodium-cooled Fast Reactor. *Struct. Eng. Mech.* **2012**, *43*, 475–502. [CrossRef]
8. Morishita, M.; Kitamura, S.; Moro, S.; Kamishima, Y.; Takahiro, S. Study on 3-dimensional seismic isolation system for next generation nuclear power plant-vertical component isolation system with coned disk spring, Technical Report No. 620. In Proceedings of the 13th World Conference on Earthquake Engineering, Vancouver, BC, Canada, 1–6 August 2004.
9. Zhou, Z.; Wong, J.; Mahin, S. Potentiality of Using Vertical and Three-Dimensional Isolation Systems in Nuclear Structures. *Nucl. Eng. Technol.* **2016**, *48*, 1237–1251. [CrossRef]

10. Tajirian, F.F.; Kelly, J.M.; Aiken, I.D.; Veljovich, W. Elastomeric bearings for three-dimensional seismic isolation. In Proceedings of the 1990 ASME PVP Conference, Nashville, TN, USA, 17–21 June 1990.
11. Suhara, J. Research on 3D base isolation system applied to new power reactor 3D seismic isolation device with rolling seal type air spring: Part 1. In Proceedings of the SMiRT 17, Paper #K09e4, Prague, Czech Republic, 17–22 August 2003.
12. Takahashi, O.; Aida, H.; Suhara, J.; Matsumoto, R.; Tsuyuki, Y.; Fujita, T. Construction of civil building using three dimensional seismic isolation system: Part 1, design of building using three dimensional seismic isolation system. In Proceedings of the 14th World Conference on Earthquake Engineering, Beijing, China, 12–17 October 2008.
13. Ogiso, S.; Nakamura, K.; Suzuki, M.; Moro, S. Development of 3D seismic isolator using metallic bellows. In Proceedings of the 17th International Conference on Structural Mechanics in Reactor Technology (SMiRT 17), Prague, Czech Republic, 17–22 August 2003.
14. Wong, J.; Lakshminpath, L.; Armas, P.J.; Paredes, A.E.; Park, C.; Campos, J.A. Design and Small-Scale Testing of 3D Printed Seismic Isolators. In Proceedings of the 2019 American Society for Engineering Education 126th Annual Conference & Exposition, Tampa, FL, USA, 15 June 2019.
15. Okada, Y.; Suhara, J.; Tamura, T.; Ohta, K.; Moro, S. Development of Three Dimensional Seismic Isolation Device with Laminated Rubber Bearing and Rolling Seal Type Air Spring. In Proceedings of the GENES4/ANP2003, Kyoto, Japan, 15–19 September 2003.
16. Koo, G.H.; Jung, J.Y.; Lee, J.H.; Shin, T.M. Development of Small-Sized Lead Inserted Laminated Rubber Bearing for Nuclear Component Seismic Isolation. *Energies* **2020**, *13*, 3193. [CrossRef]
17. Koo, G.H.; Shin, T.M.; Ma, S.J. Shaking Table Tests of Lead Inserted Small-Sized Laminated Rubber Bearing for Nuclear Component Seismic Isolation. *Appl. Sci.* **2021**, *11*, 4431. [CrossRef]
18. Sheikhi, J.; Fathi, M. Natural Rubber Bearing Incorporated with Steel Ring Damper (NRB-SRD). *Int. J. Steel Struct.* **2020**, *20*, 23–34. [CrossRef]
19. Asgari, A.; Osma, S.A.; Azlan, A. Application of HDR Dampers in Seismic Protection of LRB-Controlled Cable-Stayed Bridges. In Proceedings of the Istanbul Bridge Conference, Istanbul, Turkey, 11–13 August 2014.
20. Roh, J.E.; Hur, M.W.; Choi, H.H.; Lee, S.H. Development of a Multiaction Hybrid Damper for Passive Energy Dissipation. *Shock. Vib.* **2018**, *2018*. [CrossRef]
21. Dolati, S.S.K.; Mehrabi, A.; Dolati, S.S.K. Application of Viscous Damper and Laminated Rubber Bearing Pads for Bridges in Seismic Regions. *Metals* **2021**, *11*, 1666. [CrossRef]
22. Nuclear Regulatory Commission. *Design Response Spectra for Seismic Design of Nuclear Power Plants*; Regulatory Guide 1.60; Nuclear Regulatory Commission: Rockville, MD, USA, 1973.
23. ANSYS Mechanical APDL Release 15.0; ANSYS, Inc.: Canonsburg, PA, USA, 2013.
24. Norton, R.L. *Machine Design, An Integrated Approach*; Prentice Hall: Upper Saddle River, NJ, USA, 1996.
25. Chaboche, J.L.; Rousselier, G. On the plastic and viscoplastic constitutive equations—Part II: Application of internal variable concepts to the 316 stainless steel. *J. Press. Vessel. Technol.* **1983**, *105*, 159–164. [CrossRef]
26. Chaboche, J.L. Constitutive equations for cyclic plasticity and cyclic viscoplasticity. *Int. J. Plast.* **1989**, *5*, 247–302. [CrossRef]
27. Voce, E. A Practical Strain hardening Function. *Metallurgia* **1955**, *51*, 219–226.
28. Koo, G.H.; Yoon, J.H. Inelastic Material Models of Type 316H for Elevated Temperature Design of Advanced High Temperature Reactors. *Energies* **2020**, *13*, 4548. [CrossRef]

Article

An Experimental Study on the Mechanical Properties of a High Damping Rubber Bearing with Low Shape Factor

Zhenyuan Gu ¹, Yahui Lei ¹, Wangping Qian ^{1,2,*}, Ziru Xiang ¹, Fangzheng Hao ¹ and Yi Wang ¹

¹ School of Transportation and Civil Engineering, Nantong University, Nantong 226019, China; guzhenyuan0507@ntu.edu.cn (Z.G.); 1933110359@stmail.ntu.edu.cn (Y.L.); ziruxiang@ntu.edu.cn (Z.X.); 1933110348@stmail.ntu.edu.cn (F.H.); wang12yi@hotmail.com (Y.W.)

² School of Civil Engineering, Southwest Jiaotong University, Chengdu 610031, China

* Correspondence: qianwangping@my.swjtu.edu.cn

Abstract: A high damping rubber bearing (HDRB) is widely utilized in base-isolation structures due to its good energy dissipation capacity and environmentally friendly properties; however, it is incapable of isolating the vertical vibration caused by earthquakes and subways effectively. Thick rubber bearings with a low shape factor have become one of the important vertical isolation forms. This paper provides an experimental comparative study on high damping rubber bearings with low shape factor (HDRB-LSF), thick lead-rubber bearings (TLRB), and lead-rubber bearings (LRB). The abilities of the bearing and energy dissipation of the above bearings are analyzed contrastively considering the influence of vertical pressure, loading frequency, shear strain, and pre-pressure. Firstly, the HDRB-LSF, TLRB, and LRB are designed according to the Chinese Code for seismic design of buildings. Secondly, cyclic vertical compression tests and horizontal shear tests, as well as their correlation tests, are conducted, respectively. The vibrational characteristics and hysteresis feature of these three bearings are critically compared. Thirdly, a corrected calculation of vertical stiffness for the thick rubber bearings is proposed based on the experimental data to provide a more accurate and realistic tool measuring the vertical mechanical properties of rubber bearings. The test results proved that the HDRB-LSF has the most advanced performance of the three bearings. For the fatigue property, the hysteresis curves of the HDRB-LSF along with TLRB are plump both horizontally and vertically, thus providing a good energy dissipation effect. Regarding vertical stiffness, results from different loading cases show that the designed HDRB-LSF possesses a better vertical isolation effect and preferable environmental protection than LRB, a larger bearing capacity, and, similarly, a more environmentally friendly property than TLRB. Hence, it can avoid the unfavorable resonance effect caused by vertical periodic coupling within the structure. All the experimental data find that the proposed corrected equation can calculate the vertical stiffness of bearings with a higher accuracy. This paper presents the results of an analytical, parametric study that aimed to further explore the low shape factor concepts of rubber bearings applied in three-dimensional isolation for building structures.

Citation: Gu, Z.; Lei, Y.; Qian, W.; Xiang, Z.; Hao, F.; Wang, Y. An Experimental Study on the Mechanical Properties of a High Damping Rubber Bearing with Low Shape Factor. *Appl. Sci.* **2021**, *11*, 10059. <https://doi.org/10.3390/app112110059>

Academic Editor: Felix Weber

Received: 22 September 2021

Accepted: 20 October 2021

Published: 27 October 2021

Publisher's Note: MDPI stays neutral with regard to jurisdictional claims in published maps and institutional affiliations.

Keywords: isolation; high damping rubber bearing; low shape factor; performance test; experiment



Copyright: © 2021 by the authors. Licensee MDPI, Basel, Switzerland. This article is an open access article distributed under the terms and conditions of the Creative Commons Attribution (CC BY) license (<https://creativecommons.org/licenses/by/4.0/>).

1. Introduction

In recent years, basic isolation technology has been extensively applied in building construction and bridge engineering in China and overseas [1–3]. By the end of 2020, China had constructed more than 8000 seismic-isolated buildings. The rubber isolation system is currently the most widely used and mature isolation technology, among which the common isolation devices include the ordinary rubber bearing, natural rubber bearing (NRB) [4], LRB [5], HDRB [6], etc. The HDRB has plentiful advantages—such as a simple structure, stable mechanical performance, strong energy dissipation capacity, large stiffness before yielding, environmental protection, etc.—that make it an excellent choice for

base-isolation structures. It is made of laminated rubber pads with multi-layer steel plates that are vulcanized and bonded at a high temperature, where the steel plate layers restrain the vertical deformation of the rubber layers from guaranteeing a certain vertical stiffness of the bearing. The rubber layers adapt the high damping material with graphite and other additives to be capable of simultaneously withstanding a vertical load and resist a large horizontal shear displacement. Compared with the ordinary rubber bearing, HDRB can achieve a higher equivalent damping ratio of more than 20% without matching dampers, which saves installation space. HDRB possesses greater stiffness before yielding, a better braking effect on the structure subjected to wind load, more minor damage caused by lead when processing, and is more applicable for those places with special requirements for environmental protection, especially in contrast with the lead-rubber bearing. When the structures are subjected to an earthquake, the HDRB will produce a large deformation and reduce the stiffness, thus achieving a better isolation effect. In recent years, many researchers have conducted studies on HDRB. Burtscher et al. [7] conducted experimental studies on different forms of HDRB and analyzed the influence of the shape factor and steel plate forms on the performance of the bearings. Yamamoto et al. [8] took bidirectional coupling factors into consideration when testing the horizontal shear performance of HDRB. Chen et al. [9] and Xue et al. [10] carried out vertical compression tests along with horizontal shear tests for loading on the designed HDRB. Their results proclaimed a good energy dissipation effect. Bhuiyan et al. [11] proposed a rheological model considering the nonlinear characteristics of HDRB based on the cyclic shear test, monotone relaxation test, and multi-step relaxation test. Dong et al. [12] studied the influence of shear strain and vertical compressive stress on the shear performance of HDRB through the compression-shear performance test, and made an improvement to the restoring force model of the bearing with certain accuracy. Fabio Mazza et al. [13] applied the HDRBs to two typical r.c. framed structures and conducted the structural nonlinear incremental dynamic analyses based on the refined three-spring-two-dashpot model of the bearing.

Rubber bearings, including HDRBs, are generally horizontal isolation bearings, which can reduce the horizontal seismic acceleration response of a structure by about 60%. They are incapable of decreasing or even amplifying vertical seismic effect effectively. This can be explained by the fact that ordinary rubber bearings have a vertical stiffness equivalent to thousands of times their horizontal stiffness, which means that it is likely to obtain a smaller vertical basic period of around 0.1 s and is liable to fall within the striking part of the vertical acceleration spectrum, thus resulting in poor vertical isolation. However, recent large (extra-large) earthquakes in China and abroad indicate that strong vertical ground motions that occur in high-intensity areas, especially near faults areas, may even exceed the horizontal seismic action component. After horizontal seismic action is reduced, vertical ground motion with a high peak value will become the main cause of structural destruction, particularly for medical buildings and industrial facilities. Once damaged, the function of these buildings will be disrupted and the resilience of society will be seriously affected. Hence, scholars have developed several vertical isolation devices and three-dimensional isolation devices. Jia et al. [14] designed a new three-dimensional isolation device containing lead-core rubber pads combined with dish-shaped springs and steel plate dampers. Of those devices, some have undergone complex modeling, which is not conducive to processing, while some need additional dampers to enhance their vertical damping and causing greater vertical stiffness of the bearing. Thick rubber bearings have become one of the most important vertical isolation forms. Compared with an ordinary rubber bearing, there is a conspicuous increase in the thickness of HDRB, generally 4 to 6 times higher than that of the former. The shape factor of ordinary rubber bearing typically ranges from 15 to 30 or more, while that of HDRB is designed to vary from 2 to 5. In 1989, Aiken et al. [15] set the shape factor of the individual 1/4 scale bearings as 2.4 and characterization tests were then conducted. Warn and Vu [16] found that three-dimensional isolation for low and mid-rise structures would be achieved if the shape factors of the elastomeric bearings was set to be less than 4 and significant vertical

damping was supplemented. Kanazawa et al. [17] designed a thick rubber bearing with the second shape factor of 4.1, aiming to study the damping effect on the equipment in a nuclear reactor. Zhu et al. [18] selected three thick lead-core rubber bearings with shape factors of 8.0, 12.0, and 16.7, respectively, to conduct basic mechanical properties tests on them. Wang [19] carried out studies on the basic mechanical properties of five thick rubber bearings with shape factors between 4.13 and 5.37 and with different diameters, summarized the law of vertical stiffness parameters of new thick rubber bearings, and then proposed a design method of anti-buckling low-frequency seismic isolation bearings. Liu and Huang [20] compared the vertically seismic response spectrum between prestressed and non-prestressed thick rubber bearings with the shape factor of 3.29. Li et al. [21] conducted a series of experimental studies on shear stiffness, vertical stiffness, deformation performance, fatigue performance, creep performance, and aging performance of thick rubber bearings with the second shape factor of 1.85. The research results of many scholars around the world illustrate that compared with ordinary rubber bearings, thick rubber bearings have smaller vertical stiffness and superior vertical isolation performance, which can avoid the adverse resonance effect caused by the vertical period of vibration coupling with the structure.

In this paper, three bearings, including HDRB-LSF, TLRB, and LRB, were designed. Then, vertical compression performance tests, horizontal shear performance tests, vertical compression correlation tests, and horizontal shear correlation tests were carried out. The effects of vertical compressive stress, pre-pressure, shear strain, and loading frequency on the performance of the above three bearings were studied. The performance differences of the bearings were compared. Considering that the experimental results of HDRB-LSF displayed a big discrepancy with the theoretical values, a correction method for vertical stiffness of HDRB-LSF was proposed, and the modified values were found to be in good agreement with the experimental results.

2. Experimental Process

2.1. Specimen Design

Three bearings, including HDRB-LSF, TLRB, and LRB were adapted in the test. Figure 1 only displays the configuration of HDRB-LSF. All the bearings were fabricated with a diameter of 600 mm. The thickness and the diameter of the upper and lower sealing plate were 20 mm and 600 mm, respectively. The thickness and the diameter of the upper and lower connecting plates were 25 mm and 700 mm, respectively. The three bearings were designed according to a principle that the total thickness of 156 mm for the rubber pads in the bearings equals.

The first shape factor of the rubber bearing (S_1) is defined as $(D - d)/(4t_r)$, and the second shape factor (S_2) is defined as $D/(n_r t_r)$. D and d denote the diameter of the effective bearing surface and the diameter of the central opening for a bearing, respectively. If the central hole in the bearing is filled with rubber or lead, the opening can be ignored on the basis of the Specification GB/T20688.1-2007 [22]. n_r and t_r are the number and the thickness of rubber layers, respectively. S_1 value of LRB is 37.50, while the S_1 value of TLRB and HDRB-LSF is 12.50. Based on the research experience, t_r and S_1 are important parameters determining the bearing stiffness. The S_1 of LRB is three times that of TLRB and HDRB-LSF, indicating that LRB possesses greater vertical stiffness and more stable bearing capacity vertically. The S_2 value of all the above bearings keeps unchanged at 3.85, explaining that their horizontal stiffness is consistent.

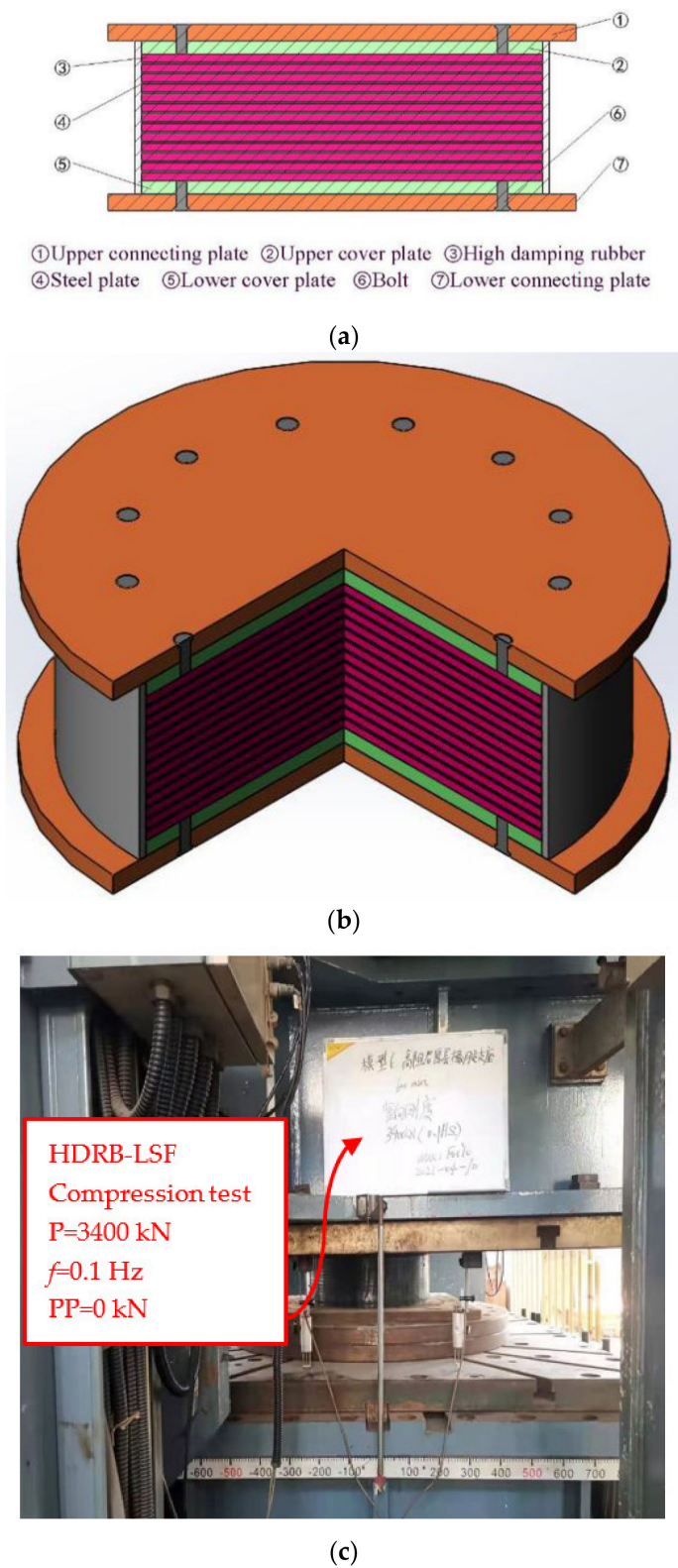


Figure 1. Cont.

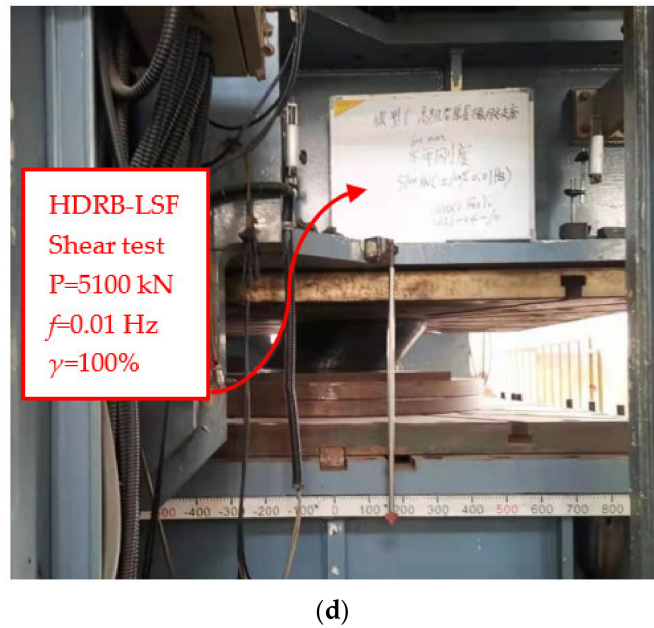


Figure 1. The configuration of HDRB-LSF: (a) cross-section view; (b) 1/4 perspective view; (c) compression test view; (d) shear test view.

The other dimension parameters of each bearing are listed in Table 1, where d_l is the diameter of lead core; n_s and t_s are the numbers and the thickness of steel plates. In the specimens steel plates were made from Q345 material; the rubber pads of HDRB-LSF were made from high damping rubber with a shear modulus of 0.392 MPa and a rubber hardness of 56 HA (Shore hardness); the rubber pads of TLRB and LRB were made from ordinary rubber material with a shear modulus of 0.6 MPa and a rubber hardness of 42 HA. Here, it should be noted that each of the two thick rubber bearings had a small hole in the center when fabricated to facilitate vulcanization. According to the specification: after vulcanization, specimens with a total height of less than 250 mm should be rested for at least 24 h, while other specimens should be rested for more than 48 h. Hence, all the test specimens were rested for more than 48 h after vulcanization and then kept in the testing environment for another 24 h before the test.

Table 1. Basic parameters of the bearings.

Bearings	D (mm)	d_l (mm)	t_r (mm)	n_r	t_s (mm)	n_s	S_1	S_2
HDRB-LSF	600	-	12	13	2.8	12	12.5	3.85
TLRB	600	120	12	13	2.8	12	12.5	3.85
LRB	600	120	4	39	2.8	38	37.5	3.85

The vertical stiffness (K_v) and the horizontal stiffness (K_h) of the ordinary rubber bearing were calculated by Equations (1) and (2) according to the specification GB/T20688.3-2006 [23], where A is the whole effective cross-section area of the bearing; E_c is the modified compressive elastic modulus of laminated rubber under vertical pressure load, which can be obtained from Equation (3); E_v is the volumetric elastic modulus of rubber; E_{cb} is the apparent elastic modulus of rubber obtained from Equation (4); E_0 represents the elastic modulus of rubber; k is a correction coefficient for the elastic model of rubber material related to rubber hardness; and G is the shear modulus of laminated rubber.

$$K_v = \frac{E_c A}{n_r t_r} = \frac{\pi D}{4} E_c S_2 \tag{1}$$

$$K_h = \frac{GA}{n_r t_r} \tag{2}$$

$$E_c = \frac{E_{cb} \times E_v}{E_{cb} + E_v} \quad (3)$$

$$E_{cb} = E_0(1 + 2ks_1^2) \quad (4)$$

For LRB, the computational formula of vertical stiffness (K_v) is the same as an ordinary rubber bearing. However, the shear stiffness obtained from Equation (2) is merely the post-yield stiffness, and its equivalent shear stiffness can be written as

$$K'_h = \frac{K_h X + Q}{X} \quad (5)$$

where X is the horizontal shear displacement of the bearing; Q is the yield force of the LRB that linearly correlated with the cross-section area of the lead core and can be acquired by the following formula [24].

$$Q = \frac{8.367\pi d_l^2}{4} + 4.682 \quad (6)$$

where d_l is the diameter of the lead core. It should be pointed out that the role of the lead core should be considered when calculating the vertical stiffness of LRB in Equation (1). The cross-section area A is not the simple addition of lead core cross-section and rubber cross-section but is the relational expression that $A = A_r + A_l (E_l/E_c - 1)$, where A_r and A_l are the cross-section area of rubber and the cross-section area of lead core, respectively; E_l is the elastic modulus of lead core.

We calculated that the designed shear stiffness of HDRB-LSF, TLRB, and LRB are 1.09 kN/mm, 1.35 kN/mm, and 1.35 kN/mm, respectively. The vertical stiffness values of the above three bearings are 706.13 kN/mm, 581.94 kN/mm, and 2116.18 kN/mm, respectively.

2.2. Test Method

The loading device used in the test is shown in Figure 2. Vertical parameters of the compression and shear test device were: the maximum pressure was 20,000 kN, the maximum tension was 6000 kN, the maximum displacement stroke was 700 mm, and the maximum loading speed was 3 mm/s. Horizontal parameters of this device were: the maximum shear test force was ± 6000 kN, the maximum displacement stroke was ± 600 mm, and the maximum loading speed was 10 mm/s. Vertical and horizontal loading adopted force control and displacement control, respectively. The acquisition of data relied on an automatic data acquisition system. The vertical pressure was assumed to be P . For the vertical compression performance test, cyclic loading was carried out within the range of $P \pm 0.3 P$. According to the Chinese Specification [19], three loading cycles are recommended for the performance test of rubber bearings. In this test, four cycles were actually loaded to guarantee the data integrity of the third cycle, and the results of the third cycle were extracted to calculate the performance of the bearings.

2.3. Test Cases

Based on the design surface pressure of 12 MPa, according to the Code, and bearing diameter of 600 mm, the specified vertical pressure P was determined as 3400 kN. In order to analyze the influencing factors of vertical stiffness of the three specimens, loading cases with different pre-pressures, vertical pressures, and loading frequencies were successively carried out, as shown in Table 2. For the horizontal compression and shear performance test, when the specified vertical pressure P (3400 kN) was used, the corresponding shear displacements under 25%, 50%, 75%, and 100% of shear strain γ were, respectively, applied at different loading frequencies of 0.01 Hz, and 0.0082 Hz. When the loading frequency was 0.01 Hz and the shear strain γ was 100%, loading cases with different vertical pressure P of 3400 kN, 4250 kN, and 5100 kN were launched to analyze the shear strain correlation of the horizontal performance for the three specimens, which can be seen in Table 3.



Figure 2. The loading device in the test.

Table 2. The cases of the vertical compression test.

Cases	Pre-Pressure (kN)	Vertical Pressure (kN)	Loading Frequency (Hz)
Case 1	0	2900	0.01
Case 2	0	2900	0.02
Case 3	0	2900	0.05
Case 4	0	2900	0.1
Case 5	0	3400	0.01
Case 6	0	3400	0.02
Case 7	0	3400	0.05
Case 8	0	3400	0.1
Case 9	0	3700	0.01
Case 10	0	3700	0.02
Case 11	0	3700	0.05
Case 12	0	3700	0.1
Case 13	1700	3400	0.1
Case 14	2040	3400	0.1
Case 15	2720	3400	0.1

Table 3. The cases of the horizontal shear test.

Cases	Vertical Pressure (kN)	Shearing Strain γ	Shear Displacement (mm)	Loading Frequency (Hz)
Case 16	3400	$\pm 25\%$	39	0.01
Case 17	3400	$\pm 50\%$	78	0.01
Case 18	3400	$\pm 75\%$	117	0.01
Case 19	3400	$\pm 100\%$	156	0.01
Case 20	3400	$\pm 25\%$	39	0.0082
Case 21	3400	$\pm 50\%$	78	0.0082
Case 22	3400	$\pm 75\%$	117	0.0082
Case 23	3400	$\pm 100\%$	156	0.0082
Case 24	4250	$\pm 100\%$	156	0.01
Case 25	5100	$\pm 100\%$	156	0.01

3. Test Results and Analysis

3.1. Vertical Compression Performance of Bearings

The vertical compression performance tests with 100% shear strain were carried out on the three bearings, respectively, under the designed vertical pressure P of 3400 kN and loading frequency of 0.1 Hz (Case 8). Four loading and unloading cycles were conducted for each test case of the three bearings within the range of $P \pm 0.3 P$, and the schematic

diagram of vertical loading mode is shown in Figure 3. Figure 4 gives the vertical load–displacement curves of the bearings. It indicates that the vertical energy dissipation effect of HDRB-LSF and TLRB is superior to LRB. With the increase of compressive stress, extrusion deformation occurred in the rubber layer causing the vertical displacement of the bearings. The slopes of hysteresis curves—i.e., the vertical stiffness of the bearings—showed an augmented tendency. Under the action of equal compressive stress, the vertical stiffness of different bearings varied, explaining that the vertical stiffness of a bearing has a close relation with the thickness and the properties of the rubber material.

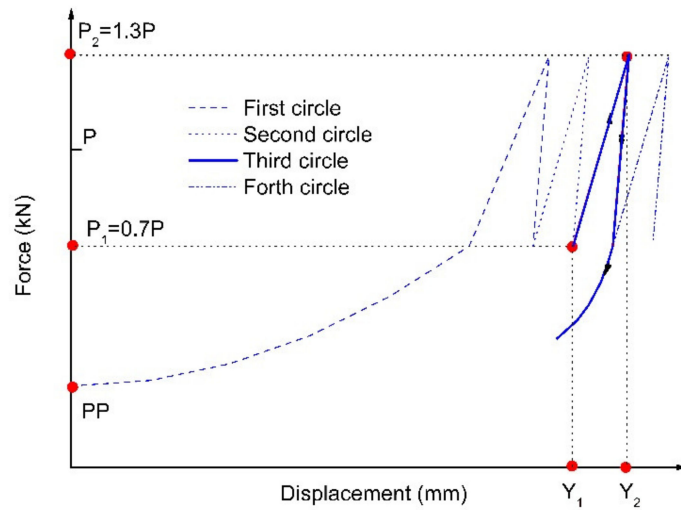


Figure 3. The schematic diagram of vertical loading mode.

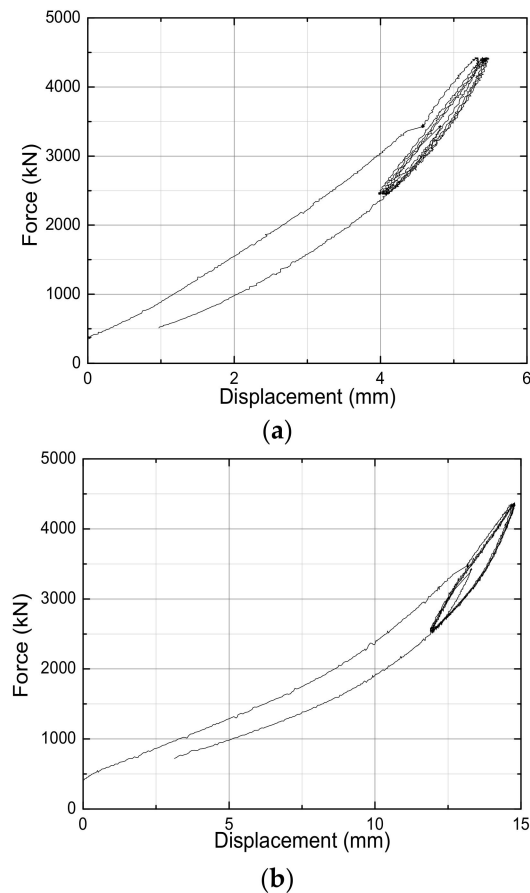


Figure 4. Cont.

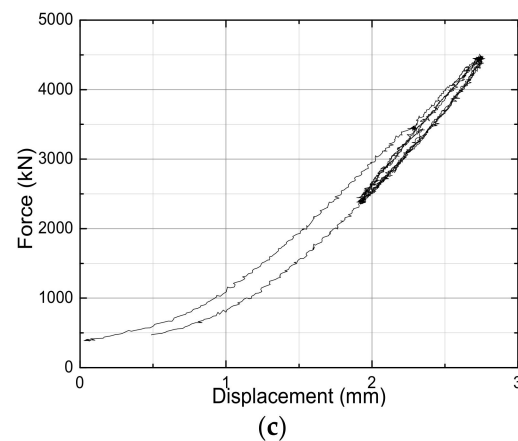


Figure 4. Load–displacement curves of vertical compression: (a) HDRB-LSF; (b) TLRB; (c) LRB.

The third cyclic results of the vertical load–displacement curves of the three bearings under different loading frequencies, pre-pressures, and vertical pressures were obtained, and the effects of these parameters on the vertical stiffness of bearings were analyzed.

3.1.1. Loading Frequency

Test data from cases 1–12 were extracted, and correlation tests of loading frequencies were carried out on three bearings, which aimed to study the influence on hysteresis behavior of high-damping isolation bearings. Due to space limitations, Figure 5 only gives the hysteresis curves of the three bearings at different loading frequencies when the vertical pressure is 3400 kN. It can be seen that the shape of the vertical hysteresis curves for all the bearings obtained by cyclic loading with different loading frequencies are basically the same. Loading frequency has a diverse effect degree on the vertical mechanical properties of different bearings; TLRB is most sensitive to it. With the augment of loading frequency, the vertical stiffness of each bearing presents an increasing trend. When the loading frequency was rather low, it had a slight influence on the vertical performance of the bearings, while the vertical compression displacements observably changed as the loading frequency was relatively high (0.05 Hz and 0.1 Hz).

3.1.2. Vertical Pressure

Figure 6 listed the load–displacement curves of the three bearings under different vertical pressures (2900 kN, 3400 kN, and 3700 kN) at a loading frequency of 0.1 Hz. It explains that the hysteretic curve slopes of the bearings, namely the vertical compression stiffness, increases significantly with the growth of vertical pressure. Among them, the curve shape for LRB is less sensitive to vertical pressure compared to TLRB and HDRB-LSF, which have thick rubber layers. This is due to the fact that as the vertical pressure increases, the thickness of the rubber layer for TLRB and HDRB-LSF diminishes, and the constraint effect of the steel plate is strengthened, ultimately leading to the rapid enlargement of compression modulus of the rubber in the triaxial compression state.

3.1.3. Pre-Pressure

From the extracted test data from cases 1–12, the effect results of different pre-pressures (1700 kN, 2040 kN, and 2720 kN) on the three bearings were obtained, under the vertical pressure of 3400 kN and the loading frequency of 0.1 Hz. The obtained vertical compression load–displacement curves are drawn in Figure 7. As can be seen from the figure, the slopes of the hysteretic curves augment significantly with the growth of pre-pressures, indicating that the pre-pressure has a great influence on the vertical stiffness of the bearings, especially for HDRB-LSF and TLRB.

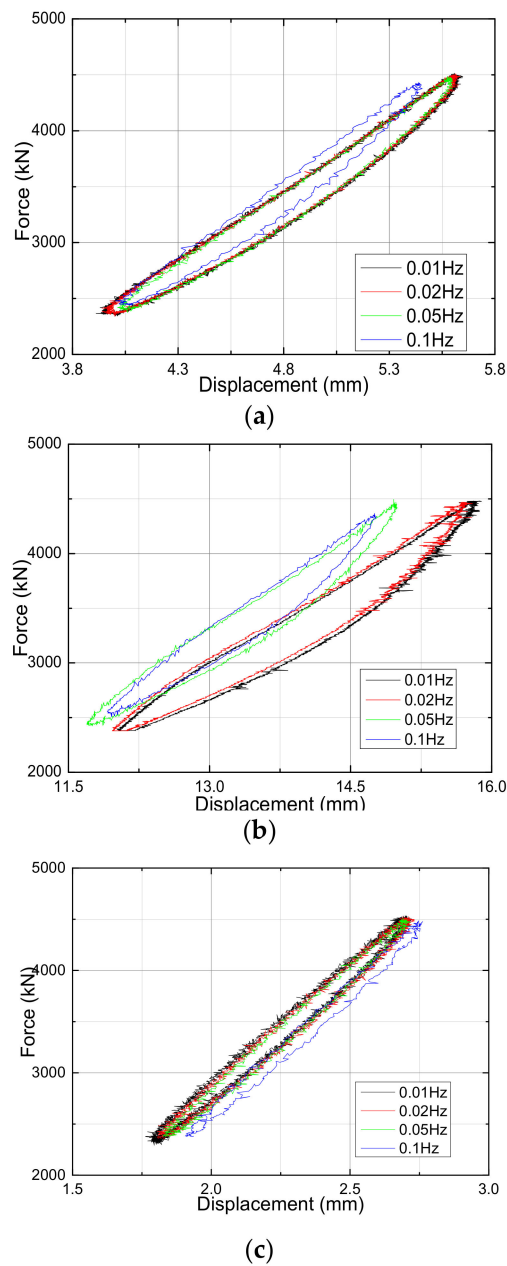
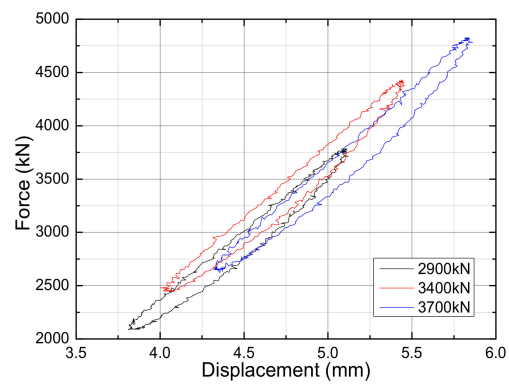


Figure 5. Vertical load–displacement curves under different loading frequencies: (a) HDRB-LSF; (b) TLRB; (c) LRB.

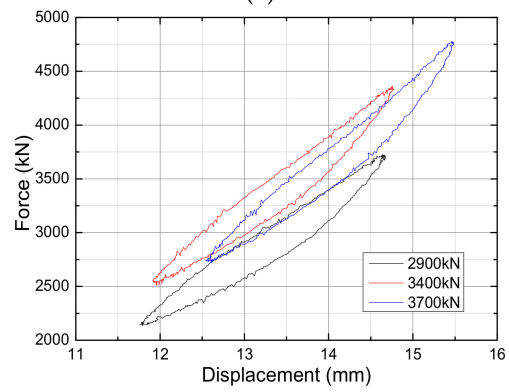
3.1.4. Results of Vertical Stiffness

We assumed P_1 and P_2 as the small pressure and the larger pressure in the third cycle, and gave them the values of $0.7 P$ and $1.3 P$, respectively. We assumed Y_1 and Y_2 were the smaller displacement and the larger displacement in the third cycle, respectively. The vertical compression stiffness of all the bearings under various test cases was calculated according to Equation (7), as shown in Figures 8–10.

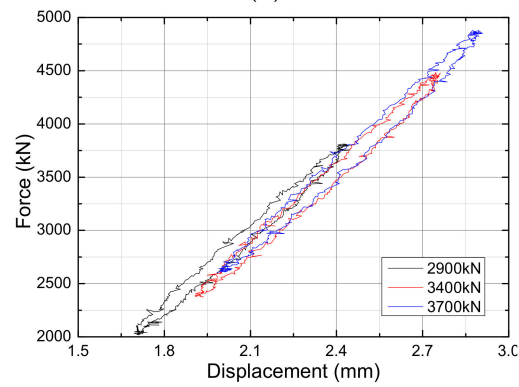
$$K_V = \frac{P_2 - P_1}{Y_2 - Y_1} \tag{7}$$



(a)



(b)



(c)

Figure 6. Vertical load–displacement curves under different vertical pressures: (a) HDRB-LSF; (b) TLRB; (c) LRB.

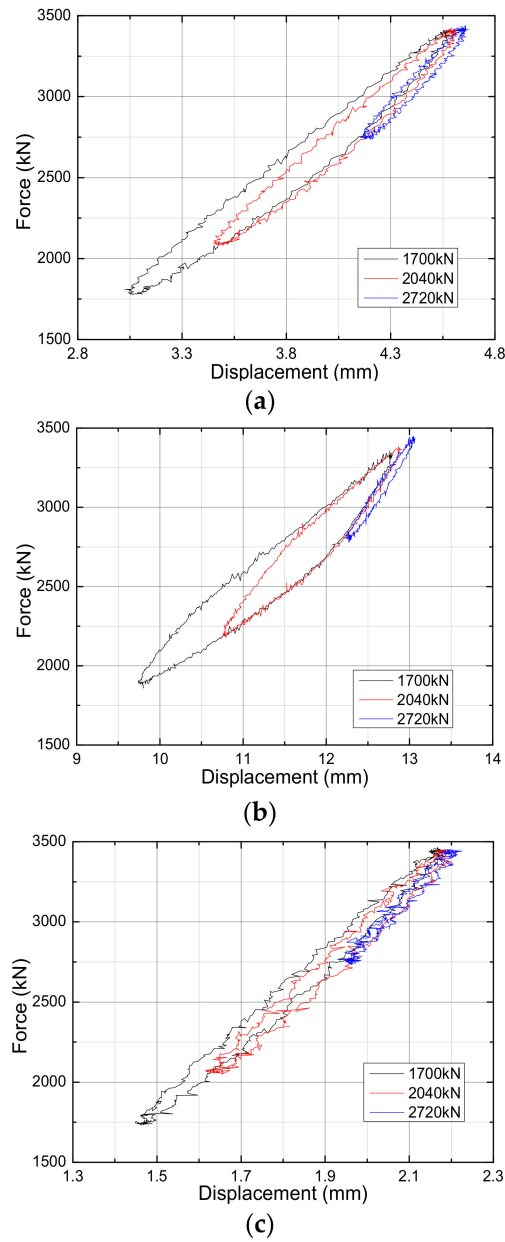


Figure 7. Vertical load–displacement curves under different pre-pressures: (a) HDRB-LSF; (b) TLRB; (c) LRB.

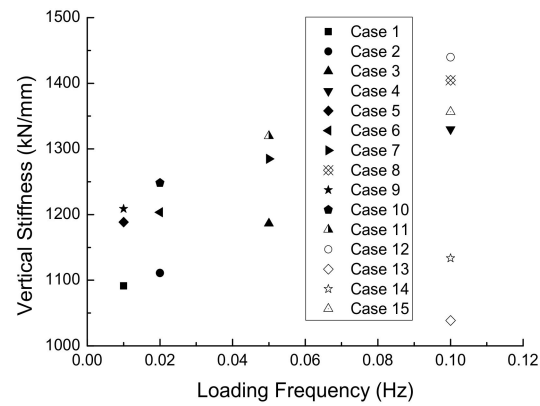


Figure 8. Vertical stiffness of HDRB-LSF.

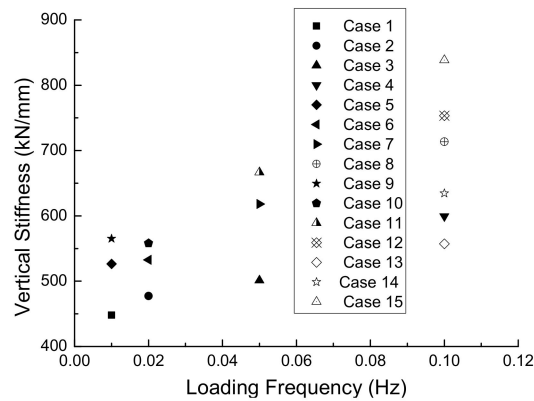


Figure 9. Vertical stiffness of TLRB.

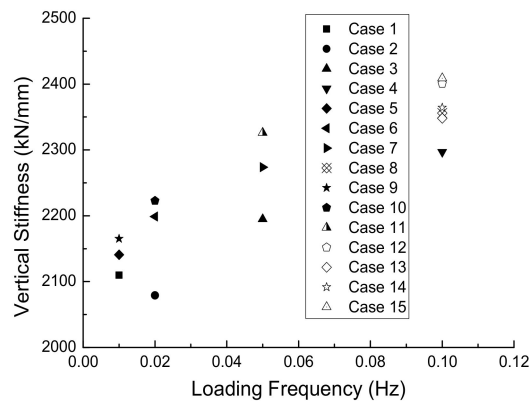


Figure 10. Vertical stiffness of LRB.

The error of the vertical stiffness for the bearings is equal to the difference between the theoretical value and the test value divided by the theoretical value. Due to the limited length of the article, Table 4 only shows the comparison results of theoretical and experimental values of vertical stiffness when the vertical pressure is 3400 kN and the pre-pressure is 0 kN.

Table 4. Vertical stiffness error between theoretical value and test value (%).

Loading Frequency (Hz)	HDRB-LSF	TLRB	LRB
0.01	68.30	−9.53	1.16
0.02	70.42	−8.49	3.91
0.05	81.96	6.19	7.44
0.1	98.88	22.59	11.32

As can be seen from Figures 8–10, under different loading cases the vertical stiffness of LRB is largest in the range between 2050 kN/m and 2450 kN/m. The vertical stiffness of HDRB-LSF takes second place within the range of 1050 kN/m and 1450 kN/m, while the vertical stiffness of TLRB is the lowest, varying from 450 kN/m and 850 kN/m. With the increase in loading frequency, the vertical stiffness of almost all bearings has an increase in different amplitude. When the loading frequency varies from 0.01 Hz to 0.02 Hz, the vertical stiffness values of the HDRB-LSF, LRB, and TLRB improve by 1.3–3.3%, about 2.7%, and 1.1–6.6%, respectively. Whereas when the loading frequency is enlarged from 0.05 Hz to 0.1 Hz, the vertical stiffness values of the HDRB-LSF, LRB, and TLRB improve by 9.1–12.1%, 3.2–4.6%, 13–19.6%. Hence, it can be concluded that the vertical stiffness of LRB is relatively stable, while that of HDRB-LSF and TLRB is sensitive to the change of loading frequency. It can be seen from the table that it is not certain whether the test value

or theoretical value is more remarkable for the vertical stiffness of TLRB, while the test values of vertical stiffness for LRB and HDRB-LSF always surpass the theoretical value. Additionally, the margin of error between the test values and the theoretical values of vertical stiffness for the LRB and TLRB are small, which is basically in line with the specific design requirements. The test values of the vertical stiffness for HDRB-LSF are larger than the theoretical value, which means that it is biased towards safety in the bearing design. However, this error has exaggerated what needs to be corrected. The vertical stiffness of LRB is larger than that of HDRB-LSF and TLRB, illustrating that: (1) in the case of equal total thickness of the rubber layer, the larger the number of rubber layers, the greater the vertical stiffness, due to the steel plate that has a strong constraint ability on the transverse deformation of rubber; (2) for the two bearings with thick rubber, the vertical stiffness of the one with the lead core is smaller than the one with high damping rubber, showing that the latter has a marginally worse isolation capability but greater bearing capacity vertically.

3.2. Horizontal Shear Performance

Horizontal shear performance tests were carried out on the three bearings, in which the pressure was slowly and continuously loaded to 3400 kN and remained constant. The shear displacement corresponding to $\gamma = 100\%$ was applied horizontally at a low frequency of 0.01 Hz, and the whole loading process consisted of four cycles. The horizontal stiffness K_h and equivalent damping ratio h_{eq} of a bearing can be calculated according to Equations (8) and (9):

$$K_h = \frac{Q_2 - Q_1}{X_2 - X_1} \tag{8}$$

$$h_{eq}(\gamma) = \frac{1}{\pi} \cdot \frac{W_d}{2K_H(\gamma T_r)^2} \tag{9}$$

where Q_1 and Q_2 are the maximum and the minimum shear forces of the third cycle, respectively; X_1 and X_2 denote the positive and the negative maximum displacement of the third cycle, respectively, and $X_1 = T_r\gamma$, $X_2 = T_r(-\gamma)$; and T_r is equal to the product of n_r and t_r . ΔW represents the envelope area of the hysteresis curve.

The horizontal hysteresis curves of the tested bearings are shown in Figure 11. It can be seen from the figure that the curves of the three bearings are respectively in crescent shape (HDRB-LSF) and spindle shape (TLRB and LRB). Among them, the hysteresis curves of HDRB-LSF are relatively less plump, that is, the energy dissipation capacity of which is surprisingly inferior to TLRB and LRB under the same shear deformation condition. The shape of hysteretic curves of each bearing is basically consistent with the specification requirements.

Horizontal shear performances of the bearings are shown in Table 5. It shows that under the same vertical pressure and shear strain the horizontal equivalent stiffness of HDRB-LSF is smaller than those of TLRB and LRB, which indicates that under the premise of the equal total thickness of rubbers, the steel plates in HDRB-LSF have less binding force on rubbers than the bearings with lead core.

Table 5. Horizontal performance error between theoretical value and test value.

Bearings		HDRB-LSF	TLRB	LRB
Equivalent stiffness (kN/mm)	Theoretical value	1.09	1.35	1.35
	Test value	1.01	1.02	1.22
	Error (%)	-7.34	-24.44	-9.63
Equivalent damping ratio (%)	Theoretical value	8.06	23.56	28.69
	Test value	9.26	38.89	31.75
	Error (%)	14.89	32.36	10.67

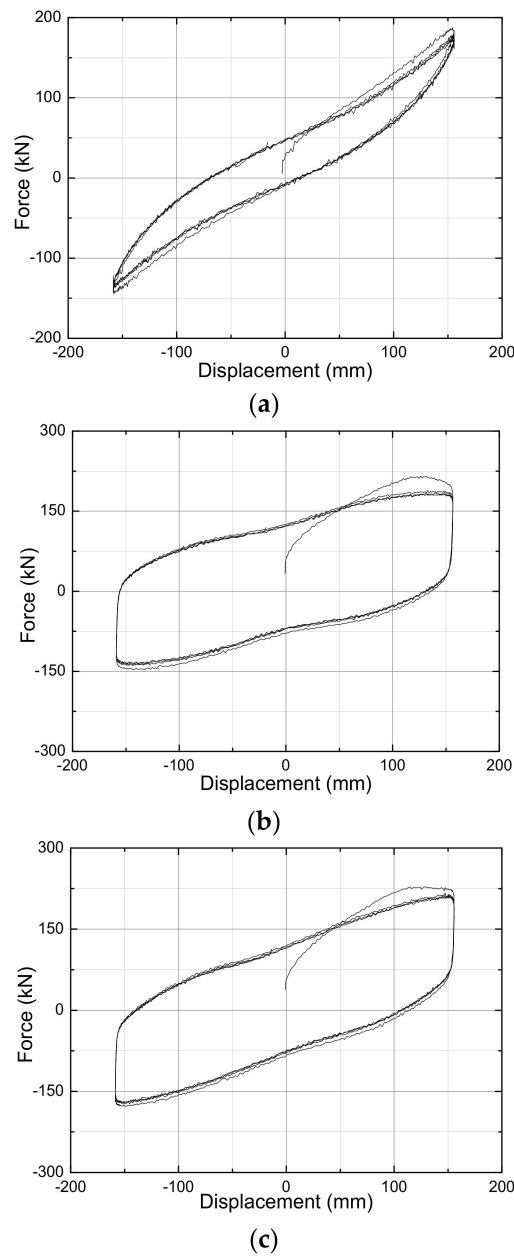


Figure 11. Horizontal shear load-displacement curves: (a) HDRB-LSF; (b) TLRB; (c) LRB.

The energy dissipation capacity of bearings is currently expressed by the equivalent damping ratio. The horizontal equivalent damping ratio of HDRB-LSF was approximately 9% in the third cyclic test (it was about 13% in the first cyclic test), expressing a better energy dissipation capacity than the NRB with a usual equivalent damping ratio of 3%. However, compared to TLRB and LRB with the lead core in the test, the energy dissipation capacity of HDRB-LSF designed in this paper is insufficient and needs improvement. When the vertical pressure is 3400 kN and the shear strain is 100%, the errors between the experimental values and the theoretical values of the horizontal performance of HDRB-LSF and LRB are both less than 15%. In contrast, the errors for TLRB are significant.

In order to quantitatively evaluate the horizontal shear stiffness of the three bearings and studying its relationship with shear deformation, axial pressure, and loading frequency, the third cyclic results of horizontal hysteresis curves of the bearings subjected to various test cases were acquired. Then, the influences of different parameters on the horizontal stiffness and equivalent damping ratio of the three bearings were analyzed.

3.2.1. Shear Strain

The designed vertical pressure of 3400 kN was smoothly exerted in the three bearings and remained unchanged during the whole test process. Under the frequency of 0.01 Hz, horizontal sinusoidal excitation waves were loaded with the shear strains of 25%, 50%, 75%, and 100% in succession, until unloading was completed in all cycles under all shear strains. The data acquisition instrument recorded the data during the whole loading process.

The designed vertical pressure of 3400 kN was smoothly exerted to the three bearings and remained unchanged during the whole test process. Under the frequency of 0.01 Hz, horizontal sinusoidal excitation waves were loaded with the shear strains of 25%, 50%, 75% and 100% in succession, until unloading was completed in all cycles under all shear strains. The data acquisition instrument recorded the data during the whole loading process.

The horizontal shear performance of each bearing can be seen in Figure 12. As the shear displacement aggrandizes, the slopes of the curves gradually reduce, due to the reason that the compression area of the bearing core decreases, which can lessen the constraint of steel plates on the internal rubbers. The hysteresis curves of the bearings become larger as the shear strain grows, indicating that their energy dissipation capacity is strengthened. It should be noted that after multiple loads, points of contraflexure appear on the load–displacement curves, as seen in Figure 12b,c, and the degree of contraflexure on the curves gradually increases as the loading displacement grows.

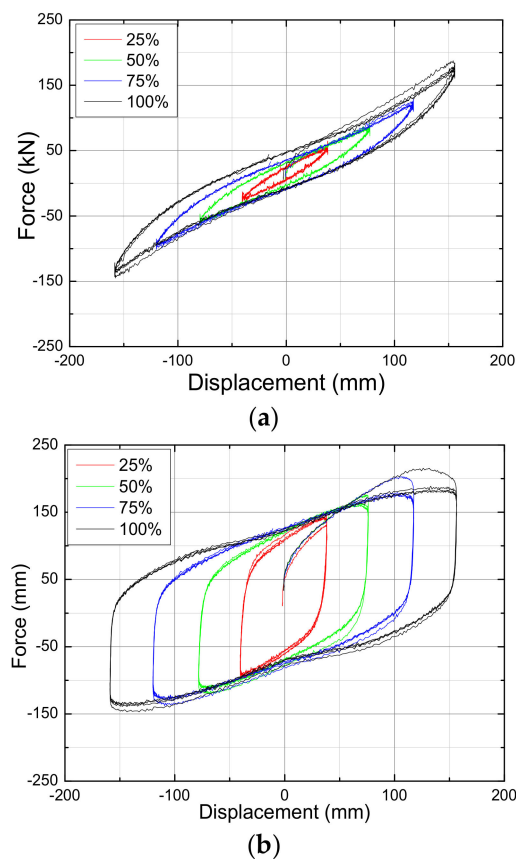


Figure 12. Cont.

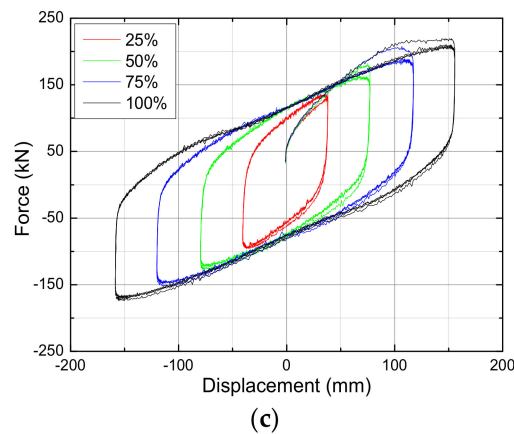


Figure 12. Horizontal shear load-displacement curves under different shear strains: (a) HDRB-LSF; (b) TLRB; (c) LRB.

The test values of horizontal equivalent stiffness and the equivalent damping ratio of the bearings are displayed in Figure 13. It can be seen that under the same shear strain, the horizontal equivalent stiffness of LRB and TLRB are adjacent throughout the test, and the stiffness of the former is slightly larger than that of the latter, while that of HDRB-LSF is the smallest. TLRB has most significant horizontal equivalent damping ratio, followed by LRB and HDRB-LSF, according to priority. The shear strain has an unnoticeable effect on HDRB-LSF and TLRB, but has an obvious impact on LRB whose growth of shear displacement is faster than the increase of the hysteretic curve area [14].

3.2.2. Loading Frequency

Similarly, the remaining vertical pressure of 3400 kN was exerted to the three bearings. Under a shear strain of 100%, horizontal reciprocating loads were applied to all the bearings at successive frequencies of 0.01 Hz and 0.0082 Hz, respectively. The horizontal hysteresis curves, horizontal equivalent stiffness, and equivalent damping ratio of the bearings obtained by the test are shown in Figure 14 and Table 6, respectively. It can be seen that the horizontal equivalent stiffness and equivalent damping ratio of the three bearings all decline with the diminution of loading frequency within a narrow varying range.

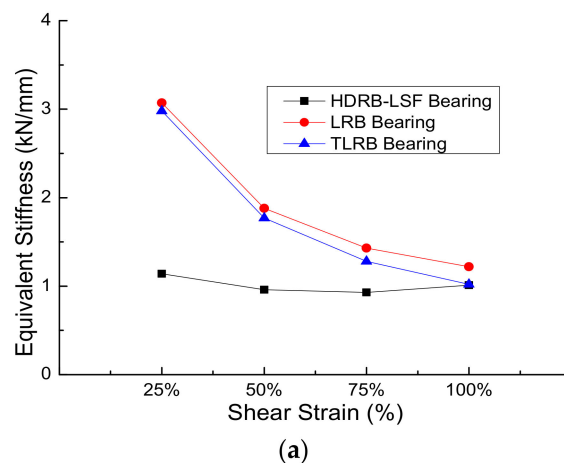


Figure 13. Cont.

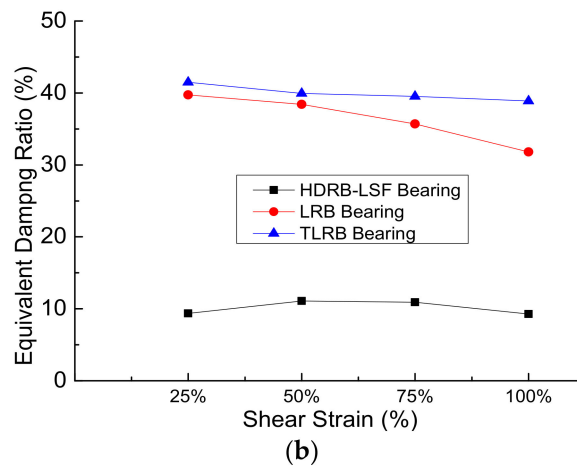


Figure 13. Horizontal performance of the bearings under different shear strains: (a) equivalent stiffness; (b) equivalent damping ratio.

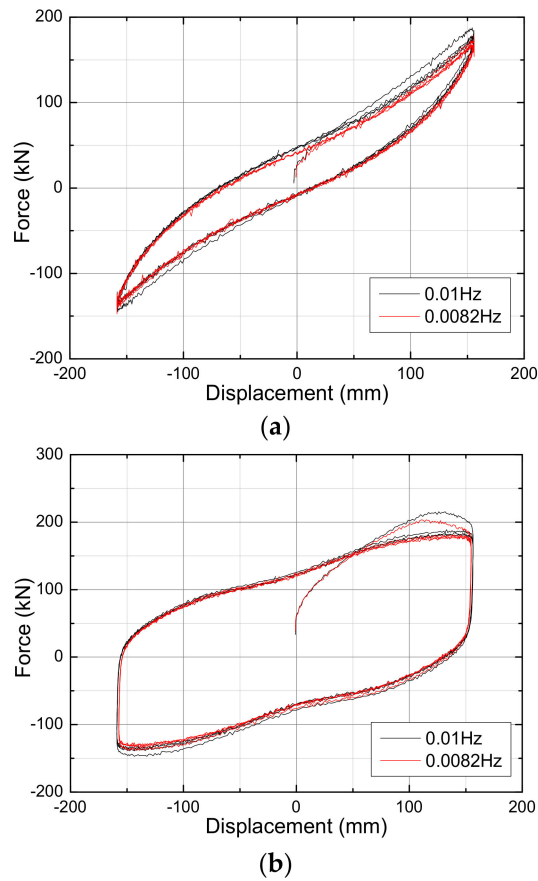


Figure 14. Cont.

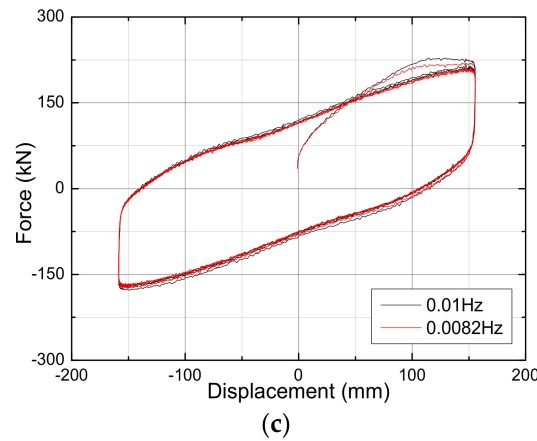


Figure 14. Horizontal shear load-displacement curves under different loading frequency: (a) HDRB-LSF; (b) TLRB; (c) LRB.

Table 6. Horizontal performance of the bearings under different loading frequencies.

Loading Frequency (Hz)	Equivalent Stiffness (kN/mm)			Equivalent Damping Ratio (%)		
	HDRB-LSF	TLRB	LRB	HDRB-LSF	TLRB	LRB
0.01	1.09	1.35	1.22	9.26	38.89	31.75
0.0082	0.97	1.01	1.21	8.90	38.29	31.15

3.2.3. Vertical Pressure

Due to the effect of the horizontal overturning moment and vertical seismic action, the vertical pressure on the rubber bearing will change considerably, which will have a certain influence on the shear performance of the bearing. Therefore, it is important to study the pressure correlation of the shear performance for the bearings. The three bearings were slowly and continuously loaded vertically with the vertical pressure loaded to 3400 kN, 4250 kN (1.25 P), and 5100 kN (1.5 P), respectively, and the pressure remained unchanged during the subsequent test. The shear strain was 100% and the horizontal reciprocating load was successively applied to each bearing at the loading frequency of 0.01 Hz. The hysteretic curves of the bearings obtained by the test are shown in Figure 15. The horizontal equivalent stiffness and equivalent damping of the bearings were calculated and are listed in Table 7.

Table 7. Horizontal performance under different vertical pressures.

	Bearings	Vertical Pressure (kN)		
		3400	4250	5100
Equivalent stiffness (kN/mm)	HDRB-LSF	1.01	1.06	0.94
	TLRB	1.02	0.91	0.82
	LRB	1.22	1.21	1.16
Equivalent damping ratio (%)	HDRB-LSF	9.26	10.14	11.39
	TLRB	38.89	43.76	49.30
	LRB	31.80	33.03	34.57

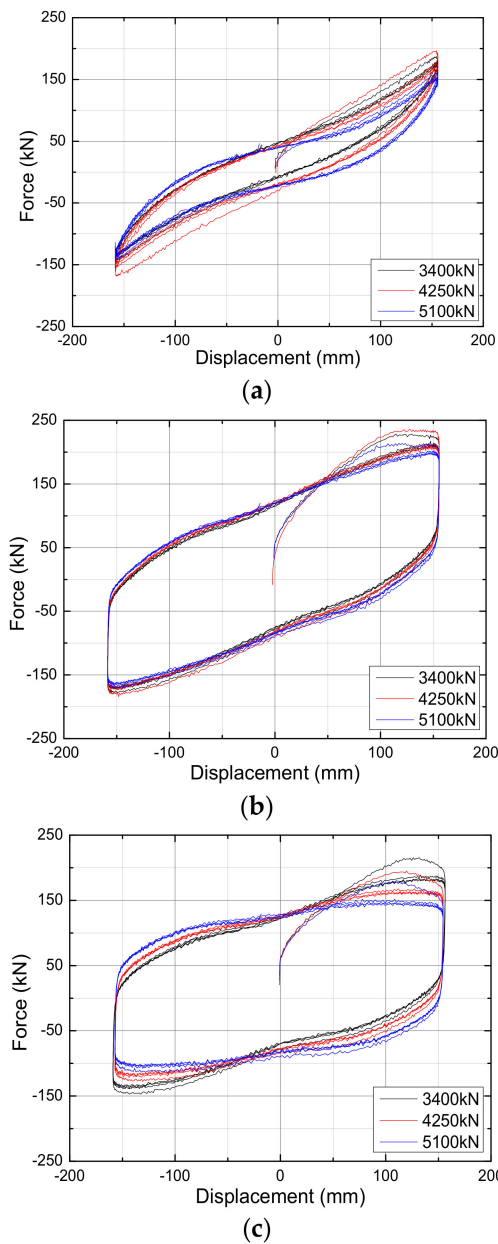


Figure 15. Horizontal shear load-displacement curves under different vertical pressures: (a) HDRB-LSF; (b) TLRB; (c) LRB.

As can be seen from the figure and table, HDRB-LSF and LRB are more sensitive to the change of vertical pressure. The horizontal equivalent stiffness of HDRB-LSF increases and then reduces with the growth of vertical pressure, while that of TLRB and LRB gradually decreases with it, which is due to the axial compression and 100% shear deformation caused the out-of-plane distortion of the steel plates, thus reducing the horizontal constraint of the steel plates on the rubber pads. Therefore, the designed surface pressure of the bearing must be strictly limited when it is employed. The equivalent damping ratios of all the three bearings enlarged as the vertical pressure grew, owing to the fact that the higher vertical pressure boosted the triaxial stress of the rubber layer, making the rubber material inside the bearing denser, and magnifying the intermolecular friction of the rubber material, leading to the increase of the hysteretic curve area and equivalent damping ratio. Although the HDRB-LSF has a certain horizontal energy dissipation capacity, the values of the equivalent damping ratio for HDRB-LSF are rather low, owing to the fact that the equivalent damping ratio of high damping rubber material was set to be around 10% when

fabricated and considering the constant cost as compared to TLRB and LRB. This paper emphasizes studying the isolation performance law of all the rubber bearings vertically and horizontally used in the base-isolation structures. Hence, the low equivalent damping ratio for HDRB-LSF is acceptable. Of course, a follow-up study of HDRB-LSF will enhance its equivalent damping ratio and reach the corresponding level of the bearings with a lead core.

4. Formula Modification

Therefore, the vertical stiffness of HDRB-LSF and TLRB with thick rubber layer deviates significantly from the theoretical results calculated according to the Lindley Formula and has exceeded the allowable range of engineering design. Hence, the vertical stiffness formulas for the bearing with a thick rubber layer will be revised in this section.

4.1. Theoretical Derivation

As can be seen from Table 4, the test values of vertical stiffness for HDRB-LSF are larger than the theoretical values. When the total thickness of the rubber is constant, the rubber pads of the ordinary thin rubber bearing under pressure are constrained by the steel plates, causing a sizeable vertical stiffness value. Whereas for the thick rubber bearing, the rubber thickness of a single layer is great, leading to the limited constraint effect of the steel plates on the rubber pads and large transverse deformation of the rubber layers, so that its vertical stiffness is more minor. The error of the vertical stiffness between the test value and the theoretical value calculated according to the code is too large to ignore, which cannot adapt to the requirements of engineering design. Hence, the theoretical formula of vertical stiffness must be modified.

It is known from the study that the error of the vertical stiffness for the bearing between the test value and the theoretical value is related to the compressive stress σ and the loading frequency f of the bearing. The theoretical formula can be modified with the following formulas:

$$K_V = \zeta_V \frac{E_c A}{n_r t_r} \quad (10)$$

$$\zeta_V = \zeta_1 \frac{\sigma}{\sigma_0} + \zeta_2 f + \zeta_3 \quad (11)$$

where ζ_V is the correction coefficient; ζ_1 , ζ_2 , and ζ_3 are the correction coefficients, which all can be obtained by the fitting of a polynomial based on the experimental data, and their values are 0.762, 3.599, and 0.8631, respectively; σ_0 is the design compressive stress, i.e., 12 Mpa.

4.2. Modification Results

Figure 16 exhibits the theoretical values, the test values, and the modified theoretical values of the vertical stiffness for HDRB-LSF.

It explains that the modified theoretical values of the vertical stiffness are closer to the test values than the original theoretical values. All the errors between them are less than 1.5%, indicating that the modified method is basically feasible. Moreover, the smaller the vertical pressure, the smaller the error. However, the accuracy of the fitting formula depends on the test samples of the fitting analysis. The test data of the bearings used are few, thus the coverage range of the sample parameters is limited. The applicability of the fitting Equation (9) needs to be further verified in future research.

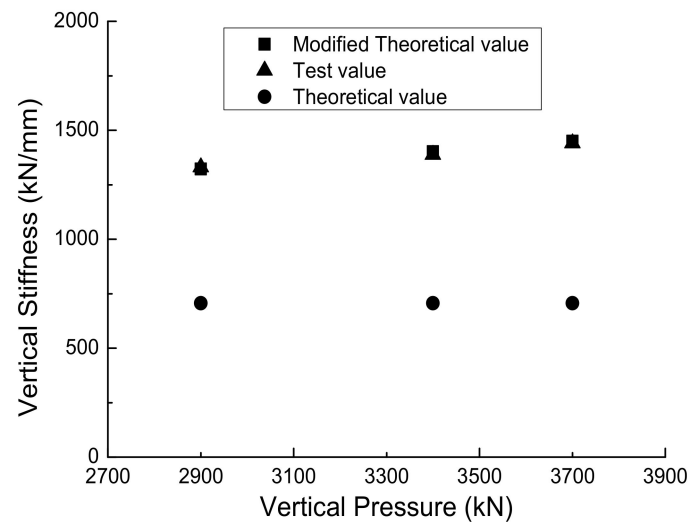


Figure 16. Comparison between theoretical value and test value of HDRB-LSF.

5. Conclusions

In this paper, three rubber bearings (HDRB-LSF, TLRB, and LRB) were analyzed contrastively via comprehensive experimental studies. The properties of vertical stiffness, horizontal equivalent stiffness, horizontal equivalent damping ratio, and hysteretic curves were tested under different vertical pressures, loading frequencies, shear strain values, and pre-pressures. A corrected calculation for the vertical stiffness of the bearing is proposed based on the results of the study. The results show that the HDRB-LSF possesses stable and reliable performance in the rubber isolation system among all the bearing types. Its vertical stiffness could be accurately calculated by our proposed modified equation. The main conclusions are as follows:

- (1) The vertical stiffness of the bearings increases with the growth of vertical pressure, loading frequency, and pre-pressure. Based on the premise of the equal total thickness of rubber, the vertical stiffness of LRB with thin rubber layer is much larger than that of TLRB and HDRB-LSF with thick rubber layers, and the ratio of LRB to TLRB for the vertical stiffness value reaches approximately 4. The vertical stiffness of TLRB is smaller than HDRB-LSF with equal conditions, which reflects that the material property and the thickness of the rubber material are equally crucial to the mechanical properties of the bearing.
- (2) The horizontal equivalent stiffness of LRB and TLRB with the lead core is greater than that of HDRB-LSF with high damping rubber. When the shear strain and the vertical pressure increase, the horizontal equivalent stiffness of the LRB and TLRB declines, and the gap of the stiffness between them and HDRB-LSF keeps narrowing. The hysteretic curves of HDRB-LSF and TLRB are sensitive to the change of pressure, while those of LRB show little difference. The horizontal mechanical properties of the bearings are affected by loading frequency in different degrees. The equivalent damping ratios of the bearings with lead cores remain above 30%, which is larger than those of HDRB-LSF, according to the designed damping ratios of the three bearings. However, the test results have already exhibited the good energy dissipation capacity of the three bearings. The follow-up study of HDRB-LSF will enhance its equivalent damping ratio, reaching the corresponding level of the bearings with a lead core.
- (3) The errors of the vertical stiffness of the thick rubber bearings between the test value and the theoretical value are exaggerated. Hence, the fitting modification of the theoretical vertical stiffness formula for the HDRB-LSF is carried out. The proposed modification method can better predict the vertical stiffness of the bearing under a certain vertical pressure.

- (4) In summary, unlike the LRB, which is usually used for horizontal isolation, the application of thick rubber bearings including HDRB-LSF and TLRB can simultaneously help important buildings avoid suffering the adverse effects of horizontal and vertical earthquakes on the structure itself and indoor equipment, as well as to improve the post-earthquake recovery of building structures. Compared with TLRB, HDRB-LSF is better suited for the structures when considering their larger bearing capacity and more environmentally friendly characteristics. It should be noted that the surface pressure on the thick rubber bearings should be strictly limited in engineering applications. This paper presents the results of an analytical, parametric study that aimed to further explore the low shape factor concept applied in three-dimensional isolation for building structures.

Author Contributions: Conceptualization, Z.G. and W.Q.; Data curation, Z.G. and Y.W.; Investigation, Y.L., W.Q. and F.H.; Methodology, Z.G., Y.L. and W.Q.; Project administration, W.Q.; Resources, Z.G. and W.Q.; Software, Z.X. and Y.W.; Visualization, Z.X. and F.H.; Writing—original draft, Z.G., Y.L., F.H. and Y.W.; Writing—review & editing, Z.X. All authors have read and agreed to the published version of the manuscript.

Funding: This research was funded by The National Natural Science Foundation of China (Grant No. 51808298), the Jiangsu Construction System Science and Technology Project (Grant No. 2019ZD013 and Grant No. 2019ZD017), Nantong Science and Technology Plan Project (Grant No. JC2020124 and Grant No. JC2021169), Natural Sciences Fund for Colleges and Universities in Jiangsu Province (Grant No. 20KJD560002), and Nantong University College Students' innovation and entrepreneurship training program (Grant No. 2021247). The authors appreciatively acknowledge the financial support of the abovementioned agencies.

Institutional Review Board Statement: Not applicable.

Informed Consent Statement: Not applicable.

Data Availability Statement: The data used to support the findings of this research are available from the corresponding author upon request.

Acknowledgments: The authors would like to equally thank Chenhui Zhu from the Nantong University, China, for linguistic assistance during the preparation of this manuscript. The insightful comments and significant suggestions from the anonymous reviewers of Applied Sciences are sincerely appreciated.

Conflicts of Interest: The authors declare that there are no conflict of interest.

References

1. Kilar, V.; Petrovčič, S.; Koren, D.; Silih, S. Seismic analysis of an asymmetric fixed base and base-isolated high-rack steel structure. *Eng. Struct.* **2011**, *33*, 3471–3482. [CrossRef]
2. Mazza, F. Base-isolation of a hospital pavilion against in-plane-out-of-plane seismic collapse of masonry infills. *Eng. Struct.* **2021**, *228*, 111504. [CrossRef]
3. D'Amato, M.; Laguardia, R.; Gigliotti, R. Seismic retrofit of an existing RC building with isolation devices applied at base. *Front. Built Environ.* **2020**, *6*, 82. [CrossRef]
4. Itoh, Y.; Gu, H.S. Prediction of Aging Characteristics in Natural Rubber Bearings Used in Bridges. *J. Bridge Eng.* **2009**, *14*, 122–128. [CrossRef]
5. Kalpakidis, I.V.; Constantinou, M.C.; Whittaker, A.S. Modeling strength degradation in lead-rubber bearings under earthquake shaking. *Earthq. Eng. Struct. Dyn.* **2010**, *39*, 1533–1549. [CrossRef]
6. Markou, A.A.; Manolis, G.D. Mechanical models for shear behavior in high damping rubber bearings. *Soil Dyn. Earthq. Eng.* **2016**, *90*, 221–226. [CrossRef]
7. Burtscher, S.L.; Dorfmann, A. Compression and shear tests of anisotropic high damping rubber bearings. *Eng. Struct.* **2004**, *26*, 1979–1991. [CrossRef]
8. Yamamoto, M.; Minewaki, S.; Yoneda, H.; Higashino, M. Nonlinear behavior of high-damping rubber bearings under horizontal bidirectional loading: Full-scale tests and analytical modeling. *Earthq. Eng. Struct. Dyn.* **2012**, *41*, 1845–1860. [CrossRef]
9. Chen, Y.-J.; Guo, K.-M.; Li, Y.; Chen, F. Behavior of high damping seismic isolation rubber bearings for bridges. *J. Vib. Shock* **2015**, *34*, 136–140. (In Chinese)

10. Xue, S.-D.; Gao, J.-Y.; Jiang, C.-H.; Li, X.-Y. Experimental research on mechanical performance of high damping isolation rubber bearings. *Build. Struct.* **2020**, *50*, 71–75. (In Chinese)
11. Bhuiyan, A.R.; Okui, Y.; Mitamura, H.; Imai, T. A rheology model of high damping rubber bearings for seismic analysis: Identification of nonlinear viscosity. *Int. J. Solids Struct.* **2009**, *46*, 1778–1792. [CrossRef]
12. Dong, W.-W.; Ding, Y.-G.; Sun, H. Research on mechanical properties and restoring force model of high damping rubber bearing. *Eng. Constr.* **2020**, *52*, 6–11. (In Chinese)
13. Mazza, F.; Mazza, M. Nonlinear modelling of HDRBs in the seismic analysis of retrofitted and new base-isolated rc buildings. *Structures* **2021**, *33*, 4148–4161. [CrossRef]
14. Jia, J.-F.; Ou, J.-P.; Liu, M.; Zhang, Z. Mechanical performance tests of a novel three-dimensional isolation bearing. *J. Civil Archit. Environ. Eng.* **2012**, *34*, 29–34. (In Chinese)
15. Aiken, I.D.; Kelly, J.M.; Tajirian, F.F. *Mechanics of Low Shape Factor Elastomeric Seismic Isolation Bearings*; Report No. UCB/EERC-89/13; Earthquake Engineering Research Center, University of California: Berkeley, CA, USA, 1989.
16. Warn, G.P.; Vu, B. Exploring the low shape factor concept to achieve three-dimensional seismic isolation. In Proceedings of the 20th Analysis & Computation Specialty Conference, Chicago, IL, USA, 29–31 March 2012.
17. Kanazawa, K.; Hirata, K.; Matsuda, A. Shaking table test of three-dimensional base isolation system using laminated thick rubber bearing. In Proceedings of the 15th SMIRT, Seoul, Korea, 15–20 August 1999; pp. 367–374.
18. Zhu, Y.-H.; Ai, F.-L.; Ren, X.-X.; Liu, W.-S. Mechanical properties of thick lead-rubber bearings. *J. Tongji Univ. Nat. Sci.* **2018**, *46*, 1189–1194. (In Chinese)
19. Wang, J.-W. *Research on Mechanical Performance and Stability Analysis of Thick Laminated Rubber Bearing*; Guangzhou University: Guangzhou, China, 2020. (In Chinese)
20. Liu, X.-H.; Huang, K. Analysis on vertically seismic response spectrum about seismically isolated structure with PRB. *Build. Struct.* **2019**, *49*, 469–473. (In Chinese) [CrossRef]
21. Li, J.-C.; Shang, Q.-X.; Luo, Q.-Y.; Wang, T. Tests for mechanical performance of thick rubber bearings. *J. Vib. Shock* **2019**, *38*, 157–165. (In Chinese)
22. GB/T 20688.1-2007. *Rubber Bearings Part 1: Seismic-Protection Isolators Test Methods*; Standards Press of China: Beijing, China, 2007.
23. GB/T 20688.3-2006. *Rubber Bearings Part 3: Elastomeric Seismic-Protection Isolators for Buildings*; Standards Press of China: Beijing, China, 2006.
24. Li, L.; Hu, Z.; Nie, S.; Long, X.-H. Optimum yield strength of LRB for isolated bridges under near-fault earthquake. *J. Vib. Shock* **2011**, *30*, 134–138. (In Chinese)

MDPI
St. Alban-Anlage 66
4052 Basel
Switzerland
Tel. +41 61 683 77 34
Fax +41 61 302 89 18
www.mdpi.com

Applied Sciences Editorial Office
E-mail: applsci@mdpi.com
www.mdpi.com/journal/applsci



MDPI
St. Alban-Anlage 66
4052 Basel
Switzerland

Tel: +41 61 683 77 34
Fax: +41 61 302 89 18

www.mdpi.com



ISBN 978-3-0365-6560-6